What controls the 3D distribution of water vapor isotopic composition in East Asia?

Di Wang

Thèses de doctorat de Campus Pierre et Marie Curie - Sorbonne Université

École doctorale n° 129 : Sciences de l'environnement d'Ile-de-France (SEIF)
Spécialité de doctorat : Sciences du climat, de l'atmosphère et des océans, terrestres et planétaires

What controls the 3D distribution of water vapor isotopic composition in East Asia?

Qu'est-ce qui contrôle la distribution 3D de la composition isotopique de la vapeur d'eau en Asie de l'Est ?

Thèse préparée dans l'unité de recherche LMD (Campus Pierre et Marie Curie - Sorbonne Université), en partenariat avec l'Université du Yunnan, en co-tutelle international de these, sous la direction de **Mme. Camille Risi**, chargée de recherche CNRS et de **M. Lide Tian**, scientifique senior.

préparée au
Laboratoire de Météorologie Dynamique / LMD, Paris France

présentée par

Di WANG

soutenue le 20 Novembre 2023 devant le jury composé de:

President:	**M. Aymeric Spiga**	Professeur, Sorbonne Université (France)
Rapporteurs:	**M. David Noone**	Professeur, University of Auckland (New Zealand)
	M. Hongxi Pang	Professeur, Nanjing University (China)
Examinateur-ice-s:	**Mme. Franziska Aemisegger**	Senior scientist and lecture, ETH Zurich (Switzerland)
	Mme. Adriana Bailey	Professeur associé, University of Michigan (USA)
	M. Peter Blossey	Professeur associé, Washington University (USA)
Directeur-ice-s:	**Mme. Camille Risi**	Chargée de recherche CNRS, HDR (France)
	M. Lide Tian	Scientifique senior, Yunnan University (China)

Acknowledgements

Through my doctoral studies, I have realized a lot of big or small dreams I had planted in my heart, and they have blossomed into fruition. I have even achieved some things I had never thought of, and I have gained an unprecedented experience in my life. This journey has enriched me, making me more confident and fostering a deeper love for the field of research, and I love where I am now. I find myself energized and prepared to move forward.

I would like to thank Mr. Lide TIAN's support and guidance on my research, Mr. Tian always grasps the most cutting-edge direction of our research field, and always puts forward a lot of very innovative proposals, thanks for the opportunity to be influenced by what I constantly see and hear. Thanks to Mr. Tian for giving me the opportunity to realize his ideas and grow from them. I am grateful to Mr. Tian for providing such a good platform, including labs, funding and study opportunities, so that we can have a basis for realizing our research projects. I am also grateful to Mr. Tian and Mr. Zhongyin CAI for teaching me how to do my first paper, which was a key part of my application materials for the study abroad program, so that I could carry out the subsequent work and study.

I would like to express my most sincere gratitude to my PhD advisor in France, Camille RISI, without her guidance and help, it would be difficult for me to grow so much and arrive at where I am today. I am very grateful that Camille was with me during my difficult stages and many helpless moments. I have also learned a lot from my almost weekly individual meetings with Camille: I am grateful to learn Camille's very rigorous and systematic way of thinking about research problems, arranging research plans, and writing articles; she always sees the essence of a problem very quickly, and quickly makes a judgment on what to do next. I am grateful to her for her timely feedback and continuous guidance every time.

I sincerely thank all my collaborators for their valuable comments. I am particularly grateful for the opportunity to discuss my work with Gabriel J. Bowen during various conferences and courses. His guidance consistently provided me with insightful and inspiring suggestions. Thanks to Peter Blossey and Franziska AEMISEGGER, members of my thesis committee, who met once a year to follow up on my research and provide advice on my current situation and dilemmas. I would like to thank Laurent Z.X Li for his guidance and help in research, life, work, etc., and especially for his inspiration for my post-doctoral program. It was a pleasure to work with Jiaping XU, Mingjian CHEN, Le CHAN and Yao YAO, and I would like to thank you all for your irreplaceable help in the development of the drone sampling. We were very excited to fly to 1000 meters from the ground for the first trial, then we finally achieved 11000 meters sampling. Special thanks to Le CHAN, the UAV engineer, for continuing to develop groundbreaking UAVs for our goals and realizing this observation that impressed a lot of people. Thanks to Nanjing Xinda Intelligent Technology Company for providing absolute support when we had not yet been able to pay for the associated costs, but desperately needed all kinds of supplies, including expensive transponders, so that I could get to work in a timely manner. Thank you to the other members of Mr. Tian's group now and before. In particular, I would like to thank Di YANG for her efforts and time to help me when I was unable to complete some lab work in China, which provided very important help in data calibration. Thanks Jiangpeng CUI for teaching the fundamentals of Picarro. Thanks to Pengbin

LIANG, Xuejie WANG, Mingxing TANG, and Jiangrong TAI for their participation in the field work of this thesis.

I am also grateful to be able to learn the French way of research and atmosphere, how to date and discuss with the most in-depth experts on the relevant aspects of a scientific problem; how to plan ahead; how to mentor students by following up on their thesis committee meetings every year. Thanks to the lab LMD, equality and freedom. Thanks to the China Scholarship Council, which gave me financial support to study and live in France, and found the most comfortable way of living and working, with no financial worries, and with the requirement of complete independence in many aspects of life and spirituality for two years of most growth, freedom, joy and relaxation.

I would like to thank Sandrine BONY for providing me with information on rare datasets and for meticulously revising my materials and CV before I participated the conference. Thanks to her for organizing the conference that provided me with a participation grant to meet the cloud and convective systems research community in Monterey, USA. I would like to thank her for her care and help during my Covid in USA; I would like to thank Ehouarn MILLOUR, Francois FORGET, Sebastien LEBONNOIS, Michael WOLFF who gave me a number of specific suggestions about career and postdoctoral search.·

I am very thankful to Xiaoyi Shi, who told me about the possibility of building a dual-university international joint cultivation agreement when I inquired on WeChat back in 2018, which was a key step for me to obtain a dual degree. She also helped me solve the biggest problem of renting an apartment in Paris, where I was unfamiliar with the city, and introduced me to an apartment with a very beautiful yard, which allowed me to recharge my batteries every Sunday in a beautiful and cozy environment, and which has been a source of joy for me in my two years of living in France. I am also grateful to Xuejie Wang, who put me in touch with Xiaoyi.

I am grateful for the time I shared with my friends and for their company and support. In particular, I would like to thank Siteng FAN, Yang XU, and Yitong YAO. Thanks for your experience sharing and accurate advice from "people who have been there" on every research-related topic. I am especially grateful to have your company during the period of writing my thesis, which allowed me to accomplish the goals I set every day, and to find a good working condition and accelerate my work progress through sharing with you every day. Lucky to have traveled with you, to have attended conferences together, to have listened to each other's presentations, to have shared important and unimportant things that make up the most photos of my photo albums. Thanks to my Chinese partners and colleagues who came to LMD before and after, Lei ZHU, Mengyang LIU, Xiaoting CHEN, Dexin LAI, Peng HAN, Yangcheng LUO, Shengjie WANG, Zhiyuan WANG, for celebrating the New Year's Eve together, organizing the New Year's Eve party at LMD, traveled, and having fun with a lot Chinese food together. Thanks to my classmates and friends from LMD, Antony DELAVOIS, Antoine BIERJON, Joseph NAAR, Lucas LANGE, Romain VANDMULEBROUCK Maelle COULON-DECRZENS and Thomas PIERRON for introducing me to the LMD community when I first arrived at LMD, for leading me to LMD events, for answering so many questions about studding at LMD. I cherish the time we spent together going to the restaurant for lunch, eating fondue with cheese, rock climbing, and going to the bar near the school after work. Thanks to my office roommates Romain VANDMULEBROUCK, Marine LANET, and Maelle, who

answered countless phone calls in French, and thanks to Raphael LEBRUN for answering a lot of questions about the dissertation and the defense. Thanks to Julie CARLES, Antoine EHRET for your help and encouragement during JDD. Thank you for Fu HAO, Hanyi CHEN and Xinan SHAO for playing badminton together and improving the food every week (may not every). Thanks to Zhijie SU, Xiaowen ZENG, Bei YUAN, Jun HU, and Kangkang YUAN, who have been my close friends for many years, for their care and encouragement.

Thanks to Bin WU and Feng LIU for their help and support in administrative work. I would like to thank Yanbo LI, Xingwu DUAN, and Yahui LIU, Ruowen ZHANG and Shucheng YANG for their help and support in getting me through the international joint training agreement. Thanks Juan TAO and Rongxiao CHE for answering my questions about my application. Thanks to Xian LUO, Yungang LI, Xuan JI, Xia LUO, Li RONG and Wenling WANG for their encouragement. Thanks Evelyne FRANCOIS-ELOCCIE and Ms. Karem WITT from LMD for their assistance in attending conferences abroad. Thanks to Jianshang TAO for her help with the use of lab equipment, reimbursement of expenses, and administrative matters of the college. Thanks to the teachers from the National Institute of Foreign Affairs for their assistance with the application for the CSC.

I am grateful to my family for letting me be myself, for giving me special space to do what I like to do, and for giving me support and love. I am grateful to my elfin sister for giving me joy.

August 21, 2023, Paris ✈️Shenzhen

Abstract

Unlike polar ice core records, the isotope variations in Tibetan ice cores challenge the interpretation of temperature signals. One of the main reasons is that in monsoon regions at low and middle latitudes, water isotope ratio are influenced by convective and cloud processes. A deeper understanding of water isotope behavior and the dynamical controls involved in moisture transpiration and convection is needed. Large-scale in-situ observations and vertical profiles of vapor isotopes during convection would be helpful. However, such data are rare. The aim of this thesis was to document horizontal, vertical, and temporal variations in the isotopic composition of water in East Asian monsoon region.

First, to document the horizontal and seasonal variations of water isotope ratio near the surface across China, we made in-situ observations of near-surface vapor isotopes over a large region (over 10000 km) across China in both pre-monsoon and monsoon seasons, using a newly-designed vehicle-based vapor isotope monitoring system. We found that the observed spatial variations of vapor $\delta^{18}O$ are mainly controlled by Rayleigh distillation along air mass trajectories during the pre-monsoon period, but are significantly influenced by different moisture sources, continental recycling processes, and convection along moisture transport during the monsoon period. These results provide an overview of the spatial distribution and seasonal variability of water isotopic composition in East Asia and their controlling factors and emphasize the need to interpret proxy records in the context of the regional system and moisture sources.

Second, to better understand the physical processes that control the vertical distribution of vapor isotopes and its intra-seasonal and seasonal variability, we observed the vertical profiles of atmosphere vapor isotopes up to the upper troposphere (from the ground surface at 3856m up to 11000m a.s.l., with a vertical resolution of 500 meters) from June to October in the southeastern Tibetan Plateau using a specially-designed unmanned-aerial-vehicle (UAV) system. For the sampling, we chose to carry air bags on UAVs as a portable sampling device, but encountered the permeability problem commonly associated with these bags. To corrected for this problem, we developed a diffusion model with diffusion parameters calibrated through laboratory experiments. This allows us to document for the first time the vertical distribution of atmospheric water vapor isotopes across the entire monsoon period up to the upper troposphere, boasting an unprecedented vertical resolution and altitude range. We find that the vertical profiles of water vapor isotopic composition reflect a combination of large-scale processes, in particular deep convection and continental recycling along trajectories, and local convective processes, in particular convective detrainment, and sublimation of ice crystals. The observed seasonal and intra-seasonal variations are generally vertically coherent, due to the strong vertical convective mixing and local convective detrainment of vapor originating from the low levels, and are mainly due to deep convection along trajectories.

Résumé

Contrairement aux carottes de glace polaires, les variations isotopiques dans les carottes de glace tibétaines compliquent l'interprétation des signaux de température. L'une des principales raisons est que dans les régions de mousson aux latitudes basses et moyennes, les isotopes de l'eau sont influencés par des processus convectifs et nuageux. Il est nécessaire de mieux comprendre le comportement des isotopes de l'eau et les contrôles dynamiques impliqués dans la transpiration et la convection de l'humidité. Des observations in situ à grande échelle et des profils verticaux des isotopes de la vapeur pendant la convection seraient utiles, mais ces données sont rares. Le but de cette thèse a été de documenter les variations horizontales, verticales et temporelles de la mousson d'Asie de l'Est.

D'abord, afin de documenter les variations horizontales près de la surface et saisonnières de la composition isotopique stable de l'eau en Chine, nous avons effectué des observations in situ des isotopes de la vapeur d'eau sur une vaste région de la Chine (plus de 10 000 km) pendant les saisons de pré-mousson et de mousson, à l'aide d'un système de mesure des isotopes de la vapeur d'eau nouvellement conçu et installé sur un véhicule. Nous avons constaté que les variations spatiales de la vapeur $\delta^{18}O$ sont principalement contrôlées par la distillation de Rayleigh le long des trajectoires des masses d'air pendant la saison de pré-mousson, et sont fortement influencées par différentes sources d'humidité, les processus de recyclage continental et la convection le long du transport de l'humidité pendant la saison de la mousson. . Ces résultats donnent un aperçu de la distribution spatiale et de la variabilité saisonnière de la composition isotopique de l'eau en Asie de l'Est et de leurs facteurs de contrôle, et soulignent la nécessité d'interpréter les enregistrements proxy dans le contexte du système régional et des sources d'humidité.

Ensuite, pour mieux comprendre les processus physiques qui contrôlent la distribution verticale des isotopes de la vapeur et sa variabilité intra-saisonnière et saisonnière, nous avons observé les profils verticaux des isotopes de la vapeur de l'atmosphère jusqu'à la haute troposphère (de la surface du sol à 3856 m jusqu'à 11000 m d'altitude) de juin à octobre dans le sud-est du plateau tibétain à l'aide d'un drone spécialement conçu à cet effet. Pour l'échantillonnage, nous avons utilisé des sacs d'air, mais avons rencontré des problèmes de perméabilité généralement associés à ces sacs. Pour corriger ces problèmes, nous avons développé un modèle de diffusion et en avons calibré les paramètres avec des expériences de laboratoire. Ceci nous a permis de documenter pour la première fois que la distribution verticale des isotopes de la vapeur d'eau atmosphérique pendant toute la période de la mousson jusqu'à la haute troposphère, avec une résolution verticale et une gamme d'altitudes sans précédent. Nous constatons que les profils verticaux de la composition isotopique de la vapeur d'eau reflètent une combinaison de processus à grande échelle, en particulier la convection profonde et le recyclage continental le long des trajectoires, et les processus convectifs locaux, en particulier le détrainement convectif et la sublimation des cristaux de glace. Les variations saisonnières et intra-saisonnières observées sont généralement cohérentes verticalement, en raison du fort mélange convectif vertical et du détrainement convectif local de la vapeur provenant des basses couches, et reflètent les variations de convection profonde le long des trajectoires.

Thesis abstract popularized to the public

Have you ever wondered about the stories water vapor could tell? By studying water's "fingerprints" in things like ice cores, we can peek into past climate and weather patterns. These fingerprints are called "water isotope ratio." This study documents the 3D variations of water isotope ratio across East Asia.

We embarked on an 10,000 km drive across China with an instrument that measures these isotopes right from the air. We did this before and during the monsoon. Before the monsoon season, there's a clear North-South difference in these fingerprints. But once the monsoon season rolls in, this difference gets muddled up due to the changing sources of moisture, the recycling of water over land, and the way clouds form along moisture transport.

We also employed special drones into the sky, capturing data from the surface up to 11,000m a.s.l.- the altitude where commercial planes fly! This was the first time someone had measured these water isotope ratio from the ground all the way up to those heights over a whole monsoon season. These water fingerprints told tales of convective clouds, ice crystals in them, and water recycling.

In conclusion, our research contributes to a better understanding of the intricate interplay of atmospheric processes governing water isotopic distribution across East Asia, providing additional references for the application of water isotope ratio in the hydro-atmospheric and paleoclimate.

Résumé de thèse vulgarisé au public

Vous êtes-vous déjà interrogé sur les histoires que la vapeur d’eau pourrait raconter ? En étudiant les "empreintes" de l'eau dans des éléments tels que les carottes de glace, nous pouvons jeter un coup d'œil sur les climats passés et les phénomènes météorologiques. Ces empreintes sont appelées "isotopes de l'eau". Cette étude présente une des variations 3D des isotopes de l’eau à travers Asie de l'Est.

Nous avons entrepris un voyage de 10 000 km à travers la Chine à l'aide d'un instrument qui mesure ces isotopes directement dans l’air. Nous l'avons fait avant et pendant la mousson. Avant la mousson, il y a une nette différence Nord-Sud dans ces empreintes. Mais une fois la mousson arrivée, cette différence s'estompe en raison des sources changeantes d'humidité, du recyclage de l'eau sur terre et de la façon dont les nuages se forment le long du transport de l'humidité.

Nous avons également utilisé des drones spéciaux dans le ciel, collectant des données depuis la surface jusqu'à 11 000 mètres d'altitude - l'altitude à laquelle volent les avions commerciaux ! C'était la première fois que l'on mesurait ces isotopes de l'eau depuis le sol jusqu'à ces hauteurs pendant toute une saison de mousson. Ces empreintes d'eau racontent des histoires de nuages convectifs, de cristaux de glace dans ces nuages et de recyclage de l'eau.

En conclusion, notre recherche contribue à une meilleure compréhension de l'interaction complexe des processus atmosphériques régissant la distribution des isotopes de l'eau en Asie de l'Est, fournissant des références supplémentaires pour l'application des isotopes de l'eau dans l'hydro-atmosphère et le paléoclimat.

Published content and contributions

Articles :

1. Di Wang, Lide Tian, Camille Risi, Xuejie Wang, Jiangpeng Cui, Gabriel J. Bowen, Kei Yoshimura, Zhongwang Wei, Laurent Z.X Li. Vehicle-based in situ observations of the water vapor isotopic composition across China: spatial and seasonal distributions and controls, Atmospheric Chemistry and Physics, 2022, 23, 3409–3433, https://doi.org/10.5194/acp-23-3409-2023.

Di WANG participated in the conception of the project, conducted the field observations, processed and analyzed the dat, and participated in the writing of the manuscript.

-Adapted for the contents in Chapter 2

2. Di Wang, Camille Risi, Di Yang, Lide Tian, Gabriel J. Bowen, Siteng Fan, Hans Christian Steen-Larsen. Correcting for water vapor diffusion in airbag samples for isotope composition analysis: example with drone-collected samples. (in preparation)

Di WANG participated in the design of experiments, analyzed the data, satellite and GCM outputs, and participated in the writing of the manuscript.

-Adapted for the contents in Chapter 3

3. Di Wang, Camille Risi, Lide Tian, Gabriel J. Bowen, Xuejie Wang, Jiaping Xu, Mingjiang Chen, Le Chan. Drone-Derived Atmospheric Vapor Isotope Profiles up to the Upper Troposphere Across the Entire Monsoon in the Southeastern Tibetan Plateau: Insights into Deep Convective Processes. (in preparation)

Di WANG participated in the conception of the project, developed the 10,000-metre altitude unmanned aircraft sampling and vapor isotope observation system, conducted the field observations (including flying drones), processed and analyzed the data, and participated in the writing of the manuscript.

-Adapted for the contents in Chapter 4

Patents :(All are designed for PhD projects on water isotope ratio)

1. Di Wang, Lide Tian, Jiangrong Tai, Pengbing Lian, Han Xie. An evaporation-proof high-precision information visualisation rain barrel: China, ZL 202121251627.6. 2021-12-07.
2. Di Wang, Lide Tian, Pengbing Lian, Jiangrong Tai, Shangshi Shi. A snow collection device： China，ZL202121251744.2. 2021-11-30
3. Di Wang, Lide Tian, Jiaping Xu, Bin Chen, Mingjiang Chen, Yao yao, Le Chan. A UAV-based aerial atmospheric water vapor acquisition and vapor isotope analysis device: China, ZL 202022382552.7. 2021-09-07.
4. Di Wang, Qin Liu, Lide Tian. A vehicle-borne mobile water vapor isotope observation device: China, ZL201921098630.1. 2020-02-19.
5. Di Wang, Xiaobo Sun, Lide Tian, Xuejie Wang, Mingxing Tang. A Mobile Weather Station Based on Car Skylight: China, ZL201921357774.4. 2020-01-16.
6. Di Wang, Lide Tian, Mingxing Tang, Xuejie Wang. An off-vehicle detection mount platform: China, ZL201921355641.3. 2020-01-10.

Table of contents

List of illustrations

List of tables

1 General Introduction

1.1 Definition of stable isotopes of water

Isotopes are atoms of the same element with different numbers of neutrons. Isotopes are atoms of an element with varying neutrons, such as hydrogen's forms: ^{1}H, ^{2}H (deuterium, D), and ^{3}H (tritium, T), or oxygen's forms: ^{16}O, ^{17}O, and ^{18}O. Water, primarily $H_2{}^{16}O$, also contains traces of $H_2{}^{17}O$, $H_2{}^{18}O$, HDO, and HTO. The relative proportion of these different molecules is called the isotopic composition and is quantified by the notation:

$$\delta = \left(\frac{R_{sample}}{R_{SMOW}} - 1\right) * 1000$$

R_{sample} represents the ratio of heavy to total molecules in a sample, while R_{SMOW} denotes this ratio in the international reference for Standard Mean Ocean Water (SMOW). The δ value, expressed in ‰, therefore quantify the enrichment of $H_2{}^{18}O$ and HDO isotopes, represented as $\delta^{18}O$ and $\delta^{2}H$, respectively.

Due to variations in mass numbers and chemical bond strengths, different water molecules exhibit distinct physical and chemical properties. Consequently, physicochemical processes like evaporation and condensation can result in varying proportions of water isotope ratio in different bodies of water, which is known as water isotope fractionation. Therefore, stable isotopes in water bodies serve as natural tracers for hydrological processes, offering new methods for hydrological cycle research.

The second-order d-excess parameter, as defined by (Dansgaard, 1964), usually used to indicate moisture source and evaporation conditions due to its higher sensitivity to non-equilibrium fractionation *(Jouzel et al., 1997)*. It is calculated as:

$$\text{d-excess} = \delta^{2}H - 8 * \delta^{18}O$$

1.2 The starting point of this Ph.D. project

Stable isotopic signals preserved in natural precipitation archives, such as ice cores (Jouzel, 2003; Thompson, 2000) provide information on past climatic changes. Water vapor isotopes have been used as proxies for past temperature (Jouzel, 2003), past precipitation amount (Hoffmann et al., 2003) and variations of atmospheric moisture source conditions and transport pathways (Sodemann et al., 2008). However, in tropical and mid-latitude regions, especially those experience monsoons, the water isotope ratio are subject to alterations by convective currents and cloud dynamics. This complexity amplifies in the mid- and low-latitude monsoon regions, introducing greater uncertainty in their application to contemporary hydrological processes and paleoclimatology. Consequently, to apply these isotopes effectively in paleoclimate studies, a better understanding of the factors controlling the 3D isotopic distribution of water is essential.

To better understand how water isotope ratio might be used in paleoclimates, we need to look at the mechanisms that control water isotope ratio in observable modern hydrological processes. Water vapor isotope studies can provide more information about water vapor

transport, convection, mixing, condensation, evaporation, sublimation, and other atmospheric processes (Noone, 2012). The incorporation of water vapor isotopes into general circulation models (GCMs) and it's combination with observations might enable more detailed diagnostics of the atmospheric water cycle (Galewsky et al., 2016). However, as the potential of isotopic measurements has proven difficult to translate into quantitative practical applications for the present-day atmospheric water cycle, some wonder whether isotopic measurements are really useful (Duan et al., 2018). But another interpretation of the difficulty to quantitatively use isotopic measurements to advance significant knowledge on atmospheric processes is that so far the understanding of the mechanisms controlling the 3D distribution of water vapor isotopes is too limited. Therefore, for present-day water cycle applications, it is also critical to better understand the mechanisms controlling the distribution of water vapor isotopes.

The climate in monsoon regions is characterized by its complexity and variability. High-resolution climate data that capture the dynamics and heterogeneous nature of the monsoon climate over a wide area are needed to provide valuable insights into its patterns and influencing factors. However, such observations are rare. Additionally, there have been a few high-altitude water vapor observations, with most studies focusing on the ground. The isotope-enabled GCMs simulate variations of near-surface vapor isotopes well, but the vertical profiles are rarely validated and calibrated with measured data, resulting in low simulation accuracy. While several satellite instruments can now observe the global distribution of water vapor isotopes, averaging data across several atmospheric layers, such observations have low vertical resolution. Therefore, this project aims at observing horizontal, vertical, and temporal variations in the isotopic composition of water vapor and use these observations to better understand the physical controls involved in the 3D variation of water isotope ratio. We focus on East Asian monsoon region to explore the mechanisms related to convective and cloud process. This will also provide additional basis for the interpretations of the water isotope records on the Tibetan Plateau in East Asia.

1.3 Studies on spatial distribution of water vapor isotopes

The spatial variation of water vapor isotopes closely mirrors the spatial variation observed in precipitation isotope ratio. The relationship between stable isotopes of precipitation and precipitation amount, temperature, latitude, altitude, and geographical location can be summarized as follows (Dansgaard, 1964; Galewsky et al., 2016; Rozanski et al., 1993):

- Precipitation effect: precipitation $\delta^{18}O$ values are negatively correlated with mean monthly precipitation.
- Temperature effect: precipitation $\delta^{18}O$ values are negatively related to the condensation temperature of rainfall clouds as well as surface air temperature.
- Latitude effect: precipitation $\delta^{18}O$ values are low at high latitudes.
- Elevation effect: above the same latitude, precipitation $\delta^{18}O$ values are lower at higher elevations.
- Continental effect: inland precipitation $\delta^{18}O$ values are lower than those in island areas.

The studies generally show that the composition of atmospheric water vapor stable isotopes is significantly correlated with local meteorological conditions, mainly temperature,

relative humidity, water vapor mixing ratio and other meteorological factors (Jacob and Sonntag, 2010; Wen et al., 2010; White and Gedzelman, 1984). Furthermore, the composition of atmospheric water vapor isotopes is influenced by multiple water exchange mechanisms. These encompass the mixing effects derived from large-scale circulation and local processes, including different water vapor sources (Angert et al., 2010; Steenlarsen et al., 2014; Tian et al., 2007), evapotranspiration supplementation (Gat and Matsui, 1991; Welp et al., 2008), continental recycling (Aemisegger et al., 2014; Risi et al., 2013b), and short time scales special weather conditions (Gedzelman, 2003; Lawrence and Gedzelman, 2013).

1.4 **Studies on vertical variations of water vapor isotopes**

In this section, we review the main processes controlling the isotopic vertical distribution based on previous studies.

(1) Vertical distillation

Ehhalt (1974) collected the D content in tropospheric water vapor profiles between 1965 and 1973 over various locations in the United States covering an altitude range from 0 to 9 km (later from 6 to 13 km), and the data suggested a continuous depletion of heavy isotopes through the Rayleigh distillation process. He recorrected and reanalyzed this dataset, found a decrease in the D content with altitude and a seasonal variation at all altitudes, explained by a simple one-dimensional convection model (Ehhalt et al., 2005).

(2) Effect of surface evaporation and turbulent mixing in the boundary layer

Surface evaporation provides water to the atmospheric column, while turbulent mixing distributes it vertically in the boundary layer. Since the water evaporated from the surface is usually relatively enriched, observed isotopic profiles usually show a gentle decrease with altitude in the atmospheric boundary layer (Taylor, 1972; Tsujimura et al., 2007). Such isotopic profiles in the boundary layer can be used to estimate the isotopic composition of the surface evaporation. Over land, this can be used to estimate the fraction of bare soil evaporation and evaporation (Moreira et al., 1997; Tsujimura et al., 2007) or the contribution of snow sublimation (Noone et al., 2013). The effect of turbulent mixing has been studied in detail using large-eddy simulations. Near boundary layer clouds, observed vertical profiles can be distorted by the evaporation of cloud droplets (Salmon et al., 2019; Sodemann et al., 2017).

(3) Effect of deep convection

Observed water vapor and precipitation are more depleted in areas and during seasons where convection is more intense. This relationship is called the “amount effect” (Dansgaard, 1964). Observational studies have highlighted the roles of rain evaporation(Worden et al., 2007) and of mesoscale downdrafts (Kurita, 2013) in depleting the boundary layer vapor. Modelling studies using single column models or GCMs with parameterized convection have highlighted the role of unsaturated downdrafts (Risi et al., 2008). It has also been shown that deep convection depletes the boundary layer vapor more strongly when convection is organized at the mesoscale (Lawrence et al., 2004), when the stratiform fraction of the convective system area is larger (Aggarwal et al., 2016) and when the convection peaks is high in altitude (Lacour et al., 2018). The effect of deep convection on the water vapor isotopic composition can be integrated along air mass trajectories. This is why in monsoon region, the water vapor and precipitation is often observed to be more depleted when upstream precipitation is more intense

(Gao et al., 2013; Risi et al., 2010a; Vimeux et al., 2005). Higher in altitude, near the level of convective detrainment, the observed water vapor isotopic composition is more enriched than what we would expect from a Rayleigh distillation. This is interpreted as the effect of the detrainment of ice lofted by convective updrafts that sublimate into the unsaturated environment (Kuang et al., 2003; Moyer et al., 1996; Webster and Heymsfield, 2003).

Isotopic composition at high altitude reaches up to 30 km. Brunamonti et al. (2018) obtained 63 balloon-borne measurements of temperature, water vapor, ozone and aerosol backscatter conducted within the StratoClim project from two stations at the southern slopes of the Himalayas during two main monsoon-season campaigns in Asian monsoon regions. They found that the composition of the tropopause transition layer and the lowermost stratosphere within the Asia summer monsoon anticyclone are influenced by deep convection up to 1.5-2 km above the cold-point tropopause, due to the horizontal confinement effect of Asia summer monsoon anticyclone. Hence, the vertical distributions and variability of water vapor in the Asian upper troposphere-lower stratosphere are controlled by the top height of the anticyclonic confinement in Asian summer monsoon anticyclone.

(4) Horizontal advection

At a given location and altitude, the specific humidity of an air parcel is controlled by the saturation specific humidity that it has encountered during its last saturation (Sherwood, 1996). This saturation may happen in any kind of clouds. The 3D field of specific humidity can thus reasonably well be predicted by a back-trajectory analysis combined with observations characterizing clouds. This interpretative framework is called “advection-condensation”. A similar framework can be applied for water isotope ratio. The humidity and isotopic ratio of air parcels are set to their saturation and Rayleigh values when they encounter a cloud, and then they are simply conserved during advection (Galewsky and Hurley, 2010).

1.5 **Methods for measuring atmospheric vapor isotope ratio**

In the 1990s and before, atmospheric water vapor isotope studies mainly used cumbersome and time-consuming condensation sampling (cold traps) (Dansgaard, 1953) (Ehhalt, 1974; Helliker et al., 2002) and followed by gas mass spectrometry measurements in the laboratory (Berman et al., 2013). This method has low sampling time resolution, existing the problems of collected water vapor partly adhering to the inner surfaces of the sampling system which caused measurement errors. With the new fast laser-based spectroscopic isotope analysis that has become available over the past decades, researchers can achieve real-time continuous observations of water vapor isotopes. As cavity ring down spectroscopy (CRDS) techniques improved, reliable measurements of water vapor d-excess became available from arid, high-altitude subtropical sites (Galewsky et al., 2016). It provides the possibility for measuring relatively accurate water vapor isotopes with lower water vapor content, even at high altitude.

Benefits from this laser the laser spectroscopic isotope analysis technique that has matured over the past decade, we can now install in-situ isotope analyzers on vehicles for large-scale, near-surface observations of spatial and seasonal variations in water vapor isotopes. This also allows for observations of vertical profiles with higher vertical and temporal resolution. For these profiles, since using aircraft or balloon equipped with in-situ isotope analyzers for high-altitude measurements of water vapor isotopes is prohibitively expensive, making long-term

vertical profile observations difficult, we employ propose to collect the air samples by using specifically designed instrumented UAVs and then measure water vapor isotope ratios.

1.6 **This Ph.D. project overview**

We first made in-situ observations of near-surface vapor isotopes over a large region across China in both pre-monsoon and monsoon seasons for a better understanding of the isotopic footprint during large-scale water vapor transport and the factors controlling it in different regions and seasons (chapter 2).

We then try to take a deeper dive into understanding the influence of local convective cloud processes on water isotope ratio. To achieve this, we measured the vertical profiles of vapor isotopes during convection across the entire monsoon, using our specially designed unmanned aerial vehicle (UAV) system, which brought forth both flexibility and cost-effectiveness in conducting long-term observations. However, we encounter challenges related to airbag permeability, we therefore develop a diffusion model to solve the potential sample contamination during airbags storage and estimated error margins to our observations (chapter 3).

Lastly, we use our vertical profile data up to the upper troposphere to analyze the physical mechanisms controlling the water vapor enrichment in the upper troposphere, the causes of variations in the vertical profile of d-excess, and seasonal variations in the surface water vapor isotopes, which is the most dominant source of water vapor in the vertical profile (chapter4).

Using an unprecedented dataset on spatial, seasonal, and vertical profile variations of water vapor isotopes, this thesis fosters a refined understanding of the behavior of water isotope ratio and the processes that control them in both large-scale water vapor transport (variations in the vapor source and the processes on the transport path) and in localized processes (continental recycling, convective processes and cloud microphysical processes). This thesis also offer methods for continuous and convenient observation of water vapor isotopes. This study provides additional rationale for exploring the overarching question of how water isotope ratio can be applied in modern hydrometeorological-atmospheric processes and paleoclimate, particularly in the mid- and low-latitude monsoon regions.

2 Vehicle-based in-situ observations of the water vapor isotopic composition across China: spatial and seasonal distributions and controls

2.1 Abstract

Stable water isotope ratio are natural tracers in the hydrological cycle and have been applied in hydrology, atmospheric science, ecology, and paleoclimatology. However, the factors controlling the isotopic distribution, both at spatial and temporal scales, are debated in low and middle latitudes regions, due to the significant influence of large-scale atmospheric circulation and complex sources of water vapor. For the first time, we made in-situ observations of near-surface vapor isotopes over a large region (over 10000 km) across China in both pre-monsoon and monsoon seasons, using a newly-designed vehicle-based vapor isotope monitoring system. Combined with daily and multi-year monthly mean outputs from the isotope-incorporated global spectral model (Iso-GSM) and IASI satellite to calculate the relative contribution, we found that the observed spatial variations in both periods represent mainly seasonal-mean spatial variations, but are influenced by more significant synoptic-scale variations during the monsoon period. The spatial variations of vapor $\delta^{18}O$ are mainly controlled by Rayleigh distillation along air mass trajectories during the pre-monsoon period, but are significantly influenced by different moisture sources, continental recycling processes and convection during moisture transport in the monsoon period. Thus, the North-South gradient observed during the pre-monsoon period is counteracted during the monsoon period. The seasonal variation of vapor $\delta^{18}O$ reflects the influence of the summer monsoon convective precipitation in southern China, and a dependence on temperature in the North. The spatial and seasonal variations in d-excess reflect the different moisture sources and the influence of continental recycling. Iso-GSM successfully captures the spatial distribution of vapor $\delta^{18}O$ during the pre-monsoon period, but the performance is weaker during the monsoon period, maybe due to the underestimation of local or short-term high-frequency synoptic variations. These results provide an overview of the spatial distribution and seasonal variability of water isotopic composition in East Asia and their controlling factors, and emphasize the need to interpret proxy records in the context of the regional system.

2.2 Introduction

Stable water isotope ratio have been applied to study a wide range of hydrological and climatic processes (Bowen et al., 2019; Gat, 1996; West et al., 2009). This is because water isotope ratio vary with the water phases (e.g., evaporation, condensation), and therefore produce a natural labeling effect within the global water cycle. Stable isotopic signals recorded in natural precipitation archives are used in the reconstructions of ancient continental climate and hydrological cycles due to their strong relationship with local meteorological conditions.

Examples include ice cores (Thompson, 2000; Tian et al., 2006; Yao et al., 1991), tree-ring cellulose (Liu et al., 2017), stalagmites (Van Breukelen et al., 2008), and lake deposits (Hou et al., 2007). However, unlike in polar ice cores, isotopic records in ice cores from low and middle latitudes regions have encountered challenges as temperature proxies (Brown et al., 2006; Thompson et al., 1997).

East Asian country China is the main distribution areas of ice cores in the low and middle latitudes (Schneider and Noone, 2007). Where the interpretation of isotopic variations in natural precipitation archives are debated, because they can be interpreted as recording temperature (Thompson, 2000; Thompson et al., 2000; Thompson et al., 1993; Thompson et al., 1997), regional-scale rainfall or strength of the Indian monsoon (Pausata et al., 2011), origin of air masses (Aggarwal et al., 2004; Risi et al., 2010). This is because China has a typical monsoon climate and moisture from several sources mix in this region (Domrös and Peng, 2012; Wang, 2002). In general, large parts of the country are affected by the Indian monsoon and the East Asian monsoon in summer, which bring humid marine moisture from the Indian Ocean, South China Sea, and Northwestern Pacific Ocean (Fig.2-1). During the non-monsoon seasons, the Westerlies influence most of northern China (Fig.2-1). Westerlies brings extremely cold and dry air masses. Occasional moisture flow from the Indian Ocean and/or Pacific Ocean brings moisture to southern China. Continental recycling, i.e. the moistening of the near-surface air by the evapo-transpiration from the land surface (transpiration by plants, evaporation of bare soil or standing water bodies,(Brubaker et al., 1993)), is also an important source of water vapor in both seasons. Some of the spatial and seasonal patterns of water vapor transport are imprinted in the observed station-based precipitation isotope ratio (Araguás-Araguás et al., 1998; Mei'e et al., 1985; Tan, 2014; Tian et al., 2007; Wright, 1993). However, precipitation isotope ratio can only be obtained at a limited number of stations and only on rainy days. The lack of continuous information makes it limited to analyze the effects of water vapor propagation and alternating monsoon and westerlies. In addition, the seasonal pattern and the spatial variation of water isotope ratio can strongly influenced by synoptic-scale processes, through their influence on moisture source, transport, convection and mixing processes (Klein et al., 2015; Sánchez-Murillo et al., 2019; Wang et al., 2021), which requires higher frequency observations. For example, some studies founded the impact of tropical cyclones (Bhattacharya et al., 2022; Gedzelman, 2003) the Northern Summer Intra-Seasonal Oscillation (BSISO) (Kikuchi, 2021), local or large-scale convections (Shi et al., 2020), cold front passages (Aemisegger et al., 2015), depressions(Saranya et al., 2018), and anticyclones (Khaykin et al., 2022) on water isotope ratio in the Asian region. Additional data and analysis refining our understanding of controls on the spatial and temporal variation of water isotope ratio in low-latitude regions therefore are needed.

Unlike precipitation, water vapor enters all stages of the hydrological cycle, experiencing frequent and intensive exchange with other water phases, in particular, directly linked with water isotope fractionation. Furthermore, vapor isotopes can be measured in regions and periods without precipitation, and therefore, have significant potential to trace how water is transported, mixed, and exchanged (Galewsky et al., 2016; Noone, 2008), and to diagnose large-scale water cycle dynamics. Water vapor isotope data have been applied to various applications ranging from the marine boundary layer to continental recycling, and to various geographical regions from tropical convection to polar climate reconstructions (Galewsky et al., 2016). The development of laser-based spectroscopic isotope analysis made the precise,

high-resolution and real-time measurements of both vapor $\delta^{18}O$ and $\delta^{2}H$ available in recent decades. However, most of the in-situ observation of water vapor isotopes are also station-based (e.g., (Aemisegger et al., 2014; Li et al., 2020; Steen-Larsen et al., 2017; Tian et al., 2020)), or performed during ocean cruises (Benetti et al., 2017; Bonne et al., 2019; JingfengLiu et al., 2014; Kurita, 2011; Thurnherr et al., 2020). One study made vehicle-based in-situ observations to document spatial variations, but this was restricted to the Hawaii island (Bailey et al., 2013). These observations provided new insight on moisture sources, synoptic influences, and sea surface evaporation fractionation processes. However, in-situ observations documenting continuous spatial variations at the continental scale do not exist. This paper presents the first isotope dataset documenting the spatial variations of vapor isotopes over a large continental region (over 10000 km) both during the pre-monsoon and monsoon periods, based on vehicle-based in-situ observations..

After describing our observed time series along the route (section 3.1 and 3.2), we quantify the relative contributions of seasonal-mean spatial variations and synoptic-scale variations that locally disturb the seasonal-mean to our observed time series (section 3.3). We show that our observed variations in both seasons are dominated by spatial variations, but are influenced by significant synoptic-scale variations during the monsoon period. On the basis of this, we then focus on analysing the main mechanisms underlying these distributions (section 4). Collectively, these data and analyses provide refined understanding of how the interaction of the summer monsoon and westerly circulation control water isotope ratios in East Asia.

2.3 Data and methods

2.3.1 Geophysical description

We conducted two campaigns to monitor vapor isotopes across a large part of China during the pre-monsoon (3rd to 26th March, 2019) and the monsoon (28th July to 18th August, 2018) periods, using a newly designed vehicle-based vapor isotope monitoring system (Fig.2-S1). The two campaigns run along almost the same route, with slight deviation in the far northeast of China (Fig.2-1). Our vehicle started from Kunming city in southwestern China, traveled northeast to Harbin, then turned to northwestern China (Hami), and returned to Kunming. The expedition traversed most of eastern China, with a total distance of above 10000km for each campaign.

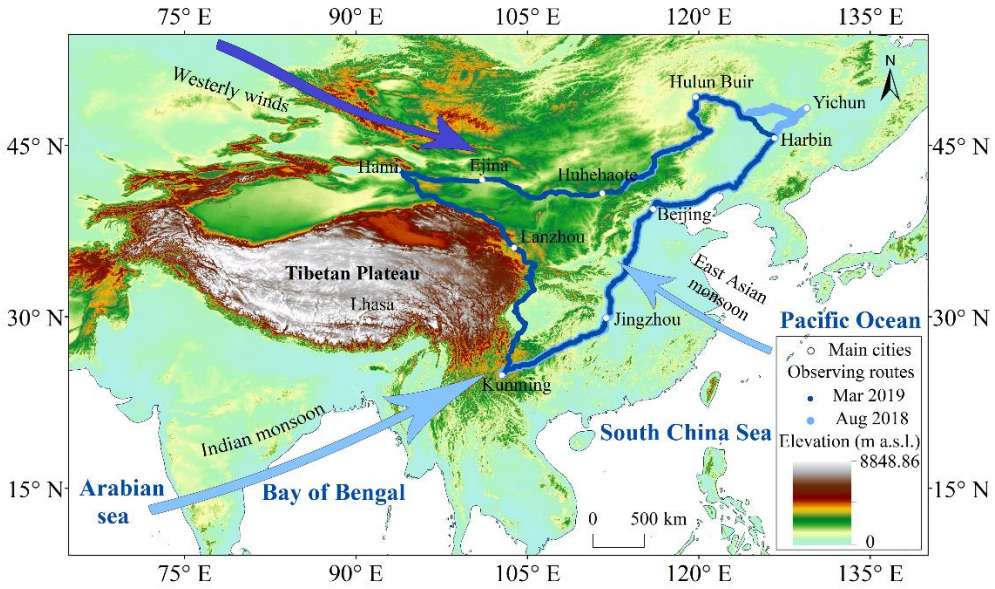

Figure 2-1 Topographical map of China, showing survey routes and the main atmospheric circulation systems (arrows). Dark blue dots indicate the observation route for the 2019 pre-monsoon period, and light blue dots show the observation route for the 2018 monsoon period, with a slight deviation in the northeast

2.3.2 Vapor isotope measurements

2.3.2.1 Isotopic definitions.

Isotopic compositions of samples were reported as the relative deviations from the standard water (Vienna Standard Mean Ocean Water, VSMOW), using the δ-notion (McKinney et al., 1950), where R_{sample} and R_{VSMOW} are the isotopic ratios ($H_2{}^{18}O/H_2{}^{16}O$ for $\delta^{18}O$, and ${}^1H^2H^{16}O/H_2{}^{16}O$ for δ^2H) of the sample and of the VSMOW, respectively:

$$\delta = (R_{sample}/R_{VSMOW}-1)*1000 \quad (1)$$

The second-order d-excess parameter is computed based on the commonly used definition (Dansgaard, 1964). The d-excess is usually interpreted as reflecting the moisture source and evaporation conditions *(Jouzel et al., 1997)*, since the d-excess is more sensitive to non-equilibrium fractionation occurs than $\delta^{18}O$:

$$\text{d-excess} = \delta^2H - 8*\delta^{18}O \quad (2)$$

2.3.2.2 Instrument

We used a Picarro 2130i CRDS water vapor isotope analyzer fixed on a vehicle to obtain large-scale in-suit measurements of near-surface vapor isotopes along the route. The analyzer was powered by a lithium battery on the vehicle, enabling over 8 hours operation with a full charge. Therefore, we only made measurements in daytime and recharged the battery at night. The ambient air inlet of the instrument was connected to the outside of the vehicle, which was 1.5 m above ground, with a waterproof cover to keep large liquid droplets from entering. A

portable GPS unit was used to record position data along the route. The measured water vapor mixing ratio and the $\delta^{18}O$ and $\delta^{2}H$ were obtained with a temporal resolution of ~1 second. The dataset present in this study had been averaged to a 10-min temporal resolution after calibration, with the horizontal footprint of about 15 km.

A standard delivery module (SDM) was used for the vapor isotope calibration during the surveys. The calibration protocols consists of humidity calibration (section 2.2.3), standard water calibration (section 2.2.4), and error estimation (section 2.2.5), following the methods of (Steen-Larsen et al., 2013). We conducted daily standard water observations throughout each campaign. Since no significant drift was observed, no additional drift corrections were performed.

2.3.2.3 Humidity-dependent isotope bias correction

The measured vapor isotopes are sensitive to air humidity (Galewsky et al., 2016; JingfengLiu et al., 2014), which vary substantially across our sampling route. The specific humidity measured by Picarro is very close to that measured by an independent sensor installed in the vehicle (Fig.2-4). The correlation between the humidity measured by the Picarro and the independent sensor are over 0.99, the slopes are approximately 1 and the average deviation are less than 1 g/kg both during pre-monsoon and monsoon periods. We develop a humidity-dependent isotope bias correction by measuring a water standard at different water concentration settings using the SDM. We define a reference level of 20,000 ppm of vapor humidity for our analysis (Eq. 3), since water vapor isotope measurement by Picarro is generally most accurate at this humidity, the calibrated vapor isotope with different air humidity would be (JingfengLiu et al., 2014; Schmidt et al., 2010):

$$\delta_{\_measured} - \delta_{\_humidity\ calibration} = f(humidity_{\_measured} - 20000) \quad (3)$$

where $\delta_{\_measured}$ represents the measured vapor isotopes (the raw data), $\delta_{\_humidity\ calibration}$ denotes the calibrated vapor isotopes, f is the function expressing δ as a function of humidity, and humidity is in ppm. E.g., if we measured that f is $\delta = a*\ln(humidity)+b$ by measuring standard water with different humidity values, then the full equation for humidity-dependent isotope bias correction would be $\delta_{\_measured} - \delta_{\_humidity\ calibration} = a*\ln(humidity_{\_measured})+b - (a*\ln(20000)+b)$.

We performed the humidity calibration before and after each campaign. In the calibration, the setting of humidity covered the actual range of humidity in the field. In the dry pre-monsoon period of 2019, the humidity was less than 5000 ppm along a large part of the route. In this case, we performed additional calibration tests with the humidity less than 5000 ppm after the field observations to guarantee the accuracy of the calibration results. The humidity-dependence calibration function is considered constant throughout each campaign (which each lasted less than 24 days).

During the pre-monsoon campaign, the correction curves are as follows:

For $\delta^{18}O$: $\delta^{18}O = 0.1612*\ln(humidity) - 11.182$

For $\delta^{2}H$: $\delta^{2}H = 1.9373*\ln(humidity) - 93.254$.

During the monsoon campaign, the correction curves are as follows:

For $\delta^{18}O$: $\delta^{18}O = 0.4179*\ln(humidity) - 14.017$

For $\delta^{2}H$: $\delta^{2}H = 2.6131*\ln(humidity) - 101.33$.

2.3.2.4 Measurement normalization

All measured vapor isotope values were calibrated to the VSMOW-SLAP scale using two laboratory standard waters ($\delta^{18}O = -10.33‰$ and $\delta^{2}H = -76.95‰$, $\delta^{18}O = -29.86‰$ and $\delta^{2}H = -222.84‰$) covering the range of the expected ambient vapor values. We made the normalization test prior to the daily measurements (two humidity levels for each standard water). We adjusted the amount of the liquid standard injected everyday to keep the humidity of the standard waters consistent with the outside vapor measurements. Our calibration shows that no significant drift of the standard values were observed over time in the observation periods (For two standard waters, the standard deviation of standard measurements are 0.2‰ and 0.11‰ for $\delta^{18}O$, and 1.16‰ and 1.2‰ for $\delta^{2}H$ during the pre-monsoon period of 2019. During the monsoon period of 2018, the standard deviation of standard measurements are 0.09‰ and 0.06‰ for $\delta^{18}O$, and 0.6‰ and 0.33‰ for $\delta^{2}H$.).

2.3.2.5 Error estimation

We estimate the uncertainty based on the error between the measured (after calibration) and true values of the two standards used during the campaigns. The estimated uncertainty is in the range of -0.05~0.17 for $\delta^{18}O$, 0.11~1.19 for $\delta^{2}H$, and -0.81~1.23‰ for d-excess during the pre-monsoon period of 2019, with the humidity ranges from 2000 ppm to 29000 ppm. During the monsoon period of 2018, the range of uncertainty is -0.10~0.55‰ for $\delta^{18}O$, -0.94~3.74‰ for $\delta^{2}H$, and -1.18~1.49‰ for d-excess, with the humidity ranges from 4000 to 34000 ppm.

2.3.2.6 Data processing

A few isotope measurements with missing GPS information were excluded from the analysis. Since we want to focus on large-scale variations, we also removed the observations during raining or snowing, to avoid situations where hydrometeor evaporation significantly influenced the observations (Tian et al., 2020). Such data represents only 0.03% and 0.05% of our observations, respectively (totally 48 data during pre-monsoon season and 59 data during the monsoon season). We observed several d-excess pulses with extremely low values as low as −18.0‰ during the pre-monsoon period and -4.9‰ during the monsoon period. These low values are unusual in previous natural vapor isotope studies and occurred mostly when the measurement vehicle was entering or leaving cities and/or stuck in traffic jams, and have a much lower intercept in the linear $\delta^{18}O$ - $\delta^{2}H$ relationship (Fig.2-S6). Previous studies on urban vapor isotopes (Fiorella et al., 2019; Fiorella et al., 2018; Gorski et al., 2015) showed that the vapor d-excess closely tracked changes in CO_2 through inversion events and during the daily cycle dominated by patterns of human activity, and combustion-derived water vapor is characterized by a low d-excess value due to its unique source. We also find that the d-excess values are especially low when the vehicle was in cities in the afternoon. The values increased to normal during the night. This diurnal cycle is likely related to the emission intensity and atmospheric processes (Fiorella et al., 2018). Some of these d-excess anomalies are not

excluded from being affected by the baseline effects emerging from rapid changes in concentrations of different trace gases (Gralher et al., 2016; Johnson and Rella, 2017). We therefore excluded these data (133 data points during the pre-monsoon period and 62 data points during the monsoon period, represents 0.10% and 0.06% of our observations, respectively) in the discussion on the general spatial feature (except Fig.2-4). Outside towns, country sources, such as irrigation, farms, and power plants, cannot be completely ruled out. However, we expect their influence to be much smaller than large-scale spatial variations.

2.3.3 Meteorological observations

We fixed a portable weather station on the roof of the vehicle to obtain air temperature (T), dew-point temperature (T_d), air pressure (Pres) and relative humidity (RH). All sensors were located near the ambient air intake. The specific humidity (q) of the near-surface air was calculated from T_d and Pres. Meteorological data, GPS location data and vapor isotope data were synchronized according to their measurement times. And all of them also had been averaged to a 10-min temporal resolution.

National Centers for Environmental Prediction/ National Center for Atmospheric Research (NCEP/NCAR) 2.5-deg global reanalysis data are used to determine the large-scale factors influencing the spatial pattern of the vapor isotopes, including the surface T, q, U-wind and V-wind, and RH, which are available at https://psl.noaa.gov/data/gridded/data.ncep.reanalysis.surface.html. Some missing meteorological data (during the pre-monsoon period: q on 8th March and 18th March 2019; during the monsoon period: T and q from 28th July to 31st July, q on 5th August) along the survey routes due to instrument failure are acquired from the NCEP/NCAR reanalysis data. To match the vapor isotope data along the route, we linearly interpolate the NCEP/NCAR data to the location and time of each measurement. The interpolated T and q from NCEP/NCAR are highly correlated with our measurement as shown in Figure 2-4h and j. The 1-deg precipitation amount (P) from the Global Precipitation Climatology Project (GPCP) are used (https://www.ncei.noaa.gov/data/global-precipitation-climatology-project-gpcp-daily/access/). When comparing the time series of GPCP data with our observed isotopes, we linearly interpolate the daily GPCP data to the location of each observation location (P-daily).We also used the average of the GPCP precipitation over the entire observation period of about one month for each observation location (P-mean). The 2.5-deg outgoing longwave radiation (OLR) data can be obtained from NOAA (http://www.esrl.noaa.gov/psd/data/gridded/data.interp_OLR.html).

2.3.4 Back-trajectory calculation and categorizing regions based on air mass origin

The vapor isotope composition is a combined result of moisture source (Araguás-Araguás et al., 1998; Tian et al., 2007), condensation and mixing processes along the moisture transport route (Galewsky et al., 2016). To interpret the observed spatial-temporal distribution of vapor isotopes, we start with a diagnosis of the geographical origin of the air masses and then analyze

the processes along the back-trajectories.

To trace the geographical origin of the air masses, the HYSPLIT-compatible meteorological dataset of the Global Data Assimilation System (GDAS) is used (available at ftp://arlftp.arlhq.noaa.gov/pub/archives/gdas1/). We select the driving locations every 2 hours as starting points for the backward trajectories, and make 10-day back-trajectories from 1000 m above ground using the Hybrid Single Particle Lagrangian Integrated Trajectory Model 4 (HYSPLIT4) (Draxler and Hess, 1998). This is representative of the water vapor near the ground (Guo et al., 2017;Bershaw et al., 2012), since most water vapor in the atmosphere is within 0–2 km above ground level (Wallace and Hobbs, 2006). The T, q, P and RH along the back-trajectories are also interpolated by HYSPLIT4 model (Fig.2-2).

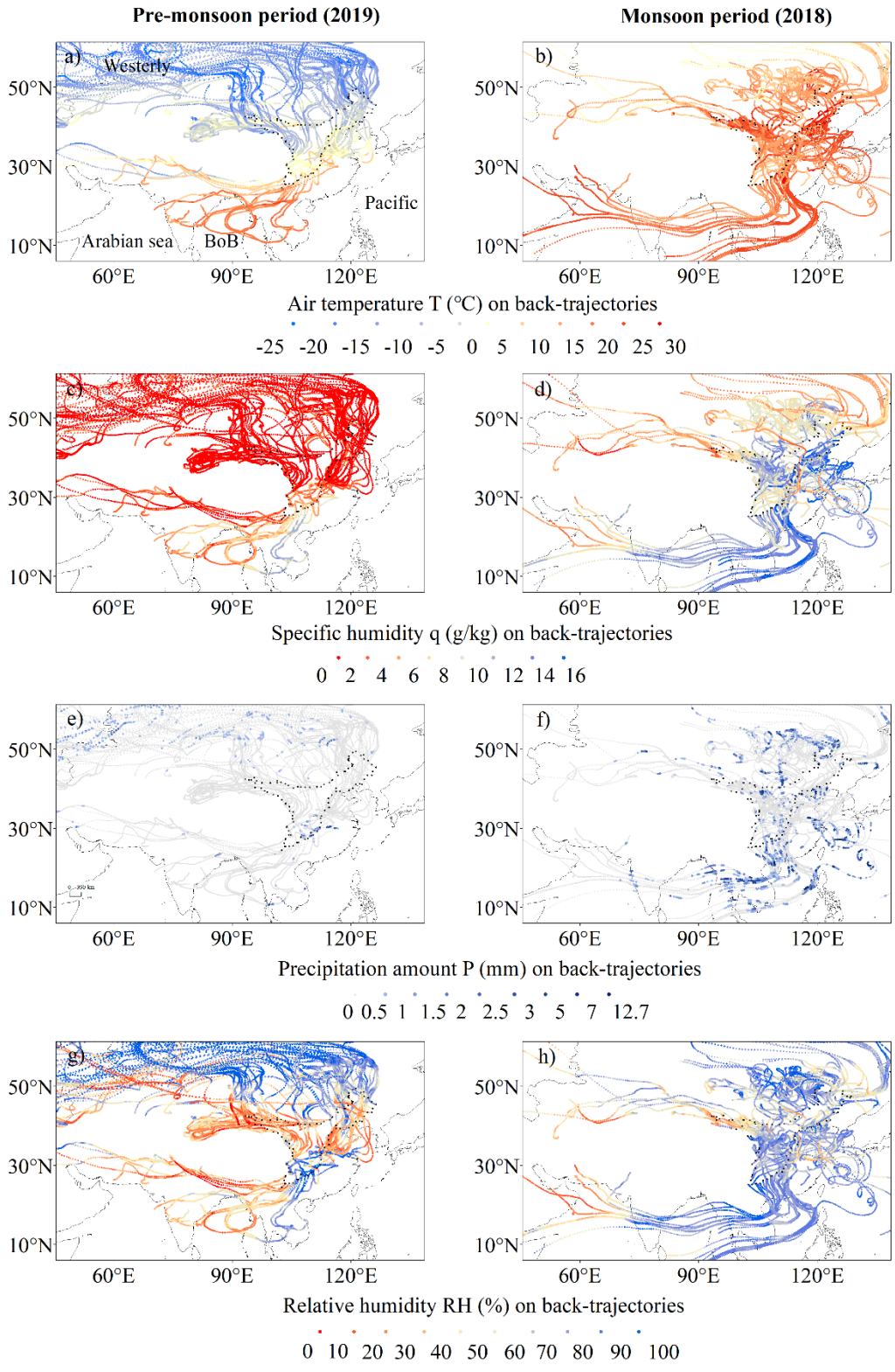

Figure 2-2 Meteorological conditions simulated by HYSPLIT4 model along the 10-day air back-trajectories for the on-route sampling positions during the two surveys: (a, b) air temperature T (℃), (c, d) specific humidity q (g/kg), (e, f) precipitation amount P (mm) and (g, h) relative humidity RH (%). The left panel is for the pre-monsoon period and the right is for the monsoon period. The driving locations and time every 2 hours are used as starting points. Note: BoB is the

abbreviation for the Bay of Bengal.

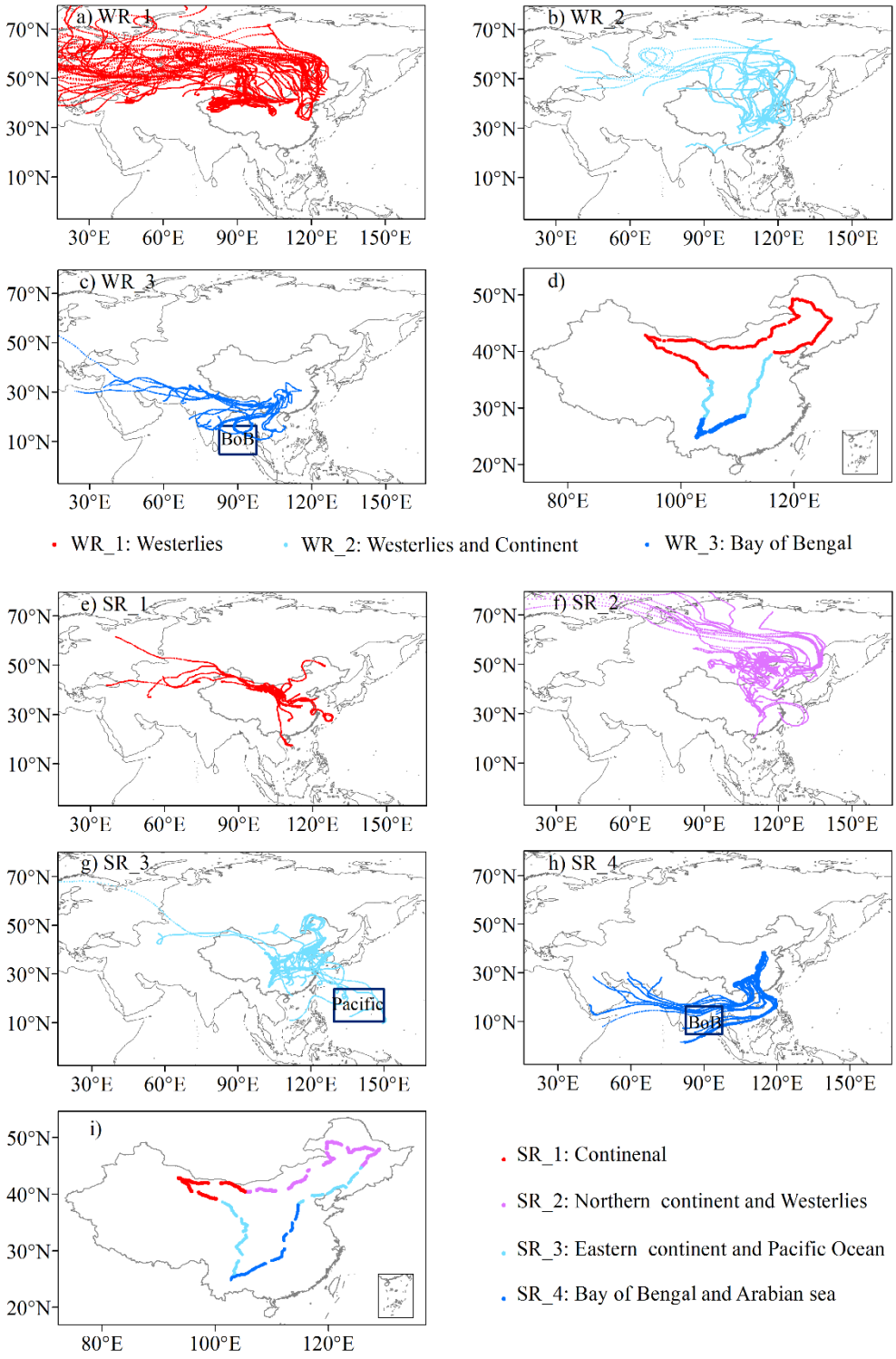

Figure 2-3 The backward trajectory results (a, b and c for the pre-monsoon period, and e, f, g and h for the monsoon period) and the dividing of the study zones based on geographical origin of the air masses (d for the pre-monsoon period and i for the monsoon period). Note: BoB is the abbreviation for the Bay of Bengal.

Based on the tracing results from HYSPLIT4 model, we speculate on the potential water

vapor sources (Fig.2-3 and Table 2-1):

During the pre-monsoon period, we categorize our domain into 3 regions (Table 2.1).

(1) In northern China (WR_1), the air is mainly advected by the Westerlies.

(2) In central China (WR_2), the air also comes from the Westerlies but with a slower wind speed (as shown by the shorter trajectories in 10 days), suggesting potential for greater interaction with the land surface and more continental recycling as moisture source.

(3) In southern China (WR_3), trajectories come from the Southwest and South with marine moisture sources from the Bay of Bengal (BoB).

During the monsoon period, we categorize our domain into 4 regions (Table 2.1):

(1) In northwestern China (SR_1), most air masses also spend considerable time over the continent, suggesting some of the vapor can be recycled by continental recycling.

(2) In northeastern China (SR_2), trajectories mainly come from the North and though the Westerlies.

(3) In central China (SR_3), both in its eastern (from Beijing to Harbin) and western part, trajectories mainly come from the East. This suggests that vapor mainly comes from the Pacific Ocean, or from continental recycling over eastern and central China.

(4) In southeastern China (SR_4), trajectories come from the South, suggesting marine moisture sources from the Arabian Sea and the BoB.

Table 2-1 The dividing of the study zones based on moisture sources and corresponding vapor $\delta^{18}O$-$\delta^{2}H$ relationship

Pre-monsoon period (2019)				
	Water sources (Fig.2-3)	Region (China)	Climate background	$\delta^{18}O$-$\delta^{2}H$ relationship
WR_1	Westerlies	The north	Westerlies domain	$\delta^{18}O=8.04\delta^{2}H+12.00$ ($r^2=0.99$, n=750, q<0.01)
WR_2	Westerlies and Continent	The middle	Transition domain	$\delta^{18}O=8.26\delta^{2}H+23.15$ ($r^2=0.99$, n=281, q<0.01)
WR_3	Bay of Bengal (BoB)	The south	Monsoon domain	$\delta^{18}O=7.98\delta^{2}H+17.13$ ($r^2=0.94$, n=158, q<0.01)
Monsoon period (2018)				
	Water sources (Fig.2-3)	Region (China)	Climate background	$\delta^{18}O$-$\delta^{2}H$ relationship
SR_1	Continent	The northwest	Transition domain	$\delta^{18}O=8.31\delta^{2}H+20.92$ ($r^2=0.99$, n=200, q<0.01)
SR_2	Northern continent & Westerlies	The northeast	Transition domain	$\delta^{18}O=7.53\delta^{2}H+5.13$ ($r^2=0.98$, n=294, q<0.01)
SR_3	Eastern continent & Pacific Ocean	The middle and west	Transition domain	$\delta^{18}O=7.49\delta^{2}H+7.09$ ($r^2=0.97$, n=271, q<0.01)
SR_4	BoB & Arabian sea	The southeast	Monsoon domain	$\delta^{18}O=8.21\delta^{2}H+17.81$ ($r^2=0.99$, n=195, q<0.01)

2.3.5 General circulation model simulation and satellite measurements

To disentangle the spatial and synoptic influences, we use surface layer variables from an isotope-enabled general circulation model (Iso-GSM) simulations (Yoshimura and Kanamitsu, 2009) at 1.915° x 1.875° and the lowest level (the altitude are about 2950m) isotope retrievals from satellite Infrared Atmospheric Sounding Interferometer (IASI) at 1°x1°. For both dataset, we use the outputs corresponding to the observation location and the observation date (daily outputs), and the multi-year monthly-mean outputs (March monthly for the pre-monsoon period and August monthly for the monsoon period) for each observation location from 2015 to 2020. When interpolating daily/multi-year monthly outputs, we select the nearest grid point for a given latitude and longitude of each measurement. For Iso-GSM simulations, because of the coarse resolution of the model, there is a difference between the altitude observed along the sampling route and that of the nearest grid point. Therefore, we correct the outputs of Iso-GSM for this altitude difference (the method is given in III. Supplementary Text). Since the satellite only retrieves δ^2H, we just use δ^2H outputs of Iso-GSM and satellite to quantify the relative contributions of seasonal-mean and synoptic-scale variations, taking into account model errors (section 3.3). Other than that, our discussion focuses on $\delta^{18}O$ and d-excess. The variations of δ^2H are consistent with those of $\delta^{18}O$. We also interpret the biases in Iso-GSM after we understand the factors influencing the spatial and seasonal variation of vapor isotopes (section 4.6).

2.3.6 Method to decompose the observed daily variations

The temporal variations observed along the route for a given period represent a mixture of synoptic-scale perturbations, and of seasonal-mean spatial distribution:

$$\delta^2H_{\_daily} = \delta^2H_{\_seaso} + \delta^2H_{\_synoptic} \quad (4)$$

The first term represents the contribution of seasonal-mean spatial variations, whereas the second term represents the contribution of synoptic-scale variations. Since these relative contributions are unknown, we use outputs from Iso-GSM and IASI. The daily variations of δ^2H simulated by Iso-GSM also represent a mixture of synoptic-scale perturbations and seasonal-mean spatial distribution, but with some errors relative to reality:

$$\delta^2H_{\_daily\_Iso\text{-}GSM} = \delta^2H_{\_seaso\_Iso\text{-}GSM} + \delta^2H_{\_synoptic\_Iso\text{-}GSM} \quad (5)$$

where $\delta^2H_{\_daily\_Iso\text{-}GSM}$ is the daily outputs of δ^2H for each location, $\delta^2H_{\_seaso\_Iso\text{-}GSM}$ is the multi-year monthly outputs of δ^2H for each location, and $\delta^2H_{\_synoptic\_Iso\text{-}GSM} = \delta^2H_{\_daily\_Iso\text{-}GSM} - \delta^2H_{\_seaso\_Iso\text{-}GSM}$, each of these terms are affected by errors relative to observations:

$$\delta^2H_{\_daily\_Iso\text{-}GSM} = \delta^2H_{\_daily} + \in = (\delta^2H_{\_seaso} + \in_{\_seaso}) + (\delta^2H_{\_synoptic} + \in_{\_synoptic}) \quad (6)$$

where $\in_{\_seaso}$ and $\in_{\_synoptic}$ are the errors on $\delta^2H_{\_seao\_Iso\text{-}GSM}$ and $\delta^2H_{\_synoptic\_Iso\text{-}GSM}$ relative to reality, respectively, $\in$ is the sum of $\in_{\_seaso}$ and $\in_{\_synoptic}$.

Correspondingly, $\delta^2H_{\_daily} = \delta^2H_{\_daily\_Iso\text{-}GSM} - \in = (\delta^2H_{\_seaso\_Iso\text{-}GSM} - \in_{\_seaso}) + (\delta^2H_{\_synoptic\_Iso\text{-}GSM} - \in_{\_synoptic})$ (7)

These individual error components $\in_{\_seaso}$ and $\in_{\_synoptic}$ are unknown, but we know the sum of them ($\in$), i.e. the difference between daily outputs and observations. For the decomposition,

we made two extreme assumptions to estimate upper and lower bounds on the contribution values:

(1) If we assume that the error is purely synoptic, i.e. $\in = \in_{\_synoptic}$, and $\in_{\_seaso} = 0$, then:

$$\delta^2H_{\_daily} = \delta^2H_{\_seaso\_Iso\text{-}GSM} + (\delta^2H_{\_synoptic\_Iso\text{-}GSM} - \in) \quad (8)$$

To evaluate the contribution of these two terms, we calculate the slopes of $\delta^2H_{\_daily}$ as a function of $\delta^2H_{\_seaso\_Iso\text{-}GSM}$ ($a_{\_seaso}$), and of $\delta^2H_{\_daily} - \delta^2H_{\_seaso\_Iso\text{-}GSM}$ ($a_{\_synoptic}$). The relative contributions of spatial and synoptic variations correspond to $a_{\_seaso}$ and $a_{\_synoptic}$ respectively. This will be the upper bound for the contribution of synoptic-scale variations, since some of the systematic errors of Iso-GSM will be included in the synoptic component. This is equivalent to using the seasonal-mean of Iso-GSM and the raw time series of observations.

(2) If we assume that the error is purely seasonal-mean, i.e. $\in = \in_{\_seaso}$, and $\in_{\_synoptic} = 0$, then:

$$\delta^2H_{\_daily} = (\delta^2H_{\_seaso\_Iso\text{-}GSM} - \in) + \delta^2H_{\_synoptic\_Iso\text{-}GSM}. \quad (9)$$

To evaluate the contribution of these two terms, we calculate the slopes of $\delta^2H_{\_daily\_Iso\text{-}GSM}$ as a function of $\delta^2H_{\_seaso\_Iso\text{-}GSM} - \in$ ($a_{\_seaso}$), and of $\delta^2H_{\_daily} - (\delta^2H_{\_seaso\_Iso\text{-}GSM} - \in)$ ($a_{\_synoptic}$). This will be the lower bound for the contribution of synoptic-scale variations, since we expect Iso-GSM to underestimate the synoptic variations.

The same analysis is also performed for δ^2H retrieved from IASI, and the Iso-GSM simulation q (Table 2.2) and reanalysis q (Table 2.3).

2.4 Spatial and seasonal variations

2.4.1 Raw time series

Our survey of the vapor isotopes yields two snapshots of the isotopic distribution along the route (Fig.2-4 & Fig.2-5). Figure 2-4 shows the variations of observed 10-min averaged surface vapor $\delta^{18}O$ and d-excess along the survey route across China during the pre-monsoon and monsoon campaigns. The figure also shows the concurrent meteorological data from the weather station installed on the vehicle and the water vapor content recorded by the Picarro water vapor isotope analyzer as a comparison. We extract daily precipitation amount (P-daily) and average precipitation amount over the entire observation period of about one month for each observation location (P-mean) (mm/day) from GPCP. The vapor $\delta^{18}O$ shows high magnitude variations in both seasons. A general decreasing-increasing trend overlapped with short-term fluctuations is observed during the pre-monsoon period, whereas no general trend but frequent fluctuations characterized the monsoon period. The $\delta^{18}O$ range is much larger during the pre-monsoon period (varying between -44‰ and -8‰) than during the monsoon period (from -11‰ to -23‰). Most measured vapor d-excess values ranges from 5 to 25‰ during the pre-monsoon period and from 10 to 22‰ during the monsoon period.

Comparison with the concurrently observed meteorological data shows a robust air temperature (T) dependence of the vapor $\delta^{18}O$ variations. In particular, the general trend of $\delta^{18}O$ is roughly consistent with T variation during the pre-monsoon period (Fig.2-4a and g). During the pre-monsoon period, humidity (Fig.2-4e and i), P-mean (Fig.2-4k) and vapor $\delta^{18}O$ (Fig.2-4a) are much higher in southwestern China (at the beginning and end of the campaign) than in

any other regions. Humidity, q, and P-mean also vary consistently throughout the route during the monsoon period (Fig.2-4f, j, l). Synoptic effects on the observed vapor isotopes are discussed in detail in Section 4.3 and 4.6.

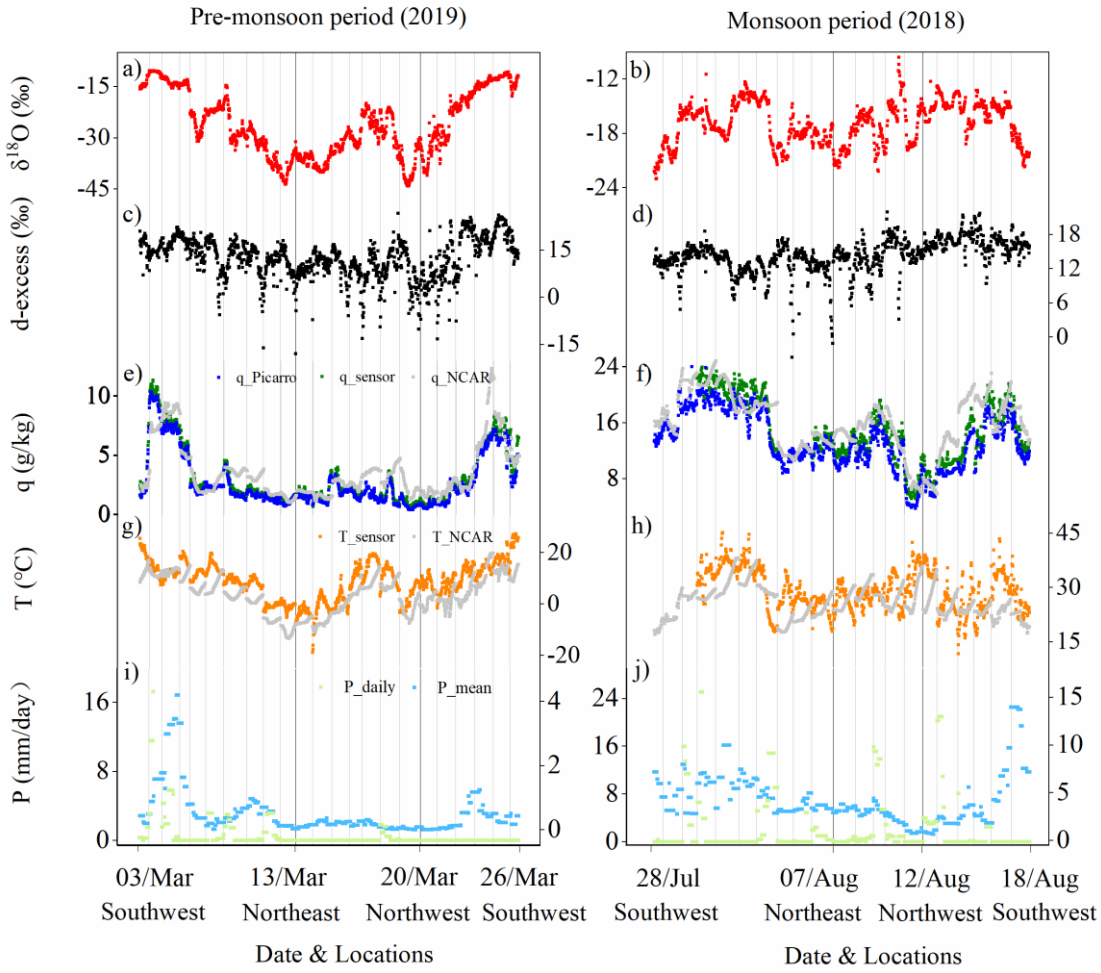

Figure 2-4 Measured vapor isotopic compositions and concurrent meteorological conditions along the survey routes during the pre-monsoon period (the left panel) and monsoon period (the right panel). (a, b) vapor δ18O (‰); (c, d) vapor d-excess (‰); (e, f) specific humidity q (g/kg) measured by sensor (in green), measured by Picarro (in blue) and linearly interpolate from NCAR reanalysis (in grey); (g, h) air temperature T (°C) measured by Picarro (in orange) and linearly interpolate from NCAR reanalysis (in grey); (i, j) the daily precipitation amount P-daily (in green, mm/day) and average precipitation amount over the entire observation period of about one month for each observation location P-mean (in blue, mm/day) extract from GPCP. Notes: the gray dots are T and q linearly interpolate from NCAR reanalysis to compensate for missing observations; Gray vertical lines space the observations for one day.

2.4.2 Spatial variations

The spatial distribution of the observed vapor $\delta^{18}O$ and d-excess during the two surveys in different seasons are presented in Figure 2-5. During the pre-monsoon period, we find a south-north gradient of vapor $\delta^{18}O$ (Fig.2-5a). The vapor $\delta^{18}O$ ranges from -8~ -16‰ in southern

China to as low as -24 ~ -44‰ in the North. A roughly similar spatial pattern is observed for the vapor d-excess during the pre-monsoon period (Fig.2-5c). The d-excess value ranges from 10 to 30‰ in southern China and from -10 to +20‰ (most observations with values from 5 to +20‰) in northern China. In previous studies, a higher precipitation d-excess during the pre-monsoon period was also observed in the Asian monsoon region owing to the lower relative humidity (RH) at the surface in the moisture source region (Jouzel et al., 1997; Tian et al., 2007). The same reason probably explains the higher vapor d-excess in southern China observed here. Alternatively, the high d-excess in south China could also result from the moisture flow from Indian/Pacific Ocean, or from the deeper convective mixed layer in south China compared to north China. The lower d-excess values (as low as −10‰ to 10‰) in northern China (between 38°N and 51°N) have rarely been reported in earlier studies. The spatial distribution of the observed vapor d-excess could reflect the general latitudinal gradient of d-excess observed at the global-scale, with a strong poleward decrease in midlatitudes (between around 20 to 60°), which were found in previous studies on large-scale distribution of d-excess in vapor (Thurnherr et al., 2020;Benetti et al., 2017) and precipitation (Bowen and Revenaugh, 2003; Pfahl and Sodemann, 2014; Risi et al., 2013a; Terzer-Wassmuth et al., 2021), based on both observations and modelling. During the monsoon period, the lowest values of vapor $\delta^{18}O$ are found in southwestern and northeastern China, with a range of -23‰ to -19‰ (Fig.2-5b). Higher vapor $\delta^{18}O$ values up to -11‰ are founded in central China. The vapor d-excess values (Fig.2-5d) in western and northwestern China (91°E-109°E, 24°N-43°N) are roughly between 16 and 22‰, higher than in eastern China (mostly between 0 and 16‰).

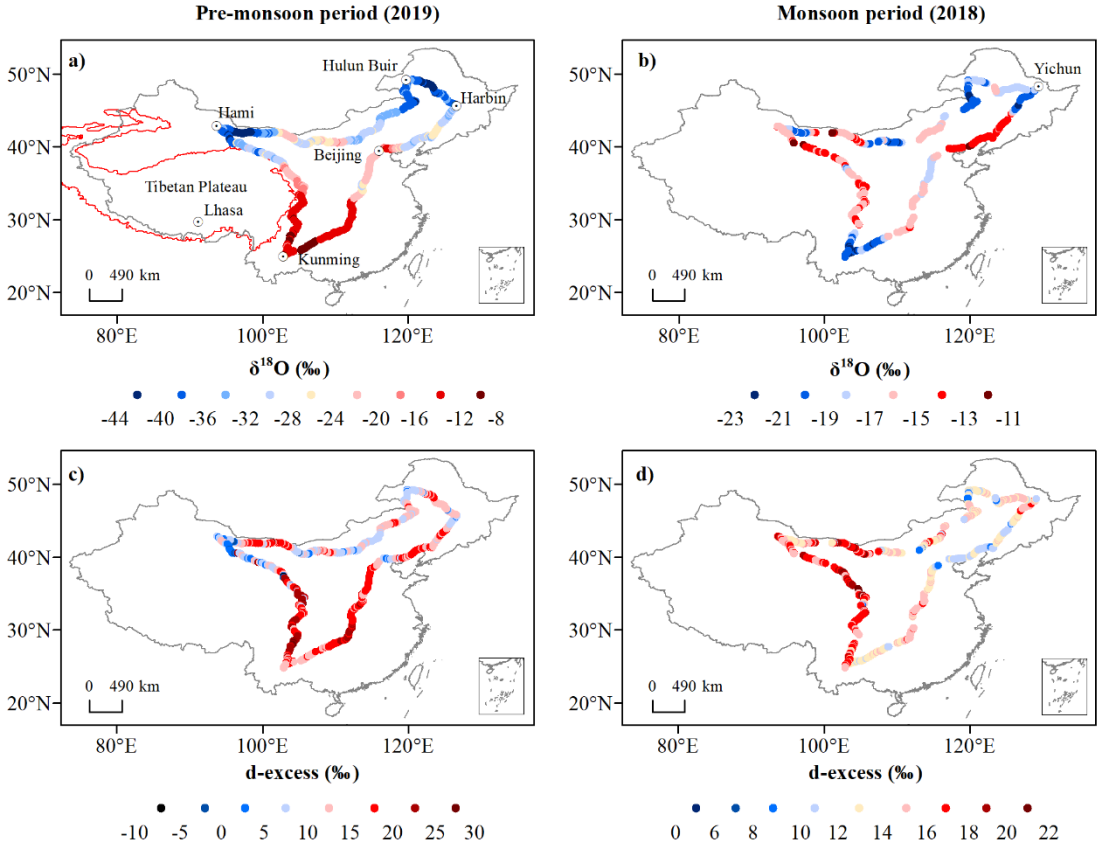

Figure 2-5 Spatial distribution of vapor $\delta^{18}O$ (a, b) and d-excess (c, d) during the pre-monsoon period (the left panel) and monsoon period (the right panel).

We don't know whether these apparent spatial variations represent the seasonal-mean, or whether it is mainly affected by synoptic perturbations. We therefore use Iso-GSM simulation results and IASI satellite measurements to quantify the relative contributions of seasonal-mean and synoptic perturbations in section 3.3.

2.4.3 Disentangling seasonal-mean and synoptic variations

Figure 2-6 shows the comparison of the measured vapor δ^2H, simulated δ^2H from Iso-GSM, and the δ^2H retrieves from IASI. Iso-GSM captures the variations in observed vapor δ^2H well during the pre-monsoon period, with correlation coefficient of $r = 0.84$ ($p<0.01$) (Table S3). The daily simulation results during the monsoon period are roughly in the range of observations, but detailed fluctuations are not well captured, with $r = 0.24$ ($p>0.05$) (Table S3). The largest differences occur in the SR_1 zone. IASI captures variations better than Iso-GSM during the monsoon period, with $r = 0.42$ ($p>0.05$). IASI observes over a broad range of altitudes above the ground level, so we expect lower δ^2H in IASI relative to ground-surface observations, but the variations of vapor isotopes are vertically coherent (Fig.2-6). The systematic differences between IASI and ground-level observations do not impact the slope of the correlation, and thus doesn't impact the contribution estimation.

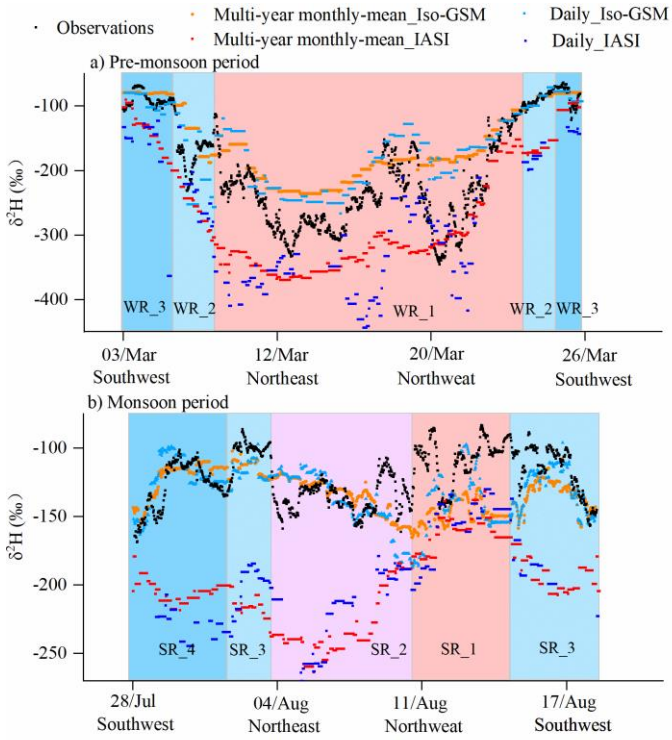

Figure 2-6 Comparison of observed vapor δ^2H (observations) with outputs of isotope-enabled general circulation model Iso-GSM and satellite IASI during the pre-monsoon period (a) and monsoon period (b). The results in this graph are from the daily and multi-year monthly outputs for the sampling locations.

The multi-year monthly-mean of δ^2H are smoother but similar to those for the daily outputs both from Iso-GSM and IASI (Fig.2-6). Using the method in section 2.6, taking into account the error, we calculate the relative contribution ranges of the seasonal-mean and synoptic-scale on our observed variations using q and δ^2H from Iso-GSM simulations, q from NCEP/NCAR reanalysis, and δ^2H from IASI.

Table 2-2 The relative contribution (in fraction) of spatial variations for a given season (a_seaso) and of synoptic-scale variations (a_synopic) to the daily variations of q and δ^2H simulated by Iso-GSM. We checked that the sum of a_seaso and a_synoptic is always 1. The two values indicate the lower and upper bounds as calculated from equations 8 and 9.

Period	Data	Variables	Controbutions	
			$a_{\_seaso}$	$a_{\_synoptic}$
Pre-monsoon (2019)	Iso_GSM	q	0.73~1.02	0.27~-0.02
		δ^2H	0.60 ~0.98	0.40~0.02
	IASI	δ^2H	1.06~0.94	-0.06~0.06
Monsoon (2018)	Iso_GSM	q	0.71~0.82	0.29~0.18
		δ^2H	0.09~0.87	0.91~0.13
	IASI	δ^2H	0.53~0.84	0.47~0.16

Table 2-3 The same as Table 2.2, but for reanalysis q.

Period	Variables	Controbutions	
		$a_{\_seaso}$	$a_{\_synoptic}$
Pre-monsoon (2019)	q	0.77~0.92	0.23~0.08
Monsoon (2018)	q	0.69~0.95	0.31~0.05

During the pre-monsoon period, based on both the Iso-GSM simulation and NCEP/NCAR reanalysis, we can find that the seasonal-mean contribution to the measured q is higher than the synoptic-scale contribution: $a_{\_seaso}$ is 73%~102% from Iso-GSM and 77%~92% from reanalysis, whereas $a_{\_synoptic}$ is 27% ~ -2% from Iso-GSM and 23% ~ 8% from reanalysis (Table 2.2 and Table 2.3). The relative contribution of seasonal-mean spatial variations to the total measured variations in δ^2H (60% ~ 98%) is also higher than that of synoptic-scale variations (40% ~2%). This suggests that the observed variability in q and δ^2H is mainly due to spatial variability, and marginally due to synoptic-scale variability. During the monsoon, seasonal-mean spatial variations are also the main contributions to the observed variations of q ($a_{\_seaso}$ is 71% ~ 82% from Iso-GSM and 69% ~ 95% from reanalysis, whereas $a_{\_synoptic}$ is 18% ~ 29% from Iso-GSM and 5% ~ 31% from reanalysis). Since Iso-GSM doesn't capture daily variations of δ^2H very well during the monsoon period, the relative contribution has a large threshold range ($a_{\_seaso}$ is 9%~87%, $a_{\_synoptic}$ is 91% ~ 13%) after accounting for the errors. Therefore, we can not conclude the dominate contribution on δ^2H from Iso-GSM outputs. IASI, which has a higher

correlation with observations, provides an more credible range of $a_{\_seaso}$ about 53% ~ 84%, and $a_{\_synoptic}$ 16% ~ 47%. These suggests that during the monsoon period, the synoptic contribution can be significant, but not dominate. Having understood the factors influencing the spatial and seasonal variation of vapor isotopes in section 4, we will be able to better understand the reasons for the inconsistent performance of Iso-GSM during the pre-monsoon and monsoon periods (in section 4.6).

2.4.4 Seasonal variations

During the monsoon season, synoptic-scale and intra-seasonal variations contribute significantly to the apparent spatial patterns. However, since these variations are not dominate, and have a smaller amplitude than seasonal differences, the comparison of the two snapshots do provide a representative picture of the climatological seasonal difference.

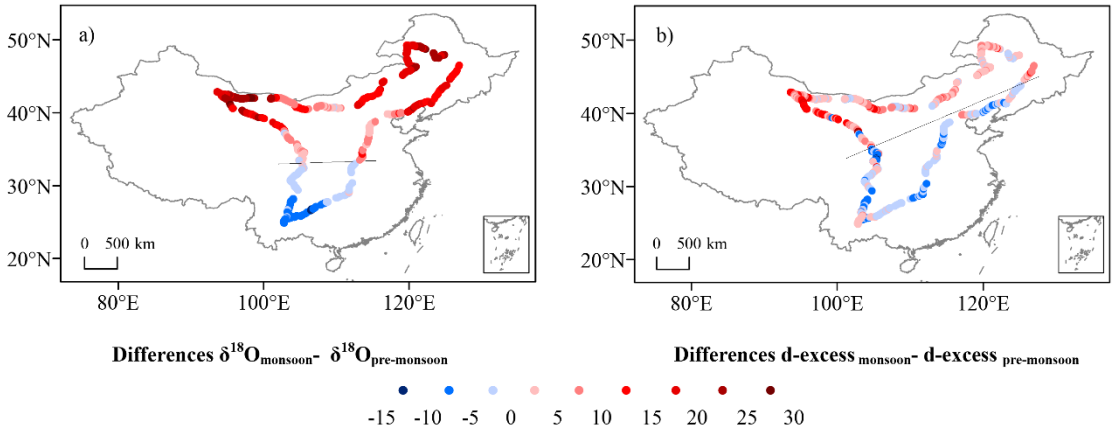

Figure 2-7 Spatial distribution of the isotope differences ($\delta^{18}O_{monsoon}$ - $\delta^{18}O_{pre-monsoon}$ (a) and d-excess$_{_monsoon}$ - d-excess$_{_pre-monsoon}$ (b)) for the observation locations. The solid black lines separate the areas of positive and negative values of the differences.

The climate in China features strong seasonality and it is captured in the snapshots of vapor isotopes (Fig.2-7). Since the observation routes of the two surveys are almost identical, we make a seasonal comparison of the observed vapor isotopes during the two surveys. The lines are drawn to distinguish between positive and negative values of seasonal isotopic differences. The seasonal differences $\delta^{18}O_{monsoon}$ - $\delta^{18}O_{pre-monsoon}$ (Fig.2-7a) show opposite sign in northern and southern China. In northern China, water vapor $\delta^{18}O$ values are higher during the monsoon period than during the pre-monsoon period, while the opposite are true in southern China. The boundary is located around 35 °N. The largest seasonal contrasts occur in southwest, northwest and northeast China, with seasonal $\delta^{18}O$ differences of -15 ‰, 30 ‰, and 30 ‰, respectively.

We also find a spatial pattern of vapor d-excess seasonality (Fig.2-7b). The line separating the areas of positive and negative values of the d-excess$_{monsoon}$ - d-excess$_{pre-monsoon}$ differences coincides with the 120 mm P-mean line (Fig.2-S2 f). In southeastern China, the water vapor d-excess is lower during the monsoon period than during the pre-monsoon period. The pattern of seasonal water vapor d-excess in northwestern China is the opposite. The two boundary lines separating the seasonal variations of $\delta^{18}O$ and d-excess do not overlap, suggesting different

controls on water vapor $\delta^{18}O$ and d-excess.

2.5 Understanding the factors controlling the spatial and seasonal distributions

To interpret the spatial and seasonal variations observed both across China and in each region defined in section 2.4, we investigate q–δ diagrams (section 4.1), $\delta^{18}O$-$\delta^{2}H$ relationships (section 4.2), relationships with meteorological conditions at the local and regional scale (sections 4.3 and 4.4), the impact of air mass origin (section 4.5) and synoptic events (section 4.6).

2.5.1 q–δ diagrams

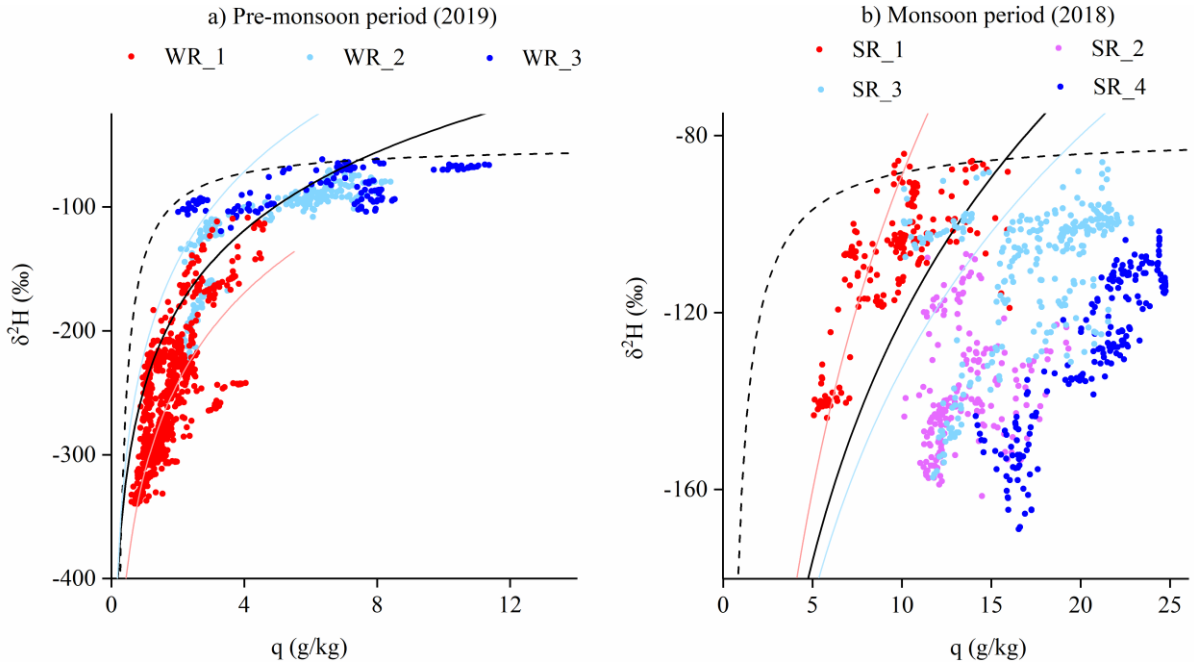

Figure 2-8 Scatterplot of observed vapor $\delta^{2}H$ (‰) versus specific humidity q (g/kg) during the pre-monsoon period (a) and monsoon (b) period. The solid black curves show the Rayleigh distillation line calculate for the initial conditions of $\delta^{2}H_0$ = -50‰, T=15 ℃ during the pre-monsoon period and $\delta^{2}H_0$ = -80‰, T=25 ℃ during the monsoon period. The mixing lines (dashed black curves) are calculated using a dry end-member with q = 0.2 g/kg and $\delta^{2}H$ = − 500 ‰ and air parcels for the corresponding Rayleigh curve as a wet end-member. The colored solid curves show the uncertainty range of the Rayleigh curve, calculated for different initial conditions of key moisture source regions: during March 2019, light red and light blue Rayleigh curve are calculated for key moisture source regions of westerlies ($\delta^{2}H_0$ = − 168.04‰, T=5℃) and BoB ($\delta^{2}H_0$= -77.37‰, T=26.46℃) separately in (a); during July-August 2018, light red and light blue Rayleigh curve are calculated for key

moisture source regions of westerlies (δ^2H_0= -149.64‰, T=6.16℃) and BoB (δ^2H_0= -82.75‰, T=27.69℃) separately in (b). These initial δ^2H are derived from Iso-GSM, the initial temperature and RH are derived from NCAR/NCEP 2.5-deg global reanalysis data.

The progressive condensation of water vapor from an air parcel from the source region to the sampling site and the subsequent removal of condensate results in a gradual reduction of humidity and vapor isotope ratios. This relationship can be visualized in a q–δ diagram, which has been used in many studies of the vapor isotopic composition (Galewsky et al., 2016; Noone, 2012). Observations along the Rayleigh distillation line indicate progressive dehydration by condensation. Observations above the Rayleigh line indicate either mixing between air masses of contrasting humidity (Galewsky and Hurley, 2010) or evapotranspiration (Galewsky et al., 2011; Noone, 2012; Samuels-Crow et al., 2015; Worden et al., 2007). Observations below the Rayleigh line, even when considering the most depleted initial vapor conditions (light blue Rayleigh curve in Fig 2-8b), indicate the influence of rain evaporation from depleted precipitation (Noone, 2012; Worden et al., 2007). Figure 2-8 shows the observed vapor q–δ^2H for different regions during the pre-monsoon (a) and monsoon (b) period. This figure will be interpreted in the light of meteorological variables along back-trajectories (Fig.2-2).

During the pre-monsoon period, most *q*-δ^2H measurements are located surrounding or overlapping the Rayleigh curve (the solid black curve in Fig.2-8a). Therefore, the observed spatial pattern can mostly be explained by the gradual depletion of vapor isotopes by condensation. The data for the three moisture sources are distributed in different positions of the Rayleigh curve, relate to different moisture origins or different original vapor isotope values. This is confirmed by the back-trajectory analysis: the Westerlies bring cold and dry air to northern China (WR_1, Fig.2-3a, Fig.2-2a and c), consistent with the vapor further along the Rayleigh distillation, and thus very depleted (Fig.2-5a). The observations in the WR_1 region (Fig.2-3c) are closer to the q-δ^2H Rayleigh distillation curve calculated for the key moisture source regions of westerlies, providing further evidence of the influence of water vapor source on vapor isotopes. The relatively high T and q along the ocean-sourced air trajectory reaching southern China (WR_3, Fig.2-3c, Fig.2-2a and c) is consistent with an early Rayleigh distillation phase during moisture transport, and thus higher water vapor δ^{18}O in southern China (Fig.2-5a). Some observations in the WR_3 region (Fig.2-3c) are located below the *q*-δ^2H Rayleigh distillation curve, indicating the influence of rain evaporation (Noone, 2012; Worden et al., 2007). This is consistent with the fact that air originates from the BoB, where deep convection begins to be active, and thus rain evaporation become a source of water vapor.

During the monsoon period, we find a scattered relationship in the *q*–δ^2H diagram for different regions, implying different moisture sources and/or water recycling patterns during moisture transport. Data measured in the SR_1 region (Fig.2-3i) fall above the Rayleigh distillation line (solid black curve in Fig.2-8b), likely due to the presence of moisture originating from continental recycling. A larger number of *q*-δ^2H measurements (most of the measurements from the SR_2, SR_3, and SR_4 regions, Fig.2-3i) are located below the Rayleigh curve, indicating moisture originating from the evaporation of rain drops within and below convective systems (Noone, 2012; Worden et al., 2007). In SR_3 and SR_4 regions, this is consistent with the high precipitation rate along Southerly and Easterly back-trajectories (Fig.2-2f). The convection is active over the Bay of Bengal, Pacific Ocean and South-Eastern

Asia, as shown by the low OLR (<240W/m 2) in these regions (Fig.2-S3) (Wang and Xu, 1997). Therefore, a significant fraction of the water vapor originates from the evaporation of rain drops in convective systems. These results support recent studies showing that convective activity depleted the vapor during transport by the Indian and East Asian monsoon flow (Cai et al., 2018; Gao et al., 2013; He et al., 2015). In SR_2 region, the relatively low water vapor $\delta^{18}O$, below the Rayleigh curve, is also probably associated with the evaporation of rain drop under deep convective systems. This is confirmed by the high precipitation rates along Northerly back-trajectories (Fig.2-2f), reflecting summer continental convection.

In northern China, q–δ diagrams show stronger distillation during the pre-monsoon period. This suggests a "temperature dominated" control. Very low regional T during the pre-monsoon period (Fig.2-S2 a and Fig.2-2a) are associated with low saturation vapor pressures and enhanced distillation, producing lower vapor $\delta^{18}O$. The T in summer is higher (Fig.2-S2 b and Fig.2-2b), allowing for higher vapor $\delta^{18}O$. The $\delta^{18}O_{monsoon}$ - $\delta^{18}O_{pre\text{-}monsoon}$ values in this region are therefore positive (Fig.2-7a). In the South, q–δ diagrams suggest the stronger influence of rain evaporation during the monsoon period. Higher precipitation amount significantly reduce $\delta^{18}O$ in the South (Fig.2-2f), even though T was higher during the monsoon period than in pre-monsoon. This suggests a "precipitation dominated" control in this region, explaining the negative values of $\delta^{18}O_{monsoon}$ - $\delta^{18}O_{pre\text{-}monsoon}$. This seasonal pattern in $\delta^{18}O$ is consistent with the results in precipitation isotope ratio (Araguás-Araguás et al., 1998; Wang and Wang, 2001). The boundary line separating the seasonal variations of $\delta^{18}O$ is also consistent with previous study on seasonal difference in vapor $\delta^{2}H$ retrieved by TES and GOSAT (Shi et al., 2020).

2.5.2 The $\delta^{18}O$-$\delta^{2}H$ relationship

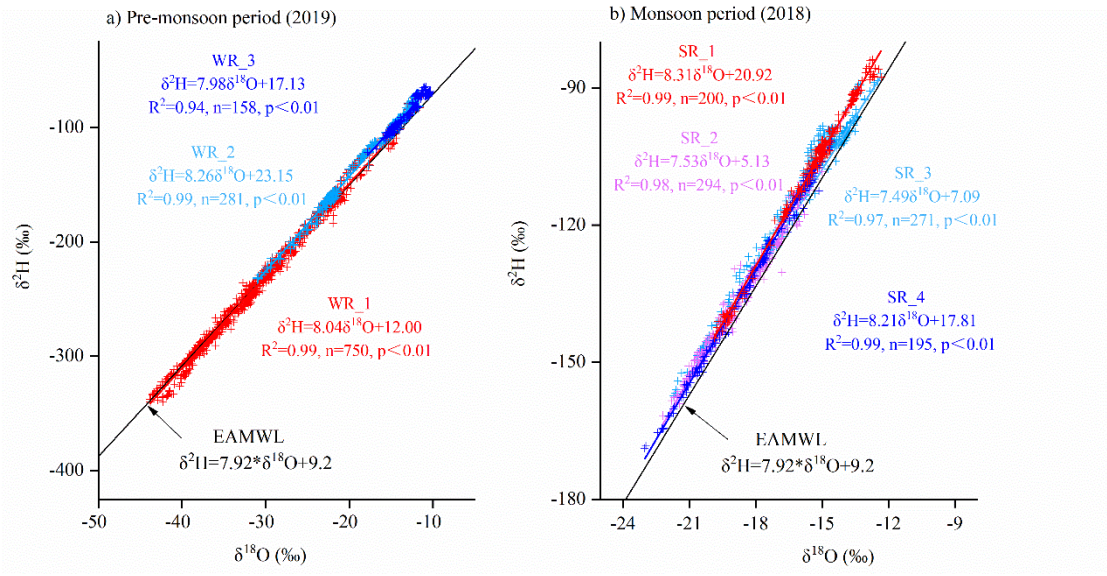

Figure 2-9 Regional patterns of vapor $\delta^{18}O$ - $\delta^{2}H$ relation during pre-monsoon period (a) and monsoon (b) period, compared with the East Asia Meteoric Water Line (EAMWL) (Araguás-Araguás et al., 1998).

The $\delta^{18}O$-$\delta^{2}H$ relationship is usually applied to diagnose the moisture source and water

cycling processes related to evaporation. Figure 2-9 and Table 2.1 show the $\delta^{18}O$-$\delta^{2}H$ relationship for different regions in the two seasons. We also plot the East Asian Meteoric Water Line (EAMWL) for a reference. Vapor $\delta^{18}O$-$\delta^{2}H$ is usually located above Meteoric Water Line owing to the liquid water and vapor fractionation.

During the pre-monsoon period (Fig.2-9a), the data in northern China (WR_1, Fig.2-3a) are located at the lower-left area in the $\delta^{18}O$-$\delta^{2}H$ graph, with similar slope and intercept as EAMWL ($\delta^{2}H = 8.04\ \delta^{18}O + 12.00$). This corresponds to air brought by the Westerlies and following Rayleigh distillation. The linear relationship for the vapor in middle China (WR_2, Fig.2-3b) has the steepest slope and highest intercept ($\delta^{2}H = 8.26\delta^{18}O + 23.15$). These properties are associated with a high d-excess, consistent with strong continental recycling by evapotranspiration (Aemisegger et al., 2014). As continental recycling is known to enrich the water vapor (Salati et al., 1979) and is associated with high d-excess (Gat and Matsui, 1991; Winnick et al., 2014). The high intercept is further consistent with a correlation between $\delta^{18}O$ and d-excess, which can typically result from continental recycling (Putman et al., 2019). The data for vapor originating from the BoB (WR_3, Fig.2-3c) are located to the upper right of the EAMWL. Their regression correlation shows similar features ($\delta^{2}H = 7.98\ \delta^{18}O + 17.13$) to that of the monsoon season (with a slope of 8.21 and an intercept of 17.81). We find similar atmospheric conditions in the BoB (with the region marked as rectangle in Fig.2-3c and h) during the two observation periods, with T=26℃ and RH=76% during pre-monsoon period and T=28℃ and RH=78% during the monsoon period, suggesting that the BoB source may have similar signals on vapor $\delta^{18}O$ and $\delta^{2}H$ in both seasons. These observed vapor $\delta^{18}O$-$\delta^{2}H$ patterns are consistent with the back-trajectory results indicating that the Westerlies persist in northern China during the pre-monsoon period, while moisture from the BoB has already reached southern China.

During the monsoon period (Fig.2-9b), the data in northwestern China (SR_1, Fig.2-3e) with continental moisture sources is located in the upper right of the graph but above the EAMWL, with the steepest slope and highest intercept for the linear $\delta^{18}O$-$\delta^{2}H$ relationship ($\delta^{2}H = 8.31\delta^{18}O + 20.92$). In contrast, the observations in southeastern China with BoB sources (SR_4, Fig.2-3h) are located in the lower left of the graph, with relatively lower intercept ($\delta^{2}H = 8.21\delta^{18}O + 17.81$). This is the opposite pattern compared to the pre-monsoon season. The observations from the SR_3 region (Fig.2-3g) also have a low slope and low intercept ($\delta^{2}H = 7.49\ \delta^{18}O + 7.09$). This is consistent with the oceanic moisture from the Pacific Ocean. Also, these $\delta^{18}O$-$\delta^{2}H$ data are located in the upper right of the graph with more scattered relation (with the lowest correlation coefficient), suggesting more diverse moisture sources. This is consistent with the mixing of water vapor from continental recycling and Pacific Ocean (Fig.2-3g). The observations in northeastern China (SR_2, Fig.2-3f) are located at the lower left of the graph, suggesting the influence of condensation along trajectories in northern Asia (Fig.2-2f). Compared to the SR_3 and SR_4 regions, the slope and intercept of the observations in SR_2 region are lower ($\delta^{2}H = 7.53\delta^{18}O + 5.13$), reflecting different origins of moisture.

2.5.3 Relationship with local meteorological variables

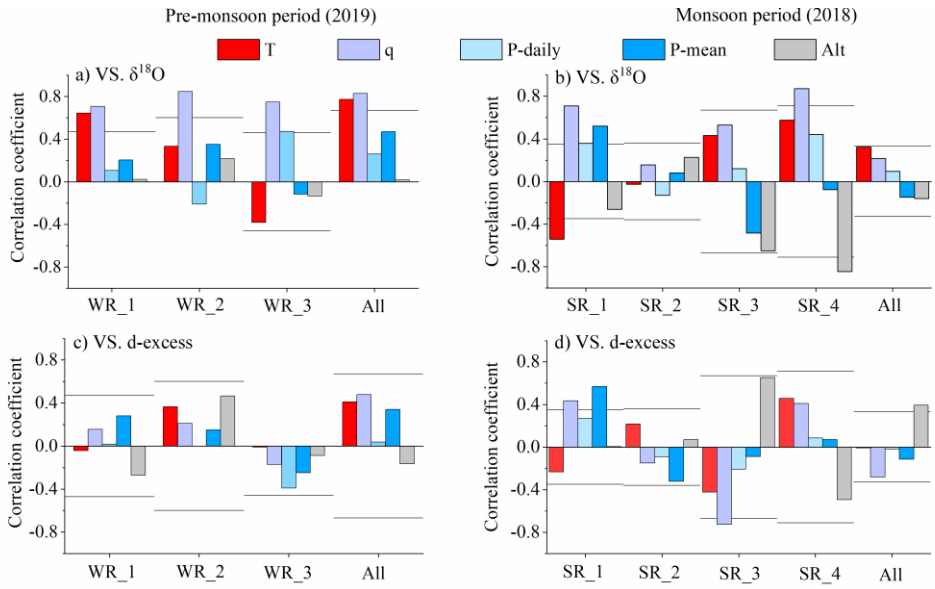

Figure 2-10 Regional patterns of the correlation between $\delta^{18}O$ (a, b), d-excess (c, d) and various local factors (temperature (T), specific humidity (q), daily precipitation amount (P-daily) and average precipitation amount over the entire observation period for each observation location (P-mean), and altitude (Alt)). The left panel is for the pre-monsoon period and the right is for the monsoon period. Horizontal lines indicate the correlation threshold for statistical significance ($p<0.05$), considered the degree of freedom.

Here we analyze the relationship between vapor $\delta^{18}O$, d-excess and local meteorological parameters, for all observations, and separately for the different regions (Fig.2-10 and Table S1).

We have taken particular care to estimate the statistical significance of the correlation coefficients. The statistical significance of a correlation depends on the correlation coefficient and on the degree of freedom D of the observed $\delta^{18}O$ and d-excess time series. Since these variables evolve smoothly in time and are sampled at a high frequency, the total number of samples overestimates the degree of freedom D of the time series. We thus estimated the degree of freedom D as Υ/η, where Υ is the length of the sampling period and η is the characteristic auto-correlation time scale of the time series (an example of this calculation is given in III. Supplementary text). A similar method was used to calculate the degree of freedom of the signal in (Roca et al., 2010). Table S2 summarizes the threshold for the correlation coefficient to be statistically significant at 95%, for the two seasons, the different regions and the variable of interest.

During the pre-monsoon period, all observations taken together exhibit a “temperature effect” (the δ’s decreasing with temperature, Dansgaard 1964) (Fig.2-10a), with significant and positive correlation between $\delta^{18}O$ and T ($r = 0.77$, $p<0.05$, Table S1). This results from the

high correlation between $\delta^{18}O$ and q ($r = 0.83$, $p<0.05$, Table S1), consistent with the Rayleigh distillation, and between T and q ($r = 0.54$, $p<0.05$), consistent with the Clausius Clapeyron relationship. The vapor $\delta^{18}O$ in the WR_1 (Fig.2-3a) region show similar correlations with T and q as for all observations. Rayleigh distillation thus contributes to the relationship between $\delta^{18}O$ and T observed in northern China. In contrast, no significant positive correlation between vapor $\delta^{18}O$ and T is observed in the WR_3 region with the BoB water source. This is consistent with the fact that the moisture from the BoB has already influenced southern China during the pre-monsoon period (Fig.2-3c). The weak positive correlation in most regions between $\delta^{18}O$ and P-daily and P-mean might simply reflect the control of q on observed vapor $\delta^{18}O$, due to the relatively high correlation between observed P-mean and q, with $r = 0.58$ for all observations (Fig.2-4).

During the monsoon period (Fig 10b), no significant correlation emerges when considering all observations. Vapor $\delta^{18}O$ is still significantly correlated with q in the SR_1 (Fig.2-3e, $r = 0.71$, $p<0.05$, Table S1) and SR_4 (Fig.2-3h, $r = 0.87$, $p<0.05$, Table S1) regions. This is consistent with different degree of rain-out. This may reflect the synoptic-scale variations of convection. The absence of correlation with T suggests that the variations in q mainly reflect variations in relative humidity that are associated with different air mass origins or rain evaporation. The $\delta^{18}O$ is significantly anti-correlated with Alt in the SR_4 region ($r = -0.85$, $p<0.05$, Table S1), consistent with the “altitude effect” (the heavy isotope concentrations in fresh water decreasing with increasing altitude) in precipitation and water vapor (Dansgaard, 1964; Galewsky et al., 2016).

The vapor d-excess for all observations during the monsoon period (Fig.2-10d) is positively correlated with Alt ($r = 0.39$, $p<0.05$, Table S1). One possible reason is that the vapor d-excess is lower in coastal areas at lower altitudes, while at higher altitudes in the west, more continental recycling of moisture leads to higher d-excess(Aemisegger et al., 2014). The positive correlation between d-excess and altitude is consistent with previous studies in region (Acharya et al., 2020). In the SR_1 region (Fig.2-3e), in arid northwestern China, vapor d-excess is positively correlated with q ($r = 0.43$, $p<0.05$, Table S1) and P-mean ($r = 0.57$, $p<0.05$, Table S1) during the monsoon period, suggesting that rain evaporation may also contribute to high d-excess (Kong and Pang, 2016). Other than these examples, the correlation coefficients between the d-excess and T, q, P, and Alt are not significant (Fig.2-10c and d), indicating that the local meteorological variables are not strongly related to vapor d-excess, as was reported in previous studies for precipitation isotope ratio (Guo et al., 2017; Tian et al., 2003).

2.5.4 Relationship with meteorological variables along trajectories

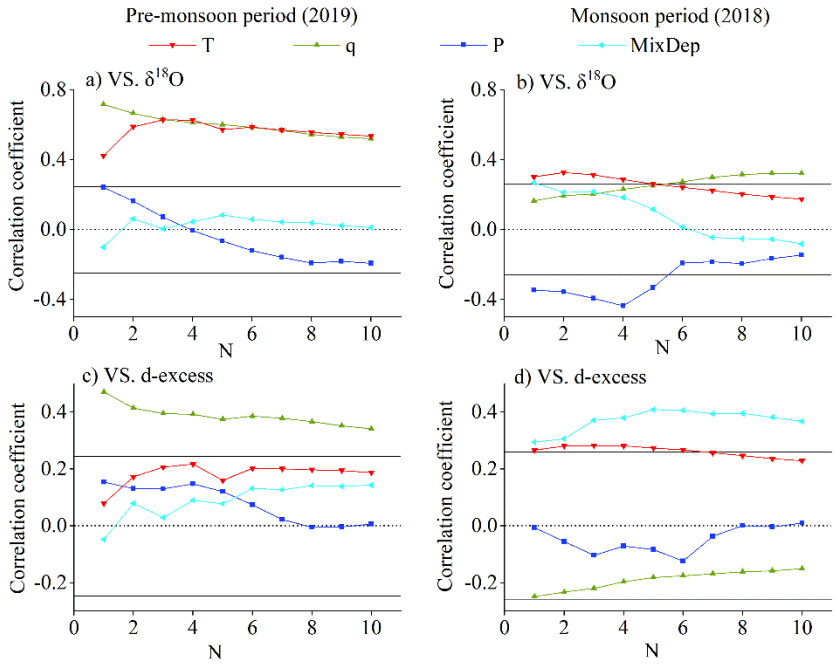

Figure 2-11 Correlation between $\delta^{18}O$ (a, b), d-excess (c, d)), and various meteorological factors (air temperature (T), specific humidity (q), precipitation (P), and mixing depth (MixDep)) along the air mass trajectories during the pre-monsoon period (the left panel) and monsoon period (the right panel). The x-axis "N" represents the number of days prior to the observations (from 1 to 10 days). For example, when the number of days is 2, the correlations is calculated with the temporal mean of meteorological data along the air mass trajectories during the 2days before the observations. Horizontal solid lines indicate the correlation threshold for statistical significance ($p<0.05$).

Reconstructions of paleoclimates using ice core isotopes have relied on relationships with local temperatures, but many previous studies have suggested that water isotope ratio are driven by remote processes along air mass trajectories. In particular, they emphasized the importance of upstream convection in controlling the isotopic composition of water (Gao et al., 2013;He et al., 2015;Vimeux et al., 2005, Cai and Tian, 2016). We therefore perform a correlation analysis between vapor isotope observations and the temporal mean meteorological conditions along air mass trajectories. The meteorological conditions are averaged over the previous days (N form 1 to 10) prior to the observations.

The $\delta^{18}O$ values have the strongest correlations with T and q along air mass trajectories during the pre-monsoon period (Fig.2-11a). The results show gradually increasing positive correlation coefficients as N changes from 10 to 3. This reflects the role of temperature and humidity along air mass trajectories and the large spatial and temporal coherence of T variations during the pre-monsoon period. During the monsoon period, the negative correlation coefficients between $\delta^{18}O$ and P (Fig.2-11b) become more significant as *N* increases from 1 to

4 and less significant as *N* increases from 5 to 10. This result indicates a maximum impact of P during a few days prior to the observations, as observed also for precipitation isotope ratio (Gao et al., 2013; Risi et al., 2008a). It is further consistent with the influence of precipitation along back-trajectories (Fig.2-2f). Mixing depth (MixDep) is stably and positively correlated with d-excess. A hypothesis to explain this correlation is that when the MixDep is higher, stronger vertical mixing of convective system transports vapor with higher d-excess values from higher altitude to the surface (Galewsky et al., 2016; Salmon et al., 2019).

2.5.5 Relationship between water vapor isotopes and moisture sources

In section 4.1 to 4.4, we have discussed that different moisture sources and corresponding processes on transport pathways are related to the observed spatial patterns both in vapor $\delta^{18}O$ and d-excess.

We also identify different isotopic values of vapor from different ocean sources during the monsoon period. The vapor $\delta^{18}O$ in the zone from Beijing to Harbin and western China with Pacific Ocean and continental origins (SR_3 region, about -17‰ to -13‰) are higher than those in the Southeast with BoB sources (SR_4 region, about -23‰ to -15‰) (Fig.2-3i and Fig.2-5b). In sections 4.1 and 4.2, we have shown that it is related to the extent of the Rayleigh distillation and rain evaporation associated with convection along trajectories. Earlier studies suggest that lower $\delta^{18}O$ values were observed from the Indian monsoon source than from Pacific Asian monsoon moisture due to the different original isotope values in the source regions (Araguás-Araguás et al., 1998). To better isolate the direct effect of moisture sources, we extract the initial vapor isotopes of the Indian and East Asian monsoon systems (the regions are marked as annotated rectangles in Fig.2-3g and h) for the sampling dates of 2018 from the Iso-GSM model. The values are about $\delta^{18}O$=-12‰ and $\delta^{2}H$ =-83‰ in the northern BoB and $\delta^{18}O$ =-14‰ and $\delta^{2}H$ =-97‰ in the eastern Pacific Ocean. The initial vapor isotope values of the two vapor sources are not significantly different. The initial vapor isotopes in the BoB are even slightly higher than those in the Pacific Ocean, contrary to moisture source hypothesis. The OLR was significantly lower in the BoB than in the Pacific Ocean (Fig.2-S3). This suggests that the deeper convection in the Indian Ocean leads to lower water vapor isotope ratios (Bony et al., 2008; Liebmann and Smith, 1996; Risi et al., 2008a; Risi et al., 2008b) in southeastern China, rather than the initial composition of the moisture source.

Continental recycling probably also contribute to higher $\delta^{18}O$ in the SR_3 region (Fig.2-3i and Fig.2-5b) (Salati et al., 1979), especially in western China (Fig.2-3i), which can be confirmed by the higher d-excess in this region (Fig.2-5d) (Gat and Matsui, 1991; Winnick et al., 2014). Except SR_3 region, continental recycling also has a strong influence on isotopes in the WR2 and SR1 regions, which suggested by the high values of $\delta^{18}O$ and d-excess, back-trajectories, the location on the q-δ diagram, and the higher slopes and intercepts of $\delta^{18}O$-$\delta^{2}H$ relationship. In the opposite, in the zone from Beijing to Harbin (Fig.2-3i), greater proportion of water vapor from Pacific sources than continental recycling and is in the early stage of Rayleigh distillation, could result in high vapor $\delta^{18}O$ (Fig.2-5b) but relatively low d-excess (Fig.2-5d).

In previous studies, the d-excess has been interpreted as reflecting the moisture source and evaporation conditions (Jouzel et al., 1997). During the pre-monsoon period, lower T and higher

RH over evaporative regions for the vapor transported by the Westerlies (Fig.2-2a and g, Fig.2-S2 a and g) reduces the non-equilibrium fractionation at the moisture source and produces lower vapor d-excess in the WR_1 region (Fig.2-3a, Fig.2-5c) (Jouzel et al., 1997; Merlivat and Jouzel, 1979). In contrast, higher T and lower RH over evaporative regions (Fig.2-2 a and g, Fig.2-S2 a and g) for the vapor coming from the South leads to higher d-excess in southern China (WR_3, Fig.2-3c, Fig.2-5c). This is consistent with the global-scale poleward decrease in T and increase in surface RH over the oceans (despite the occurrence of very low RH at the sea ice edge during cold air outbreaks (Aemisegger and Papritz, 2018; Thurnherr et al., 2020)), resulting in global-scale poleward decrease in d-excess at mid-latitudes (Bowen and Revenaugh, 2003; Risi et al., 2013a). Alternatively, the low d-excess during the night over the continent in Northern China during the pre-monsoon could also have contributions (Li et al., 2021). During the monsoon period, the lower vapor d-excess observed in eastern China (Fig.2-5d) is likely a sign of the oceanic moisture, derived from source regions where RH at the surface is high (Fig.2-2h and Fig.2-S2 h) and thus reduce non-equilibrium fractionation and lower d-excess. The high d-excess values observed in western and northwestern China (Fig.2-5d) reflect the influence of continental recycling (Fig.2-3e and g).

The seasonal variation of moisture sources also results in a seasonal difference in d-excess (Fig.2-8b). In southeastern China, RH over the ocean surface in summer is higher than in winter (Fig.2-S2 g and h, and Fig.2-2g and h), resulting in negative values of $\text{d-excess}_{\text{monsoon}}$ - $\text{d-excess}_{\text{pre-monsoon}}$ (Fig.2-8b). Northwestern China has an opposite pattern of seasonal vapor d-excess. This result largely due to the extremely low vapor d-excess during the pre-monsoon period (Fig.2-5c). Also, we speculate that a greater contribution of continental recycling leads to higher d-excess during the monsoon period than during the pre-monsoon period (Risi et al., 2013b) and the positive values of the $\text{d-excess}_{\text{monsoon}}$ - $\text{d-excess}_{\text{pre-monsoon}}$ (Fig.2-8b).

2.5.6 Possible reasons for the biases in Iso-GSM

In section 3.3, we showed that Iso-GSM captured the isotopic variations during the pre-monsoon season better than during the monsoon season. We hypothesize that this mainly could be due to the larger contribution of synoptic-scale variations to the observed variations during the monsoon season. Iso-GSM performs well during the pre-monsoon season, when seasonal mean spatial variability dominates q and isotope ratio. In contrast, it performs less well during the monsoon season, when isotopic variations are significantly influenced by the synoptic-scale variability. Among the synoptic influences, tropical cyclones, the Northern Summer Intra-Seasonal Oscillation (BSISO) and local processes probably played a role. For example, during our monsoon observations, landfall of tropical cyclones Jongdari and Yagi correspond to the low values of $\delta^{18}O$ we observed in the eastern China (Fig.2-S7a). Bebinca corresponds to the low values of $\delta^{18}O$ we observed in the southwestern China (Fig.2-S7a). Typhoons are known to be associated with depleted rain and vapor (Bhattacharya et al., 2022; Gedzelman, 2003). Three Northern Summer Intra-Seasonal Oscillation (BSISO) events occurred in China during about July 28 - 31, August 5 - 8th and August 14 – 16 (Fig S8). The northward propagation of the BSISO is associated with strong convection (Kikuchi, 2021) (Fig.2- S8). Moreover, short-lived convective events that frequently occurred during our observation period (Wang et al., 2018). It is possible that these rapid high-frequency synoptic events are not fully captured by

Iso-GSM. We expect that Iso-GSM captures the large-scale circulation. Yet, we notice that Iso-GSM underestimates the depletion associated with tropical cyclones (Fig.2- 12b). We hypothesize that given its coarse resolution, it underestimates the depletion associated with the meso-scale structure. This might contribute to the overestimation of vapor $\delta^{18}O$ in southeastern China (Fig.2-12b). In Northwestern China, Iso-GSM underestimates vapor $\delta^{18}O$, but also underestimates precipitation, q and T (Fig.2-12b, d, f and h, Fig.2- S4). It is possible that Iso-GSM underestimates the latitudinal extent of the monsoonal influence, which brings moist conditions, while overestimating the influence of continental air, bringing dry conditions associated with depleted vapor through Rayleigh distillation. It is also possible that Iso-GSM underestimates the enriching effect of continental recycling. During the pre-monsoon period, Iso-GSM overestimates the observed $\delta^{18}O$ along most of the survey route (Fig.2-12a), with the largest difference in northwestern China, and underestimates the vapor $\delta^{18}O$ in the southern part of the study region. Our results are consistent with previous studies showing that many models underestimate the heavy isotope depletion in pre-monsoon seasons in subtropical and mid-latitudes, especially in very dry regions (Risi et al., 2012). This was interpreted as overestimated vertical mixing. The differences in $\delta^{18}O$ (Fig.2-12a) and q (Fig.2-12c) are spatially consistent. The overestimation of $\delta^{18}O$ therefore could be due to the overestimation of q, and vice versa. These biases could be associated with shortcomings in the representation of convection or in continental recycling. Despite this, the good agreement during pre-monsoon period is probably due to the dominant control by Rayleigh distillation on seasonal-mean spatial variations of isotopes in this season, as concluded in the above. The q variation, in relation with T, drives vapor isotope variations and is well captured by Iso-GSM spatially, with significant correlations between observed and simulated q ($r = 0.84$, slope=0.70 in Table S3) and T ($r = 0.87$, slope=0.70 in Table S3), though q is overestimated in the North and underestimated in the South.

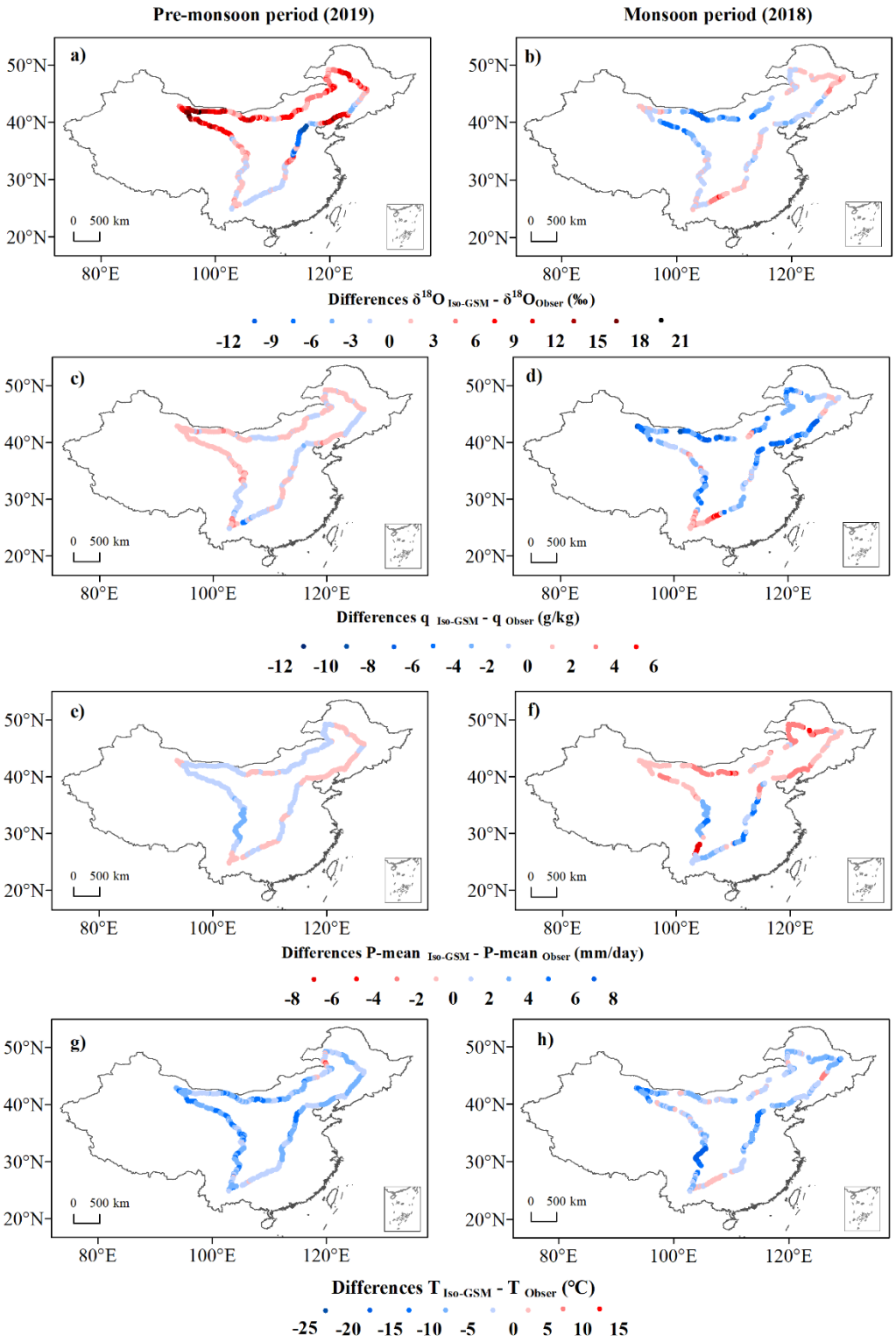

Figure 2-12 Spatial distribution of the differences between the outputs of Iso-GSM (subscripts are Iso-GSM) and observations (subscripts are Obser) during the pre-monsoon period (the left panel) and monsoon period (the right panel): $\delta^{18}O$ (a and b, ‰), specific humidity q (c and d, g/kg), P-mean for the sampling dates (e and f, mm/day), and temperature T (g and h, °C).

2.6 **Conclusion**

Our new, vehicle-based observations document spatial and seasonal variability in surface water vapor isotopic composition across a large part of China. Both during the pre-monsoon and monsoon periods, it is clear that different moisture sources and corresponding processes on transport pathways explain the spatial patterns both in vapor $\delta^{18}O$ and d-excess (summarized in Fig.2-13):

(1) During the pre-monsoon period (Fig.2-13a), the latitudinal gradient of vapor $\delta^{18}O$ and d-excess were observed. The gradient in $\delta^{18}O$ reflects the "temperature effect", Rayleigh distillation appears to be the dominant control, roughly consistent with earlier studies on precipitation. Vapor in northern China, derived from westerlies, and subject to stronger Rayleigh distillation (arrows fading from red to blue), is characterized by very low isotope ratios (blue shades). Less complete Rayleigh distillation (arrows fading from red to light red) results in less depleted vapor in southern China (light red shades). The vapor d-excess in northern China is low (green triangles series), probably due to the high RH over high-latitude oceanic moisture sources for the vapor transported by the Westerlies (green arrow), reducing the kinetic fractionation during ocean evaporation. In contrast, the lower RH over low-latitude moisture sources (yellow arrow) for the vapor transported to southern China leads to higher d-excess (yellow triangles series). Additional vapor sourced from continental recycling (orange twisted arrows), further increases the d-excess values in middle China. This distribution is consistent with the back-trajectory results showing that during the pre-monsoon period, the vapor in southwestern China comes from the BoB, whereas Westerly moisture sources still persist in northern China.

(2) During the monsoon period (Fig.2-13b), the lowest vapor $\delta^{18}O$ occurred in southwestern and northeastern China, and higher vapor $\delta^{18}O$ values were observed in between, while the d-excess features a west-east contrast. The relatively lower vapor $\delta^{18}O$ result from deep convection along the moisture transport pathway (blue clouds; arrows fading to blue). Meanwhile, the mixing with moisture from continental recycling (orange twisted arrows) increases the vapor $\delta^{18}O$ values in middle and northwestern China. We observed lower vapor $\delta^{18}O$ values when the moisture originates from the BoB than from the Pacific Ocean, consistent with stronger convection during transport. The dominance of oceanic-wet moisture (green arrows) results in the lower vapor d-excess (green triangles series) in eastern China, whereas continental recycling produces higher vapor d-excess in western and northwestern China (yellow triangles series).

(3) Variation in temperature drive the seasonal variations of vapor $\delta^{18}O$ in northern China, whereas convective activity along trajectories produces low vapor $\delta^{18}O$ curing the monsoon season and drive the seasonal variation in south China. Seasonal d-excess variation reflects different conditions in the sources of vapor: in southeastern China it is mainly due to differences in the RH over the adjacent ocean surface, while in northwestern China it is mainly due to the vapor transported by the Westerlies during the pre-monsoon period and a great contribution of continental recycling during the monsoon period.

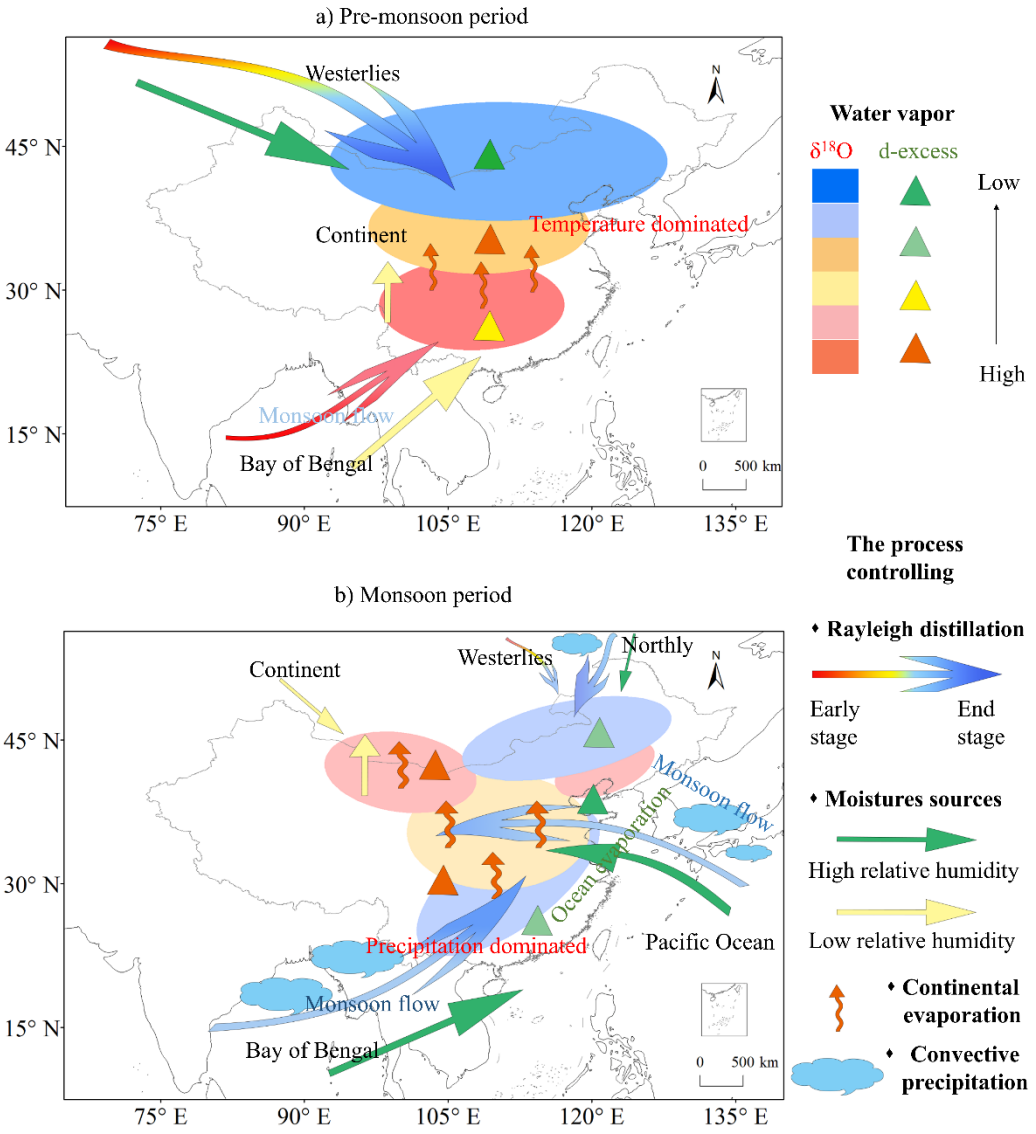

Figure 2-13 Schematic picture summarizing the different processes controlling the observed spatial patterns and seasonality of vapor isotopes. Color gradient arrows from red to blue represent the initial to subsequent extension of the Rayleigh distillation process along the water vapor trajectory, corresponding to high to low values of $\delta^{18}O$; green arrows represent high relative humidity and yellow arrows represent low relative humidity; orange twisted arrows represent continental recycling; blue-sized clouds represent strong and weak convective processes; green triangles series representing low values of d-excess; yellow triangles series representing high values of d-excess.

Iso-GSM simulations and IASI satellite measurements indicate that during the pre-monsoon period, the observed temporal variations along the route across China are mainly due to multi-year seasonal-mean-spatial variations, and marginally due to synoptic-scale variations. During the monsoon season, synoptic-scale and intra-seasonal variations might contribute significantly to the apparent spatial patterns. However, since these variations have a smaller amplitude than seasonal differences, the comparison of the two snapshots do provide a

representative picture of the climatological seasonal difference.

Our study on the processes governing water vapor isotopic composition at the regional scale provides an overview of the spatial distribution and seasonal variability of water isotope ratio and their controlling factors, providing an improved framework for interpreting the paleoclimate proxy records of the hydrological cycle in low and mid-latitudes. In particular, our results suggest a strong interaction between local factors and circulation, emphasizing the need to interpret proxy records in the context of the regional system. This also suggests the potential for changes in circulation to confound interpretations of proxy data.

2.7 **Data availability**

The data acquired during the field campaigns used can be accessed via the following link or DOI: (1) Wang, Di; Tian, Lide (2022): Vehicle-based in-situ observations of the water vapor isotopic composition across China during the monsoon season 2018. PANGAEA, https://doi.org/10.1594/PANGAEA.947606; (2)Wang, Di; Tian, Lide (2022): Vehicle-based in-situ observations of the water vapor isotopic composition across China during the pre-monsoon season 2019. PANGAEA, https://doi.org/10.1594/PANGAEA.947627. . Other data used can be downloaded from the corresponding website which were listed in the text.

2.8 Supporting Information

Supplement of Vehicle-based in situ observations of the water vapor isotopic composition across China:spatial and seasonal distributions and controls

Di Wang[1,2,3], Lide Tian[1, 3], Camille Risi[2], Xuejie Wang[1,3], Jiangpeng Cui[4], Gabriel J. Bowen[5], Kei Yoshimura[6], Zhongwang Wei[7], Laurent Z.X Li[2]

[1] Institute of International Rivers and Eco-security, Yunnan University, Kunming 650500, Yunnan, China

[2] Laboratoire de Météorologie Dynamique, IPSL, CNRS, Sorbonne Université, Campus Pierre et Marie Curie, Paris 75005, France

[3] Yunnan Key Laboratory of International Rivers and Transboundary Eco–security, Kunming 650500, Yunnan, China

[4] Sino-French Institute for Earth System Science, College of Urban and Environmental Sciences, Peking University, Beijing 100871, China

[5] Department of Geology and Geophysics, and Global Change and Sustainability Center, University of Utah, Salt Lake City, Utah 84108, USA

[6] Institute of Industrial Science, The University of Tokyo, Tokyo113-8654, Japan

[7] School of Atmospheric Sciences, Sun Yat-sen University, Guangzhou 510275, Guangdong, China

Figures S1 to S9
Table S1 to S3
Text S1 to S2

2.8.1 Supplement I. Figures

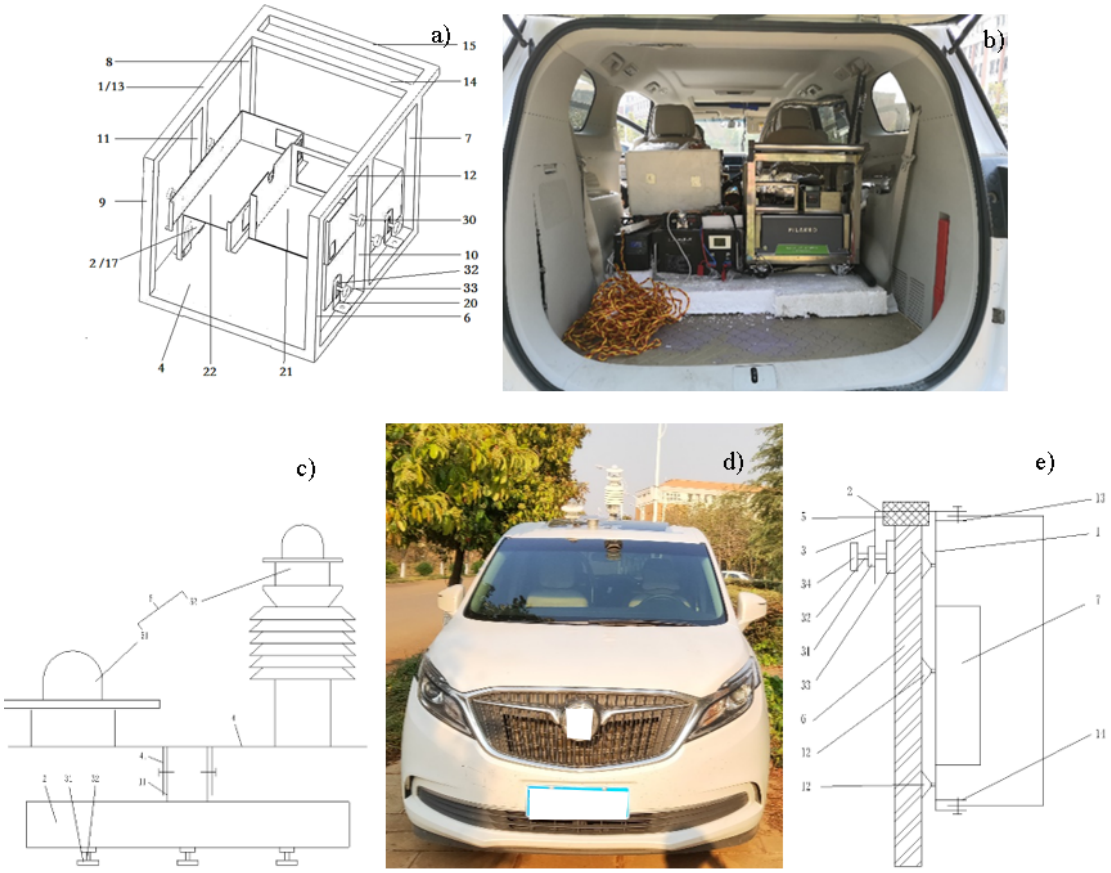

Figure 2-S1 The design diagram (a) and real product (b) of vehicle-borne mobile water vapor isotope observation device, the design diagrams of the mobile weather station based on car skylight (c) and off-vehicle detection mount platform (e). The location of the vapor isotopes sampling inlet and measurement instrument on the car (d).

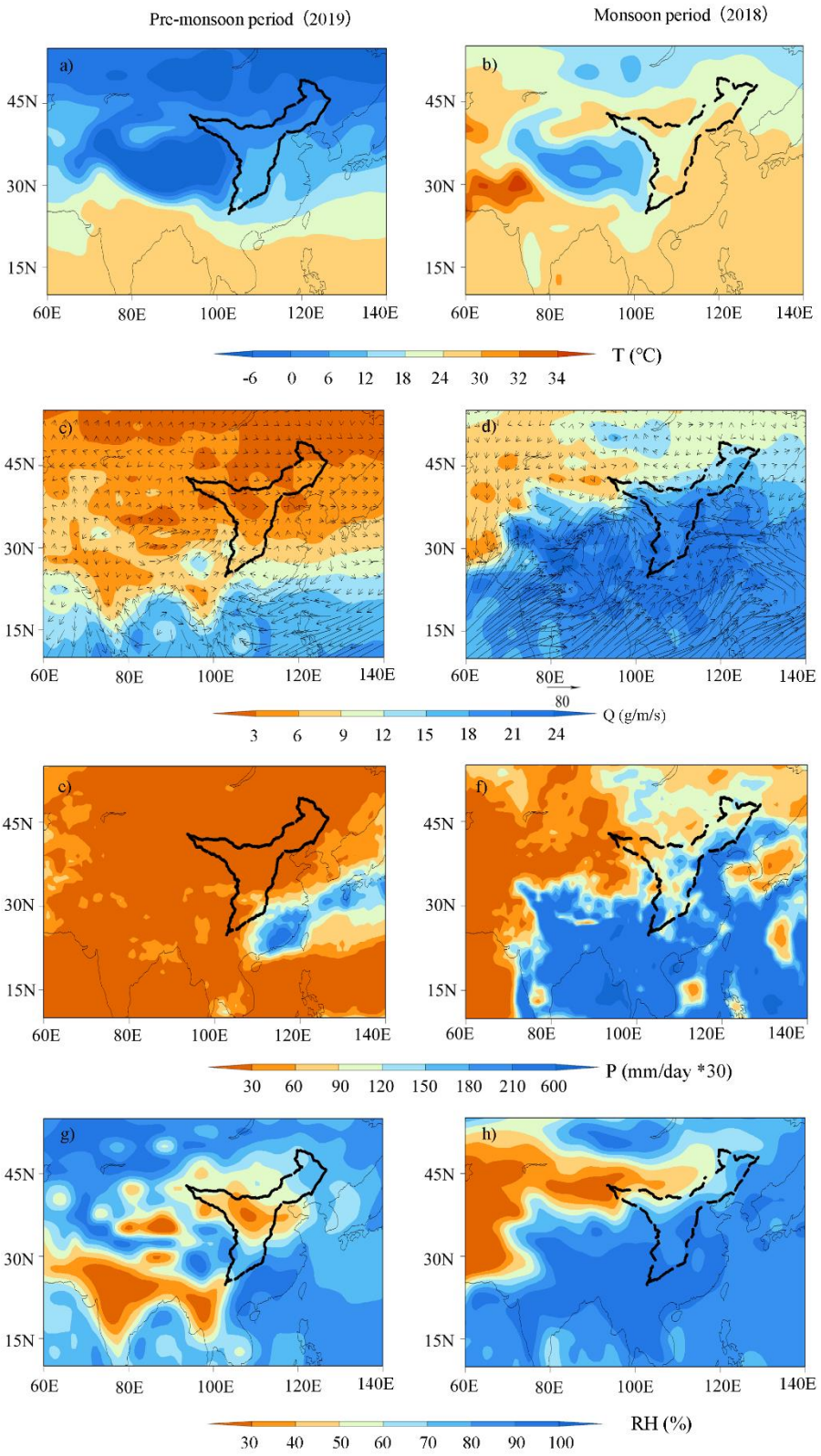

*Figure 2-2-S2 The temporal-mean surface air temperature T (℃, a and b), the vertically-integrated moisture flux from the surface to an altitude of 300 hpa Q (g/m/s, c and d) (Connolley and King, 1993), precipitation amount P (mm/day *30, e and f), and surface relative humidity RH (%, g and h) for the sampling dates. The left panel is for the pre-monsoon period and the right for the monsoon period.*

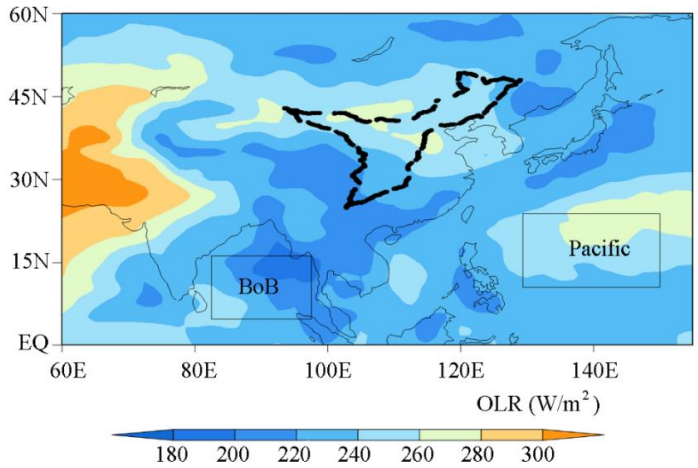

Figure 2--S3 Spatial distribution of monthly outgoing longwave radiation (OLR, W/m2) in August 2018. Note: BoB is the abbreviation for the Bay of Bengal.

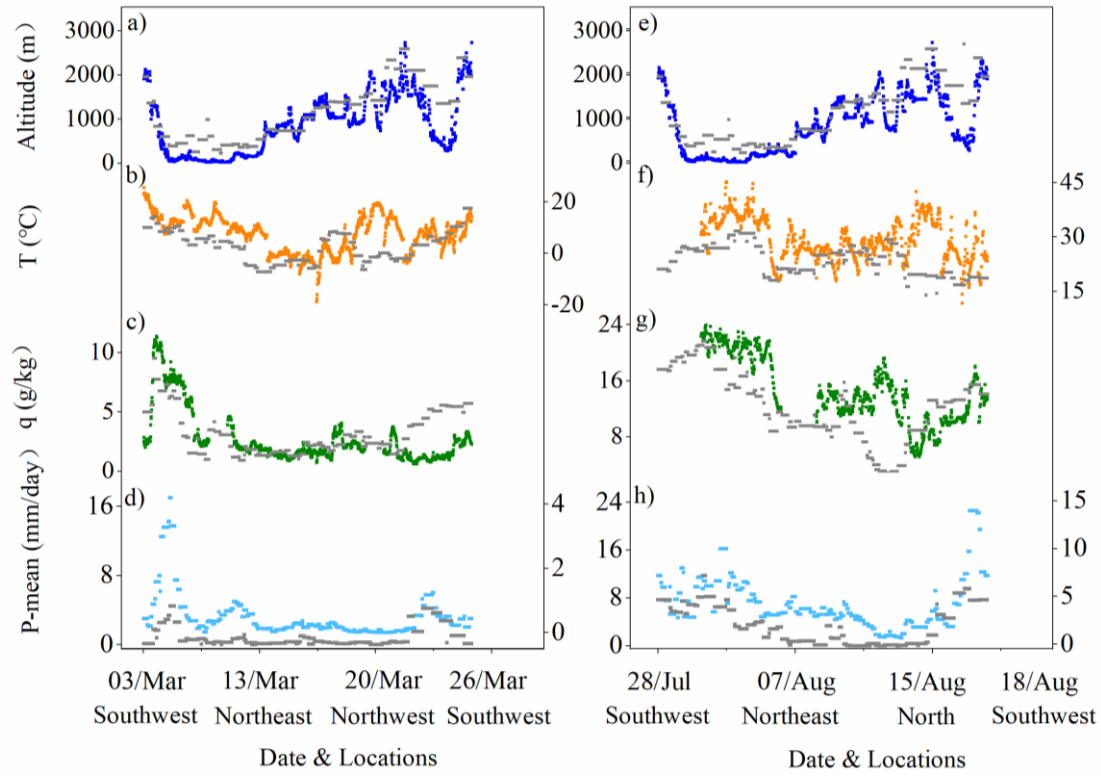

Figure 2- S4 Concurrent meteorological conditions along the survey routes of observations (colourful dots) and simulations of Iso-GSM (gray dots) during the pre-monsoon (the left panel) and monsoon period (the right panel). (a, e) altitude (m); (b, f) air temperature T (℃); (e, g) specific humidity q (g/kg); and (d, h) temporal-mean precipitation amount for the sampling dates P-mean (mm/day). Notes: the colourful dots of P-mean are extracted from GPCP.

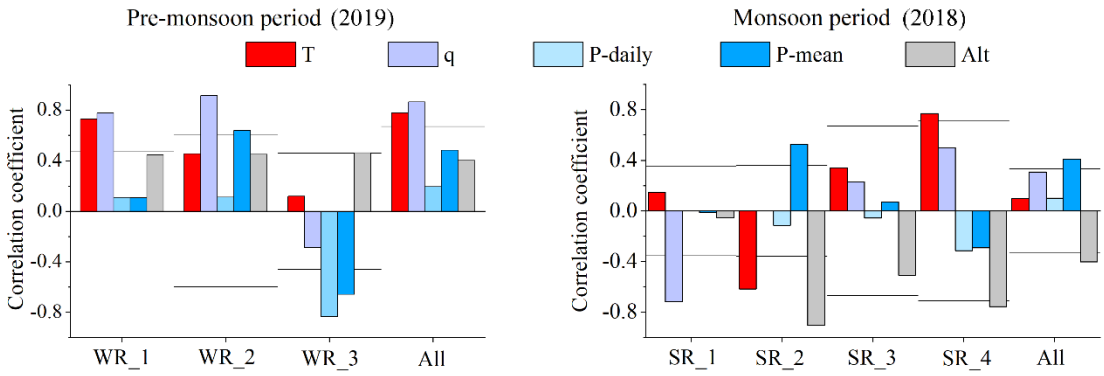

Figure 2- S5 Regional patterns of the correlation between $\delta^{18}O$ (a, b), d-excess (c, d) and various local factors (temperature (T), specific humidity (q), daily precipitation amount (P-daily) and temporal-mean precipitation amount for the sampling dates (P-mean), and altitude (Alt)) simulated by Iso-GSM. The left panel is for the pre-monsoon period and the right for the monsoon period. Horizontal lines indicate the correlation threshold for statistical significance ($p<0.05$).

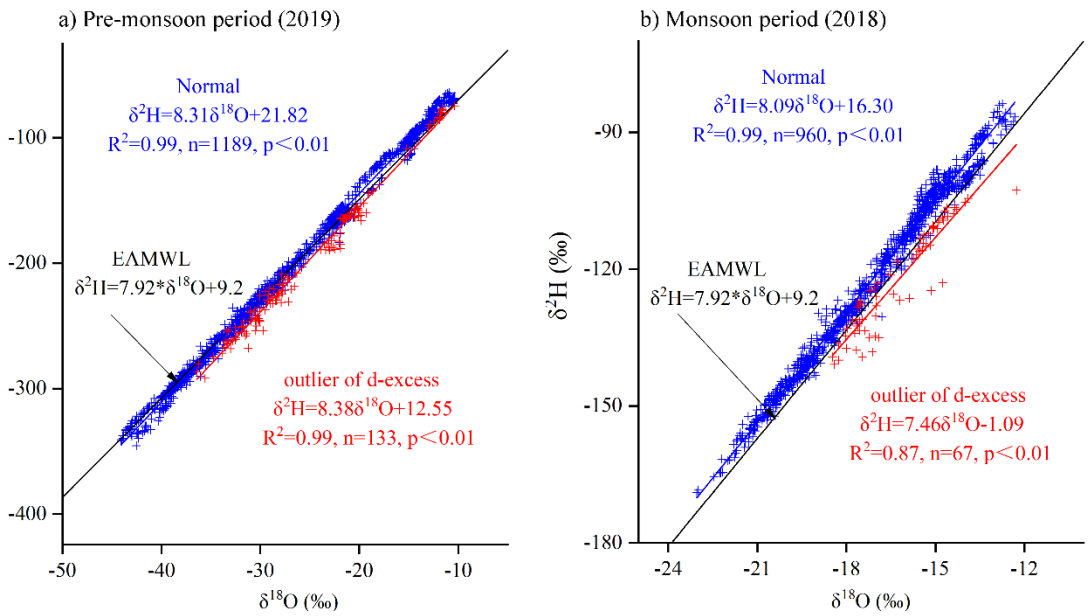

Figure 2- S6 $\delta^{18}O$ vs $\delta^{2}H$ for data with anomalous intercepts and the rest of the data used in this study, compared with the EAMWL.

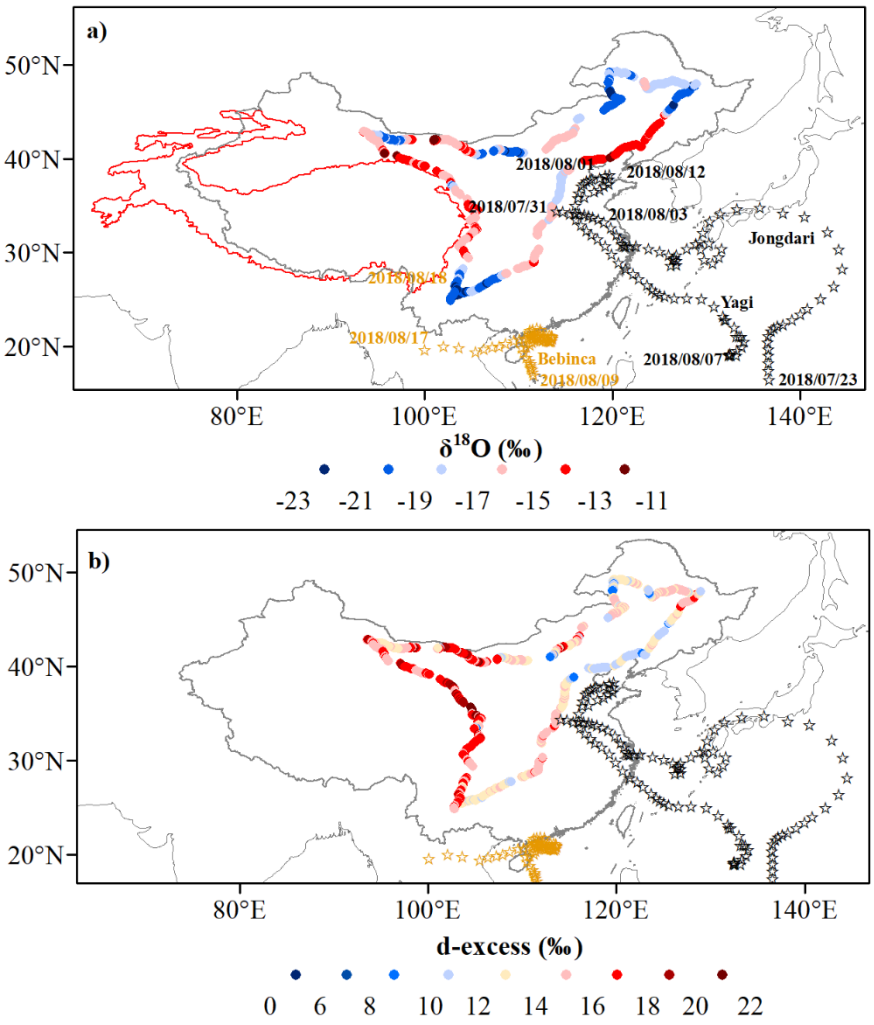

Figure 2- S7 Tropical cyclones that made landfall in mainland China during the 2018 monsoon observation period and the timing of tropical cyclone activity: Super typhoon Jongdari: July 23 started, August 03 arrived; Super Tropical Storm Yagi August 07 started, August 12 arrived; Super Tropical Storm Bebinca: August 09 started, August 17 arrived. (a) The bottom map shows the observed spatial distribution of $\delta^{18}O$; (b) The bottom map shows the observed spatial distribution of d-excess.

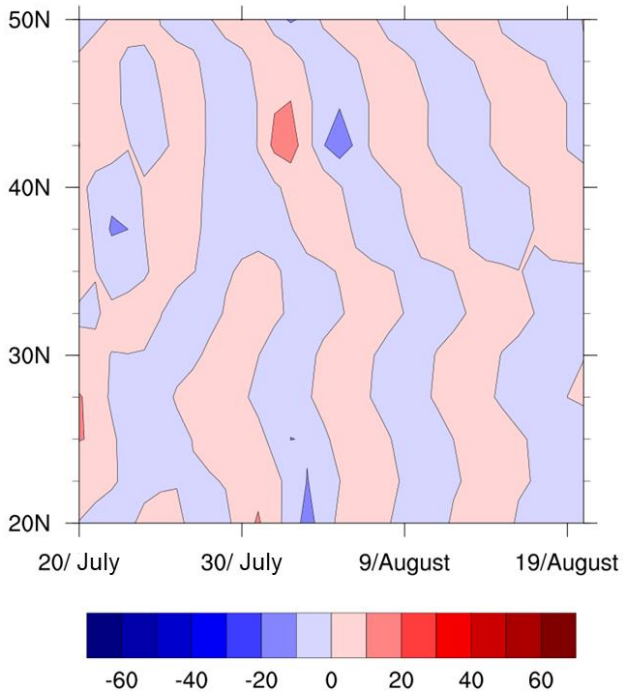

Figure 2- S8 Longitude averaged (100°E to 125°E) time-latitude representation (Hovmoller plot) of 5 to 10 day filtered OLR anomaly (shaded, in W/m2) during July 2018 to August.

2.8.2 Supplement II. Tables

Table 2-S1 Correlation between vapor isotopes ($\delta^{18}O$ and d-excess) and local temperature (T), specific humidity (q), daily precipitation amount (P-daily), temporal-mean precipitation amount for the sampling dates (P-mean) and altitude (Alt) over different regions during the pre-monsoon period and monsoon period. Boldface values indicate the most significant correlations ($p<0.05$), considered the degree of freedom.

Sampling period		$\delta^{18}O$	$\delta^{2}H$	d	H^2O	T	q	P_{-daily}	P_{-mean}	Alt
						WR_1				
	$\delta^{18}O$	1.00	1.00	0.14	**0.68**	**0.65**	**0.72**	0.11	0.20	0.02
	d			1.00	0.23	-0.04	0.15	0.02	0.28	-0.27
						WR_2				
	$\delta^{18}O$	1.00	1.00	0.43	**0.85**	0.33	**0.85**	-0.21	0.35	0.22
	d			1.00	0.18	0.37	0.21	0	0.15	0.47
						WR_3				
Pre-monsoon (2019)	$\delta^{18}O$	1.00	0.97	0.24	**0.74**	-0.38	**0.75**	**0.47**	-0.12	-0.13
	d			1.00	-0.16	-0.01	-0.17	-0.39	-0.25	-0.09
						All Zone				
	$\delta^{18}O$	1.00	1.00	0.60	**0.80**	**0.77**	**0.83**	0.26	0.47	0.02
	d			1.00	0.49	0.41	0.48	0.04	0.34	-0.17
						SR_1				
	$\delta^{18}O$	1.00	1.00	**0.40**	**0.80**	**-0.54**	**0.71**	**0.36**	**0.52**	-0.26
	d			1.00	**0.40**	-0.23	**0.43**	0.27	**0.57**	0
						SR_2				
Monsoon (2018)	$\delta^{18}O$	1.00	0.99	**-0.38**	0.31	-0.03	0.16	-0.13	0.08	0.23
	d			1.00	-0.28	0.22	-0.15	-0.09	-0.32	0.07
						SR_3				
	$\delta^{18}O$	1.00	0.99	-0.38	0.48	0.43	0.53	0.12	-0.48	-0.65
	d			1.00	**-0.75**	-0.42	**-0.73**	-0.21	-0.09	0.65
						SR_4				
	$\delta^{18}O$	1.00	0.99	0.35	**0.87**	0.58	**0.87**	0.44	-0.08	**-0.85**
	d			1.00	0.44	0.46	0.41	0.08	0.07	-0.49
						All Zone				
	$\delta^{18}O$	1.00	0.99	0.10	0.20	0.32	0.22	0.10	-0.15	-0.16
	d			1.00	**-0.33**	0	-0.28	-0.02	-0.12	**0.39**

Table 2-S2 The degree of freedom D (reserved as integer) and threshold for the correlation coefficient to be statistically significant at 95% (r).

Sampling period	Region	Degree of freedom D	r
Pre-monsoon (2019)	WR_1	16	0.47
	WR_2	9	0.60
	WR_3	17	0.46
	All	7	0.67
Monsoon (2018)	SR_1	32	0.35
	SR_2	28	0.36
	SR_3	7	0.67
	SR_4	6	0.71
	All	36	0.33

Table 2-S3 Correlation coefficients and slopes of the relationship between observed and simulated $\delta^{18}O$, temperature (T), specific humidity (q), daily precipitation amount (P-daily) and temporal-mean precipitation amount for the ssampling dates (P-mean) from Iso-GSM. Boldface values indicate the most significant correlations ($p<0.05$), considered the degree of freedom.

		r	Slope
Pre-monsoon (2019)	$\delta^{18}O$	**0.84**	0.61
	d-excess	0.16	0.10
	T	**0.87**	0.70
	q	**0.84**	0.70
	P-daily	0.2	0.13
	P-mean	0.63	1.05
Monsoon (2018)	$\delta^{18}O$	0.24	0.25
	d-excess	0.15	0.13
	T	**0.46**	0.32
	q	**0.85**	0.89
	P-daily	0.18	0.15
	P-mean	**0.66**	0.79

2.8.3 Supplement III. Text

(1) Method to estimate the degree of freedom of time series

The statistical significance of correlation coefficients between two time series depends on the degree of freedom D of these time series. If the samples of the time series are all independent from each other, then D=N-2, where N is the number of samples.

Our time series evolves smoothly, therefore consecutive samples are not completely independent from each other. For example, the ith sample is typically intermediate between the (i-1)th sample and the (i+1)th sample.

Therefore, to estimate the degree of freedom D, we need to know what is the typical duration between 2 samples (η), that ensures that the 2 samples are independent. η is called the auto-correlation time scale.

D can be calculated as: D= Τ/η

where Τ is the duration of the sampling period (e.g. 24 days during the pre-monsoon period)

A similar approach was followed in Roca et al 2010.

We estimate η for each time series X ($\delta^{18}O$ or d-excess) for each season and region. Here is an example for all regions of the pre-monsoon period:

* We have 1189 samples averaged to a 10-min temporal resolution . We therefore have a time series that is evenly sampled in time. For each lag l from -6h to +6h, with a spacing of 1 hour, we calculate the correlation r between the time series X and the same time series lagged by l. For example, if l =0, then this is the correlation between X and itself, so it is 1. As l increases, the correlation decreases and tends to 0.

* Then we plot -ln(r) as a function of |l|. We find a linear relationship with slope s. For example in this case, we find a slope of 0.0342 $hour^{-1}$.

* we calculate η as 1/s. For example in this case, we find η=1/0.0342=29.24.

* Calculate D= Τ/η =1189/6/29.24=6.77. Note: 1189 samples have a 10-min temporal resolution, and we select the l with a 1 hour temporal resolution, so here we divide by 6.

* The same calculation of the degree of freedom have been done for each period/region and each season.

Roca, R., Chambon, P., Jobard, I., Kirstetter, P. E., Gosset, M., & Bergès, J. C. (2010). Comparing satellite and surface rainfall products over West Africa at meteorologically relevant scales during the AMMA campaign using error estimates. Journal of Applied Meteorology and Climatology, 49(4), 715-731.

(2) Method to make the altitude correction for the outputs of Iso-GSM:

In observations, altitude varies at short spatial scales as the route goes up and down hills. This contributes to δ variations. Iso-GSM, as a coarse resolution global model, cannot capture such small-scale vaiations of altitude. We thus need to correct for the altitude difference between observations and Iso-GSM.

At each location, the altitude corrected δ from Iso-GSM (δ_{corr}), is calculated as:

$\delta_{corr} = \delta_{Iso\text{-}GSM} + a\_alt * (Alt_{obse} - Alt_{Iso\text{-}GSM})$

where $\delta_{Iso\text{-}GSM}$ s the original output of iso-GSM, a_alt is the slope of $\delta_{Iso\text{-}GSM}$ as a function of altitude used in iso-GSM ($Alt_{Iso\text{-}GSM}$), and Alt_{obs} is the measured altitude by our portable GPS unit.

Because the relationship between δ and altitude is significant only during the monsoon season, we apply this correction only for the outputs during the monsoon season.

We found that $Alt_{Iso\text{-}GSM}$ is higher than Alt_{obs} in the southwest corner of China (Fig S6). This tends to make $\delta_{Iso\text{-}GSM}$ more depleted compared to observations. The altitude correction partially corrects this bias (Fig SIII-1). In addition, the correlation between the simulated $\delta^{18}O$ and measured $\delta^{18}O$ is improved from 0.09 to 0.24, due to the account for the small-scale variations in altitude.

Only $\delta^{18}O$ and $\delta^{2}H$ during the monsoon period are strongly correlated with altitude in the Iso-GSM simulations, with r=0.79 and r=0.80 (n=960, $p<0.01$, considered the degree of freedom), respectively. So no altitude corrections were made for the other parameters and the simulations during the pre-monsoon period.

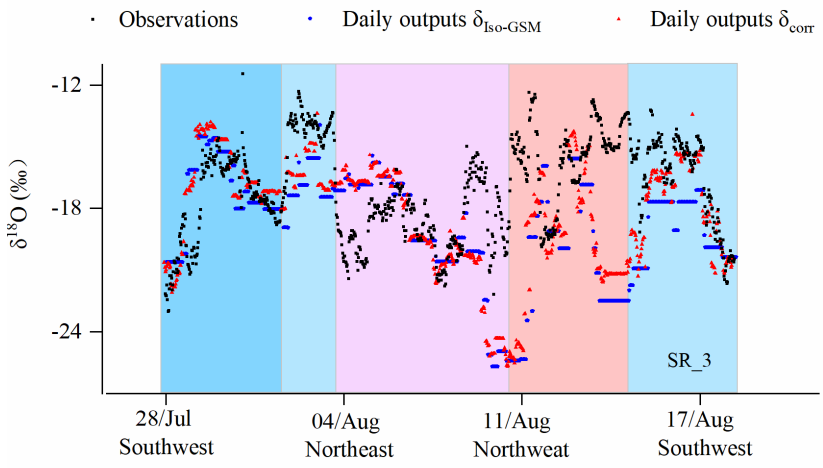

Fig 2-S9. Comparison of the observed vapor $\delta^{18}O$ (observations) with that simulated at the daily scale by Iso-GSM, without the altitude correction ($\delta_{Iso\text{-}GSM}$) and with the correction (δ_{corr}).

3 Correcting for water vapor diffusion in airbag samples for isotope composition analysis: example with drone-collected samples

3.1 Abstract

Traditional methodologies, such as Mass Spectrometry and Laser Spectroscopy, have long been used for accurate water vapor isotope measurements. However, these techniques are limited by logistical challenges and constraints in temporal and spatial resolution. Portable sampling devices, such as airbags and glass bottles, has emerged as a needed and promising approach. They offer a practical and efficient method for collecting, storing, and transporting gaseous samples from a wide range of environments. When collecting samples at higher altitudes by drone, air bags are preferred because they are lighter and more flexible than glass bottles. However, they introduce specific challenges associated with potential sample contamination and isotopic fractionation during sample storage, primarily due to the permeability common to most airbags. To address this issue, we developed a theoretical model of water vapor through the sampling bag surface, whose parameters are calibrated by laboratory experiments. This model allows us to estimate the initial isotopic composition of the sampled vapor given the composition measured in the bag and in the environment. We applied this correction method to samples collected at different air pressures using an air bag mounted on drones and we estimated the range of error for our observations. The corrected observations were compared with satellite data. Our correction method significantly enhances the reliability and applicability of water vapor isotope drone-based observations. It capitalizes on the strengths of drone-based air bag sampling while mitigating its limitations, contributing to a more profound understanding of atmospheric and hydrological processes.

3.2 Introduction

Water vapor isotopes provide unique insights into the transport and phase changes of water in the environment. These insights are critical for understanding the climate system, water cycle, and weather patterns. Furthermore, they have applications in climate modeling, weather prediction, and water resource management (Galewsky et al., 2016; Gat, 1996).

Traditionally, Mass Spectrometry, which ionizes water molecules and differentiates the ions based on their mass-to-charge ratios, has been a standard in water isotope analysis. However, it usually requires laborious sample preparation and lacks portability. Cryogenic trapping, chemical trapping, and adsorption on desiccants are common techniques for collecting water vapor (Michener and Lajtha, 2008). These methods require long collection periods to obtain sufficient sample volumes for water isotope measurements, hence restricting the spaces and times of observation (Merlivat, 1978). Furthermore, these methods may present issues such as the adhesion of collected water vapor to the inner surfaces of the sampling system, leading

to measurement errors. In addition, they could potentially involve the use of hazardous chemicals. Over the past three decades, laser Spectroscopy methods like Cavity Ring-Down Spectroscopy (CRDS) and Off-Axis Integrated Cavity Output Spectroscopy (OA-ICOS) have been transformative, introducing the possibility for faster, continuous measurements, even when dealing with small quantities of gas in challenging environments such as high altitudes or arid regions where water vapor content is low (Galewsky et al., 2016).

However, due to the heavy instrumentation, the requirement for a significant power supply, and low mobility, these techniques have limited usability in diverse environments. Consequently, there has been a demand for a more convenient and efficient acquisition method. Airbags and glass bottles emerged as pragmatic solutions to collect, store, and transport gaseous samples from varied environments (Rozmiarek et al., 2021). To extend the scope of collection to higher altitudes, we have developed a drone-based water vapor sample collection device. Given the necessity for lighter and more flexible tools for this application, we chose air bags over glass bottles. These not only facilitate transportation but also reduce the risk of breakage. Despite these advantages, challenges such as sample contamination, alteration of isotopic ratios due to bag material interaction, sample leakage, and the risk of isotope fractionation call for meticulous handling to ensure data reliability (Jiménez-Rodríguez et al., 2019).

We carried sampling bags on the drone to collect air samples, and then returned to the surface for water vapor isotope measurements. The main goal of this work is to obtain data on vertical profiles of atmospheric water vapor isotope composition at a higher temporal and spatial resolution than satellite observations. However, in our observations we encountered diffusion issues that needed to be addressed due to the potential permeability of the sampling bag itself. Over time, there can be an exchange of water vapor molecules between the air inside the bag and the surrounding ambient air. Water vapor molecules usually diffuse from areas of high humidity to drier air, a process in which heavier isotopes (e.g., $H_2{}^{18}O$ and HDO) move more slowly than lighter isotopes due to their greater mass, and thus lighter isotopes (e.g., $H_2{}^{16}O$) diffuse preferentially. This selective exchange, or fractionation, could then alter the original isotopic composition of the collected air sample.

In previous studies, air bags have been most frequently used in water vapor isotope observations to determine the isotope signature of soil water samples under equilibrium (Gralher et al., 2018; Hendry et al., 2015). However, there are highlighted concerns about using varied sampling materials for storing these samples due to the potential for water diffusion through the container wall. This kind of diffusion problem generally exist in the sampling bag used for water vapor isotope analysis (Jiménez-Rodríguez et al., 2019). This potential diffusion issue has been a long-standing problem in the field. Some materials that exhibit weaker permeability are more suitable for water vapor isotope measurements (Herbstritt et al., 2023).

Given these findings, further research and development are needed to alleviate these issues. This may include, but is not limited to, exploring alternative materials for lower permeable sampling bags, improving sealing methods to better isolate sampled air, and even developing alternative sample collection techniques that are less prone to diffusion. Resolution of these issues is critical to ensuring the reliability of water vapor isotope observations and contributing to a broader understanding of atmospheric and hydrological processes. Until these techniques are fully developed and refined, we constructed a diffusion model whose parameters are calibrated using laboratory experiments. The model is validated against experiments conducted

under diverse conditions. This ensured that the model was not only theoretically sound but also practical and reliable when applied to real-world situations. The results obtained via the application of our diffusion model were then compared with satellite data to assess precision and consistency. This comparative analysis further reinforced the model's reliability and provided a robust basis for evaluating its accuracy.

3.3 Method

3.3.1 Water isotope measurements

We used a Picarro 2130i CRDS water vapor isotope analyzer to perform our vapor isotope measurements. In order to correct the humidity-dependent isotope bias, we employed a calibration function, which made use of a standard delivery module (SDM) in combination with our laboratory standard water measurements at varying water concentration settings. We established a reference level at 20,000 ppm for vapor humidity in our analysis, considering the Picarro analyzer demonstrates optimal accuracy at this specific humidity level (JingfengLiu et al., 2014; Schmidt et al., 2010). All acquired vapor isotope values were subsequently calibrated to match the VSMOW-SLAP scale, accomplished by utilizing two distinct laboratory standard waters. Before conducting the daily measurements, we altered the quantity of the injected liquid standard to equate the humidity of the outside vapor measurements.

3.3.2 Use of airbags in isotope measurements

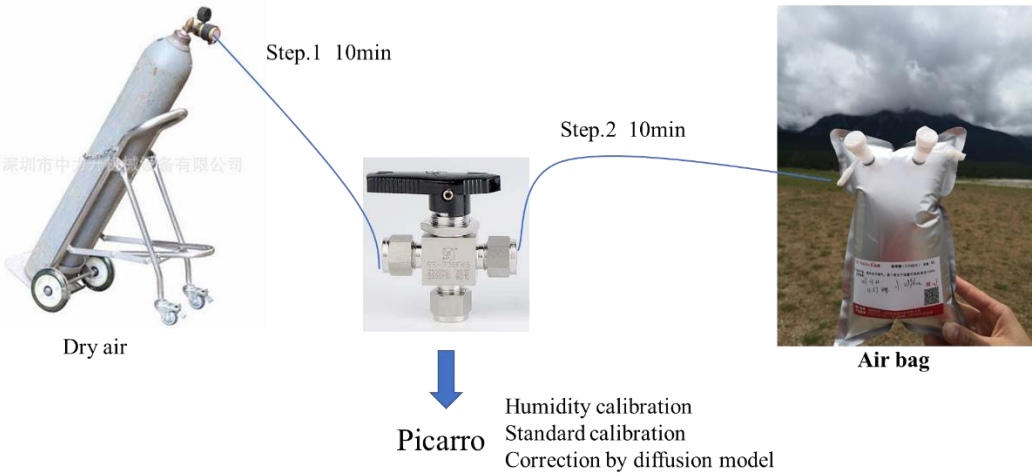

Figure 3-1 The procedure for using air bags with a Picarro atmospheric water vapor stable isotope analyzer.

We collected atmospheric water vapor samples using 0.5 L airbags and performed isotope measurements using a Picarro atmospheric water vapor stable isotope analyzer (Fig. 3-1). The specifications for the air flow rate of the Picarro analyzer indicate that 0.5L is sufficient for

around half an hour of analysis. The outlet valve of the air bag was connected to a three-way valve via Teflon tubing. The remaining two ends of the three-way valve were connected to the air inlet of the Picarro Atmospheric Water Vapor Stable Isotope Analyzer and the dry air cylinder, respectively. During storage and observation, we turned on the thermostatic heating casing and thermostat box in the water vapor path to maintain a constant temperature for the air bag and pipeline.

First, we opened the dry air cylinder switch and the pressure reducing valve, controlling the flow rate at the output of the pressure reducing valve at 2 psi (pounds of force per square inch). We then opened the valve channel connected to the dry air cylinder in the three-way valve, allowing dry air to pass into the atmospheric water vapor stable isotope analyzer. This process lasted for 10 minutes, serving to dry and clean the air path. After this, we closed the dry air channel, opened the air bag outlet valve, and the valve channel connected to the air bag in the three-way valve. This allowed the collected atmospheric water vapor samples to flow into the Picarro atmospheric water vapor stable isotope analyzer for constant temperature measurement of atmospheric water vapor isotope values. This process lasted for 5-10 minutes. Once the measurements were completed, we switched the valve to measure the dry air. By repeatedly measuring atmospheric water vapor isotope values for the parallel samples, we could obtain more accurate isotope values of the atmospheric water vapor samples.

3.3.3 Sampling systems mounted on drones

We have designed a collection module to execute fixed-height sampling at predetermined altitudes, using air pumps and rudder mounted on the UAV, and a control module associated with a remote operating system (Fig. 3-2). However, as air pressure increases during descent, the airbags can deflate, leading to potential leakage of the air sample. To counter this, we've installed a one-way valve that only allows air to enter the bag, preventing backflow. Importantly, this one-way valve also stops large droplets from entering the air bag during the collection process. This design ensures that air samples remain sealed and uncontaminated throughout the collection and descent.

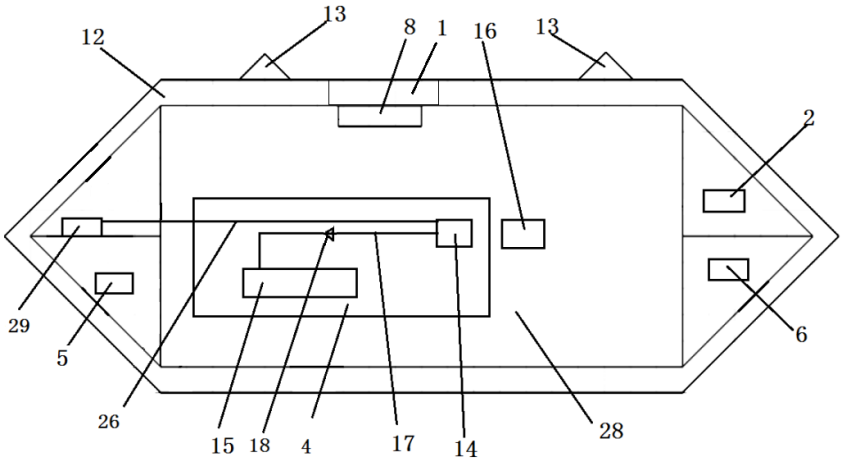

Figure 3-2 UAV-based high-altitude atmospheric water vapor collection device.

3.3.4 Field campaign

The sampling module was mounted on a UAV and applied during a field campaign at a pristine forest of Mountain Laojun, specifically at 99 Longtan, located in Lijiang on the southeastern edge of the Tibetan Plateau, China, from June 25th,2020 to October 17th, 2020. A video of the field campaign is available in SI.

By combining high-altitude UAV sampling with water vapor stable isotope in-situ observation technology, we obtained vapor isotopic profiles up to 11km in altitude. Unlike traditional methods, which involve the sampling and transportation of condensed liquid water samples back to the lab for determination, it requires less sample volume and allows for direct in-situ measurements, ensuring the samples aren't subjected to natural changes due to phase transformation or transportation.

3.3.5 Laboratory experiments to evaluate the influence of airbags characteristics and quantify diffusion parameters

We storage air inside the airbags before conducting the water vapor isotope measurement. This process could potentially alter the water vapor isotope values within the airbags, compared to the actual values, due to the adsorption and permeability characteristics of the airbags themselves. To assess this potential impact, we evaluate the effect of the airbags on water vapor isotope determination by measuring standard water vapor with known isotopic values within the airbags.

We start by filling clean air bags with dry air. We then inject a specific quantity of standard water into these bags, which carries known isotopic values that notably diverge from ambient isotopic values. Using the measurement method in section 2.2, we monitor the changes in the isotopic ratio inside the air bag at several time intervals: 5 minutes, 2 hours, 4 hours, 6 hours, 8 hours, 10 hours, and 24 hours. We then use the observed pattern of water vapor isotope variations in the airbags over time, along with physical mechanisms and mathematical methods, to develop a diffusion model for correcting water vapor isotopes (see Section 3). To ensure the consistency and reliability of our data, we repeated these measurements multiple times using different airbags of the same size.

3.3.6 Satellite data IASI

Of the available instruments, the Infrared Atmospheric Sounding Interferometer (IASI) boasts the best spatiotemporal sampling capabilities for δ^2H retrieval (Lacour et al., 2012; Lacour et al., 2018). It has a horizontal footprint of about 12 km at nadir (directly below the satellite) which increases with the angle of observation. This ensures nearly global coverage twice daily.

Due to the intermittent availability of IASI data for any given location, to establish a meaningful comparison of our observational results across different altitudes at our study site, we only considered the days on which IASI data coincided with our observational dates.

Satellite measurements, particularly those related to water vapor isotopes, often come with constrained vertical resolution. Typically, IASI readings signify three distinct vertical heights: 2950m, 4220m, and 6380m. Given that our study commenced at an altitude of 3856 m, we zeroed in on the δ^2H inversion data for altitudes 4220 m and 6380 m. However, these measurements represent a vertical average over a layer that depends on the averaging kernels. Consequently, it predominantly maintains a qualitative character due to these intrinsic factors..

3.4 Diffusion model

3.4.1 Model equations

We present a mathematical model for the diffusion and the fractionation of isotopes through the sampling bag surface (Fig. 3-3).

The flux of water towards the bag writes:

$$F = k * (q_e - q(t)) \quad (1)$$

where q represents the humidity in the bag (g/kg), q_e denotes the environmental humidity (g/kg), and k is a constant, the unit of k is kg/m^2/s

Similarly, the flux of isotopes, either $H_2{}^{18}O$ or HDO, moving towards the bag writes:

$$F_i = k_i * (R_e * q_e - R(t) * q(t)) \quad (2)$$

In this equation, k_i stands for a constant specific to each isotope, R_e denotes the isotopic ratio in the environment, and R(t) is the isotopic ratio within the bag. Notably, the fractionation coefficient can be denoted by $\alpha = k/k_i$.

The change in humidity over time can be predicted by the following differential equation:

$$\frac{d(q(t)*M)}{dt} = F * A \quad (3)$$

where A represents the exchange area and M is the mass of air within the bag.

Consequently, this equation can be simplified to:

$$\frac{dq(t)}{dt} = \frac{F*A}{M} = \frac{k*A*(q_e - q(t))}{M} \quad (4)$$

Here, we define k*A/M as λ.

Similarly, the change in isotopic ratio over time can be predicted by the following differential equation:

$$\frac{d(R(t)*q(t)*M)}{dt} = M * (q(t) * \frac{dR(t)}{dt} + R(t) * \frac{dq(t)}{dt})$$

$$= F_i * A = k_i * (R_e * q_e - R(t) * q(t)) * A \quad (5)$$

Simplifying further, the equation can be expressed as:

$$\frac{dR(t)}{dt} = \frac{ki*(R_e*q_e - R(t)*q(t))*A - R(t)*\frac{dq(t)}{dt}}{q(t)}$$

$$= \frac{k*A/M/\alpha*(R_e*q_e - R(t)*q(t)) - R(t)*k*A/M*(q_e - q(t))}{q(t)} \quad (6)$$

The differential equation for humidity (Eq 4) can be analytically solved :

$$q_e - q(t) = (q_e - q_0) * e^{(-k*A/M*t)} \quad (7)$$

Where q_0 is the initial humidity at t=0. By taking the natural logarithm, this equation can also be expressed as:

$$\ln(q_e - q(t)) = \ln(q_e - q_0) - \lambda * t \quad (8)$$

The slope of $\ln(q_e - q(t))$ against time is thus λ.

For isotopic ratio, an analytical solution can be found only in cases where the initial humidity equals the environmental humidity ($q_0 = q_e$) :

$$\frac{dR(t)}{dt} = k * A/M/\alpha * (R_e - R(t)) \quad (9)$$

$$\text{so } R_e - R(t) = (R_e - R_0) * e^{(-k*A/M/\alpha*t)} \quad (10)$$

Where R_0 denotes the initial isotopic ratio at t=0. Again, taking the natural logarithm, we obtain:

$$\ln(R_e - R(t)) = \ln(R_e - R_0) - \lambda/\alpha * t \quad (11)$$

This equation indicates that the slope of ln(Re-R(t)) against time is λ/α. Having knowledge of λ, we can deduce α for each isotope.

However, in cases where the environmental humidity differs from the initial humidity, a numerical solution is required to solve the differential equation for R (Equation 6).

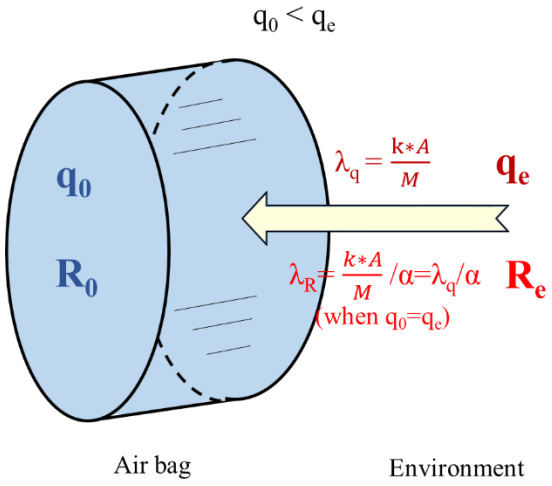

Figure 3-3 Schematic illustrating the simple diffusion model

3.4.2 Reconstructing initial water vapor composition

In the case of $q_0 = q_e$, the isotopic composition follow an exponential decay equation with time. An exponential decay of the isotopic composition has already been applied to reconstruct the isotopic composition for example in the context of environmental forensics (Ayliffe et al., 2004; Cerling et al., 2006). Here we use a similar method except that equation 6 does not have any analytical solution in the general case.

We experimentally obtain the constants (λ, $\alpha\_\delta^{18}O$, $\alpha\_\delta^{2}H$). If we have know of the initial value within the air bag (q_0, $\delta^{18}O_0$, $\delta^{2}H_0$), the ambient value (q_e, $\delta^{18}O_e$, $\delta^{2}H_e$), and the storage time of the sampling bag, we are able to simulate the variations in humidity and isotopic ratios

inside the air bag according to Equations 4 and 6. Correspondingly, if we know the storage time, along with the corresponding humidity and isotopic values (q(t), $\delta^{18}O_t$, $\delta^{2}H_t$), and the ambient values, we can also deduce the initial value at t = 0 by working backwards.

3.4.3 Parameter estimation

We estimate λ and α coefficients through laboratory experiments. To more precisely measure humidity and isotope variation with storage time in the air bag, we selected initial values inside the air bag that significantly differed from ambient conditions for the experiment.

We filled the clean air bag with dry air for the humidity experiment, and measured the variation in humidity within the air bag using a Picarro analyzer at intervals of 1 min, 2 h, 4 h, 6 h, 8 h, and 10 h, respectively. We conducted multiple measurements on both the same air bag and different air bags of the same size (see the times of experiment in table 1). According to equation 8, we estimated λ to be 0.0255 (Fig. 3-4a).

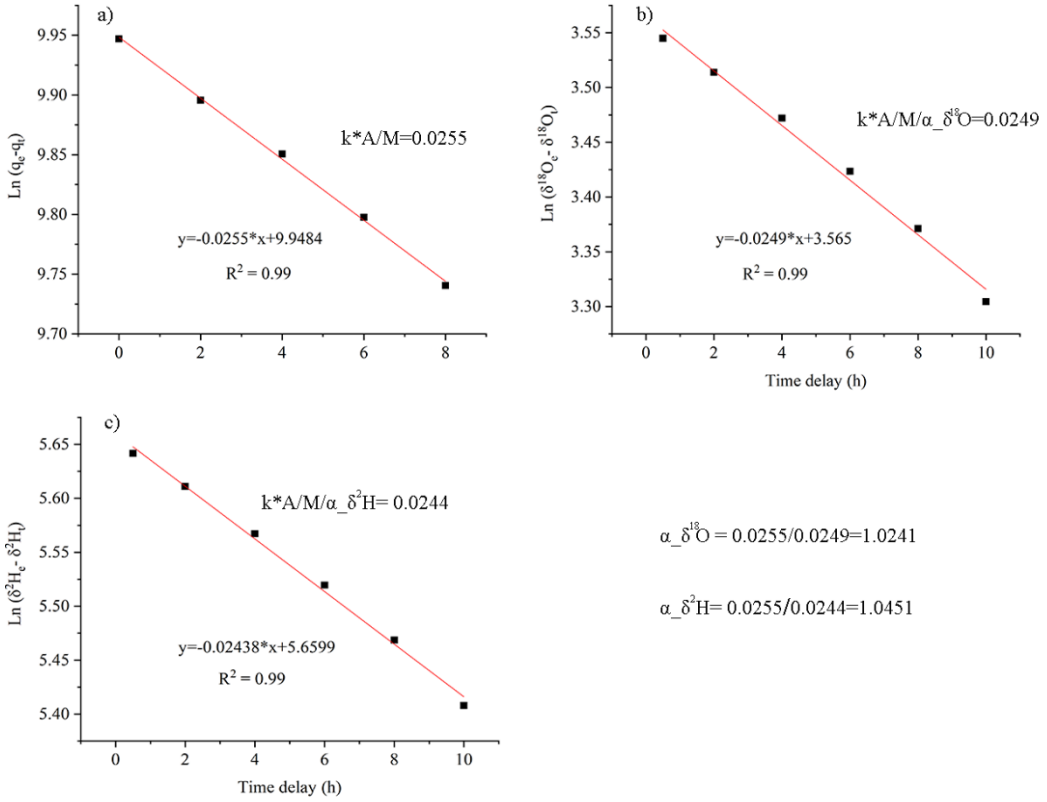

Figure 3-4 Determination of 3 parameters of our model: λ (a), α_$\delta^{18}O$ (b), and α_$\delta^{2}H$ (c).

For isotopic ratios, we fill clean air bags with dry air and inject a specific quantity of standard water, ensuring that the known isotopic values differ significantly from ambient values and that q_0 is approximately equal to q_e. We then measure the variation in isotopic ratio inside the air bag using a Picarro analyzer at intervals of 5 min, 2 h, 4 h, 6 h, 8 h, 10 h, and 24 h, respectively. Measurements are also performed multiple times on the same air bag, as well as

on different air bags of the same size. From the averaged results of these multiple measurements, and by using equation 11, we estimate the variation constant of isotopic ratio inside the air bag with ambient, expressed as λ/α, is 0.0249 for $\delta^{18}O$, and is 0.0244 for $\delta^{2}H$. We therefore can estimate $\alpha\_\delta^{18}O$ is 0.0255/0.0249 = 1.0241, $\alpha\_\delta^{2}H$ is 0.0255/0.0244 = 1.0451 (Fig. 3-4).

It's important to note that the parameters are influenced by factors such as the type of air bag, material, and ambient temperature. The parameters we've estimated pertain specifically to the Teflon air bag detailed in Figure 3-S1, which was tested at an ambient temperature of 16°C. The primary aim of this study is to provide a methodology.

3.4.4 Model validation

1) General case

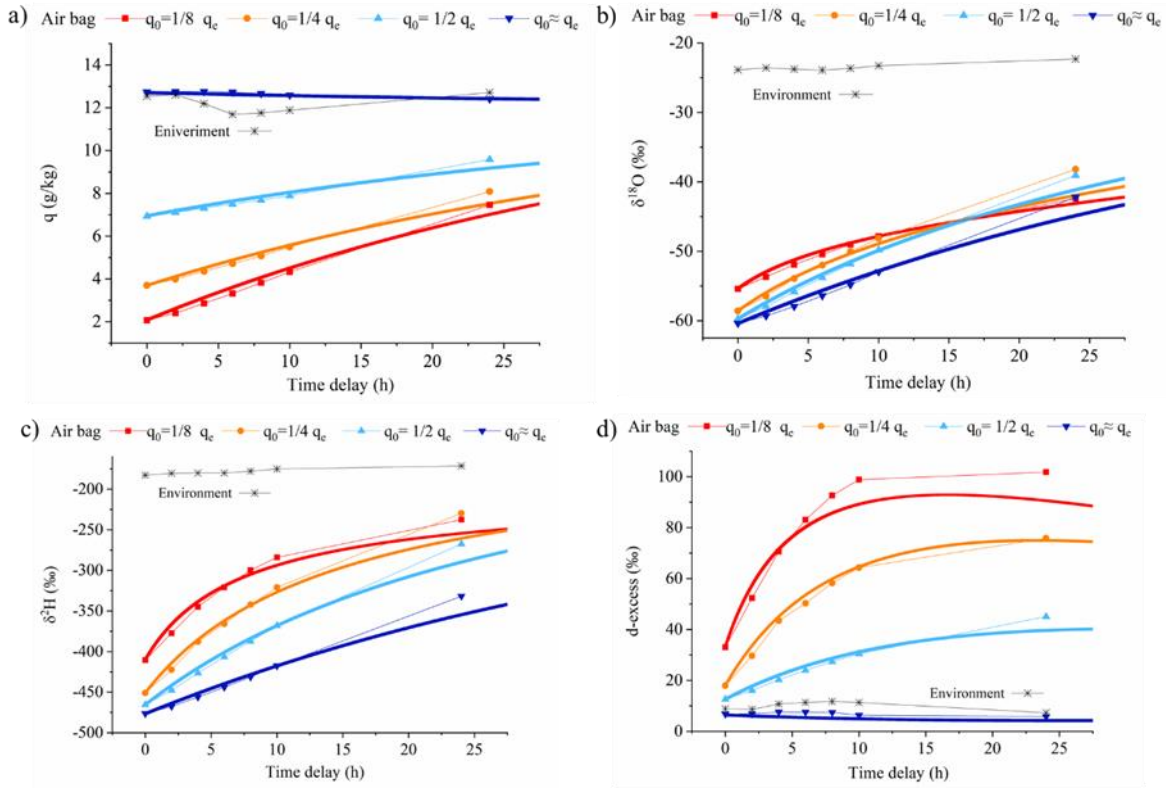

Figure 3-5 Comparison of laboratory experiments (markers) and diffusion model simulations (lines).

We start by filling a clean air bag with dry air, into which we inject varying amounts of standard water with a known isotopic value. Following this, we measure the isotopic ratio inside the air bag using a Picarro analyzer at intervals of 5 min, 2 h, 4 h, 6 h, 8 h, 10 h, and 24 h, respectively (represented by different shapes of the dotted lines in Fig. 3-5). For our diffusion model, we use the measurements taken after a 5-minute delay as the initial conditions for our diffusion model, as it is necessary to allow time for the injected standard water to fully evaporate into water vapor in the air bag. We then simulate the temporal changes in vapor isotopes inside the air bag, using a time step of 5 minutes (lines formed by densely packed

points in Fig. 3-5). The results from our diffusion model are in close agreement with our experimental observations, with only slight deviations noted. It is noteworthy that shorter delay times produce reduced deviations. When the humidity inside the air bag is lower than the ambient value, higher humidity vapor from the environment enters the airbag (Fig 5a). When water vapor isotopes in the air pocket differ significantly from ambient values, over time, $\delta^{18}O$ and $\delta^{2}H$ within the air bags gradually converge to ambient values (Fig 5b and c). In contrast, the d-excess value exhibits an increase as the time delay progresses (Fig 5d).

2) Particular cases

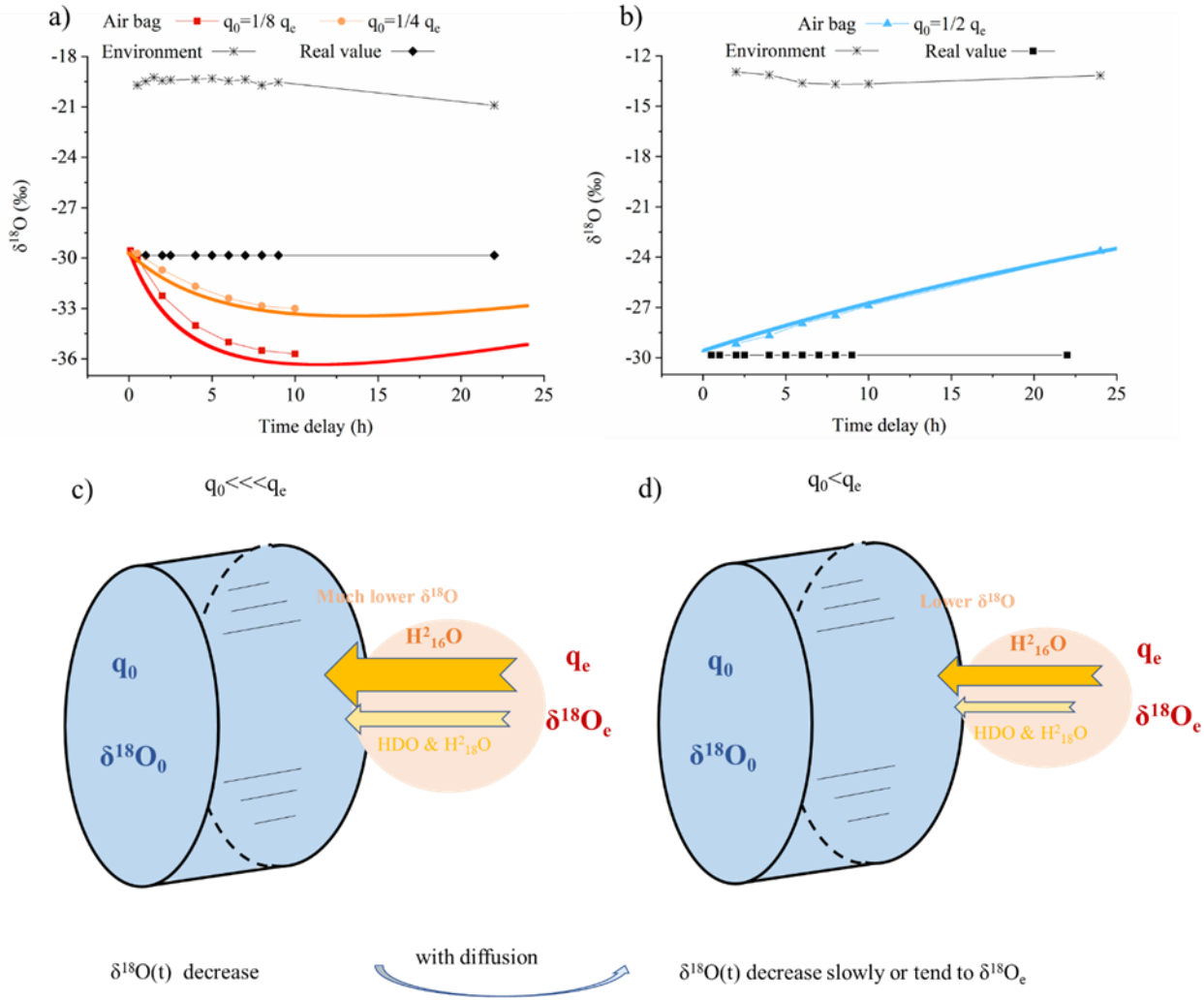

Figure 3-6(a-b) Evolution of $\delta^{18}O$ in scenarios: (a) where the difference between $\delta^{18}O$ and $\delta^{2}H$ values inside and outside the air bag is minimal, and/or when q_0 is significantly lower than q_e; (b) where $\delta^{18}O$ and $\delta^{2}H$ within the air bag are notably lower than ambient values. (c-d) Schematic illustrations of the underlying mechanisms.

Due to isotopic fractionation, the $H_2{}^{16}O$ enters the air bag preferentially relative to HDO and $H_2{}^{18}O$, yielding a vapor flux with lower $\delta^{18}O$ (Fig. 3-3). In cases where $\delta^{18}O$ and $\delta^{2}H$ within the air bag are significantly lower than the ambient values, the lower $\delta^{18}O$ and $\delta^{2}H$ (in comparison with ambient values) that enter the air bag are still higher than the initial values

inside the bag. This leads to an increase in $\delta^{18}O$ and $\delta^{2}H$ in the air bag towards the ambient values (Fig. 3-5 b andc, 6b and d). When the difference between $\delta^{18}O$ and $\delta^{2}H$ values inside and outside of the air bag is not substantial, and/or when q_0 is much lower than q_e, more low-value $\delta^{18}O$ and $\delta^{2}H$ vapors preferentially enter the airbag and dominate more quickly. This results in a decrease in $\delta^{18}O$ and $\delta^{2}H$ values inside the air bag (Fig. 3-6a and c). However, these values then converge to the first scenario as the differences in humidity and isotope values between the interior and exterior of the air bag decrease (from Fig. 3-6c to Fig. 3-6d). The smaller the difference in humidity and isotopes between the inside and outside of the air bag, the smaller and slower the isotopic change in the vapor within the air bag (Fig. 3-6 and Fig. 3-7).

In addition, due to isotopic fractionation, HDO enters preferentially relative to $H_2{}^{18}O$, yielding a vapor flux with higher d-excess. Consequently, the d-excess increases during the storage of the air bags.When the humidity difference between the inside and outside of the air bag increases, the d-excess of the vapor flux entering the air bag increases. This causes the value of vapor d-excess inside the bag to rise faster (Fig. 3-7 a and c). Also, post-correction, a relatively larger error is observed.

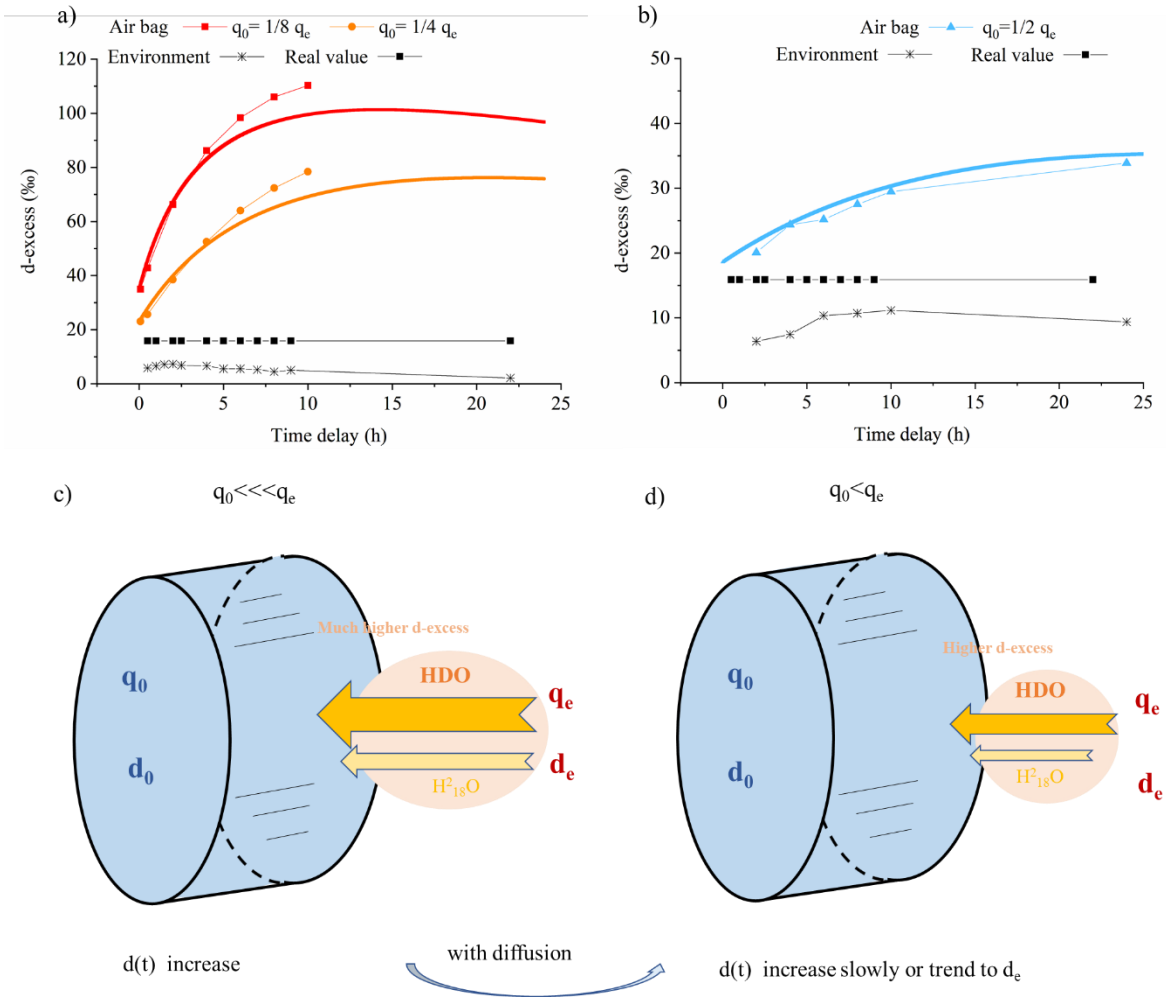

Figure 3-7 Variation of d-excess in different situations (a and b) and the cause (c and d).

3) Correction for laboratory experiments

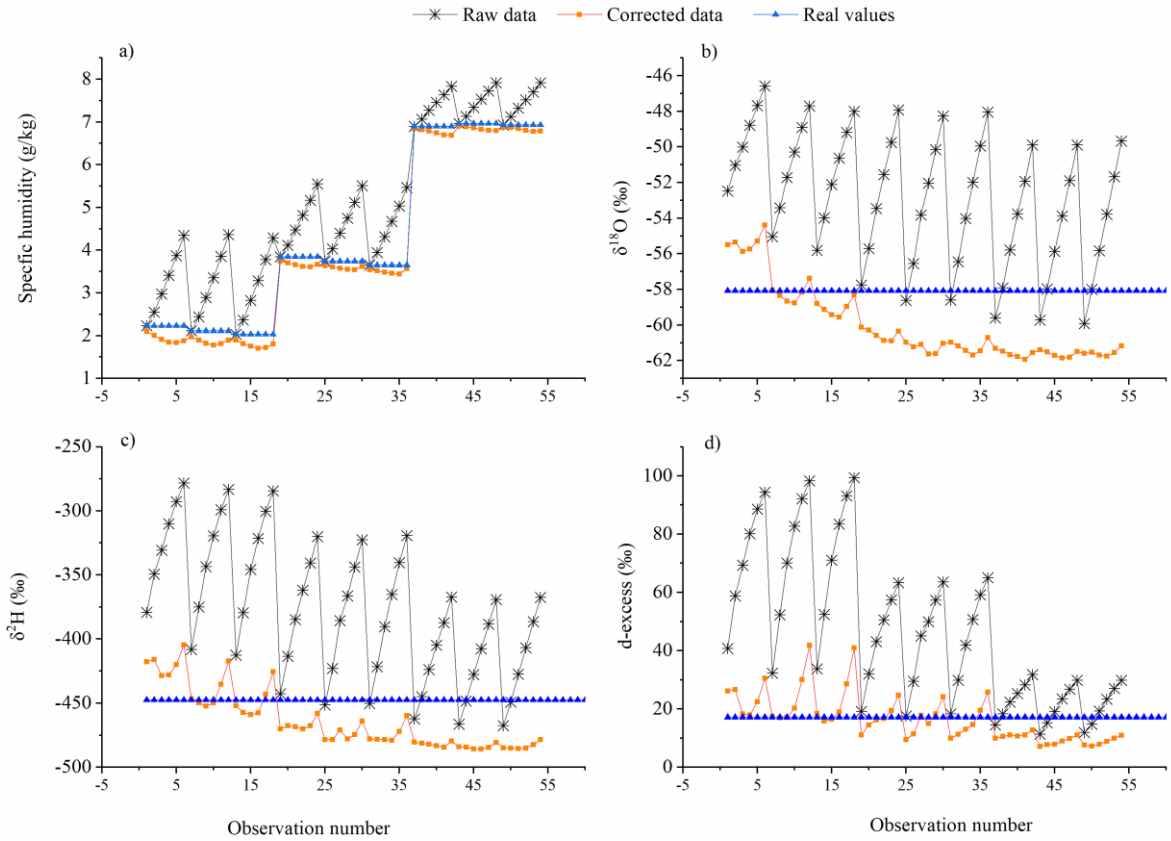

Figure 3-8 Comparison of experimental raw data, corrected data with diffusion model and real values: a) specific humidity, b) $\delta^{18}O$, c) $\delta^{2}H$, and d) d-excess

To assess the correction method in realistic simulations, we performed tests with various humidity. Figure 3-8 displays the raw experimental data, data corrected using the diffusion model, and the actual values. Due to varying storage times, there are discrepancies in the humidity differences between the interior and exterior of the air bag, leading to diverse alterations in the original experimental data within the bag. Upon correction using the diffusion model, even though the errors are not uniform, the data align more closely with the actual values. This demonstrates that our model can accurately adjust for the effects of environmental conditions on water vapor isotopes within the air bag.

3.5 Application to vertical profiles

3.5.1 Estimating the air mass in the bag

For the vertical profile samples obtained using UAVs, since λ (k*A/M) is related to M, the λ will be different because the sampling is done at high altitude with low air pressure and the M acquired by the sampling bag is different. We cannot estimate λ for different altitudes ($\lambda_{\_alt}$) by experiments, we will estimate it based on the variation of the collected M.

At a higher altitude, the air pressure $P_{\_alt}$ is lower than at surface $P_{\_surface}$, so less air is pumped into the bag. To compensate for this effect, we used a larger sampling time in altitude Sampling $time_{\_alt}$ than a surface Sampling $time_{\_surface}$. Therefore,

$$\lambda_{\_alt}=\lambda_{\_surface}*P_{\_surface}/P_{\_alt}*\text{ Sampling time}_{\_alt}/\text{Sampling time}_{\_surface} \quad (12)$$

where $\lambda_{\_surface}$ is λ estimated in the surface, Sampling $time_{\_surface}$ is the sampling time in the surface, and Sampling $time_{\_alt}$ is the sampling at different altitude.

During the sampling process, we recorded the sampling time. Given the variables Sampling $time_{\_alt}$, Sampling $time_{\_surface}$, $P_{\_surface}$ and $P_{\_alt}$,we could estimate $\lambda_{\_alt}$ at different altitudes using Eq. 13 and correct the observed vertical profiles of vapor isotopes with the diffusion model described in Section 3. Such estimates are subject to errors, which we will address in the subsequent section 4.3.

In the dataset derived from the UAVs and subsequently corrected using the aforementioned methods and diffusion modeling, we have omitted data points where the d-excess is less than 1, likely due to overcorrection, as these are less realistic. This represents a data exclusion ratio of 6 out of 1039.

3.5.2 Uncertainty estimation

Table 3-1 Uncertainty sources and estimation methods

Error contributions	Number of experiments	Estimation method	Used value (min~max for error estimation)
$\lambda_{\_surface}$	7	obtained from lab experiments (max & min)	0.031(0.0291~0.0317)
$\alpha\_\delta_{\_surface}$	5	obtained from lab experiments	$\alpha\_\delta^{18}O$ is 1.0241, $\alpha\_\delta^{2}H$ is 1.0451 ($\alpha\_\delta^{18}O$ is 1.0254, $\alpha\_\delta^{2}H$ is 1.0506 and $\alpha\_\delta^{18}O$ is 1.0264, $\alpha\_\delta^{2}H$ is 1.0380)
Sampling $time_{\_alt}$	-	recorded sampling time	± ¼
Mismatches between model and experiments	88	Average of correction error for all experimental results	2 ‰ for $\delta^{18}O$, 24 ‰ for $\delta^{2}H$, 9 ‰ for d-excess

Potential sources of error in the diffusion model correction process can arise from estimating $\lambda_{\_surface}$, $\alpha\_\delta_{\_surface}$, $\lambda_{\_alt}$, and from mismatches between model and experiments (Table 1).

For $\lambda_{\_surface}$, the uncertainty range can be estimated through laboratory experiments by taking the minimum and maximum value from all experiments.

For $\alpha\_\delta_{\_surface}$, we first need to validate the parameters obtained from the experiment. In section 3.3, we derived the average values of λ and λ/α from several experiments and then employed Eq. 11 to estimate α. In Section 3.4, we observed that the values simulated by the model exhibit minor discrepancies when compared to experimental results, thereby affirming the accuracy of our parameter selection. As highlighted in Section 3.1, it's necessary to estimate λ/α (and then calculate α) using outcomes from cases where $q_0 = q_e$. However, across these numerous experiments, it cannot be ensured that q_0 exactly equal to q_e, and q_e also might vary

over time. And part of the error has been considered as a mismatch between the model and the experiments. Therefore, we selected only those α that accurately simulate the majority of the experimental results for error assessment.

Regarding the sampling time, we recognize that employing the same air pump to extract air under varying atmospheric pressures for an identical time duration could produce different air quantities, denoted as 'M'. To compensate for this potential variability, we have factored in a more substantial margin of error for the recorded sampling time. As such, we assume a relative uncertainty range of ± ¼ for the recording sampling time when calculating $\lambda_{\_alt}$ using Equation 12.

For the mismatch between model and experiment, we first gather all experimental data and correct it using the diffusion model (Fig. 3-8). We calculate the difference between the corrected value and the actual values of the standard water. Note that after model correction, these data were subject to VSMOW normalization and humidity-dependent isotope bias correction as with the usual water vapor isotope corrections. Finally, we compute the average of all the error values.

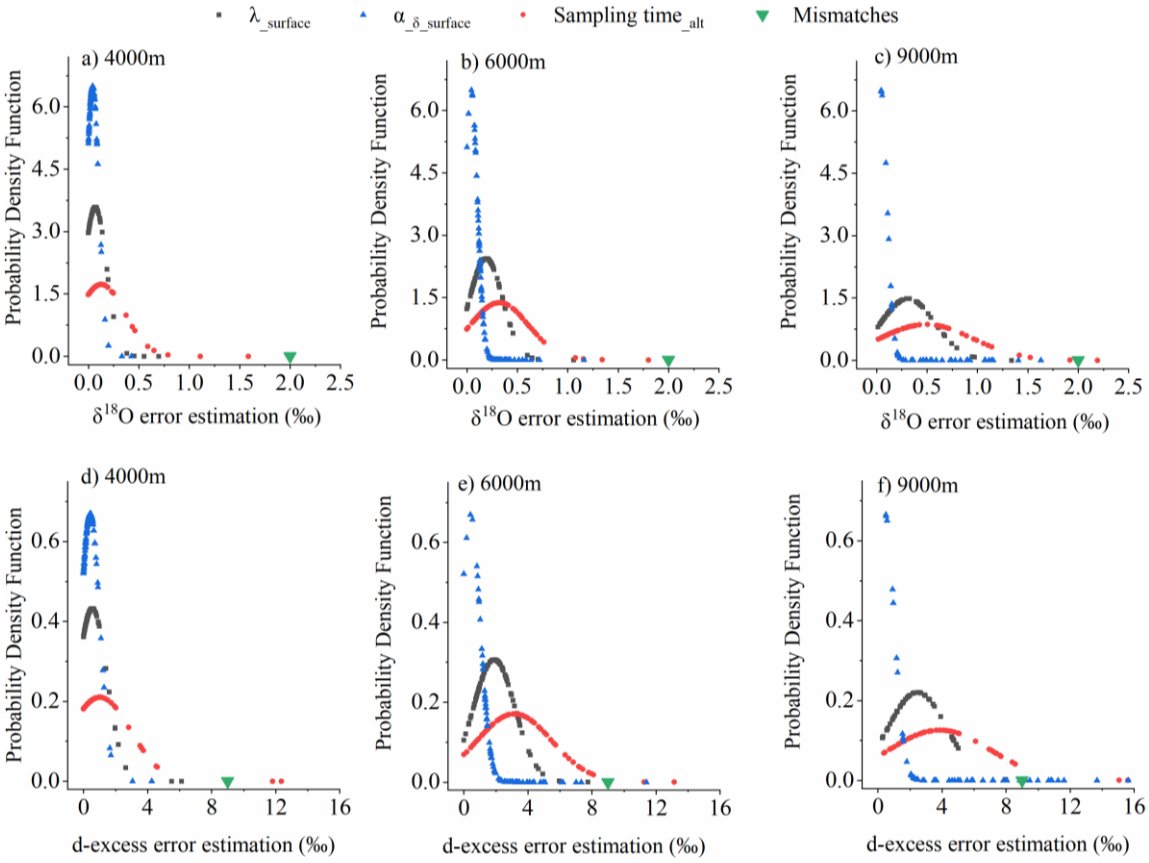

Figure 3-9 The contributions of different sources of errors of $\delta^{18}O$ (a, b, c for 4000m, 6000m, 9000m, separately) and d-excess (d, e, f for 4000m, 6000m, 9000m, separately).

We analyzed the contributions from different sources of error using probability density function plots (Fig. 3- 9). At all altitudes, the main contribution to the total error is the mismatch between model and experiments, which is assumed constant (green marker). The three other sources, at various heights and irrespective of whether they concern $\delta^{18}O$ or d-excess, adhere

to a unimodal normal distribution. Errors attributed to variations in the sampling time is the second major source of error and exhibits the largest spread. It increases with altitude since sampling time increases with altitude (Fig. 3- 10). Errors associated with differing $\lambda_{\_surface}$ and $\alpha_\delta$values exhibit an increase with altitude (Fig. 3-10). This pattern arises because the magnitude of the correction intensifies with increasing altitude. Detailed discussions on this are provided in section 4.3. Overall, the total error remains within a limit of 3‰ for $\delta^{18}O$ and 20‰ for d-excess.

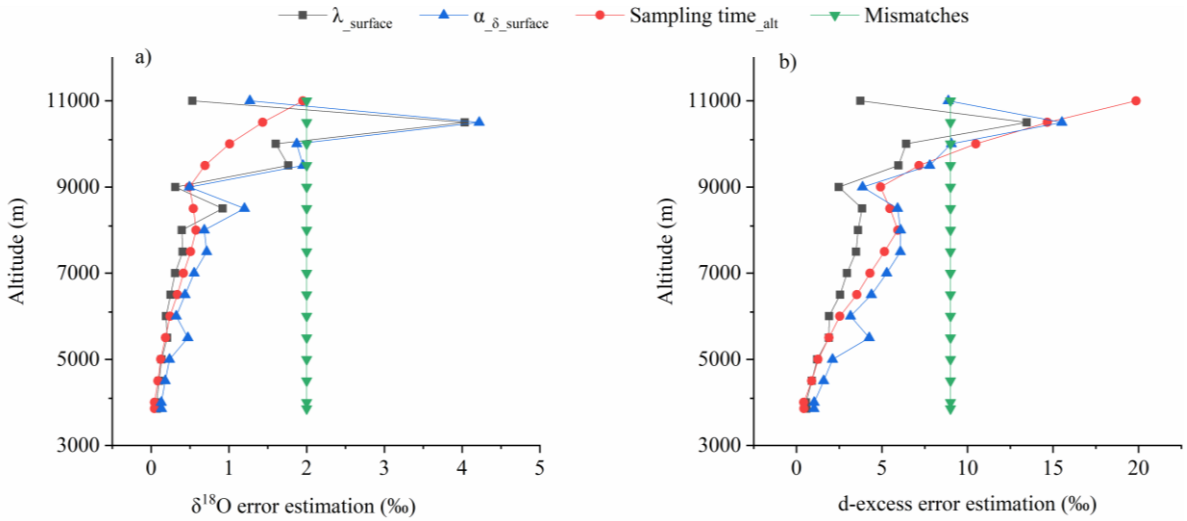

Figure 3-10 Mean values of $\delta^{18}O$ errors (a) and d-excess error (b) for different sources at different altitudes.

As delineated in Section 3, we employed experimental data from ground-based laboratories to discern the alterations of vapor isotopes within the air bag under atmospheric conditions at ground level, to estimate $\lambda_{\_surface}$ and $\alpha\_\delta_{\_surface}$. In Section 4.1, by estimating the difference in air mass across varying atmospheric pressures at distinct altitudes, we derived an estimation for $\lambda_{\_alt.}$ These process introduce more significant error in high altitude, which is exacerbated by the reduced humidity encountered at elevated altitudes, thus compromising correction accuracy. Consequently, as altitude increases, we observed an amplification of the errors in both $\delta^{18}O$ and d-excess (Fig. 3-10). This also explains the pronounced dispersion observed in the error attributed to $\lambda_{\_alt}$ in Fig. 3- 9. Contrarily, errors pertaining to $\lambda_{\_surface}$ and $\alpha\_\delta_{\_surface}$ diminish at altitudes exceeding 10500 meters.

To determine the total error, we compute the maximal discrepancy between all calibration results and the corrected data we employed. To this value, we add the average of the mismatch values observed between the model and the experiments (2 ‰ for $\delta^{18}O$, 24 ‰ for $\delta^{2}H$, and 8 ‰ for d-excess). The final result represents the maximum value derived from all four error sources.

3.5.3 Comparison for raw data, corrected data and satellite data

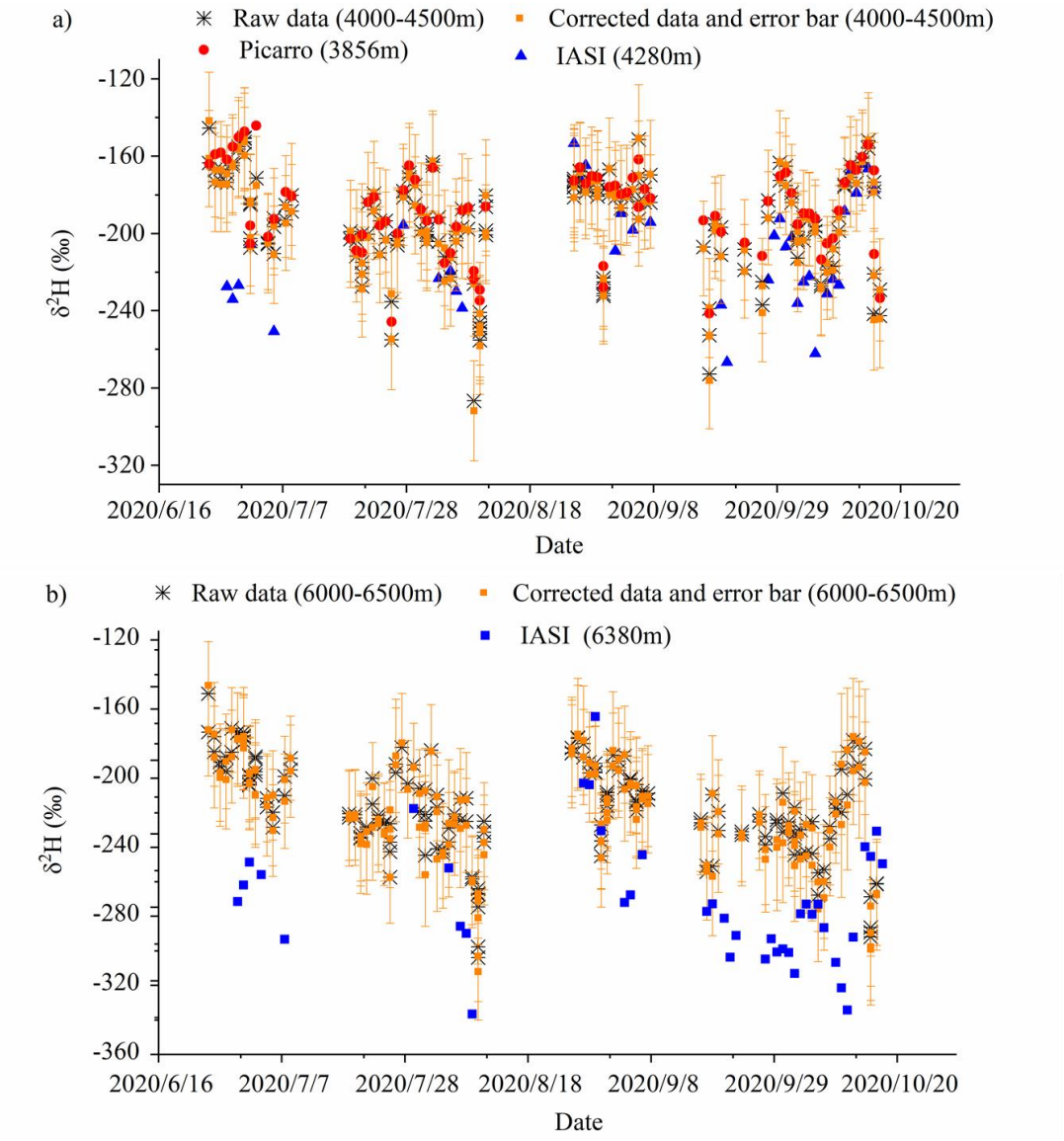

Figure 3-11 Comparison of time series for raw data, corrected data and satellite data IASI, and associated uncertainties for $\delta^{18}O$ at altitude 4000-4500m (a) and 6000-6500m (b).

As illustrated in Fig. 3- 11a, there is a notable agreement between both the raw and corrected data with the water vapor isotopes observed directly by Picarro at ground level (3856m), and all showcasing consistent seasonal variations. The water vapor isotopes observed directly by the ground-based Picarro instrument serve as the most reliable reference for our air bags observations from low altitude. Air bags samples collected at the ground level and approximately 4000 m altitude exhibit negligible differences in both water vapor isotopes and humidity compared to the ground-based measurements. This arises because, for these samples, the ambient humidity and isotopic composition closely match those sampled within the bag,

minimizing the impact of diffusion through the bag. To compare our corrected measurements with independent observations at higher altitudes, we reference the IASI satellite dataset. It's crucial to recognize, however, that this comparison is nuanced by the differences in horizontal and vertical footprints of the measurements, as well as disparities in spatio-temporal sampling (Shi et al., 2020). Thus, the comparison remains largely qualitative. For most time intervals, IASI is consistent with our observations (Fig. 3-11 a and b). Nonetheless, during some periods, like the data from June 2020, the satellite data are markedly lower than both the direct water vapor isotope measurements from Picarro and the isotope observations from the air bags. The evaluation of the diffusion model indicates a broader margin of error; when accounting for these errors, parts of the observations align more closely with the IASI data.

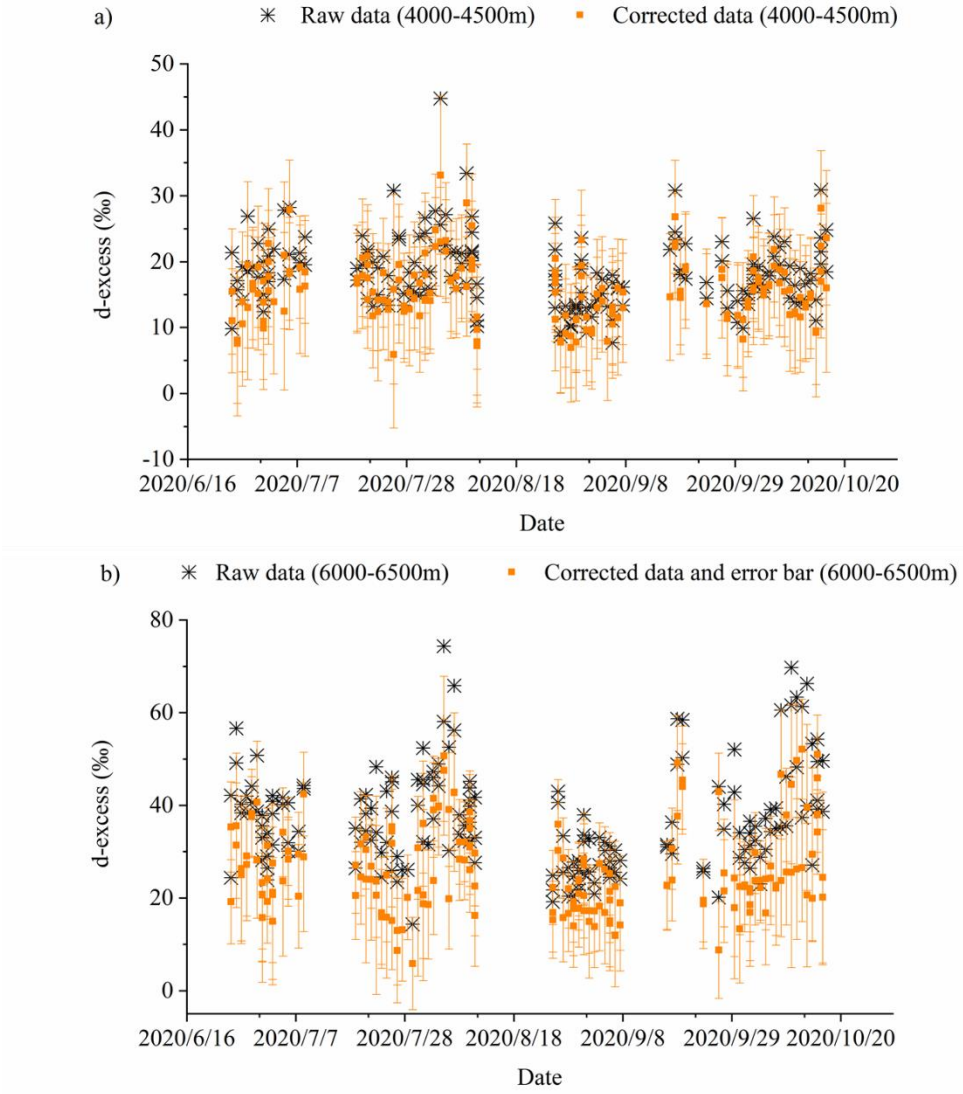

Figure 3-12 Comparison of time series for raw data and corrected data, and associated uncertainties for d-excess at altitude 4000-4500m (a) and 6000-6500m (b).

As delineated in Section 3.4, during storage in the air bag, HDO is preferentially admitted over $H_2{}^{18}O$. This leads to an increased d-excess vapor flux and a consequent elevation in d-excess in the air bags. Consequently, the diffusion model applies corrections, resulting in a lower value of d-excess post-correction (Fig. 3-12).

3.6 **Conclusion**

Acquiring high spatial and temporal resolution water vapor isotope data is critical for a comprehensive understanding of hydrologic cycle processes. Specifically, there is a shortage of observations of water vapor isotope vertical profiles, and satellite data are only available at limited vertical and temporal resolution. The challenge of obtaining high spatial and temporal resolution water vapor isotope data, especially in conditions where direct measurements are difficult, has been a significant hurdle for the scientific community. This study showcases the potential of using a drone-based airbag sampling method to overcome this challenge. It effectively addresses the issues associated with the inconvenient portability of traditional methods such as Mass Spectrometry and Laser Spectroscopy. Notably, our approach satisfies the need for lightweight equipment, providing a more economical, efficient, and flexible solution for high-altitude water vapor measurements compared to traditional methods involving manned aircraft. This feature significantly expands its potential applications across various environments, thus enhancing the range and richness of data that can be gathered for water vapor isotope observations.

While airbags offer the advantage of collecting samples, their inherent permeability can compromise the integrity of the sample. This issue is related not only to the materials used but also to the valves or interfaces associated with non-integrated designs, leading to variability in permeability, with some materials showing lower permeability. We recommend prioritizing glass containers or airbags with the lowest permeability for those collecting water vapor using portable devices. Furthermore, conducting the permeability experiments described in this article before any experimental undertaking is crucial. This includes storing water vapor with known isotopic values in the portable collection device for an extended period before re-measuring the isotopic values to assess or determine the device's permeability parameters.

To address the permeability issue, we developed a mathematical model to assess the impact of diffusion and fractionation, ensuring the reliability of isotope observations. Consequently, our model aims to provide a comprehensive means to both assess and correct data. This model, whose parameters are calibrated using laboratory experiments, offers a practical solution to the prevalent permeability of the air bag material. Through rigorous validation against observational experiments under varying conditions, and comparison with satellite data, we demonstrated the efficacy and robustness of our model. Hence, we assert that the model significantly enhances the reliability and applicability of water vapor isotope observations with airbag sampling. It allows us to exploit the benefits of drone-based air bag sampling while effectively mitigating its potential limitations. Our drone-based sampling system, in conjunction with our diffusion model, provide a more efficient, economical, and flexible method for collecting high-altitude water vapor measurements, adds a valuable tool to the scientific community's toolkit, significantly advances the field of water vapor isotope studies and its potential.

3.7 **Supplement 1-Vedio**

Video showcasing our field work:
https://drive.google.com/file/d/1uYDhY7TMzFbyWOjJCaxhOpAHX0G-LL7t/view?usp=sharing

4 Drone-Derived Atmospheric Vapor Isotope Profiles up to the Upper Troposphere Across the Entire Monsoon in the Southeastern Tibetan Plateau: Insights into Deep Convective Processes

4.1 Abstract

Stable isotopic signals preserved in natural precipitation archives, such as ice cores, offer insights into historical climatic shifts. When analyzed in water vapor, these isotopes illuminate insights into atmospheric dynamics like large-scale transport, convection, and cloud-related processes. To better understand the physical processes that control the vertical distribution of vapor isotopes and the added value of vapor isotopic measurements to infer deep convective processes, we have conducted pioneering observations of the vertical profiles of atmospheric vapor isotopes up to the upper troposphere (from the ground surface at 3856m up to 11000m a.s.l.) from June to October in the southeastern Tibetan Plateau, using a specially-designed unmanned-aerial-vehicle system. This marks the first time the vertical distribution of atmospheric water vapor isotopes has been measured across the entire monsoon period up to the upper troposphere, boasting an unprecedented vertical resolution and altitude range.

We find that the vertical profiles of water vapor isotopic composition reflects a combination of large-scale processes, in particular deep convection along trajectories, and local convective processes, in particular convective detrainment, sublimation of ice crystals and continental recycling. The observed vapor $\delta^{18}O$ and $\delta^{2}H$ decreases and its d-excess increases with altitude up to 8-10km, consistent with the progressive condensation of water vapor and precipitation. Beyond this altitude, where the maximum convective detrainment occurs, the vapor $\delta^{18}O$ and $\delta^{2}H$ re-increases with altitude, reflecting the sublimation of ice crystals detrained from convective clouds and continental recycling. The vapor is more depleted during the monsoon season and in October, and are mainly due to deep convection along trajectories. In this study, we present the first-ever vertical profiles of d-excess extending to the upper troposphere. Notably, we observed elevated levels during the monsoon period, which can be attributed to the initial vapor for the Rayleigh distillation being more depleted. The observed seasonal and intra-seasonal variations are generally vertically coherent, due to the strong vertical convective mixing and local convective detrainment of vapor originating from the low levels. Our observations offer valuable and rare data that enhance our understanding of vertical variations in water vapor isotopes, influences of convection, variations in upper tropospheric humidity, and paleoclimatic interpretations based on both $\delta^{18}O$ and d-excess.

4.2 **Introduction**

Stable isotopic signals (marked as $\delta^{18}O$ and $\delta^{2}H$) preserved in natural precipitation archives such as ice cores (Jouzel, 2003; Thompson, 2000), serve as invaluable tools for understanding historical climatic data. Precipitation is a product of water vapor that originates at varying altitudes. Researchers also collect and study natural precipitation archives from different altitudinal points. As a result, a comprehensive understanding of vertical isotope variations becomes imperative for accurately interpreting these paleoclimate records.

Water vapor isotopes potentially offers refined diagnostics of the atmospheric water cycle (Galewsky et al., 2016). However, the translation of isotopic measurements into quantitative applications for the current atmospheric water cycle has been challenging, prompting skepticism about the utility of these measurements (Duan et al., 2018). An alternative perspective posits that quantitative interpretation of water isotope measurements are hindered by the limited understanding of mechanisms governing the vertical profiles of water vapor isotopes. Consequently, to optimize the application of these isotopes in both paleoclimate and contemporary water cycle studies, it becomes paramount to enhance our grasp on the mechanisms shaping the vertical distribution of water vapor isotopes.

Several studies utilizing aircraft and balloon-borne instruments have illuminated the complexities of water vapor isotope vertical profiles. Between 1965 and 1973, (Ehhalt, 1974) pioneered measurements of D content in the troposphere over the U.S., uncovering a consistent isotope depletion via the Rayleigh fractionation process. Subsequent reanalysis (Ehhalt et al., 2005) indicated both an altitude and seasonal effect on this depletion. Taylor's airborne studies over southern Germany (Taylor, 1972) underscored the significant roles of turbulent mixing and horizontal transport. Furthermore, (Dyroff et al., 2015) and (Sodemann et al., 2017) both highlighted the significance of boundary layer processes in the lower troposphere, while (Webster and Heymsfield, 2003) highlighted the role of convective detrainment of ice crystals in the upper troposphere. With an expanding repository of aircraft-derived vertical water vapor isotope profiles, like those from EUREC^{4}A and ORACLES, the role of convection and clouds process emerge as recurrent themes. While deep convection depletes the free tropospheric water vapor, it enriches the upper troposphere (Lacour et al., 2018). Several studies have also documented the water vapor d-excess in the lower troposphere (He and Smith, 1999; Salmon et al., 2019)

Most of these studies were however limited in the range of altitude that were observed. Satellite instruments can observe vapor $\delta^{2}H$ distribution globally at different ranges of altitude, from the lower troposphere (Frankenberg et al., 2013; Frankenberg et al., 2009), middle troposphere (Lacour et al., 2012; Toride et al., 2021; Worden et al., 2006; Worden et al., 2019), upper troposphere (Nassar et al 2007, Steinwagner et al 2010). However, these observations are restricted to $\delta^{2}H$, and thus cannot document the second parameter d-excess. Consequently, the processes governing these profiles of water d-excess remain only partially understood.

In the context of the important role of atmospheric water vapor for the hydrological cycle and climate(Sherwood and Dessler, 2000), isotopic profiles of vapor have the potential to illuminate processes controlling its distribution and changes, including convection patterns, vertical mixing, atmospheric transport, vapor origins, condensation mechanisms and

convective intensity. Such insights are also particularly crucial for deciphering processes in the upper troposphere, where the humidity plays a critical role in Earth's radiation budget, cloud processes, and the water vapor feedback (John and Soden, 2007). In the upper troposphere, even minute concentrations of water vapor can markedly alter radiative forcing, inducing significant global temperature fluctuations. Understanding the sources of upper-tropospheric humidity is essential for modeling climate and predicting how water vapor feedback might amplify or mitigate future warming (Bony et al., 2006; John and Soden, 2007). The role of ice sublimation in controlling upper tropospheric humidity is still debated. While some studies posit that it is primarily governed by the last saturation temperature (Salathé and Hartmann, 1997; Sherwood, 1996), others emphasize the significance of ice sublimation from cirrus clouds and anvils of deep convective clouds (Folkins and Martin, 2005; Sherwood and Dessler, 2000). One of our objective is to leverage water vapor isotopes in the upper troposphere as tracers to clarify this matter.

Seasonal variations could significantly influence the vertical profiles of water vapor and water vapor isotopes. Intra-seasonal fluctuations in surface precipitation or vapor isotopes at low latitudes can be as large as seasonal and inter-annual variations, adding complexities to isotope-based paleoclimate interpretations and introducing uncertainties in dating isotope signals from ice cores (Shao et al., 2017; Wang et al., 2023). The Boreal Summer Intra-seasonal Oscillation (BSISO), representative of the Northern Hemisphere's most notable intra-seasonal variations during summer, exhibits a characteristic northward progression (Kikuchi, 2021). This variability profoundly influences rainfall distribution across extensive regions of South and East Asia, affecting various weather and climatic events, from typhoon genesis to the onset and cessation of the monsoon (Lee et al., 2013; Wang and Xie, 1996). The BSISO significantly influences the isotopic ratios of precipitation and vapor at low latitudes during the summer monsoon season. The extended observation period from pre-monsoon to post-monsoon could capture the changes under diverse large-scale or local atmospheric processes and enhance our understanding of water vapor isotopic behavior throughout different seasons.

To gain insights into the factors governing the vertical distribution of $\delta^{18}O$, $\delta^{2}H$ and d-excess in water vapor, we opted for a uniquely designed unmanned-aerial-vehicle system (UAVs). This UAVs provides greater flexibility and cost-effectiveness compared to alternatives like pontoon boats and larger drones. Detailed specifications of the sampling system are elaborated upon in chapter 3. We recorded the vertical profiles of atmospheric vapor isotopes from the ground surface at 3856m to 11000m a.s.l. between June and October in the southeastern Tibetan Plateau. This pioneering study offers an unprecedented vertical resolution and altitude range, capturing the complete monsoon period up to the upper troposphere. By fusing our insights into the modern water cycle, as revealed by vertical profiles of water vapor isotopes, with the rich tapestry of the paleoclimate record, we aspire to offer a more nuanced, interconnected interpretation of climatic history, emphasizing both $\delta^{18}O$ and d-excess.

4.3 Data and Methods

4.3.1 Geophysical description

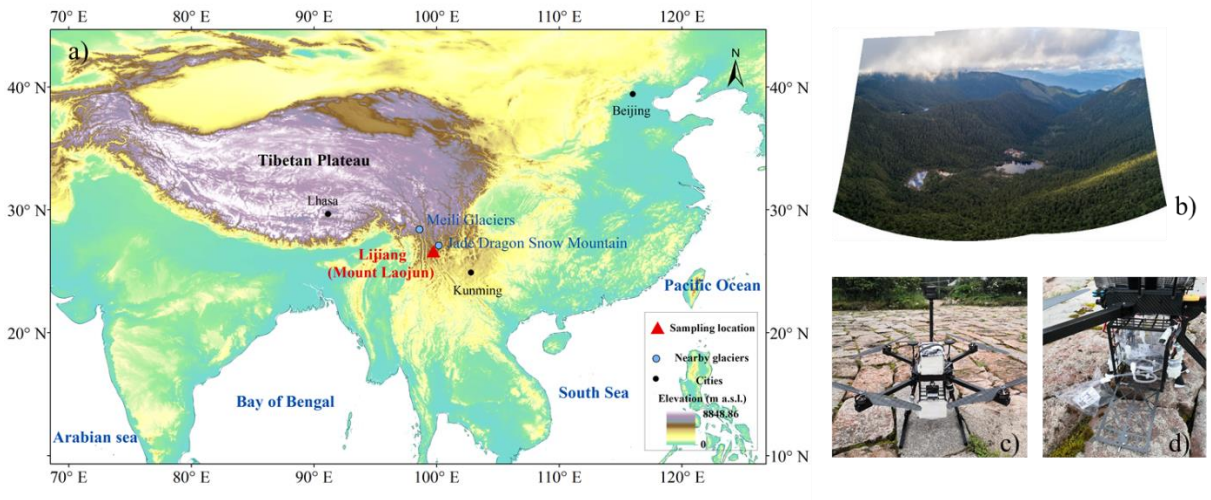

Figure 4-1 Geographic location of the site (a), landscape of the sampling site (b), one of the drones used (c), and sampling system (d).

Our drone sampling was conducted at a pristine forest of Mountain Laojun, specifically at 99 Longtan, located in Lijiang on the southeastern edge of the Tibetan Plateau (Fig.4-1a and b). This location lies at the crossroads of water vapor transport channels from both the southwest and southeast monsoons (Yao et al., 2012), making it an ideal site for vertical profile measurements and studding the vertical mixing process of different water vapor sources during altitude transport in the free atmosphere. This site, over 50 kilometers from the nearest small villages, offering a pristine research environment devoid of human interference. Laojun Mountain's main peak stands at 4,220 meters, while our UAV's launch altitude was 3,856 meters, ensuring our observations are free from interference by neighboring mountains. These natural advantages make the site ideal for observations of the free troposphere, allowing for a true representation of natural atmospheric processes. Moreover, its proximity—100 kilometers from the Jade Dragon Snow Mountain group and 400 kilometers from the Meili Glacier group—renders our atmospheric vertical profiling pivotal for hydrological and paleoclimatic studies of glaciers in the southeastern region of the Tibetan Plateau. Figure 4-1c displays one of our specially-designed drone, which is capable of reaching altitudes up to 11,000m. Figure 4-1d illustrates the collection module designed for fixed-height sampling at predefined altitudes. This module uses air pumps and a rudder mounted on the UAV, paired with a control module that operates in conjunction with a remote operating system. This drones-based vapor sampling system was cooperated with Nanjing University of Information Science and Technology.

4.3.2 Vapor isotope observations

The dry air will be sent to the Picarro to flush background water vapor before measurement of the bag air. We employed the Picarro 2130i CRDS analyzer for vapor $\delta^{18}O$ and $\delta^{2}H$ measurements and used a calibration function with a standard delivery module (SDM) and lab standard water for bias correction. Vapor isotope values were calibrated to the VSMOW-SLAP scale. Our observations show that at altitudes above 10,000 meters, water vapor concentrations predominantly fall within the 500-1500 ppm range. To calibrate our measurements, we determined the values of standard water for concentrations within this specific range, allowing the correction of our observed water vapor concentrations. To achieve high-altitude UAV sampling, we opted for portable sampling bags. The dry air and our sampled bag air will be delivered to the isotope analyzer by a three-way valve. These introduced contamination and fractionation challenges due to permeability. To counter this, we formulated a diffusion model to track water vapor across the bag's surface, refining its parameters through laboratory experiments. This model allows us to estimate the initial isotopic composition of the sampled vapor. Our results were compared with existing satellite data, and we delved deeper into potential calibration inaccuracies of the diffusion model via laboratory examinations, establishing the error boundaries for our findings. An in-depth discussion of this diffusion model is available in chapter 3 of this thesis.

4.3.3 Meteorological observations

The UAV's on-board sensors and GPS captured data including air temperature (°C), humidity (%), altitude (meters above sea level), latitude (degrees), longitude (degrees), and speed (m/s) of the UAV throughout its flight. Additionally, meteorological data was acquired from a nearby meteorological station located 50 kilometers from our observation point. This data, obtained daily at 8:00 p.m. via a balloon, encompassed geopotential height (meters) corresponding to wind direction (degrees) and speed (m/s), temperature (°C), and dew point temperature (°C). Using this data, we were able to compute relative humidity (%), specific humidity (g/kg), and saturation specific humidity (g/kg). The drone is equipped with a camera, allowing us to observe its surroundings in real-time from the ground. We documented the time and altitude at which the drone entered and exited the clouds during each flight, enabling us to calculate the cloud fraction as follows (Rossow and Schiffer, 1999):

$$Cloud\ Fraction = \frac{\text{Days with cloud at specific altitude}}{\text{Total days observed}}$$

4.3.4 Rayleigh distillation model including ice sublimation

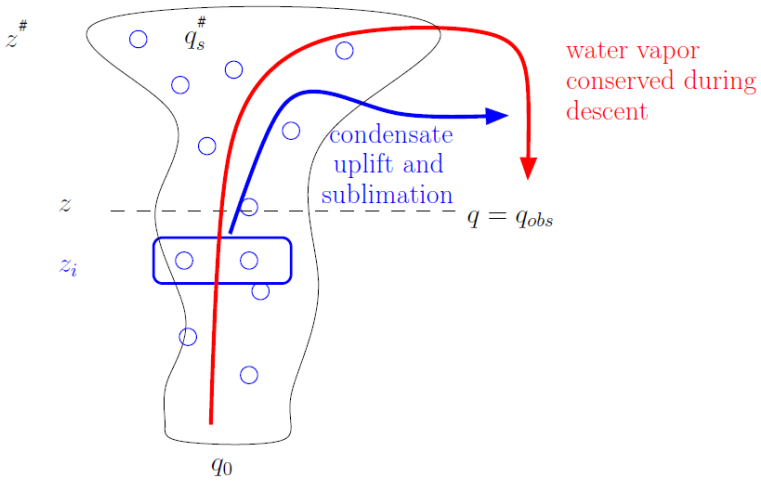

Figure 4-2 Schematic diagram of the Rayleigh distillation model including ice sublimation

We adopt a framework grounded in the Rayleigh distillation concept, inspired by last saturation paradigm (Sherwood, 1996) and by the two-plume model by Duan et al 2018. It incorporates moistening effects due to ice sublimation (Bony et al., 2008), while accounting for the origin altitude of the condensate. We postulate that the air parcel undergoes distillation until reaching an altitude $z^{\#}$, termed the last-saturation altitude. At this altitude, the saturation humidity is $q_s^{\#}$. The parcel subsequently descends to level z. As it descends, the total water is conserved. As the air becomes unsaturated, some ice crystals sublimate into the parcel (Fig.4-2). After the descent and sublimation, the humidity is what we observed at altitude z:

$q = q_{obs}$

The humidity conservation equation can be expressed as: $q = q_s^{\#} + q_i$.

We define ρ as the fraction of the observed vapor that has its origins in ice sublimation:

$$\rho = \frac{q_i}{q}$$

The isotopic ratio of the vapor detrained at $z^{\#}$ is:

$$R_s^{\#} = R_0 * \left(\frac{q_s^{\#}}{q_0}\right)^{(\alpha^{\#}-1)} \quad (1)$$

where α* is the average α from z_0 to $z^{\#}$, weighted by $d\ln(q_s)$.

For the ice component, pinpointing the condensate's origin poses challenges. This condensate might be derived from droplets that were initially lifted, frozen, and then sublimated. Alternatively, it could originate from localized ice crystals present in a storm's anvil that undergo sublimation. For simplification, we assume this condensate typifies condensate generated at an altitude $z_i = z + \Delta z$ (Duan et al., 2018).

Therefore,

$$R_i = \alpha(z_i) * R_0 * \left(\frac{q_s(z_i)}{q_0}\right)^{(\alpha(z_i)-1)} \quad (2)$$

The equation of mixing between the descending vapor and the sublimating ice is:

$R*q = R_s^{\#} * q_s^{\#} + R_i*q_i$

From which, R is given by:

$$R = \frac{R_s^{\#} * q_s^{\#} + R_i*q_i}{q} \quad (3)$$

To calculate the profile of R, we need the profile of q, and some values for ρ and Δz:

1) Select a value for ρ (ranging from 0 to 1) and a value for Δz ((spanning, for example, from -4km to +4km).

2) Compute $q_s^{\#}$ and q_i using: $q_s^{\#} = (1 - \rho)*q_{obs}$ and $q_i = \rho*q_{obs}$

3) Ascertain $R_s^{\#}$ based on Eq.1

4) Determine z_i via : $z_i = \max(\min(z + \Delta z, z_{top}), z_0)$, where z_{top} is the cloud top height

5) Calculate R_i using Eq.2.

6) Derive R employing Eq.3.

Diverse values for ρ and for Δz.

4.3.5 Water vapor isotopic retrievals by satellite IASI

Of the available instruments, the Infrared Atmospheric Sounding Interferometer (IASI) boasts the best spatiotemporal sampling capabilities for δ^2H retrieval (Lacour et al., 2012; Lacour et al., 2018). Its horizontal footprint is approximately 12 km at nadir (directly beneath the satellite), and as the observation angle increases, IASI's coverage expands, ensuring almost global coverage twice daily. For this study, in order to compare the spatial distribution of δ^2H near our observation site over different periods, we use the monthly average data for the specific month in focus. Satellite-derived measurements of water vapor isotopes typically have a constrained vertical resolution. IASI's retrievals typically represent three distinct vertical altitudes: 2950m, 4220m, and 6380m. Given our study's starting altitude of 3856m, we use the δ^2H retrievals at 4220m and 6380m above ground level for a more relevant comparative analysis.

4.3.6 Back trajectories

In our study, we employed the Hybrid Single-Particle Lagrangian Integrated Trajectory (HYSPLIT) model, a widely-used tool for atmospheric trajectory analysis, driven by the GDAS dataset, to conduct 10-day trajectory frequency distribution analyses (Stein et al., 2015). We initiated trajectories at altitudes of 4000m, 6000m, and 9000m above ground level. As most of our sampling was conducted from 10am to 6pm local time, we computed 10-day back-trajectories at CST 10:00, 14:00, and 18:00 for each day. Using HYSPLIT's capability to generate a grid over the study area, the frequency distributions were derived by counting the number of trajectory endpoints in each grid cell. This allowed us to delineate predominant airflow patterns influencing the study region during the observation period and understand potential source regions.

4.3.7 Cloud resolving model simulations

In this study, we employed a Cloud Resolving Model (CRM) from (Risi et al., 2020; Risi et al., 2023) — the System for Atmospheric Modeling (SAM) non-hydrostatic model (Khairoutdinov and Randall, 2003), version 6.10.9, which is equipped with water isotope ratio capabilities (Blossey et al., 2010). Within the model, an elastic conservation equations are applied to components like momentum, energy, and water across its six phases: vapor, cloud liquid, cloud ice, and the precipitates of liquid, snow, and graupel.

We use simulations at a 750m resolution in a radiative-convective equilibrium, maintaining a consistent sea surface temperature (SST) of 30°C, on a three-dimensional, doubly periodic domain. We use two simulations, with and without large-scale ascent to emulate isotope variations in varying convection intensities (Risi et al., 2020). The entire modeling process spanned 50 days, with the last 10 days analyzed via a daily three-dimensional output. Further insights and details can be found in (Risi et al., 2020; Risi et al., 2023).

4.4 Results

Figure 4-3 illustrates the evolution of $\delta^{18}O$ and d-excess from June to October at various altitudes. According to the monsoon monitoring report of the National Climate Center of China, the summer monsoon in 2020 began on May 4, 2020, and receded on October 6, 2020. Based on these information, we preliminarily classified our observations into Monsoon periods (from 25th June to 7th October) and Post-monsoon_Oct (from 7th October to 17th October).

We note the seasonal and intra-seasonal variations in vapor $\delta^{18}O$, exhibiting vertical coherence (Fig.4- 3a). Observations across various elevations consistently show more enriched values in the early June (representing the early monsoon) and early September (following the peak monsoon). In contrast, more depleted values emerge during the peak monsoon months of July and August and the end of September (the end of monsoon). This is consistent with observations and simulations from the Tibetan Plateau (Yao et al., 2013), and has been interpreted in terms of the depleting effect of deep convection along trajectories (Gao et al., 2013; He et al., 2015). Significant intra-seasonal declines in $\delta^{18}O$ are evident during specific intervals: early July (as indicated by number 1 in Fig.4- 3a), early August (number 2 in Fig.4- 3a), early to mid-September (number 3 in Fig.4- 3a), and the end of September (number 4 in Fig.4- 3a). We observed a gradual increase in vapor $\delta^{18}O$ following the recession of the monsoon, and followed by a significant decline in isotopic values approximately half a month after the monsoon's end, as illustrated by point number 5 in Figure 4-3a.

During the peak monsoon months of July and August, the d-excess was notably higher compared to other periods (Fig.4- 3b). This period of maximum d-excess coincides with the minimum $\delta^{18}O$ values (Fig.4- 3).

To further analyze the seasonal variations in water vapor isotopes, which displayed four prominent fluctuations, we further categorized our observations into four distinct periods:

1) Early Monsoon_June (from 25th June to 1st July);
2) Peak Monsoon_Jul-Aug (from 2nd July to 11stAugust);
3) End of Monsoon_Sep (from 12th August to 06th October);
4) Post-monsoon_Oct (from 07th October to 17th October).

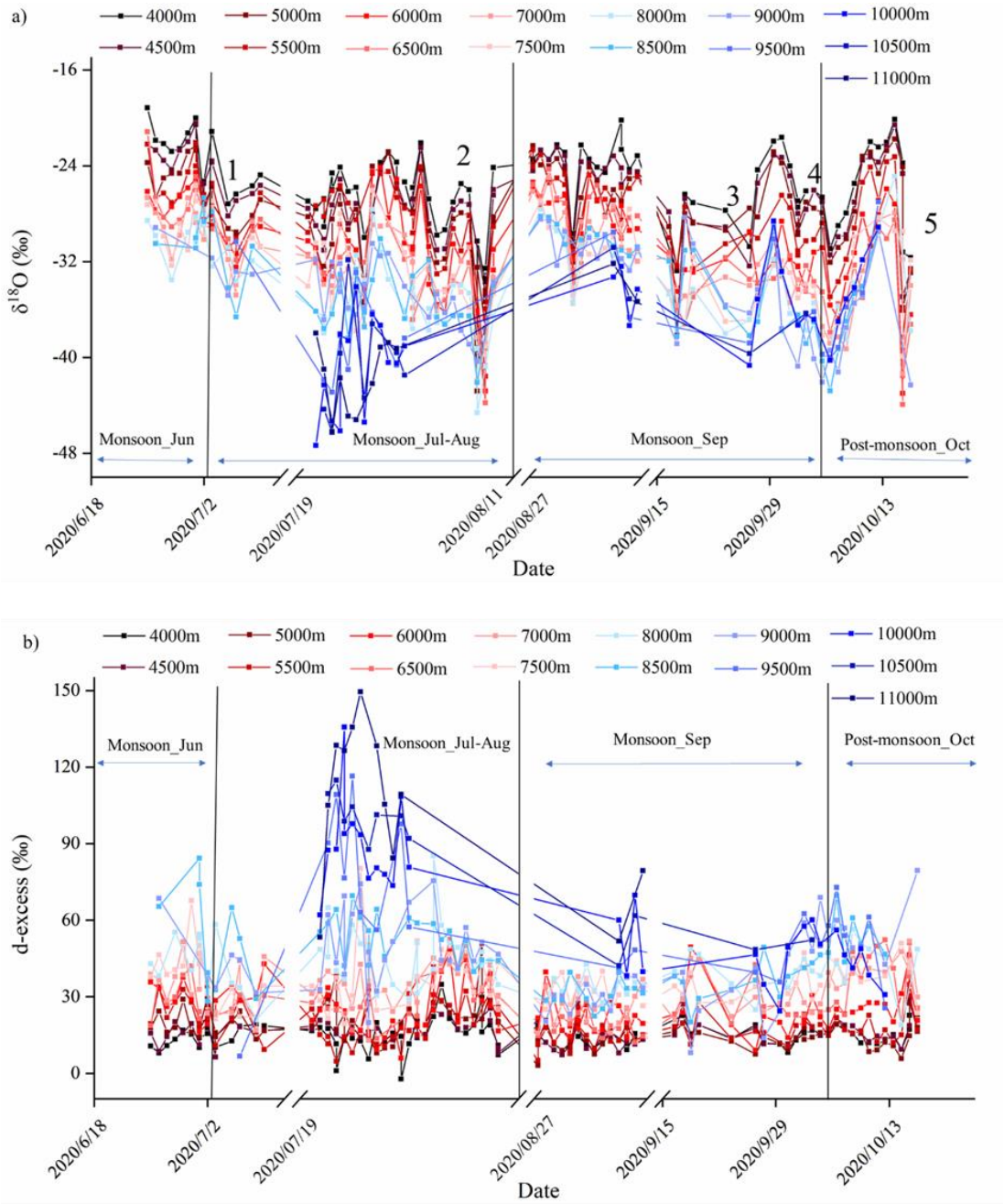

Figure 4-3 The seasonal and intra-seasonal variations of the vertical profiles of vapor $\delta^{18}O$ (a) and d-excess (b).

In line with the progressive condensation of water vapor and precipitation, $\delta^{18}O$ shows a decrease with increasing altitude (Fig.4-4a). However, a re-increase in $\delta^{18}O$ with altitude is observed above 8km during early Monsoon_June and above approximately 9km for the other

periods. These altitudes correspond to cloud layers (Fig.4-4b). As altitude increases, resulting in decreased vapor humidity, the vapor δ^2H decreases (Fig.4-4c). Yet, beyond a specific vapor humidity threshold, the vapor δ^2H begins to increase again, further substantiating evidence for the enrichment of vapor isotopes in the upper troposphere (Fig.4-4c). Isotopic enrichment in the upper troposphere has previously been interpreted in terms of convective detrainment and sublimation of ice crystals (Kuang et al., 2003; Moyer et al., 1996; Vries et al., 2021). At altitudes below 9km, $\delta^{18}O$ exhibits similar patterns during both the peak Monsoon_Jul-Aug, end of Monsoon_Sep and Post-monsoon_Oct, with greater discrepancies observed at higher altitudes (Fig.4-4a).

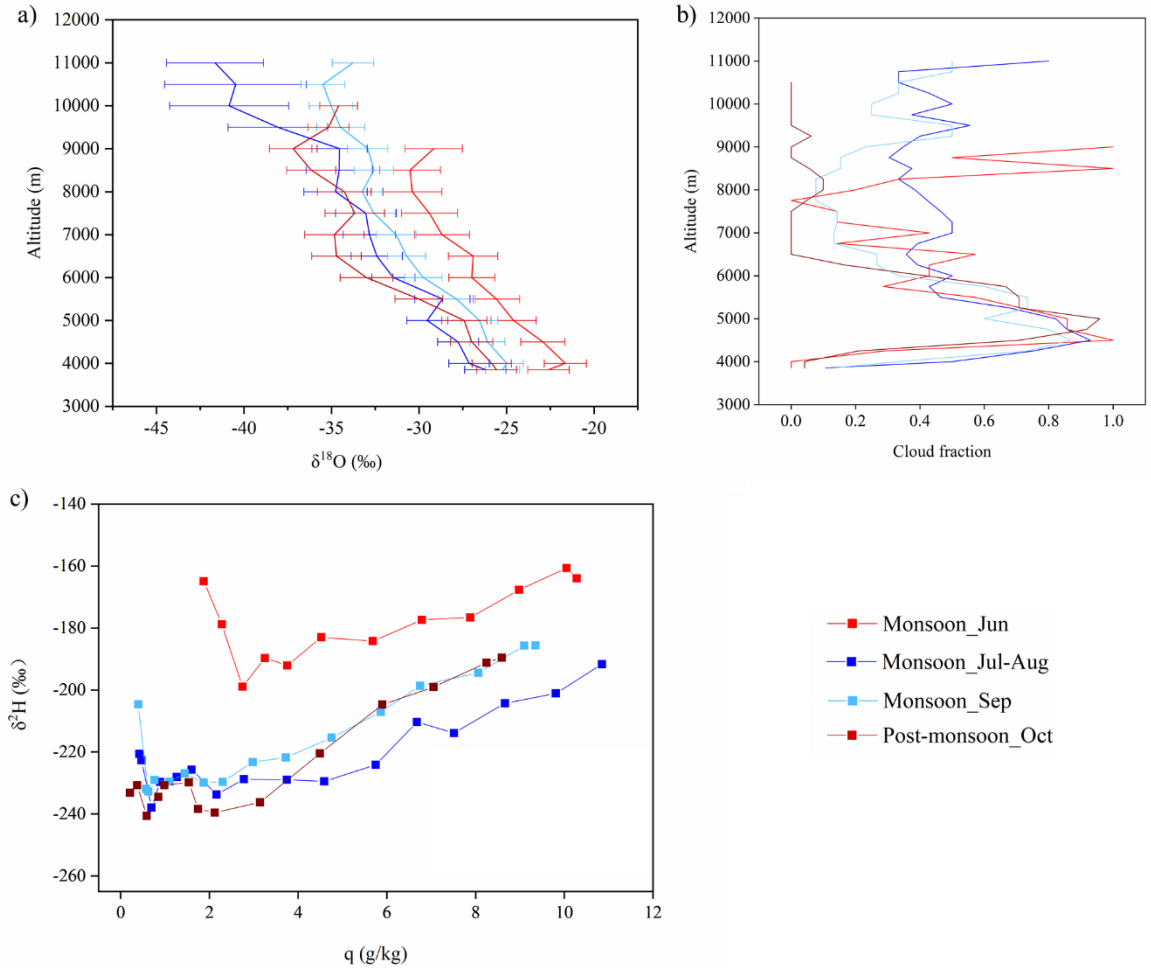

Figure 4-4 The average vapor $\delta^{18}O$ in altitude in different periods (a), cloud fraction (b), and q-δ^2H diagram (c).

The d-excess also demonstrates marked differences between these three periods: exceptionally high values are observed during the peak Monsoon_Jul-Aug, especially at higher altitudes, whereas the Monsoon_Sep and entire Post-monsoon_Oct period registers lower vapor d-excess values (Fig.4-5).

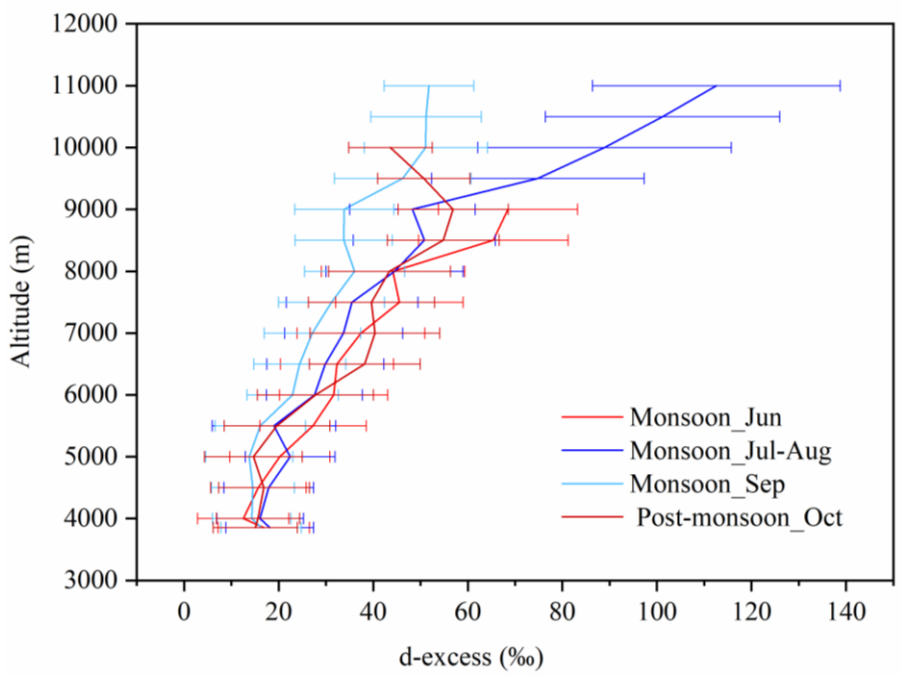

Figure 4-5 The average vapor d-excess in altitude in different periods.

Determining the dominant drivers of surface $\delta^{18}O$ variation is pivotal as it underpins our comprehension of vertical distribution and coherence. Isotopic enrichment in the upper troposphere challenges conventional wisdom on fractionation processes with altitude. The pronounced differences in d-excess values between the peak Monsoon_Jul-Aug and the other periods, especially in the upper troposphere, warrant attention. Given these observations, in the discussion section we will address three critical scientific questions:

1) What explains $\delta^{18}O$ variations at the surface?
2) What accounts for the vapor enrichment in the upper troposphere?
3) What drives the observed higher d-excess in the upper troposphere during the monsoon?

4.5 **Discussion**

4.5.1 The seasonal and intra-seasonal variations of $\delta^{18}O$

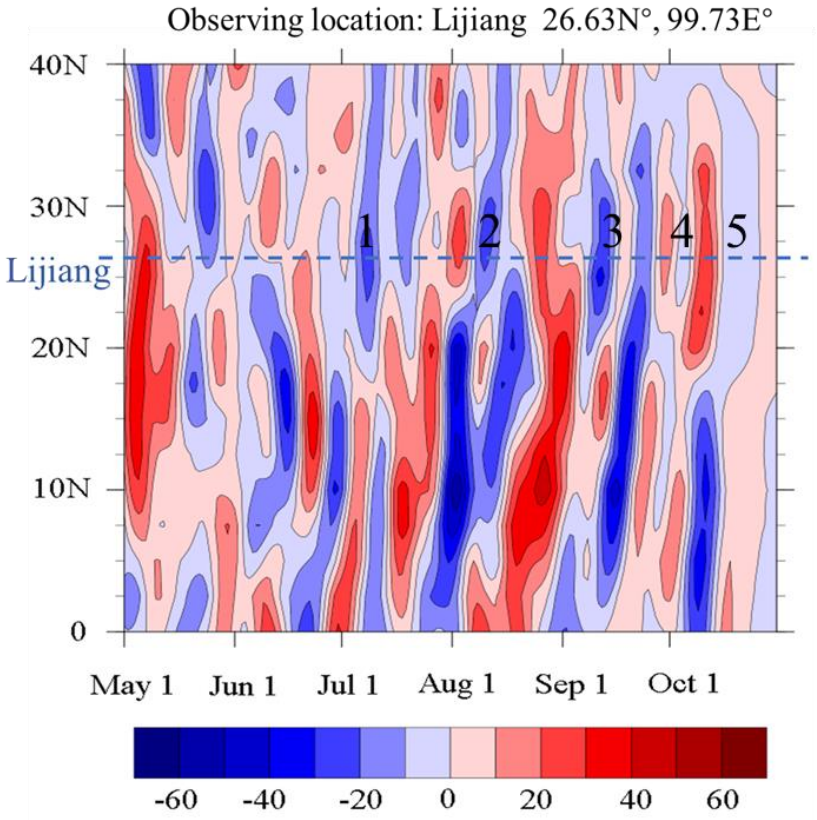

Figure 4-6 Time-Latitude Hovmoller plot of 10-80 day filtered OLR anomaly (W/m²) averaged over 90°E-110°E from May to October 2020.

In this section, we test the hypothesis that the $\delta^{18}O$ intraseasonal variability that we observe is related to the BSISO. Figure 4-6 shows the Time-Latitude Hovmoller plot of the 10-80 day bandpass filtered Outgoing Longwave Radiation (OLR) anomaly. This plot reveals notable intra-seasonal fluctuations throughout the summer monsoon. Between June and October 2020, the plot displays distinct events of low-value OLR, suggesting increased convective activity, propagating from the south to the north. Our observational site in Lijiang recorded five BSISO events: in early July, early August and mid-September, and to a lesser extent at the end of September and mid-October (Fig.4-6). These events correspond with the five pronounced declines in vapor $\delta^{18}O$ we identified (Fig.4- 3a) and with the precipitation $\delta^{18}O$ observed during the same period (Fig.4- S1). These depletion can generally be ascribed to the "amount effect." This effect posits that intensified convection and heavier rainfall correlate with more depleted $\delta^{18}O$ values (Dansgaard, 1964). Upstream convection leads to the depletion of isotopic water vapor in the lower troposphere (Kurita, 2013; Risi et al., 2008a).

The magnitude of the five drops in surface water vapor $\delta^{18}O$ (Fig 3a) corresponding to

these five convective events (Fig 6) are 10‰, 7‰, 14‰, 8‰ and 12‰, which might be related to the intensity of convective events. The third isotopic decrease observed in mid-September stands out most prominently, correlating with a propagation of low OLR anomalies from Soth to North. The observed fifth decrease around half a month post-monsoon is also prominent (highlighted as number 5 in Fig.4- 3a). The vapor depletion during post-monsoon aligns with observations stretching from northeast India (Breitenbach et al., 2010), the periphery of the Bay of Bengal (BOB) to the southeast and south Tibetan Plateau (Cai and Tian, 2020). The milder transmissions registered towards mid-October may not fully explain such pronounced $\delta^{18}O$ declines (Fig.4-6). This intensification of the decline could be attributed to differing moisture transport pathways, as posited by (Cai and Tian, 2020). The same shift in water vapor sources as their study can be found in Figure 4-S2 a, d, g and j.

Owing to the substantial influence of the BSISO and vapor sources on water vapor isotopic compositions, intra-seasonal oscillations might be mistaken for interannual variability. Consequently, meticulous attention is required when dating ice cores and interpreting paleoclimate data derived from isotopic signals (Shao et al., 2017; Wang et al., 2023).

4.5.2 The vapor enrichment in the upper troposphere

4.5.2.1 Contribution of ice sublimation

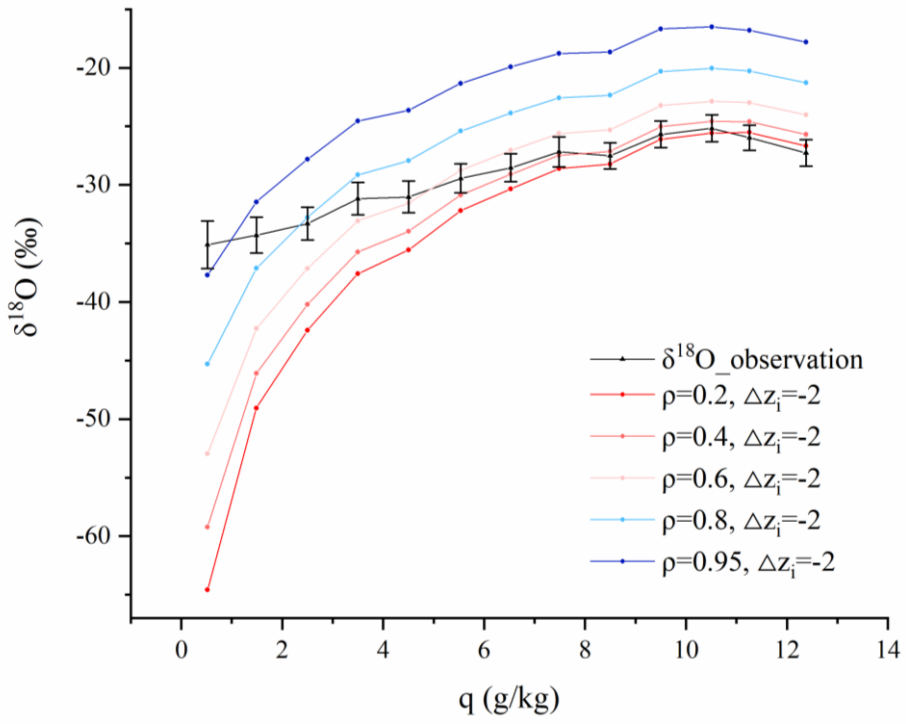

Figure 4-7 Simulation results of Rayleigh distillation model including ice sublimation with varying ice sublimation contribution ratios compared to observations.

The goal of this section is to identify the mechanisms for the $\delta^{18}O$ enrichment in the upper troposphere, and to explore to what extent it can provide information on the contribution of ice sublimation to upper tropospheric humidity. Several observational and modeling studies, including those by (Kuang et al., 2003; Moyer et al., 1996; Smith et al., 2006; Webster and Heymsfield, 2003) (Nassar et al 2007, Hanisco et al 2007) have previously identified the enrichment in vapor isotopes in the upper troposphere and linked it to the sublimation of ice crystals ejected from convective clouds.

To check this hypothesis, we use the cloud fraction profiles obtained from a camera onboard our UAV. The $\delta^{18}O$ enrichment layers align with maximum cloud fraction layers, pointing to regions of convective detrainment (Fig.4-4b). To further test this hypothesis, we've devised a Rayleigh distillation model, detailed in section 4.3.3, that incorporates ice sublimation.

We tested the sensitivity to parameters such as the relative height of condensate origin ($\triangle z_i$) and ρ, which signifies the proportion of observed water vapor derived from ice sublimation. Notably, the origin height, z_i, exerts a negligible impact on our results. Therefore, Fig.4- 7 predominantly displays outcomes when z_i = -2 km. Our observations are consistent with a fraction ρ of water vapor originating from ice sublimation of 20% at lower altitudes, where the specific humidity (q) is relatively low. This ratio increases with altitude. In the upper troposphere, our observations are consistent with a fraction rho of water vapor originating from ice sublimation of 80 to 95%. This is much higher than suggested by previous studies showing that microphysical processes have a minor role on the humidity distribution in the upper troposphere (Horváth and Soden, 2008; Salathé and Hartmann, 1997; Sherwood and Dessler, 2000). Such a substantial contribution compels us to consider the potential role of additional processes that might be enriching the water vapor content in the upper troposphere.

4.5.2.2 Contribution of continental recycling and origins

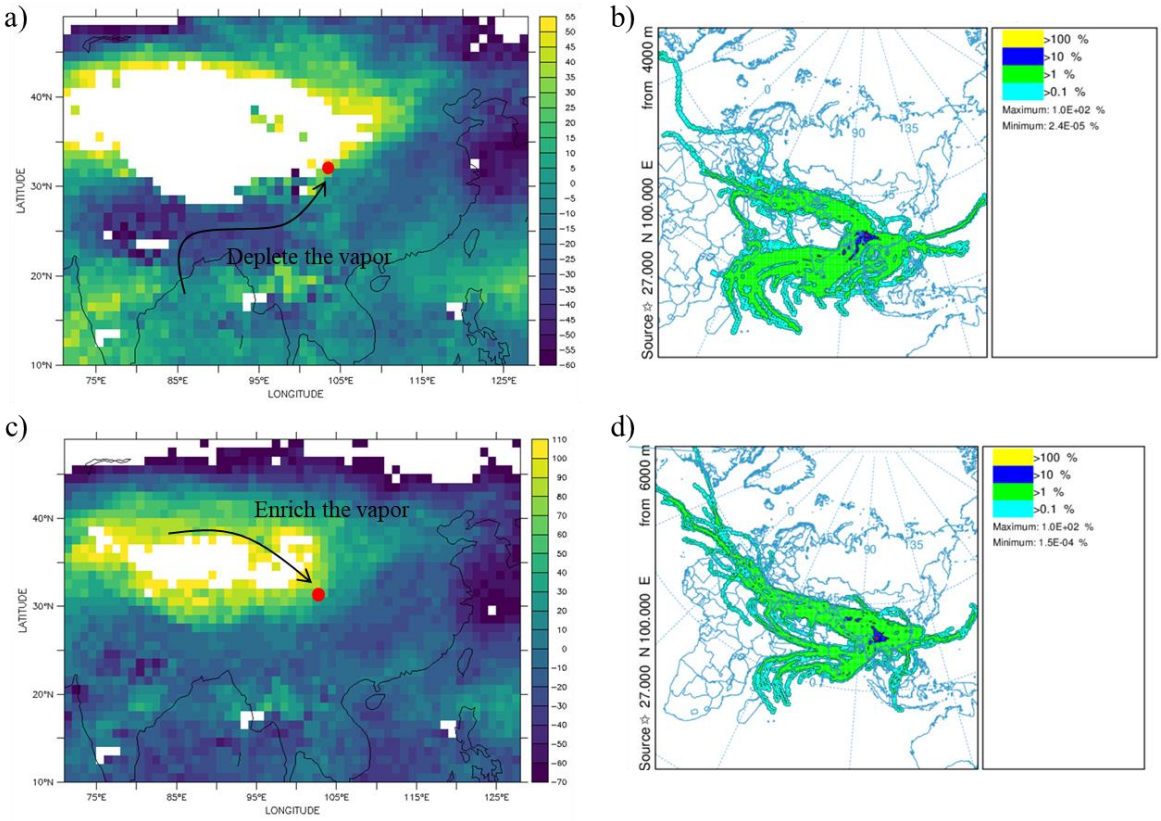

Figure 4-8 IASI satellite δ^2H anomaly at 4220m (a) and 6380m (c); 10-day trajectory frequency distribution at 4220m (b) and 6380m (d). Red dots denote the Lijiang observation site. Results pertain to August; see Fig.4-S2 for additional observation periods.

The Tibetan Plateau, due to its large area and significant altitude, has a considerable influence on regional climate dynamics. Observations from the IASI satellite indicate that the δ^2H values over the Tibetan Plateau are consistently higher than those in surrounding regions at equivalent altitudes, as depicted in Fig.4-8a and c. This pattern is also evident in the LMDZ and ECHAM GCMs, as shown in Fig.4-S1. This isotopic signature could be attributed, in part, to the pronounced influence of continental recycling over the plateau (Yao et al., 2013). Specifically, the high elevation of the plateau means that the same altitude is closer to the surface here than in surrounding areas, and thus more subject to continental recycling.

At lower altitudes, the water vapor over our observation site primarily originates from the southwestern monsoon (Fig.4-8b; Fig.4-S2), known to transport moisture with comparatively lower δ^2H values (Tian et al., 2007), and we also can find it in Fig.4-8a, c and Fig.4-S1. Consequently, this leads to a depletion of δ^2H values in the vapor at our observation site.

However, as the altitude increases, there is a shift in the source of water vapor. At higher altitudes, our observation site experiences greater influence from the central of Tibetan Plateau (Fig.4-8d; Fig.4-S2), which carry moisture with higher δ^2H values (Fig.4-8 a and c ; Fig.4-S1)

related to strong continental recycling, consequently enriching the water vapor (Salati et al., 1979).

Therefore, our results indicate that estimating ice sublimation in the upper troposphere is challenging due to other factors, such as continental recycling, affecting vapor isotopes. Nerveless, our observations could be used in the future to benchmark GCMs.

4.5.3 Higher d-excess in the upper troposphere during monsoon

4.5.3.1 The d-excess variations during convective processes in cloud resolving model

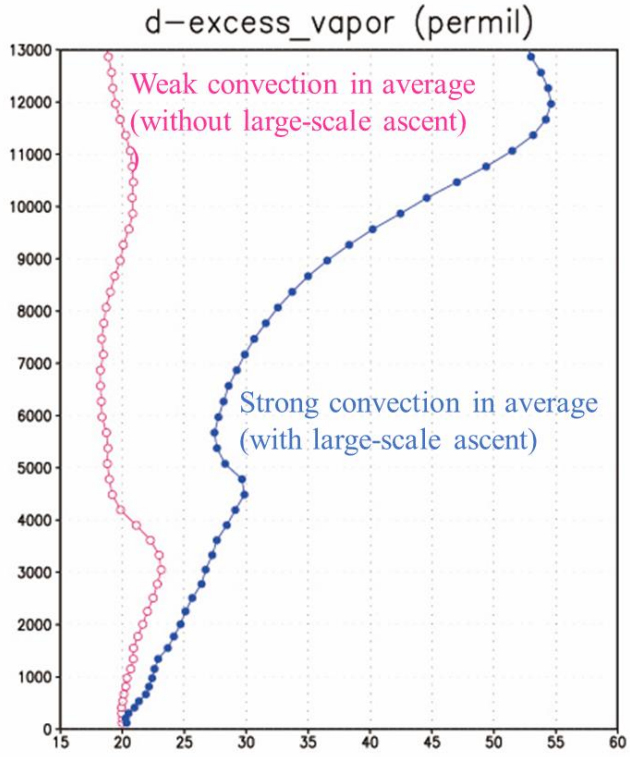

Figure 4-9 Simulations using the cloud-resolving model SAM, at 750m resolution, in radiative-convective equilibrium over an ocean of prescribed sea surface temperature.

According to the Rayleigh distillation, there exists an inverse relationship between humidity levels and vapor d-excess values; lower humidity often corresponds to higher vapor d-excess (Galewsky et al., 2016). This relationship is rooted in the selective removal of heavier isotopes during condensation, leading to the decrease in $\delta^{18}O$ and $\delta^{2}H$ and a mathematical increase in d-excess in the remaining vapor (in the extreme case where $\delta^{18}O$ and $\delta^{2}H$ reach -1000 ‰, d-excess reaches 7000 ‰). Despite monsoons in August experiencing higher humidity levels compared to September and the post-monsoon period, the d-excess values during the monsoons in August are surprisingly elevated. Using idealized cloud-resolving simulations in

radiative-convective equilibrium with SAM, we observe higher d-excess values in scenarios with stronger convection. Such simulations consistently show increased d-excess values associated with more intense convective events (Fig.4-9).

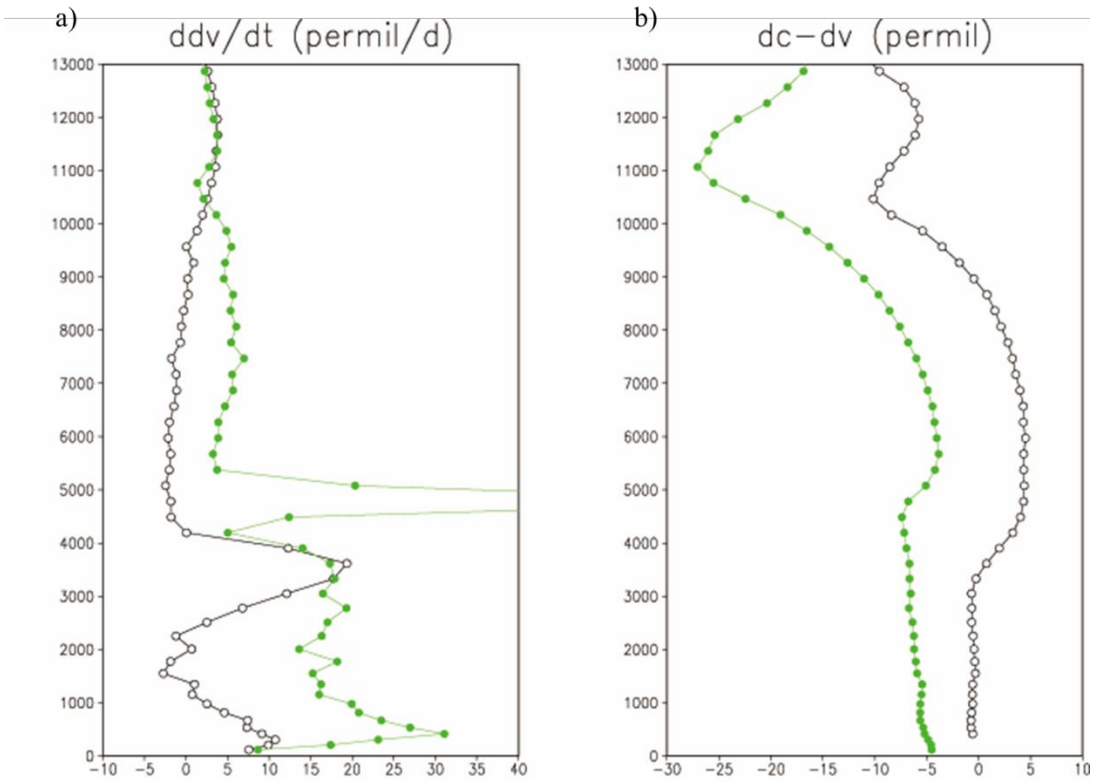

Figure 4-10 Tendency of vapor d-excess (d_v) during weak (black line in a) and strong convection (green line in a); Difference between d-excess of condensation (d_c) and dv during weak (black line in b) and strong (green line in b) convection.

We then examined the factors influencing vapor d-excess (d_v) in our simulations. We plotted the tendencies of d_v associated with condensation as simulated in the CRM. In scenarios with strong convection, this tendency is notably greater than 0 (green line in Fig.4-10a). This suggests that condensation contributes to increase the d_v. It can be attributed to the d-excess of condensation (d_c) being lower than d_v in simulations characterized by stronger convection (negative values of green line in Fig.4-10b). Contrarily, in simulations with weaker convection, the opposite trend is simulated (black line in Fig.4-10).

4.5.3.2 Decomposition of different contributions

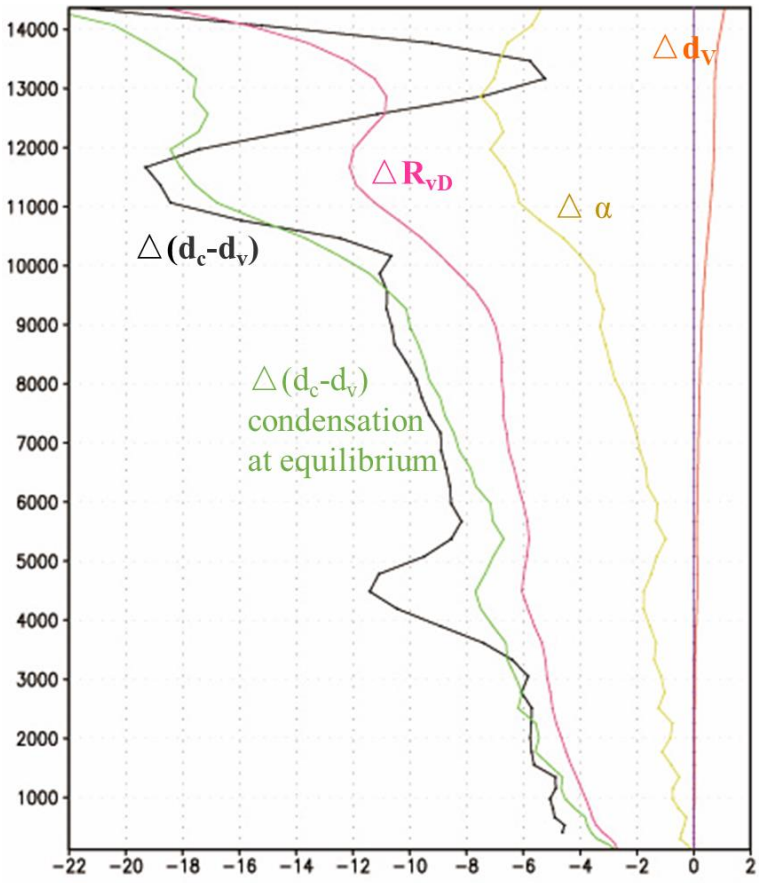

Figure 4-11 The d-excess comparison in condensation (d_c) vs. vapor (d_v) for strong and weak convection: differences (△) and key Contributors. Black lines depict $\triangle(d_c\text{-}d_v)$, green indicates its differences at equilibrium ($\triangle(d_c\text{-}d_v)_{eq}$); while four contributing factors to $\triangle(d_c\text{-}d_v)_{eq}$ are color-coded: $\triangle R_{vD}$ (^2H isotopic ratio in vapor) in pink, $\triangle\alpha$ (equilibrium fractionation factor) in yellow, and $\triangle d_v$ (difference in d_v) in orange.

The difference between d_c and d_v, denoted as d_c-d_v, exhibits more pronounced negative values in simulations characterized by stronger convection (green line in Fig.4-10b). This implies that d_v is higher. The black line in Fig.4-11 highlights the d_c-d_v difference between the two simulations. When plotted under the assumption of isotopic equilibrium, the d_c-d_v difference produces a curve (represented by the green line in Fig.4-11) that closely aligns with our previous simulation outcomes. To gain a deeper understanding why this curve has negative values, we dissected the d_c-d_v difference into several contributions:

$d_v=(R_{vD}\text{-}1)*1000\text{-}8000*(R_{vO}\text{-}1)$

where d_v represents the d-excess of vapor, R_{vD} and R_{vO} denote the ^2H and ^{18}O isotopic ratio of vapor, respectively, normalized by the SMOW ratio.

At equilibrium, $R_{ceqD}=\alpha_{eqD}* R_{vD}$ and $R_{ceqO}=\alpha_{eqO}* R_{vO,}$

Here, α_{eqO} and α_{eqD} represent the equilibrium fractionation factor for oxygen isotopes and

hydrogen isotopes, respectively.

So the difference between d_c and d_v at equilibrium ($(dc\text{-}d_v)_{eq}$) writes:

$(dc\text{-}d_v)_{eq}=\varepsilon_{O*}(d_v - 7000) + R_{Vd*}1000*(\varepsilon_D - \varepsilon_O)$

Where ε_O is defined as α_{eqO} -1, while ε_D is α_{eqD} -1.

The symbol △ is used to denote the differences between the two simulations of strong convection and weak convection. The difference in the equilibrium values of dc and dv for these simulations is expressed as:

$$\begin{aligned}\triangle (dc\text{-}d_v)_{eq} = {} & 1000*(\varepsilon_D - \varepsilon_O)* \triangle R_{vD} \\ & + (d_v\text{-}7000) * \triangle \varepsilon_O \\ & + R_{vD}*1000* \triangle(\varepsilon_D - \varepsilon_O) \\ & + \varepsilon_O *\triangle d_v\end{aligned}$$

Fig 9d plots the difference △ $(dc\text{-}d_v)_{eq}$ (green) and its four contributions (colors). The most pronounced contribution to this difference is the pink line corresponding to the effect of R_{vD} variations between the two simulation simulations. Consequently, the leading cause for the more negative $d_c - d_v$ (corresponding to a higher d_v) is the larger depletion of the vapor. This finding aligns with the mathematical effects noted in earlier simulations (Bony et al., 2008). Our observations, combined with the cloud-resolving model, corroborate these previous simulations.

Our results shed light on the temporal fluctuations of d-excess observed in precipitation and ice cores from the Tibetan Plateau. The d-excess, like $\delta^{18}O$ and $\delta^{2}H$ in precipitation and ice cores from the Tibetan Plateau, decrease during the summer monsoon (Thompson, 2000). This is the opposite of what we observe. It is possible that post-condensational processes distorts the d-excess in precipitation relative to that in the vapor.

The d-excess is sensitive to variations in relative humidity and temperature during the evaporation of water, especially from the ocean's surface (Merlivat and Jouzel, 1979; Pfahl and Sodemann, 2014). High d-excess values found in precipitation, ice cores and other paleoclimatic proxy archives are often interpreted as indications of drier and warmer source regions or a drier year (Jouzel et al., 1982; Jouzel et al., 2007; Masson-Delmotte et al., 2008; Shao et al., 2017; Uemura et al., 2012). However, in very high elevated regions, our recent analyses suggests that d-excess variations could also be due to the depletion of the water vapor. As a result, the influence of convective precipitation processes on d-excess could lead to misconceptions when interpreting ice core d-excess as indicators of water vapor source regions.

4.6 **Conclusion**

Figure 4-12 Schematic summarizing the different processes controlling the vertical profiles of vapor isotopes.

This study, utilizing a bespoke UAV system, has shed light on the vertical distribution of atmospheric vapor isotopes, ranging from the surface at 3856m to an impressive 11000m a.s.l., encompassing the entire monsoon season in the southeastern Tibetan Plateau. Figure 4-12 provides a schematic representation of the processes influencing our observed isotopic profiles,

including large-scale processes, especially deep convection along trajectories, and local convective processes, notably convective detrainment, ice crystal sublimation, and continental recycling.

The water vapor at lower elevations predominantly stems from the southwest monsoon transport (the pink arrow on the left). Its isotopes manifest intra-seasonal fluctuations, primarily influenced by the BSISO's large-scale convection as it traverses from south to north (represented by the light pink cloud process). This work accentuates the pivotal role of deep convection in producing a more depleted vapor. The vertical coherence between seasonal and intra-seasonal variations underscores the vertical convective mixing and the local convective detrainment, sourcing vapor from the lower troposphere (dark blue arrows and blue cloud process). Interestingly, the depletion of vapor results in a higher d-excess, which is more pronounced in the upper troposphere. This phenomenon arises predominantly from mathematical effects, offering a fresh perspective on interpreting d-excess records at high altitudes. The observed vapor $\delta^{18}O$ and $\delta^{2}H$ and their d-excess up to 8-10km align with prevailing theories of water vapor condensation and precipitation. However, beyond this altitude, we detect an increase in both vapor $\delta^{18}O$ and $\delta^{2}H$, a phenomenon potentially attributable to the sublimation of ice crystals detrained from convective formations (light blue arrows and cloud process). Additionally, given the vapor's origin at high altitudes predominantly from the Tibetan Plateau's interior (pink arrow on the right), there's a notable influence from continental recycling processes (green arrows).

This study emphasizes the potential of UAVs in atmospheric and climate research. It sets the stage for addressing insufficient observations of water vapor isotope profiles. This groundbreaking exploration underscores the significance of discerning vertical isotopic signal variations for accurate paleoclimatic readings. We've offered a new dataset that advances our comprehension of water vapor isotopic vertical variations, convective impacts, upper tropospheric humidity shifts, and high-altitude $\delta^{18}O$ and d-excess paleoclimatic interpretations.

4.7 **Perspectives**

In this study, the unprecedented vertical resolution and altitude range achieved have enabled us to gain novel insights into the atmospheric vapor isotopic dynamics, during the monsoon period. In the future, we propose to:

1) Generalize measurements by UAV to other regions: The flexibility, cost-effectiveness, and ability of UAVs to access challenging altitudinal points underscore their transformative potential in atmospheric research. The methodologies and insights might well be applicable to other regions. Different geographic and climatic zones could exhibit distinct isotopic behaviors, and deploying UAVs in these varied settings can elucidate region-specific nuances.
2) Apply our observations to estimate moistening by sublimation of detrained ice: A salient potential application of our findings is in estimating the moistening effects from sublimation of detrained ice. Yet, numerous confounding factors can convolute the estimation process, for example, the influence of continental recycling suggested in our study, making it arduous to secure a precise quantitative measure. This complexity would necessitate interpreting our UAV-derived data using cloud-resolving

simulations in realistic settings, such as those proposed by (Vries et al., 2021).

3) Use our observations to evaluate General Circulation Models (GCMs): The isotopic measurements can serve as a benchmark to evaluate the realism of GCMs. By comparing model predictions with the observed UAV measurements, potential discrepancies can be highlighted, which can inform refinements and calibrations of convective parameterizations in GCMs.

4.8 **Supplements**

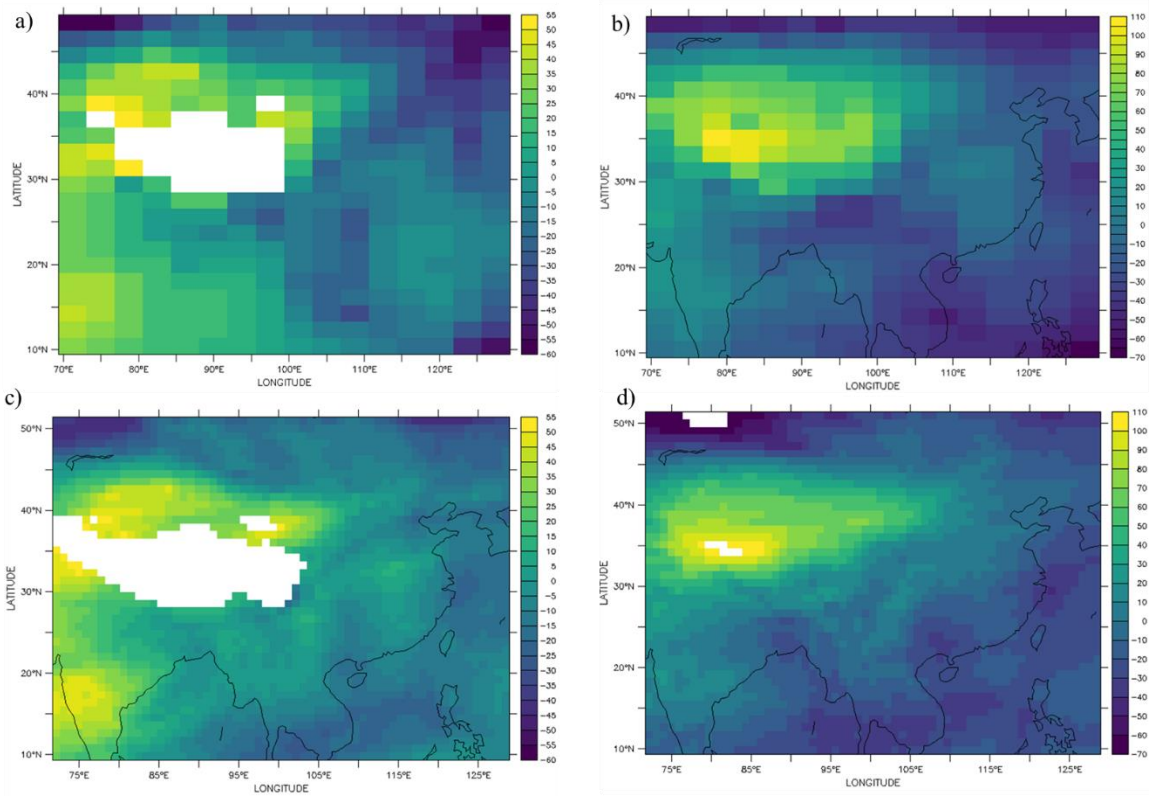

Fig.4-S1. δ^2H anomaly from GCMs: (a) ~4220m from LMDZ, (b) ~6380m from LMDZ, (c) ~4220m from ECHAM, and (d) ~6380m from ECHAM.

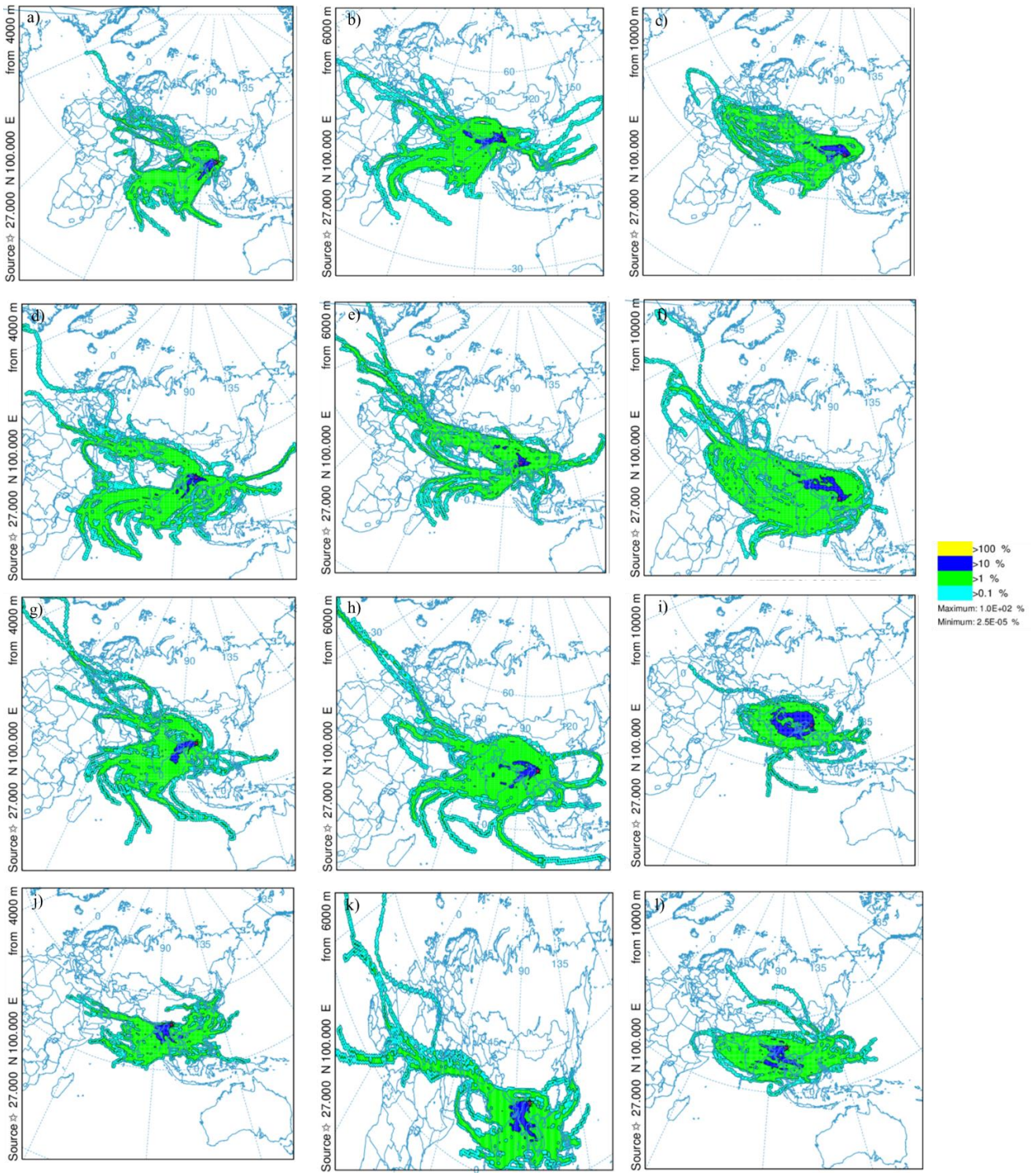

Fig.4-S2 10-day trajectory frequency distribution for the months July (a-c), August (d-f), September (g-i), and October (j-l) at altitudes of 4000m, 6000m, and 10000m.

From panels a, d, g, and j, it is evident that surface vapor predominantly originates from the Bay of Bengal in July, August, and September. However, in October, the vapor is influenced by currents from the India Trough. By comparing the sources of water vapor at different altitudes in July, August, and September, we observe that at lower altitudes, water vapor primarily stems from the Bay of Bengal in the southwest direction. As the altitude increases, the water vapor source shifts more towards the Tibetan Plateau in the northwest.

5 Conclusions and Future Directions

The thesis provides unprecedented datasets on the spatial, seasonal, and vertical profile variations of water vapor isotopes, along with a deeper and systematic understanding of the controlling processes and mechanisms, ranging from large-scale water vapor transport to local processes such as continental recycling and local convection, extending to cloud microphysical processes. This research offers more basis for the application of water isotope ratio in modern hydro-atmospheric processes and paleoclimate, particularly within the mid- to low-latitude monsoon regions.

We used a newly designed vehicle-based water isotope monitoring system to make the first in situ observations of near-surface water vapor isotope spatial distributions and seasonal variations over a substantial area in China (more than 10,000 kilometers), covering both the pre-monsoon and monsoon periods. By combining these observations with data simulated by the IASI satellite and the Iso-GSM atmospheric circulation model, we determined that the observed spatial variations during the two periods are indicative of seasonally averaged spatial variations. However, the monsoon period exhibited more pronounced synoptic-scale variations, influencing the spatial distribution of water vapor isotopes. Despite this, snapshots from both periods still provide a representative depiction of seasonal climatological differences. We systematically analyze the controlling factors for this spatial distribution and seasonal variation. In the pre-monsoon period, the spatial variation of $\delta^{18}O$ is mainly controlled by Rayleigh distillation, which is consistent with the temperature effect. In the monsoon period, the spatial variation of $\delta^{18}O$ is significantly affected by different water vapor sources, convection on the water vapor transport path and continental recycling. The spatial variation of d-excess during both pre-monsoon and monsoon periods mainly reflect the relative humidity of the water vapor sources and the replenishment of water vapor from the continental evaporation. Our results highlight the influence of convection, weather processes and continental recycling on water vapor isotopes in different regions and from different water vapor sources, obtaining information on the intersection and interaction of different air streams.

To better understand the influence of local convective cloud microphysical processes on water isotope ratio, we conducted measurements of vertical profiles of water vapor isotopes during convection. Utilizing an specially designed unmanned aerial vehicle (UAV) system allowed us flexibility and cost-effectiveness for long-term observations throughout the monsoon period. To observe deep convective processes, we aimed to reach higher altitudes, selecting light air bags as portable sampling devices. This allowed us to observe vertical profiles over the entire monsoon period from the end of June to mid-October 2020, and up to a maximum altitude of 11 km. However, we found that commercially available airbags generally suffer from permeability problems, leading to potential contamination from the environment due to diffusion during storage. To address this issue, we developed a diffusion model based on a mathematical approach, the parameters of which were obtained through laboratory experiments, to provide a practical digital solution to the air bag permeability problem. Using this model, we were able to correct the isotopic values of stored airbag samples to their initial values based on the storage time of the airbags, the water vapor concentration and the isotopic values in the airbags as well as in the environment, effectively eliminating the influence of

ambient air. Through rigorous validation of observational experiments under different conditions and comparison with satellite data, we demonstrate the validity and robustness of the model.

After resolving the permeability issue of the air bags, we analyze the observed vertical profiles of water vapor isotopes during convective processes in the East Asian monsoon region. Near-surface water vapor is the main source of water vapor in the vertical profiles, and our observations show a vertical coherence. Therefore, understanding the controlling factors of near-surface water vapor isotopes is fundamental to understanding the variations in the vertical profiles. Our analysis of water vapor sources and processes on the path through backward trajectories reveals that at low elevations, water vapor mainly originates from southwest monsoon flows, and its isotopes show intra-seasonal fluctuations consistent with the south-to-north traversal of the BSISO, suggesting a significant influence of upstream large-scale convection. For the vertical profiles of $\delta^{18}O$ and $\delta^{2}H$, we find that the 8-10 km altitude region shows a trend consistent with the Rayleigh distillation, where $\delta^{18}O$ and $\delta^{2}H$ decrease as water vapor condenses decrease. However, above this altitude, the values of $\delta^{18}O$ and $\delta^{2}H$ increase again. We constructed a Rayleigh distillation model incorporating ice sublimation to simulate water vapor isotope variations at different ice sublimation ratios, and found that the ice sublimation contribution is small at low altitudes, but increases with increasing altitude. However, in the upper troposphere the ice sublimation ratio needs to reach about 95% to match our observations, so we think there may be contributions from other processes. We also found that with increasing altitude, more water vapor comes from the northwestern continent of the Tibetan Plateau, which has higher water vapor isotope values than other regions at the same altitude. This is because at the same altitude, the Tibetan Plateau is closer to the surface and therefore has higher temperatures and humidity, and water vapor isotopes are higher due to the greater influence of the continental recycling. Because our site is drier at the same elevation, even the small contribution of water vapor from this source to our site has a significant effect on the water vapor isotopes. This provides new insights into the source of the upper tropospheric humidity contribution. We observed significant high values of water vapor d-excess during the peak monsoon, especially in the upper troposphere. We also find higher water vapor d-excess under stronger convection in cloud-resolving simulations, which is due to Rayleigh distillation, where strong convection reduces water vapor $\delta^{18}O$ and $\delta^{2}H$, and the mathematical effect leads to higher calculated d-excess. And the cumulative effect leads to significantly higher d-excesses with increasing altitude. While previous studies have often interpreted the high values of d-excess found in high-elevation ice cores as a result of drier and warmer sources of water vapor or drier years, however, in very high elevated regions, our recent analyses suggests that d-excess variations could also be due to the depletion of the water vapor. Our results provide new perspectives for interpreting the d-excess record at high elevations, and provide additional information and a framework for benchmarking cloud resolution models and GCMs.

Looking ahead, we plan to:

Use the measured data for comparative analysis with more model datasets, aiming to assess the simulation accuracy of 3D spatial and temporal variations of water vapor isotopes in GCMs and analyze the reasons for the errors.

Conducting continuous in-situ observations in the Tibetan Plateau area: Due to the limited

accessibility of transportation in parts of Tibet, our campaign did not include observations in the Tibetan region. The climate on the plateau is complex and variable, and these changes are difficult to capture well in GCMs. Vehicle-based in-situ observations can provide continuous time series and cover a wide area of data, offering high-quality benchmark for climate models. This is important for understanding the water cycle mechanism of the plateau and predicting future changes in water resources.

Make more observations of vertical profiles of water vapor isotopes up to the upper troposphere by our unmanned aerial vehicle (UAV) system to establish the observation network in different subsurface or atmospheric processes, and to quantitatively study more atmospheric processes and mechanisms.

Use the extend observation network to enhance the parameterization of GCMs and global-scale cloud resolution models.

6 Bibliography

Acharya, S., Yang, X., Yao, T., Shrestha, D., 2020. Stable isotopes of precipitation in Nepal Himalaya highlight the topographic influence on moisture transport. Quaternary International 565, 22-30.

Aemisegger, F., Papritz, L., 2018. A climatology of strong large-scale ocean evaporation events. Part I: Identification, global distribution, and associated climate conditions. Journal of Climate 31, 7287-7312.

Aemisegger, F., Pfahl, S., Sodemann, H., Lehner, I., Seneviratne, S.I., Wernli, H., 2014. Deuterium excess as a proxy for continental moisture recycling and plant transpiration. Atmospheric Chemistry and Physics 14, 4029-4054.

Aemisegger, F., Spiegel, J., Pfahl, S., Sodemann, H., Eugster, W., Wernli, H., 2015. Isotope meteorology of cold front passages: A case study combining observations and modeling. Geophysical Research Letters 42, 5652-5660.

Aggarwal, P.K., Fröhlich, K., Kulkarni, K.M., Gourcy, L.L., 2004. Stable isotope evidence for moisture sources in the asian summer monsoon under present and past climate regimes. Geophysical Research Letters 31, 239-261.

Angert, A., Lee, J.E., Dan, Y., 2010. Seasonal variations in the isotopic composition of near-surface water vapour in the eastern Mediterranean. Tellus 60, 674-684.

Araguás-Araguás, L., Froehlich, K., Rozanski, K., 1998. Stable isotope composition of precipitation over southeast Asia. Journal of Geophysical Research: Atmospheres 103, 28721-28742.

Ayliffe, L., Cerling, T., Robinson, T., West, A., Sponheimer, M., Passey, B., Hammer, J., Roeder, B., Dearing, M., Ehleringer, J., 2004. Turnover of carbon isotopes in tail hair and breath CO 2 of horses fed an isotopically varied diet. Oecologia 139, 11-22.

Bailey, A., Toohey, D., Noone, D., 2013. Characterizing moisture exchange between the Hawaiian convective boundary layer and free troposphere using stable isotopes in water. Journal of Geophysical Research: Atmospheres 118, 8208-8221.

Benetti, M., Steen-Larsen, H.C., Reverdin, G., Sveinbjörnsdóttir, Á.E., Aloisi, G., Berkelhammer, M.B., Bourlès, B., Bourras, D., De Coetlogon, G., Cosgrove, A., 2017. Stable isotopes in the atmospheric marine boundary layer water vapour over the Atlantic Ocean, 2012–2015. Scientific data 4, 1-17.

Berman, E.S., Levin, N.E., Landais, A., Li, S., Owano, T., 2013. Measurement of δ18O, δ17O, and 17O-excess in water by off-axis integrated cavity output spectroscopy and isotope ratio mass spectrometry. Analytical chemistry 85, 10392-10398.

Bhattacharya, S.K., Sarkar, A., Liang, M.C., 2022. Vapor isotope probing of typhoons invading the Taiwan region in 2016. Journal of Geophysical Research: Atmospheres 127, e2022JD036578.

Blossey, P.N., Kuang, Z., Romps, D.M., 2010. Isotopic composition of water in the tropical tropopause layer in cloud-resolving simulations of an idealized tropical circulation. Journal of Geophysical Research: Atmospheres 115.

Bonne, J.-L., Behrens, M., Meyer, H., Kipfstuhl, S., Rabe, B., Schönicke, L., Steen-Larsen, H.C., Werner, M., 2019. Resolving the controls of water vapour isotopes in the Atlantic sector. Nature communications 10, 1632.

Bony, S., Colman, R., Kattsov, V.M., Allan, R.P., Bretherton, C.S., Dufresne, J.-L., Hall, A., Hallegatte, S., Holland, M.M., Ingram, W., 2006. How well do we understand and evaluate climate

change feedback processes? Journal of Climate 19, 3445-3482.

Bony, S., Risi, C., Vimeux, F., 2008. Influence of convective processes on the isotopic composition (δ18O and δD) of precipitation and water vapor in the tropics: 1. Radiative-convective equilibrium and Tropical Ocean–Global Atmosphere–Coupled Ocean-Atmosphere Response Experiment (TOGA-COARE) simulations. Journal of Geophysical Research: Atmospheres 113.

Bowen, G.J., Cai, Z., Fiorella, R.P., Putman, A.L., 2019. Isotopes in the Water Cycle: Regional-to Global-Scale Patterns and Applications. Annual Review of Earth and Planetary Sciences 47.

Bowen, G.J., Revenaugh, J., 2003. Interpolating the isotopic composition of modern meteoric precipitation. Water resources research 39.

Breitenbach, S.F.M., Adkins, J.F., Meyer, H., Marwan, N., Kumar, K.K., Haug, G.H., 2010. Strong influence of water vapor source dynamics on stable isotopes in precipitation observed in Southern Meghalaya, NE India. Earth and Planetary Science Letters 292, 212-220.

Brown, J., Simmonds, I., Noone, D., 2006. Modeling δ18O in tropical precipitation and the surface ocean for present-day climate. Journal of Geophysical Research Atmospheres 111, -.

Brubaker, K.L., Entekhabi, D., Eagleson, P., 1993. Estimation of continental precipitation recycling. Journal of Climate 6, 1077-1089.

Cai, Z., Tian, L., 2020. What Causes the Postmonsoon 18O Depletion Over Bay of Bengal Head and Beyond? Geophysical Research Letters 47.

Cai, Z., Tian, L., Bowen, G.J., 2018. Spatial-seasonal patterns reveal large-scale atmospheric controls on Asian Monsoon precipitation water isotope ratios. Earth and Planetary Science Letters 503, 158-169.

Cerling, T.E., Wittemyer, G., Rasmussen, H.B., Vollrath, F., Cerling, C.E., Robinson, T.J., Douglas-Hamilton, I., 2006. Stable isotopes in elephant hair document migration patterns and diet changes. Proceedings of the National Academy of Sciences 103, 371-373.

Connolley, W.M., King, J.C., 1993. Atmospheric water vapour transport to Antarctica inferred from radiosondes. Quarterly Journal of the Royal Meteorological Society 119, 325-342.

Dansgaard, W., 1953. The abundance of O18 in atmospheric water and water vapour. Tellus 5, 461-469.

Dansgaard, W., 1964. Stable isotopes in precipitation. Tellus 16, 436-468.

Domrös, M., Peng, G., 2012. The climate of China. Springer Science & Business Media.

Duan, S.Q., Wright, J.S., Romps, D.M., 2018. On the utility (or futility) of using stable water isotopes to constrain the bulk properties of tropical convection. Journal of Advances in Modeling Earth Systems 10, 516-529.

Dyroff, C., Sanati, S., Christner, E., Zahn, A., Balzer, M., Bouquet, H., Mcmanus, J.B., González-Ramos, Y., Schneider, M., 2015. Airborne in situ vertical profiling of HDO / H216O in the subtropical troposphere during the MUSICA remote sensing validation campaign. Atmospheric Measurement Techniques 8, 2037-2015.

Ehhalt, D., Rohrer, F., Fried, A., 2005. Vertical profiles of HDO/H2O in the troposphere. Journal of Geophysical Research: Atmospheres 110.

Ehhalt, D.H., 1974. Vertical profiles of HTO, HDO, and H2O in the troposphere. Atmospheric Quality and Modification Division, National Center for ….

Fiorella, R.P., Bares, R., Lin, J.C., Bowen, G.J., 2019. Wintertime decoupling of urban valley and rural ridge hydrological processes revealed through stable water isotopes. Atmospheric environment 213, 337-348.

Fiorella, R.P., Bares, R., Lin, J.C., Ehleringer, J.R., Bowen, G.J., 2018. Detection and variability of combustion-derived vapor in an urban basin. Atmospheric Chemistry and Physics 18, 8529-8547.

Folkins, I., Martin, R.V., 2005. The vertical structure of tropical convection and its impact on the budgets of water vapor and ozone. Journal of the atmospheric sciences 62, 1560-1573.

Frankenberg, C., Wunch, D., Toon, G., Risi, C., Scheepmaker, R., Lee, J.E., Wennberg, P., Worden, J., 2013. Water vapor isotopologue retrievals from high-resolution GOSAT shortwave infrared spectra. Atmospheric Measurement Techniques 6, 263-274.

Frankenberg, C., Yoshimura, K., Warneke, T., Aben, I., Butz, A., Deutscher, N., Griffith, D., Hase, F., Notholt, J., Schneider, M., Schrijver, H., Rockmann, T., 2009. Dynamic Processes Governing Lower-Tropospheric HDO/H2O Ratios as Observed from Space and Ground. Science 325, 1374-1377.

Galewsky, J., Hurley, J.V., 2010. An advection-condensation model for subtropical water vapor isotopic ratios. Journal of Geophysical Research Atmospheres 115.

Galewsky, J., Rella, C., Sharp, Z., Samuels, K., Ward, D., 2011. Surface measurements of upper tropospheric water vapor isotopic composition on the Chajnantor Plateau, Chile. Geophysical Research Letters 38, 198-205.

Galewsky, J., Steen-Larsen, H.C., Field, R.D., Worden, J., Risi, C., Schneider, M., 2016. Stable isotopes in atmospheric water vapor and applications to the hydrologic cycle. Reviews of Geophysics 54.

Gao, J., MassonDelmotte, V., Risi, C., He, Y., Yao, T., 2013. What controls precipitation δ18O in the southern Tibetan Plateau at seasonal and intra-seasonal scales? A case study at Lhasa and Nyalam. Tellus B 65.

Gat, J.R., 1996. Oxygen and hydrogen isotopes in the hydrologic cycle. Annual Review of Earth and Planetary Sciences 24, 225-262.

Gat, J.R., Matsui, E., 1991. Atmospheric water balance in the Amazon Basin: an isotopic evapotranspiration model. Journal of Geophysical Research: Atmospheres 96, 13179-13188.

Gedzelman, S., 2003. Probing hurricanes with stable isotopes of rain and water vapor. Monthly Weather Review 131, 1112-1127.

Gorski, G., Strong, C., Good, S.P., Bares, R., Ehleringer, J.R., Bowen, G.J., 2015. Vapor hydrogen and oxygen isotopes reflect water of combustion in the urban atmosphere. Proceedings of the National Academy of Sciences 112, 3247-3252.

Gralher, B., Herbstritt, B., Weiler, M., Wassenaar, L.I., Stumpp, C., 2016. Correcting laser-based water stable isotope readings biased by carrier gas changes. Environmental science & technology 50, 7074-7081.

Gralher, B., Herbstritt, B., Weiler, M., Wassenaar, L.I., Stumpp, C., 2018. Correcting for biogenic gas matrix effects on laser-based pore water-vapor stable isotope measurements. Vadose Zone Journal 17, 1-10.

Guo, X., Tian, L., Wen, R., Yu, W., Qu, D., 2017. Controls of precipitation δ 18 O on the northwestern Tibetan Plateau: A case study at Ngari station. Atmospheric Research 189, 141-151.

He, H., Smith, R.B., 1999. Stable isotope composition of water vapor in the atmospheric boundary layer above the forests of New England. Journal of Geophysical Research Atmospheres 104, 11657-11673.

He, Y., Risi, C., Gao, J., Masson-Delmotte, V., Yao, T., Lai, C.T., Ding, Y., Worden, J., Frankenberg, C., Chepfer, H., 2015. Impact of atmospheric convection on south Tibet summer precipitation isotopologue composition using a combination of in situ measurements, satellite data, and atmospheric general circulation modeling. Journal of Geophysical Research Atmospheres 120, 3852-3871.

Helliker, B.R., Roden, J.S., Cook, C., Ehleringer, J.R., 2002. A rapid and precise method for sampling and determining the oxygen isotope ratio of atmospheric water vapor. Rapid Communications in Mass Spectrometry 16, 929-932.

Hendry, M., Schmeling, E., Wassenaar, L., Barbour, S., Pratt, D., 2015. Determining the stable isotope composition of pore water from saturated and unsaturated zone core: improvements to the direct vapour equilibration laser spectrometry method. Hydrology and Earth System Sciences 19, 4427-4440.

Herbstritt, B., Gralher, B., Seeger, S., Rinderer, M., Weiler, M., 2023. Discrete in situ vapor sampling for subsequent lab-based water stable isotope analysis. Hydrology and Earth System Sciences 27, 3701-3718.

Horváth, Á., Soden, B.J., 2008. Lagrangian Diagnostics of Tropical Deep Convection and Its Effect upon Upper-Tropospheric Humidity. Journal of Climate 21, 1013.

Hou, J., Huang, Y., Oswald, W.W., Foster, D.R., Shuman, B., 2007. Centennial-scale compound-specific hydrogen isotope record of Pleistocene–Holocene climate transition from southern New England. Geophysical Research Letters 34.

Jacob, H., Sonntag, C., 2010. An 8-year record of the seasonal variation of 2H and 18O in atmospheric water vapour and precipitation at Heidelberg, Germany. Tellus 43, 291-300.

Jiménez-Rodríguez, C.D., Coenders-Gerrits, M., Bogaard, T., Vatiero, E., Savenije, H., 2019. comparison of water vapor sampling techniques for stable isotope analysis. Hydrology and Earth System Sciences Discussions, 1-15.

JingfengLiu, CundeXiao, MinghuDing, JiawenRen, 2014. Variationsinstablehydrogenandoxygenisotopesinatmosphericwatervaporinthemarineboundarylayeracrossawidelatituderange. Journal of Environmental Sciences 26, 2266-2276.

John, V., Soden, B., 2007. Temperature and humidity biases in global climate models and their impact on climate feedbacks. Geophysical Research Letters 34.

Johnson, J.E., Rella, C.W., 2017. Effects of variation in background mixing ratios of N 2, O 2, and Ar on the measurement of δ 18 O–H 2 O and δ 2 H–H 2 O values by cavity ring-down spectroscopy. Atmospheric Measurement Techniques 10, 3073-3091.

Jouzel, J., Alley, R., Cuffey, K., Dansgaard, W., Grootes, P., Hoffmann, G., Johnsen, S., Koster, R., Peel, D., Shuman, C., 1997. Validity of the temperature reconstruction from water isotopes in ice cores. Journal of Geophysical Research: Oceans 102, 26471-26487.

Jouzel, J., Merlivat, L., Lorius, C., 1982. Deuterium excess in an East Antarctic ice core suggests higher relative humidity at the oceanic surface during the last glacial maximum. Nature 299, 688-691.

Jouzel, J., Stiévenard, M., Johnsen, S., Landais, A., Masson-Delmotte, V., Sveinbjornsdottir, A., Vimeux, F., Von Grafenstein, U., White, J.C., 2007. The GRIP deuterium-excess record. Quaternary Science Reviews 26, 1-17.

Khairoutdinov, M.F., Randall, D.A., 2003. Cloud resolving modeling of the ARM summer 1997 IOP: Model formulation, results, uncertainties, and sensitivities. Journal of the Atmospheric Sciences 60, 607-625.

Khaykin, S.M., Moyer, E., Krämer, M., Clouser, B., Bucci, S., Legras, B., Lykov, A., Afchine, A., Cairo, F., Formanyuk, I., 2022. Persistence of moist plumes from overshooting convection in the Asian monsoon anticyclone. Atmospheric Chemistry and Physics 22, 3169-3189.

Kikuchi, K., 2021. The boreal summer intraseasonal oscillation (BSISO): A review. Journal of the Meteorological Society of Japan. Ser. II.

Klein, E.S., Cherry, J., Young, J., Noone, D., Leffler, A., Welker, J., 2015. Arctic cyclone water

vapor isotopes support past sea ice retreat recorded in Greenland ice. Scientific reports 5, 10295.

Kong, Y., Pang, Z., 2016. A positive altitude gradient of isotopes in the precipitation over the Tianshan Mountains: Effects of moisture recycling and sub-cloud evaporation. Journal of Hydrology 542, 222-230.

Kuang, Z., Toon, G.C., Wennberg, P.O., Yung, Y.L., 2003. Measured HDO/H2O ratios across the tropical tropopause. Geophysical Research Letters 30.

Kurita, N., 2011. Origin of Arctic water vapor during the ice-growth season. Geophysical Research Letters 38.

Kurita, N., 2013. Water isotopic variability in response to mesoscale convective system over the tropical ocean. Journal of Geophysical Research-Atmospheres 118, 10376-10390.

Lacour, J.-L., Risi, C., Clarisse, L., Bony, S., Hurtmans, D., Clerbaux, C., Coheur, P.-F., 2012. Mid-tropospheric δD observations from IASI/MetOp at high spatial and temporal resolution. Atmospheric chemistry and physics 12, 10817-10832.

Lacour, J.-L., Risi, C., Worden, J., Clerbaux, C., Coheur, P.-F., 2018. Importance of depth and intensity of convection on the isotopic composition of water vapor as seen from IASI and TES δD observations. Earth and planetary science letters 481, 387-394.

Lawrence, R.J., Gedzelman, D.S., 2013. Low stable isotope ratios of tropical cyclone rains. Geophysical Research Letters 23, 527-530.

Lee, J.-Y., Wang, B., Wheeler, M.C., Fu, X., Waliser, D.E., Kang, I.-S., 2013. Real-time multivariate indices for the boreal summer intraseasonal oscillation over the Asian summer monsoon region. Climate Dynamics 40, 493-509.

Li, Y., Aemisegger, F., Riedl, A., Buchmann, N., Eugster, W., 2021. The role of dew and radiation fog inputs in the local water cycling of a temperate grassland during dry spells in central Europe. Hydrology and Earth System Sciences 25, 2617-2648.

Li, Y., An, W., Pang, H., Wu, S.Y., Tang, Y., Zhang, W., Hou, S., 2020. Variations of Stable Isotopic Composition in Atmospheric Water Vapor and their Controlling Factors—A 6-Year Continuous Sampling Study in Nanjing, Eastern China. Journal of Geophysical Research Atmospheres 125.

Liebmann, B., Smith, C.A., 1996. Description of a complete (interpolated) outgoing longwave radiation dataset. Bulletin of the American Meteorological Society 77, 1275-1277.

Liu, Y., Cobb, K.M., Song, H., Li, Q., Li, C.-Y., Nakatsuka, T., An, Z., Zhou, W., Cai, Q., Li, J., 2017. Recent enhancement of central Pacific El Niño variability relative to last eight centuries. Nature communications 8, 15386.

Masson-Delmotte, V., Hou, S., Ekaykin, A., Jouzel, J., Aristarain, A., Bernardo, R., Bromwich, D., Cattani, O., Delmotte, M., Falourd, S., 2008. A review of Antarctic surface snow isotopic composition: Observations, atmospheric circulation, and isotopic modeling. Journal of climate 21, 3359-3387.

McKinney, C.R., McCrea, J.M., Epstein, S., Allen, H., Urey, H.C., 1950. Improvements in mass spectrometers for the measurement of small differences in isotope abundance ratios. Review of Scientific Instruments 21, 724-730.

Mei'e, R., Renzhang, Y., Haosheng, B., 1985. An outline of China's physical geography.

Merlivat, L., 1978. MOLECULAR DIFFUSIVITIES OF (H2O)-O-1 6 HD16O, AND (H2O)-O-18 IN GASES. Journal of Chemical Physics 69, 2864-2871.

Merlivat, L., Jouzel, J., 1979. Global climatic interpretation of the deuterium-oxygen 18 relationship for precipitation. Journal of Geophysical Research: Oceans 84, 5029-5033.

Michener, R., Lajtha, K., 2008. Stable isotopes in ecology and environmental science. John Wiley

& Sons.

Moyer, E.J., Irion, F.W., Yung, Y.L., Gunson, M.R., 1996. ATMOS stratospheric deuterated water and implications for troposphere-stratosphere transport. Geophysical Research Letters 23, 2385-2388.

Noone, D., 2008. The influence of midlatitude and tropical overturning circulation on the isotopic composition of atmospheric water vapor and Antarctic precipitation. Journal of Geophysical Research: Atmospheres 113.

Noone, D., 2012. Pairing Measurements of the Water Vapor Isotope Ratio with Humidity to Deduce Atmospheric Moistening and Dehydration in the Tropical Midtroposphere. Journal of Climate 25, 4476-4494.

Pausata, F.S.R., Battisti, D.S., Nisancioglu, K.H., Bitz, C.M., 2011. Chinese stalagmite delta O-18 controlled by changes in the Indian monsoon during a simulated Heinrich event. Nature Geoscience 4, 474-480.

Pfahl, S., Sodemann, H., 2014. What controls deuterium excess in global precipitation? Climate of the Past 10, 771-781.

Putman, A.L., Fiorella, R.P., Bowen, G.J., Cai, Z., 2019. A global perspective on local meteoric water lines: Meta-analytic insight into fundamental controls and practical constraints. Water Resources Research 55, 6896-6910.

Risi, C., Bony, S., Vimeux, F., 2008a. Influence of convective processes on the isotopic composition (δ18O and δD) of precipitation and water vapor in the tropics: 2. Physical interpretation of the amount effect. Journal of Geophysical Research: Atmospheres 113, -.

Risi, C., Bony, S., Vimeux, F., Descroix, L., Ibrahim, B., Lebreton, E., Mamadou, I., Sultan, B., 2008b. What controls the isotopic composition of the African monsoon precipitation? Insights from event-based precipitation collected during the 2006 AMMA field campaign. Geophysical Research Letters 35, 851-854.

Risi, C., Bony, S., Vimeux, F., Jouzel, J., 2010. Water-stable isotopes in the LMDZ4 general circulation model: Model evaluation for present-day and past climates and applications to climatic interpretations of tropical isotopic records. Journal of Geophysical Research-Atmospheres 115.

Risi, C., Landais, A., Winkler, R., Vimeux, F., 2013a. Can we determine what controls the spatio-temporal distribution of d-excess and 17 O-excess in precipitation using the LMDZ general circulation model? Climate of the Past 9, 2173-2193.

Risi, C., Muller, C., Blossey, P., 2020. What Controls the Water Vapor Isotopic Composition Near the Surface of Tropical Oceans? Results From an Analytical Model Constrained by Large-Eddy Simulations. Journal of Advances in Modeling Earth Systems 12.

Risi, C., Muller, C., Vimeux, F., Blossey, P., Védeau, G., Dufaux, C., Abramian, S., 2023. What Controls the Mesoscale Variations in Water Isotopic Composition Within Tropical Cyclones and Squall Lines? Cloud Resolving Model Simulations in Radiative-Convective Equilibrium. Journal of Advances in Modeling Earth Systems 15, e2022MS003331.

Risi, C., Noone, D., Frankenberg, C., Worden, J., 2013b. Role of continental recycling in intraseasonal variations of continental moisture as deduced from model simulations and water vapor isotopic measurements. Water Resources Research 49, 4136-4156.

Risi, C., Noone, D., Worden, J., Frankenberg, C., Stiller, G., Kiefer, M., Funke, B., Walker, K., Bernath, P., Schneider, M., Wunch, D., Sherlock, V., Deutscher, N., Griffith, D., Wennberg, P.O., Strong, K., Smale, D., Mahieu, E., Barthlott, S., Hase, F., Garcia, O., Notholt, J., Warneke, T., Toon, G., Sayres, D., Bony, S., Lee, J., Brown, D., Uemura, R., Sturm, C., 2012. Process-evaluation of tropospheric

humidity simulated by general circulation models using water vapor isotopologues: 1. Comparison between models and observations. Journal of Geophysical Research-Atmospheres 117.

Roca, R., Chambon, P., Jobard, I., Kirstetter, P.-E., Gosset, M., Bergès, J.C., 2010. Comparing satellite and surface rainfall products over West Africa at meteorologically relevant scales during the AMMA campaign using error estimates. Journal of Applied Meteorology and Climatology 49, 715-731.

Rossow, W.B., Schiffer, R.A., 1999. Advances in understanding clouds from ISCCP. Bulletin of the American Meteorological Society 80, 2261-2288.

Rozanski, K., Araguás-Araguás, L., Gonfiantini, R., 1993. Isotopic patterns in modern global precipitation. Climate change in continental isotopic records 78, 1-36.

Rozmiarek, K.S., Vaughn, B.H., Jones, T.R., Morris, V., Skorski, W.B., Hughes, A.G., Elston, J., Wahl, S., Faber, A.-K., Steen-Larsen, H.C., 2021. An unmanned aerial vehicle sampling platform for atmospheric water vapor isotopes in polar environments. Atmospheric Measurement Techniques 14, 7045-7067.

Salathé, E.P., Hartmann, D.L., 1997. A trajectory analysis of tropical upper-tropospheric moisture and convection. Journal of Climate 10, 2533-2547.

Salati, E., Dall'Olio, A., Matsui, E., Gat, J.R., 1979. Recycling of water in the Amazon basin: an isotopic study. Water resources research 15, 1250-1258.

Salmon, O.E., Welp, L.R., Baldwin, M.E., Hajny, K.D., Stirm, B.H., Shepson, P.B., 2019. Vertical profile observations of water vapor deuterium excess in the lower troposphere. Atmospheric Chemistry and Physics 19, 11525-11543.

Samuels-Crow, K.E., Galewsky, J., Sharp, Z.D., Dennis, K.J., 2015. Deuterium excess in subtropical free troposphere water vapor: Continuous measurements from the Chajnantor Plateau, northern Chile. Geophysical Research Letters 41, 8652-8659.

Sánchez-Murillo, R., Durán-Quesada, A.M., Esquivel-Hernández, G., Rojas-Cantillano, D., Birkel, C., Welsh, K., Sánchez-Llull, M., Alonso-Hernández, C.M., Tetzlaff, D., Soulsby, C., 2019. Deciphering key processes controlling rainfall isotopic variability during extreme tropical cyclones. Nature communications 10, 1-10.

Saranya, P., Krishan, G., Rao, M., Kumar, S., Kumar, B., 2018. Controls on water vapor isotopes over Roorkee, India: Impact of convective activities and depression systems. Journal of Hydrology 557, 679-687.

Schmidt, M., Maseyk, K., Lett, C., Biron, P., Richard, P., Bariac, T., Seibt, U., 2010. Concentration effects on laser-based δ18O and δ2H measurements and implications for the calibration of vapour measurements with liquid standards. Rapid Communications in Mass Spectrometry 24, 3553-3561.

Schneider, D.P., Noone, D.C., 2007. Spatial covariance of water isotope records in a global network of ice cores spanning twentieth-century climate change. Journal of Geophysical Research: Atmospheres 112.

Shao, L., Tian, L., Cai, Z., Cui, J., Zhu, D., Chen, Y., Palcsu, L., 2017. Driver of the interannual variations of isotope in ice core from the middle of Tibetan Plateau. Atmospheric Research 188, 48-54.

Sherwood, S.C., 1996. Maintenance of the free-tropospheric tropical water vapor distribution. Part II: Simulation by large-scale advection. Journal of Climate, 2919-2934.

Sherwood, S.C., Dessler, A.E., 2000. On the control of stratospheric humidity. Geophysical research letters 27, 2513-2516.

Shi, X., Risi, C., Pu, T., Lacour, J.l., Kong, Y., Wang, K., He, Y., Xia, D., 2020. Variability of isotope composition of precipitation in the southeastern Tibetan Plateau from the synoptic to seasonal time scale.

Journal of Geophysical Research: Atmospheres 125, e2019JD031751.

Smith, J.A., Ackerman, A.S., Jensen, E.J., Toon, O.B., 2006. Role of deep convection in establishing the isotopic composition of water vapor in the tropical transition layer. Geophysical Research Letters 33, 0_46-40_47.

Sodemann, H., Aemisegger, F., Pfahl, S., Bitter, M., Corsmeier, U., Feuerle, T., Graf, P., Hankers, R., Hsiao, G., Schulz, H., 2017. The stable isotopic composition of water vapour above Corsica during the HyMeX SOP1 campaign: insight into vertical mixing processes from lower-tropospheric survey flights. Atmospheric Chemistry and Physics 17, 6125-6151.

Steen-Larsen, H.C., Johnsen, S., Masson-Delmotte, V., Stenni, B., Risi, C., Sodemann, H., Balslev-Clausen, D., Blunier, T., Dahl-Jensen, D., Ellehøj, M.D., 2013. Continuous monitoring of summer surface water vapor isotopic composition above the Greenland Ice Sheet. Atmospheric Chemistry and Physics 13, 4815-4828.

Steen-Larsen, H.C., Risi, C., Werner, M., Yoshimura, K., Masson-Delmotte, V., 2017. Evaluating the skills of isotope-enabled General Circulation Models against in-situ atmospheric water vapor isotope observations. Journal of Geophysical Research 122, 246-263.

Steenlarsen, H.C., Johnsen, S.J., Massondelmotte, V., Stenni, B., 2014. Continuous monitoring of summer surface water vapour isotopic composition above the Greenland Ice Sheet. Atmospheric Chemistry & Physics 13, 4815-4828.

Stein, A., Draxler, R.R., Rolph, G.D., Stunder, B.J., Cohen, M.D., Ngan, F., 2015. NOAA's HYSPLIT atmospheric transport and dispersion modeling system. Bulletin of the American Meteorological Society 96, 2059-2077.

Tan, M., 2014. Circulation effect: response of precipitation delta O-18 to the ENSO cycle in monsoon regions of China. Climate Dynamics 42, 1067-1077.

Taylor, C., 1972. The vertical variations of isotopic compositions of tropospheric water vapour over continental Europe and their relations to tropospheric structure. Inst. Nucl. Sci. Rep. INSR-107, Lower Hutt, New Zealand.

Terzer-Wassmuth, S., Wassenaar, L.I., Welker, J.M., Araguás-Araguás, L.J., 2021. Improved high-resolution global and regionalized isoscapes of δ 18O, δ 2H and d-excess in precipitation. Hydrological Processes 35, e14254.

Thompson, L.G., 2000. Ice core evidence for climate change in the Tropics: implications for our future. Quaternary Science Reviews 19, 19-35.

Thompson, L.G., Yao, T., Mosley-Thompson, E., Davis, M., Henderson, K., Lin, P.-N., 2000. A high-resolution millennial record of the South Asian monsoon from Himalayan ice cores. Science 289, 1916-1919.

Thompson, L.o., Mosley-Thompson, E., Davis, M., Lin, P., Yao, T., Dyurgerov, M., Dai, J., 1993. "Recent warming": ice core evidence from tropical ice cores with emphasis on Central Asia. Global and Planetary Change 7, 145-156.

Thompson, L.o., Yao, T., Davis, M., Henderson, K., Mosley-Thompson, E., Lin, P.-N., Beer, J., Synal, H.-A., Cole-Dai, J., Bolzan, J., 1997. Tropical climate instability: The last glacial cycle from a Qinghai-Tibetan ice core. science 276, 1821-1825.

Thurnherr, I., Kozachek, A., Graf, P., Weng, Y., Bolshiyanov, D., Landwehr, S., Pfahl, S., Schmale, J., Sodemann, H., Steen-Larsen, H.C., 2020. Meridional and vertical variations of the water vapour isotopic composition in the marine boundary layer over the Atlantic and Southern Ocean. Atmospheric Chemistry and Physics 20, 5811-5835.

Tian, L., Yao, T., Li, Z., MacClune, K., Wu, G., Xu, B., Li, Y., Lu, A., Shen, Y., 2006. Recent rapid warming trend revealed from the isotopic record in Muztagata ice core, eastern Pamirs. Journal of Geophysical Research: Atmospheres 111.

Tian, L., Yao, T., MacClune, K., White, J.W.C., Schilla, A., Vaughn, B., Vachon, R., Ichiyanagi, K., 2007. Stable isotopic variations in west China: A consideration of moisture sources. Journal of Geophysical Research-Atmospheres 112.

Tian, L., Yao, T., Schuster, P.F., White, J.W.C., Ichiyanagi, K., Pendall, E., Pu, J., Yu, W., 2003. Oxygen-18 concentrations in recent precipitation and ice cores on the Tibetan Plateau. Journal of Geophysical Research Atmospheres 108, -.

Tian, L., Yu, W., Schuster, P.F., Wen, R., Cai, Z., Wang, D., Shao, L., Cui, J., Guo, X., 2020. Control of seasonal water vapor isotope variations at Lhasa, southern Tibetan Plateau. Journal of Hydrology 580, 124237.

Toride, K., Yoshimura, K., Tada, M., Diekmann, C., Schneider, M., 2021. Potential of mid-tropospheric water vapor isotopes to improve large ‐ cale circulation and weather predictability. Geophysical Research Letters.

Uemura, R., Masson-Delmotte, V., Jouzel, J., Landais, A., Motoyama, H., Stenni, B., 2012. Ranges of moisture-source temperature estimated from Antarctic ice cores stable isotope records over glacial–interglacial cycles. Climate of the Past 8, 1109-1125.

Van Breukelen, M., Vonhof, H., Hellstrom, J., Wester, W., Kroon, D., 2008. Fossil dripwater in stalagmites reveals Holocene temperature and rainfall variation in Amazonia. Earth and Planetary Science Letters 275, 54-60.

Vries, A.D., Aemisegger, F., Pfahl, S., Wernli, H., 2021. Stable water isotope signals in tropical ice clouds in the West African monsoon simulated with a regional convection-permitting model.

Wallace, J.M., Hobbs, P.V., 2006. Atmospheric science: an introductory survey. Elsevier.

Wang, B., 2002. Rainy season of the Asian–Pacific summer monsoon. Journal of Climate 15, 386-398.

Wang, B., Xie, X., 1996. Low-frequency equatorial waves in vertically sheared zonal flow. Part I: Stable waves. Journal of Atmospheric Sciences 53, 449-467.

Wang, B., Xu, X., 1997. Northern Hemisphere summer monsoon singularities and climatological intraseasonal oscillation. Journal of Climate 10, 1071-1085.

Wang, D., Wang, K., 2001. Isotopes in precipitation in China (1986–1999). Science in China Series E: Technological Sciences 44, 48-51.

Wang, G., Lan, H., Liu, Z., 2021. Stable isotope record of super typhoon Lekima (2019). Atmospheric Research 264, 105822.

Wang, X., Tian, L., Yan, H., Mao, J., Cai, Z., Wang, D., Cheng, Y., Liu, F., 2023. The intra-seasonal oscillation of precipitation δ18O over the Asian equatorial and monsoon regions. Journal of Geophysical Research: Atmospheres, e2023JD038869.

Webster, C.R., Heymsfield, A.J., 2003. Water isotope ratios D/H, O-18/O-16, O-17/O-16 in and out of clouds map dehydration pathways. Science 302, 1742-1745.

Welp, L.R., Lee, X., Kim, K., Griffis, T.J., Billmark, K.A., Baker, J.M., 2008. delta O-18 of water vapour, evapotranspiration and the sites of leaf water evaporation in a soybean canopy. Plant Cell and Environment 31, 1214-1228.

Wen, X.F., Zhang, S.C., Sun, X.M., Yu, G.R., Lee, X., 2010. Water vapor and precipitation isotope

ratios in Beijing, China. Journal of Geophysical Research Atmospheres 115, -.

West, J.B., Bowen, G.J., Dawson, T.E., Tu, K.P., 2009. Isoscapes: understanding movement, pattern, and process on Earth through isotope mapping. Springer.

White, J.W.C., Gedzelman, S.D., 1984. The isotopic composition of atmospheric water vapor and the concurrent meteorological conditions. Journal of Geophysical Research Atmospheres 89, 4937-4939.

Winnick, M.J., Chamberlain, C.P., Caves, J.K., Welker, J.M., 2014. Quantifying the isotopic 'continental effect'. Earth and Planetary Science Letters 406, 123-133.

Worden, J., Bowman, K., Noone, D., Beer, R., Clough, S., Eldering, A., Fisher, B., Goldman, A., Gunson, M., Herman, R., Kulawik, S.S., Lampel, M., Luo, M., Osterman, G., Rinsland, C., Rodgers, C., Sander, S., Shephard, M., Worden, H., 2006. Tropospheric emission spectrometer observations of the tropospheric HDO/H2O ratio: Estimation approach and characterization. Journal of Geophysical Research-Atmospheres 111.

Worden, J., Noone, D., Bowman, K., Tropospheric Emission, S., 2007. Importance of rain evaporation and continental convection in the tropical water cycle. Nature 445, 528-532.

Worden, J.R., Kulawik, S.S., Fu, D., Payne, V.H., Bowman, K.W., 2019. Characterization and evaluation of AIRS-based estimates of the deuterium content of water vapor. Atmospheric Measurement Techniques 12, 2331-2339.

Wright, H.E., 1993. Global climates since the last glacial maximum. U of Minnesota Press.

Yao, T., Ding, L., Pu, J., Liu, J., Yang, Z., 1991. Characteristic of δ18O in snow and its relation with moisture sources in Tanggula Mountains, Tibetan Plateau. Chinese Science Bulletin 36, 1570-1573.

Yao, T., Masson-Delmotte, V., Gao, J., Yu, W., Yang, X., Risi, C., Sturm, C., Werner, M., Zhao, H., He, Y., Ren, W., Tian, L., Shi, C., Hou, S., 2013. A review of climatic controls on δ18O in precipitation over the Tibetan Plateau: Observations and simulations. Reviews of Geophysics 51, 525-548.

Yao, T., Thompson, L., Yang, W., Yu, W., Yang, G., Guo, X., Yang, X., Duan, K., Zhao, H., Xu, B., 2012. Different glacier status with atmospheric circulations in Tibetan Plateau and surroundings. Nature Climate Change 2, 663-667.

Yoshimura, K., Kanamitsu, M., 2009. Specification of External Forcing for Regional Model Integrations. Mon.wea.rev 137, 1409-1421.

7 Appendix

Published version of Wang et al (2023)

Atmos. Chem. Phys., 23, 3409–3433, 2023
https://doi.org/10.5194/acp-23-3409-2023

Atmospheric Chemistry and Physics
Open Access
EGU

Research article

Vehicle-based in situ observations of the water vapor isotopic composition across China: spatial and seasonal distributions and controls

Di Wang[1,2,3], Lide Tian[1,3], Camille Risi[2], Xuejie Wang[1,3], Jiangpeng Cui[4], Gabriel J. Bowen[5], Kei Yoshimura[6], Zhongwang Wei[7], and Laurent Z. X. Li[2]

[1]Institute of International Rivers and Eco-security, Yunnan University, Kunming 650500, Yunnan, China
[2]Laboratoire de Météorologie Dynamique, IPSL, CNRS, Sorbonne Université, Campus Pierre et Marie Curie, Paris 75005, France
[3]Yunnan Key Laboratory of International Rivers and Transboundary Eco-security, Kunming 650500, Yunnan, China
[4]Sino-French Institute for Earth System Science, College of Urban and Environmental Sciences, Peking University, Beijing 100871, China
[5]Department of Geology and Geophysics, and Global Change and Sustainability Center, University of Utah, Salt Lake City, Utah 84108, USA
[6]Institute of Industrial Science, The University of Tokyo, Tokyo 113-8654, Japan
[7]School of Atmospheric Sciences, Sun Yat-sen University, Guangzhou 510275, Guangdong, China

Correspondence: Di Wang (di.wang@lmd.ipsl.fr) and Lide Tian (ldtian@ynu.edu.cn)

Received: 22 March 2022 – Discussion started: 4 May 2022
Revised: 6 February 2023 – Accepted: 13 February 2023 – Published: 20 March 2023

Abstract. Stable water isotopes are natural tracers in the hydrological cycle and have been applied in hydrology, atmospheric science, ecology, and paleoclimatology. However, the factors controlling the isotopic distribution, both at spatial and temporal scales, are debated in low and middle latitude regions, due to the significant influence of large-scale atmospheric circulation and complex sources of water vapor. For the first time, we made in situ observations of near-surface vapor isotopes over a large region (over 10 000 km) across China in both pre-monsoon and monsoon seasons, using a newly designed vehicle-based vapor isotope monitoring system. Combined with daily and multiyear monthly mean outputs from the isotope-incorporated global spectral model (Iso-GSM) and infrared atmospheric sounding interferometer (IASI) satellite to calculate the relative contribution, we found that the observed spatial variations in both periods represent mainly seasonal mean spatial variations, but are influenced by more significant synoptic-scale variations during the monsoon period. The spatial variations of vapor $\delta^{18}O$ are mainly controlled by Rayleigh distillation along air mass trajectories during the pre-monsoon period, but are significantly influenced by different moisture sources, continental recycling processes, and convection during moisture transport in the monsoon period. Thus, the North–South gradient observed during the pre-monsoon period is counteracted during the monsoon period. The seasonal variation of vapor $\delta^{18}O$ reflects the influence of the summer monsoon convective precipitation in southern China and a dependence on temperature in the North. The spatial and seasonal variations in d-excess reflect the different moisture sources and the influence of continental recycling. Iso-GSM successfully captures the spatial distribution of vapor $\delta^{18}O$ during the pre-monsoon period, but the performance is weaker during the monsoon period, maybe due to the underestimation of local or short-term high-frequency synoptic variations. These results provide an overview of the spatial distribution and seasonal variability of water isotopic composition in East Asia and their controlling factors, and they emphasize the need to interpret proxy records in the context of the regional system.

Published by Copernicus Publications on behalf of the European Geosciences Union.

1 Introduction

Stable water isotopes have been applied to study a wide range of hydrological and climatic processes (Gat, 1996; Bowen et al., 2019; West et al., 2009). This is because water isotopes vary with the water phases (e.g., evaporation, condensation), and therefore produce a natural labeling effect within the global water cycle. Stable isotopic signals recorded in natural precipitation archives are used in the reconstructions of ancient continental climate and hydrological cycles due to their strong relationship with local meteorological conditions. Examples include ice cores (Thompson, 2000; Yao et al., 1991; Tian et al., 2006), tree-ring cellulose (Liu et al., 2017), stalagmites (Van Breukelen et al., 2008), and lake deposits (Hou et al., 2007). However, unlike in polar ice cores, isotopic records in ice cores from low and middle latitude regions have encountered challenges as temperature proxies (Brown et al., 2006; Thompson et al., 1997).

The East Asian country of China is the main distribution area of ice cores in the low and middle latitudes (Schneider and Noone, 2007), where the interpretation of isotopic variations in natural precipitation archives are debated, because they can be interpreted as recording temperature (Thompson et al., 1993, 1997, 2000; Thompson, 2000), regional-scale rainfall or strength of the Indian monsoon (Pausata et al., 2011), or the origin of air masses (Aggarwal et al., 2004; Risi et al., 2010). This is because China has a typical monsoon climate, and moisture from several sources mix in this region (Wang, 2002; Domrös and Peng, 2012). In general, large parts of the country are affected by the Indian monsoon and the East Asian monsoon in summer, which bring humid marine moisture from the Indian Ocean, South China Sea, and northwestern Pacific Ocean (Fig. 1). During the non-monsoon seasons, the westerlies influence most of northern China (Fig. 1). Westerlies brings extremely cold and dry air masses. Occasional moisture flow from the Indian Ocean and/or Pacific Ocean brings moisture to southern China. Continental recycling, i.e., the moistening of the near-surface air by the evapotranspiration from the land surface (transpiration by plants, evaporation of bare soil or standing water bodies; Brubaker et al., 1993), is also an important source of water vapor in both seasons. Some of the spatial and seasonal patterns of water vapor transport are imprinted in the observed station-based precipitation isotopes (Araguás-Araguás et al., 1998; Tian et al., 2007; Gray and Wright, 1993; Mei'e et al., 1985; Tan, 2014). However, precipitation isotopes can only be obtained at a limited number of stations and only on rainy days. The lack of continuous information makes it limited to analyze the effects of water vapor propagation and alternating monsoon and westerlies. In addition, the seasonal pattern and the spatial variation of water isotopes can strongly influenced by synoptic-scale processes, through their influence on moisture source, transport, convection, and mixing processes (Klein et al., 2015; Sánchez-Murillo et al., 2019; Wang et al., 2021), which requires higher frequency observations. For example, some studies found the impact of tropical cyclones (Gedzelman, 2003; Bhattacharya et al., 2022), the boreal summer intraseasonal oscillation (BSISO) (Kikuchi, 2021), local or large-scale convections (Shi et al., 2020), cold front passages (Aemisegger et al., 2015), depressions (Saranya et al., 2018), and anticyclones (Khaykin et al., 2022) on water isotopes in the Asian region. Additional data and analysis refining our understanding of controls on the spatial and temporal variation of water isotopes in low-latitude regions therefore are needed.

Unlike precipitation, water vapor enters all stages of the hydrological cycle, experiencing frequent and intensive exchange with other water phases; in particular, it is directly linked with water isotope fractionation. Furthermore, vapor isotopes can be measured in regions and periods without precipitation, and therefore have significant potential to trace how water is transported, mixed, and exchanged (Galewsky et al., 2016; Noone, 2008), as well as to diagnose large-scale water cycle dynamics. Water vapor isotope data have been applied to various applications ranging from the marine boundary layer to continental recycling and to various geographical regions from tropical convection to polar climate reconstructions (Galewsky et al., 2016). The development of laser-based spectroscopic isotope analysis made the precise, high-resolution, and real-time measurements of both vapor $\delta^{18}O$ and $\delta^{2}H$ available in recent decades. However, most of the in situ observations of water vapor isotopes are also station based (e.g., Li et al., 2020; Tian et al., 2020; Steen-Larsen et al., 2017; Aemisegger et al., 2014) or performed during ocean cruises (Thurnherr et al., 2020; Bonne et al., 2019; Liu et al., 2014; Kurita, 2011; Benetti et al., 2017). One study made vehicle-based in situ observations to document spatial variations, but this was restricted to the Hawai'i island (Bailey et al., 2013). These observations provided new insight on moisture sources, synoptic influences, and sea surface evaporation fractionation processes. However, in situ observations documenting continuous spatial variations at the large continental scale do not exist. This paper presents the first isotope dataset documenting the spatial variations of vapor isotopes over a large continental region (over 10 000 km), both during the pre-monsoon and monsoon periods, based on vehicle-based in situ observations.

After describing our observed time series along the route (Sect. 3.1 and 3.2), we quantify the relative contributions of seasonal mean spatial variations and synoptic-scale variations that locally disturb the seasonal mean to our observed time series (Sect. 3.3). We show that our observed variations in both seasons are dominated by spatial variations but are influenced by significant synoptic-scale variations during the monsoon period. On the basis of this we then focus on an-

alyzing the main mechanisms underlying these distributions (Sect. 4). Collectively, these data and analyses provide a refined understanding of how the interaction of the summer monsoon and westerly circulation controls water isotope ratios in East Asia.

2 Data and methods

2.1 Geophysical description

We conducted two campaigns to monitor vapor isotopes across a large part of China during the pre-monsoon (3 to 26 March 2019) and the monsoon (28 July to 18 August 2018) periods, using a newly designed vehicle-based vapor isotope monitoring system (Fig. S1). The two campaigns run along almost the same route, with slight deviation in the far northeast of China (Fig. 1). Our vehicle started from Kunming city in southwestern China, traveled northeast to Harbin, then turned to northwestern China (Hami), and returned to Kunming. The expedition traversed most of East Asia, with a total distance of above 10 000 km for each campaign.

2.2 Vapor isotope measurements

2.2.1 Isotopic definitions

Isotopic compositions of samples were reported as the relative deviations from the standard water (Vienna Standard Mean Ocean Water, VSMOW), using the δ notion (McKinney et al., 1950), where R_{sample} and R_{VSMOW} are the isotopic ratios ($H_2^{18}O/H_2^{16}O$ for $\delta^{18}O$ and $^1H^2H^{16}O/H_2^{16}O$ for δ^2H) of the sample and of the VSMOW, respectively, as follows:

$$\delta = (R_{\text{sample}}/R_{\text{VSMOW}} - 1) \times 1000. \quad (1)$$

The second-order d-excess parameter is computed based on the commonly used definition (Dansgaard, 1964). The d-excess is usually interpreted as reflecting the moisture source and evaporation conditions (Jouzel et al., 1997), since the d-excess is more sensitive to non-equilibrium fractionation occurring than $\delta^{18}O$:

$$\text{d-excess} = \delta^2H - 8 \times \delta^{18}O. \quad (2)$$

2.2.2 Instrument

We used a Picarro 2130i cavity ring-down spectroscopy (CRDS) water vapor isotope analyzer fixed on a vehicle to obtain large-scale in situ measurements of near-surface vapor isotopes along the route. The analyzer was powered by a lithium battery on the vehicle, enabling over 8 h operation with a full charge. Therefore, we only made measurements in daytime and recharged the battery at night. The ambient air inlet of the instrument was connected to the outside of the vehicle, which was 1.5 m a.g.l. (meters above ground level), with a waterproof cover to keep large liquid droplets from entering. A portable GPS unit was used to record position data along the route. The measured water vapor mixing ratio and the $\delta^{18}O$ and δ^2H were obtained with a temporal resolution of $\sim$ 1 s. The dataset present in this study had been averaged to a 10 min temporal resolution after calibration, with a horizontal footprint of about 15 km.

A standard delivery module (SDM) was used for the vapor isotope calibration during the surveys. The calibration protocols consist of humidity calibration (Sect. 2.2.3), standard water calibration (Sect. 2.2.4), and error estimation (Sect. 2.2.5), following the methods of Steen-Larsen et al. (2013).

2.2.3 Humidity-dependent isotope bias correction

The measured vapor isotopes are sensitive to air humidity (Liu et al., 2014; Galewsky et al., 2016), which varies substantially across our sampling route. The specific humidity measured by Picarro is very close to that measured by an independent sensor installed in the vehicle (Fig. 4). The correlation between the humidity measured by the Picarro and the independent sensor are over 0.99, the slopes are approximately 1, and the average deviations are less than 1 g kg^{-1} both during pre-monsoon and monsoon periods. We develop a humidity-dependent isotope bias correction by measuring a water standard at different water concentration settings using the SDM. We define a reference level of 20 000 ppm of vapor humidity for our analysis (Eq. 3), since the water vapor isotope measurement by Picarro is generally most accurate at this humidity. The calibrated vapor isotope with different air humidity would be as follows (Liu et al., 2014; Schmidt et al., 2010):

$$\delta_{\_\text{measured}} - \delta_{\_\text{humidity calibration}} = f(\text{humidity}_{\_\text{measured}} - 20\,000), \quad (3)$$

where $\delta_{\_\text{measured}}$ represents the measured vapor isotopes (the raw data), $\delta_{\_\text{humidity calibration}}$ denotes the calibrated vapor isotopes, f is the equation of δ as a function of humidity , and humidity is in ppm. For example, if we measured that f is $\delta = a \times \ln(\text{humidity}) + b$) by measuring standard water with different humidity, then the full equation for humidity-dependent isotope bias correction would be $\delta_{\_\text{measured}} - \delta_{\_\text{humidity calibration}} = a \times \ln(\text{humidity}_{\_\text{measured}}) + b - (a \times \ln(20\,000) + b)$.

We performed the humidity calibration before and after each campaign. In the calibration, the setting of humidity covered the actual range of humidity in the field. In the dry pre-monsoon period of 2019, the humidity was less than 5000 ppm along a large part of the route. In this case, we performed additional calibration tests with the humidity less than 5000 ppm after the field observations, to guarantee the accuracy of the calibration results. The humidity-dependence calibration function is considered constant throughout each campaign (which each lasted less than 24 d).

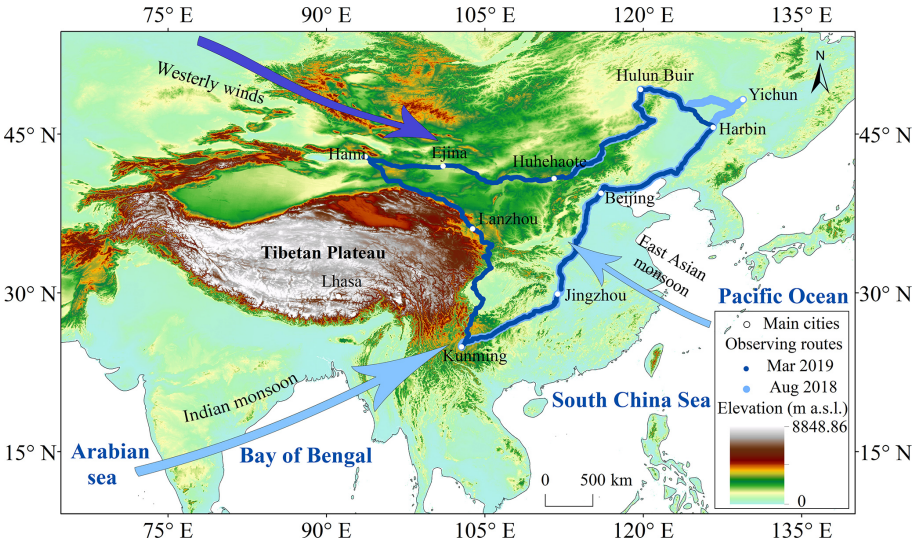

Figure 1. Topographical map of China, showing survey routes and the main atmospheric circulation systems (arrows). Dark blue dots indicate the observation route for the 2019 pre-monsoon period, and light blue dots show the observation route for the 2018 monsoon period, with a slight deviation in the northeast.

2.2.4 Measurement normalization

All measured vapor isotope values were calibrated to the VSMOW scale using two laboratory standard waters ($\delta^{18}O = -10.33‰$ and $\delta^{2}H = -76.95‰$, $\delta^{18}O = -29.86‰$ and $\delta^{2}H = -222.84‰$) covering the range of the expected ambient vapor values. We made the normalization test prior to the daily measurements (two humidity levels for each standard water). We adjusted the amount of the liquid standard injected everyday to keep the humidity of the standard waters consistent with the outside vapor measurements. Our calibration shows that no significant drift of the standard values were observed over time in the observation periods. For two standard waters, the standard deviation of standard measurements are 0.2‰ and 0.11‰ for $\delta^{18}O$, and 1.16‰ and 1.2‰ for $\delta^{2}H$ during the pre-monsoon period of 2019. During the monsoon period of 2018, the standard deviation of standard measurements are 0.09‰ and 0.06‰ for $\delta^{18}O$ and 0.6‰ and 0.33‰ for $\delta^{2}H$).

2.2.5 Error estimation

We estimate the uncertainty based on the error between the measured (after calibration) and true values of the two standards used during the campaigns. The estimated uncertainty is in the range of −0.05 to 0.17 for $\delta^{18}O$, 0.11 to 1.19 for $\delta^{2}H$, and −0.81‰ to 1.23‰ for d-excess during the pre-monsoon period of 2019, with the humidity ranges from 2000 to 29 000 ppm. During the monsoon period of 2018, the range of uncertainty is −0.10‰–0.55‰ for $\delta^{18}O$, −0.94‰–3.74‰ for $\delta^{2}H$, and −1.18‰–1.49‰ for d-excess, with the humidity ranges from 4000 to 34 000 ppm.

2.2.6 Data processing

A few isotope measurements with missing GPS information were excluded from the analysis. Since we want to focus on large-scale variations, we also removed the observations during rain or snow, to avoid situations where hydrometeor evaporation significantly influenced the observations (Tian et al., 2020). Such data represent only 0.03 % and 0.05 % of our observations, respectively (totally, 48 data during the pre-monsoon season and 59 data during the monsoon season). We observed several d-excess pulses with extremely low values, as low as −18.0‰, during the pre-monsoon period and −4.9‰ during the monsoon period. These low values are unusual in previous natural vapor isotope studies and occurred mostly when the measurement vehicle was entering or leaving cities and/or stuck in traffic jams, and they have a much lower intercept in the linear $\delta^{18}O$–$\delta^{2}H$ relationship (Fig. S6). Previous studies on urban vapor isotopes (Gorski et al., 2015; Fiorella et al., 2018, 2019) showed that the vapor d-excess closely tracked changes in CO_2 through inversion events and during the daily cycle dominated by patterns of human activity, and combustion-derived water vapor is characterized by a low d-excess value due to its unique source. We also find that the d-excess values are especially low when the vehicle was in cities in the afternoon. The values increased to normal during the night. This diurnal cycle is likely related to the emission intensity and atmospheric processes (Fiorella et al., 2018). Some of these d-excess anomalies are not excluded from being affected by the baseline effects emerging from rapid changes in concentrations of different trace gases (Johnson and Rella, 2017; Gralher et al., 2016). We therefore excluded these data (133 data points during the pre-monsoon period and 62 data points during the monsoon period repre-

sent 0.10 % and 0.06 % of our observations, respectively) in the discussion on the general spatial feature (except Fig. 4). Outside of towns, country sources, such as irrigation, farms, and power plants, cannot be completely ruled out. However, we expect their influence to be much smaller than large-scale spatial variations.

2.3 Meteorological observations

We fixed a portable weather station on the roof of the vehicle to obtain air temperature (T), dew-point temperature (T_d), air pressure (Pres), and relative humidity (RH). All sensors were located near the ambient air intake. The specific humidity (q) of the near-surface air was calculated from T_d and Pres. Meteorological data, GPS location data, and vapor isotope data were synchronized according to their measurement times. And all of them also had been averaged to a 10 min temporal resolution.

National Centers for Environmental Prediction/National Center for Atmospheric Research (NCEP/NCAR) 2.5° global reanalysis data are used to determine the large-scale factors influencing the spatial pattern of the vapor isotopes, including the surface T, q, U wind and V wind, and RH, which are available at https://psl.noaa.gov/data/gridded/data.ncep.reanalysis.surface.html (last access: March 2022). Some missing meteorological data (during the pre-monsoon period: q on 8 and 18 March 2019; during the monsoon period: T and q from 28 to 31 July 2018, and q on 5 August 2018) along the survey routes due to instrument failure are acquired from the NCEP/NCAR reanalysis data. To match the vapor isotope data along the route, we linearly interpolate the NCEP/NCAR data to the location and time of each measurement. The interpolated T and q from NCEP/NCAR are highly correlated with our measurement, as shown in Fig. 4h and j. The 1° precipitation amount (P) from the Global Precipitation Climatology Project (GPCP) is used (https://www.ncei.noaa.gov/data/global-precipitation-climatology-project-gpcp-daily/access/, last access: March 2022). When comparing the time series of GPCP data with our observed isotopes, we linearly interpolate the daily GPCP data to the location of each observation location (P daily). We also used the average of the GPCP precipitation over the entire observation period of about 1 month for each observation location (P mean). The 2.5° outgoing longwave radiation (OLR) data can be obtained from NOAA (http://www.esrl.noaa.gov/psd/data/gridded/data.interp_OLR.html, last access: March 2022).

2.4 Back-trajectory calculation and categorizing regions based on air mass origin

The vapor isotope composition is a combined result of moisture source (Tian et al., 2007; Araguás-Araguás et al., 1998), condensation, and mixing processes along the moisture transport route (Galewsky et al., 2016). To interpret the observed spatial–temporal distribution of vapor isotopes, we start with a diagnosis of the geographical origin of the air masses and then analyze the processes along the back trajectories.

To trace the geographical origin of the air masses, the HYSPLIT-compatible meteorological dataset of the global data assimilation system (GDAS) is used (available at ftp://arlftp.arlhq.noaa.gov/pub/archives/gdas1/, last access: March 2022). We select the driving locations every 2 h as starting points for the backward trajectories and make 10 d back trajectories from 1000 m a.g.l. using the Hybrid Single Particle Lagrangian Integrated Trajectory model 4 (HYSPLIT4) (Draxler and Hess, 1998). This is representative of the water vapor near the ground (Guo et al., 2017; Bershaw et al., 2012), since most water vapor in the atmosphere is within 0–2 km a.g.l. (Wallace and Hobbs, 2006). The T, q, P, and RH along the back trajectories are also interpolated by the HYSPLIT4 model (Fig. 2).

Based on the tracing results from HYSPLIT4 model, we speculate on the potential water vapor sources (Fig. 3 and Table 1):

During the pre-monsoon period, we categorize our domain into three regions (Table 1) as follows:

1. In northern China (WR_1), the air is mainly advected by the westerlies.

2. In central China (WR_2), the air also comes from the westerlies but with a slower wind speed (as shown by the shorter trajectories in 10 d), suggesting the potential for greater interaction with the land surface and more continental recycling as the moisture source.

3. In southern China (WR_3), trajectories come from the southwest and South with marine moisture sources from the Bay of Bengal (BoB).

During the monsoon period, we categorize our domain into four regions (Table 1) as follows:

1. In northwestern China (SR_1), most air masses also spend considerable time over the continent, suggesting some of the vapor can be recycled by continental recycling.

2. In northeastern China (SR_2), trajectories mainly come from the North and though the westerlies.

3. In central China (SR_3), both in its eastern (from Beijing to Harbin) and western part, trajectories mainly come from the East. This suggests that vapor mainly comes from the Pacific Ocean or from continental recycling over eastern and central China.

4. In southeastern China (SR_4), trajectories come from the South, suggesting marine moisture sources from the Arabian Sea and the BoB.

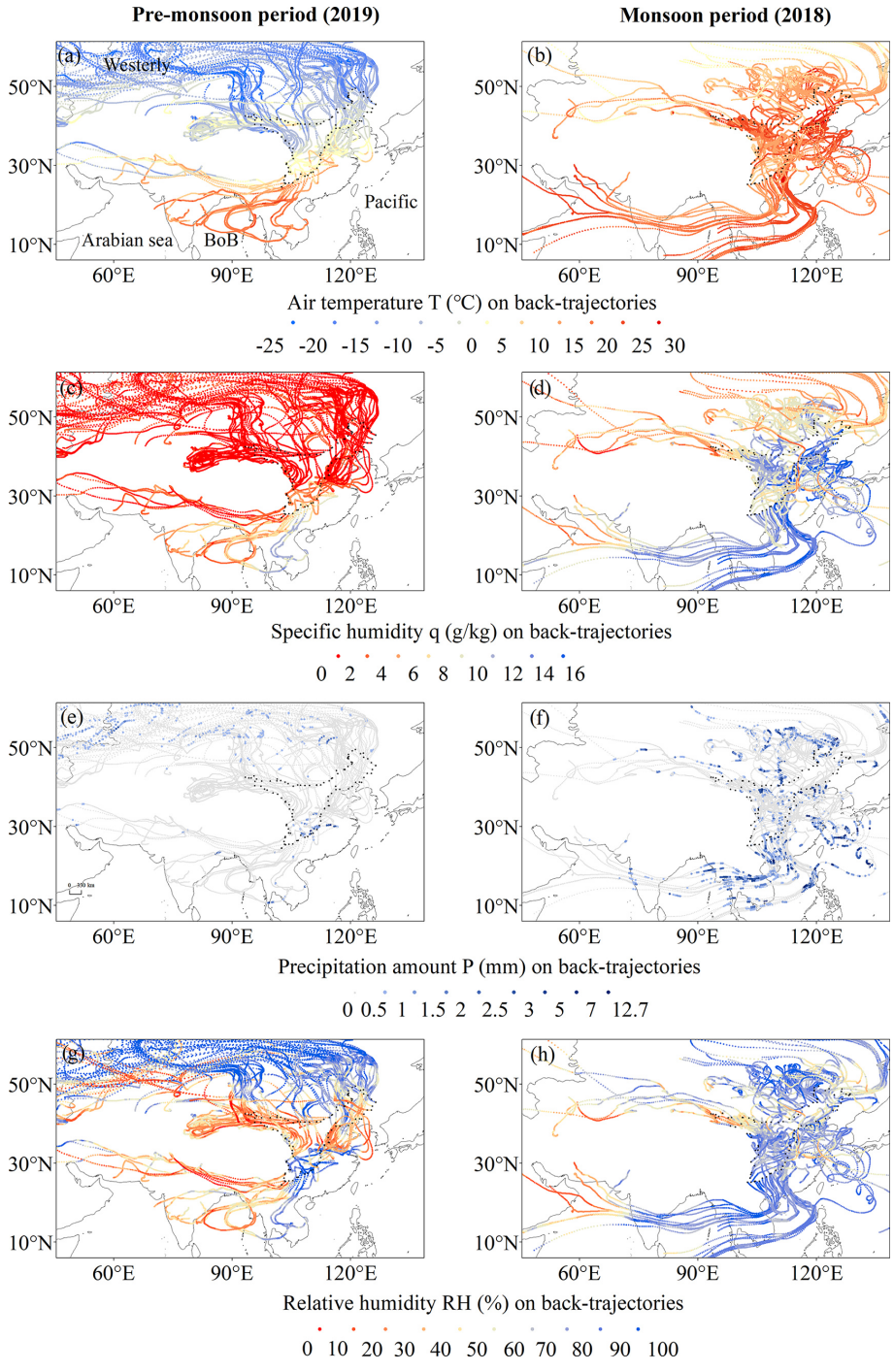

Figure 2. Meteorological conditions simulated by the HYSPLIT4 model along the 10 d air back trajectories for the on-route sampling positions during the two surveys: **(a, b)** air temperature T (°C), **(c, d)** specific humidity q ($g\,kg^{-1}$), **(e, f)** precipitation amount P (mm), and **(g, h)** relative humidity RH (%). The left panel is for the pre-monsoon period, and the right is for the monsoon period. The driving locations and time every 2 h are used as starting points. Note: BoB is the abbreviation for the Bay of Bengal.

2.5 General circulation model simulation and satellite measurements

To disentangle the spatial and synoptic influences, we use surface layer variables from an isotope-enabled general circulation model (Iso-GSM) simulations (Yoshimura and Kanamitsu, 2009) at 1.915° × 1.875° and the lowest level (the altitude is about 2950 m) isotope retrievals from satellite infrared atmospheric sounding interferometer (IASI) at

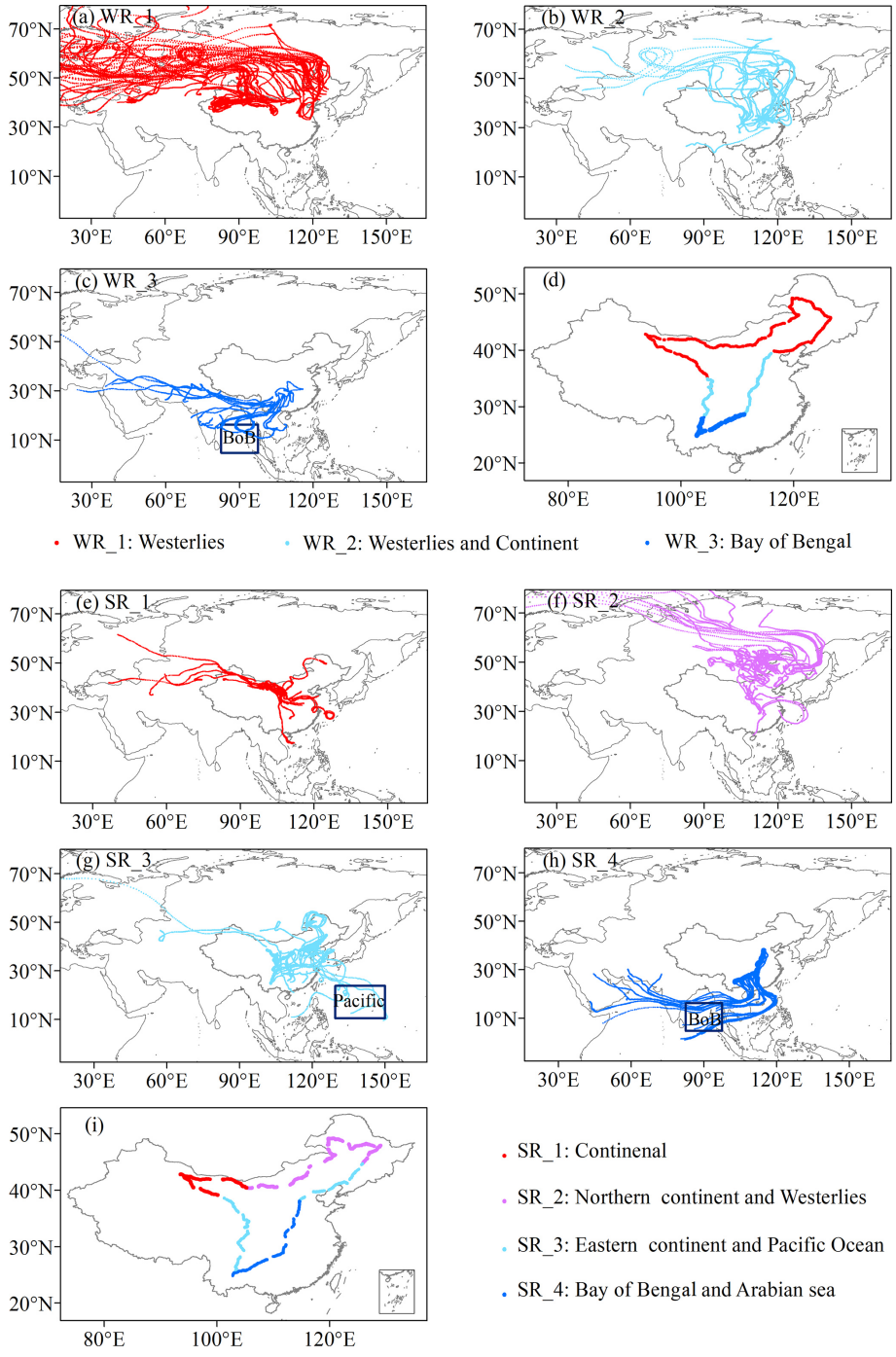

Figure 3. The backward trajectory results (**a**, **b**, and **c** for the pre-monsoon period, and **e**, **f**, **g**, and **h** for the monsoon period) and the dividing of the study zones based on geographical origin of the air masses (**d** for the pre-monsoon period and **i** for the monsoon period). Note: BoB is the abbreviation for the Bay of Bengal.

1° × 1°. For both datasets, we use the outputs corresponding to the observation location and the observation date (daily outputs) and the multiyear monthly mean outputs (March monthly for the pre-monsoon period and August monthly for the monsoon period) for each observation location from 2015 to 2020. When interpolating daily/multiyear monthly outputs, we select the nearest grid point for a given latitude and longitude of each measurement. For Iso-GSM simulations, because of the coarse resolution of the model, there is a difference between the altitude observed along the sampling route and that of the nearest grid point. Therefore, we correct the outputs of Iso-GSM for this altitude difference (the

Table 1. The dividing of the study zones based on moisture sources and corresponding vapor $\delta^{18}O$–$\delta^{2}H$ relationship.

Pre-monsoon period (2019)				
	Water sources (Fig. 3)	Region (China)	Climate background	$\delta^{18}O$–$\delta^{2}H$ relationship
WR_1	Westerlies	The North	Westerlies domain	$\delta^{18}O = 8.04\delta^{2}H + 12.00$ ($r^2 = 0.99$, $n = 750$, $q < 0.01$)
WR_2	Westerlies and continent	The middle	Transition domain	$\delta^{18}O = 8.26\delta^{2}H + 23.15$ ($r^2 = 0.99$, $n = 281$, $q < 0.01$)
WR_3	Bay of Bengal (BoB)	The South	Monsoon domain	$\delta^{18}O = 7.98\delta^{2}H + 17.13$ ($r^2 = 0.94$, $n = 158$, $q < 0.01$)
Monsoon period (2018)				
	Water sources (Fig. 3)	Region (China)	Climate background	$\delta^{18}O$–$\delta^{2}H$ relationship
SR_1	Continent	The northwest	Transition domain	$\delta^{18}O = 8.31\delta^{2}H + 20.92$ ($r^2 = 0.99$, $n = 200$, $q < 0.01$)
SR_2	Northern continent & Westerlies	The northeast	Transition domain	$\delta^{18}O = 7.53\delta^{2}H + 5.13$ ($r^2 = 0.98$, $n = 294$, $q < 0.01$)
SR_3	Eastern continent & Pacific Ocean	The middle and West	Transition domain	$\delta^{18}O = 7.49\delta^{2}H + 7.09$ ($r^2 = 0.97$, $n = 271$, $q < 0.01$)
SR_4	BoB & Arabian sea	The southeast	Monsoon domain	$\delta^{18}O = 8.21\delta^{2}H + 17.81$ ($r^2 = 0.99$, $n = 195$, $q < 0.01$)

method is given in the Supplement under "III. Supplementary Text"). Since the satellite only retrieves $\delta^{2}H$, we just use $\delta^{2}H$ outputs of Iso-GSM and satellite to quantify the relative contributions of seasonal mean and synoptic-scale variations (Sect. 3.3). Other than that, our discussion focuses on $\delta^{18}O$ and d-excess. The variations of $\delta^{2}H$ are consistent with those of $\delta^{18}O$. We also interpret the biases in Iso-GSM after we understand the factors influencing the spatial and seasonal variation of vapor isotopes (Sect. 4.6).

2.6 Method to decompose the observed daily variations

The temporal variations observed along the route for a given period represent a mixture of synoptic-scale perturbations and of seasonal mean spatial distribution as follows:

$$\delta^{2}H_{\_daily} = \delta^{2}H_{\_seaso} + \delta^{2}H_{\_synoptic}. \quad (4)$$

The first term represents the contribution of seasonal mean spatial variations, whereas the second term represents the contribution of synoptic-scale variations. Since these relative contributions are unknown, we use outputs from Iso-GSM and IASI. The daily variations of $\delta^{2}H$ simulated by Iso-GSM also represent a mixture of synoptic-scale perturbations and seasonal mean spatial distribution, but with some errors relative to reality:

$$\delta^{2}H_{\_daily\_Iso\text{-}GSM} = \delta^{2}H_{\_seaso\_Iso\text{-}GSM} + \delta^{2}H_{\_synoptic\_Iso\text{-}GSM}, \quad (5)$$

where $\delta^{2}H_{\_daily\_Iso\text{-}GSM}$ is the daily outputs of $\delta^{2}H$ for each location, $\delta^{2}H_{\_seaso\_Iso\text{-}GSM}$ is the multi-year monthly outputs of $\delta^{2}H$ for each location, and $\delta^{2}H_{\_synoptic\_Iso\text{-}GSM} = \delta^{2}H_{\_daily\_Iso\text{-}GSM} - \delta^{2}H_{\_seaso\_Iso\text{-}GSM}$; each of these terms are affected by errors relative to observations as follows:

$$\begin{aligned}\delta^{2}H_{\_daily\_Iso\text{-}GSM} &= \delta^{2}H_{\_daily} + \in = (\delta^{2}H_{\_seaso} + \in_{\_seaso}) \\ &\quad + (\delta^{2}H_{\_synoptic} + \in_{\_synoptic}), \end{aligned} \quad (6)$$

where $\in_{\_seaso}$ and $\in_{\_synoptic}$ are the errors on $\delta^{2}H_{\_seao\_Iso\text{-}GSM}$ and $\delta^{2}H_{\_synoptic\_Iso\text{-}GSM}$ relative to reality, respectively, and $\in$ is the sum of $\in_{\_seaso}$ and $\in_{\_synoptic}$.

Correspondingly,

$$\begin{aligned}\delta^{2}H_{\_daily} &= \delta^{2}H_{\_daily\_Iso\text{-}GSM} - \in \\ &= (\delta^{2}H_{\_seaso\_Iso\text{-}GSM} - \in_{\_seaso}) \\ &\quad + (\delta^{2}H_{\_synoptic\_Iso\text{-}GSM} - \in_{\_synoptic}). \end{aligned} \quad (7)$$

These individual error components $\in_{\_seaso}$ and $\in_{\_synoptic}$ are unknown, but we know the sum of them ($\in$), i.e., the difference between daily outputs and observations. For the decomposition, we made two extreme assumptions to estimate upper and lower bounds on the contribution values as follows:

1. If we assume that the error is purely synoptic, i.e., $\in = \in_{\_synoptic}$, and $\in_{\_seaso} = 0$, then

$$\delta^{2}H_{\_daily} = \delta^{2}H_{\_seaso\_Iso\text{-}GSM} + (\delta^{2}H_{\_synoptic\_Iso\text{-}GSM} - \in). \quad (8)$$

   To evaluate the contribution of these two terms, we calculate the slopes of $\delta^{2}H_{\_daily}$ as a function of $\delta^{2}H_{\_seaso\_Iso\text{-}GSM}$ ($a_{\_seaso}$) and of $\delta^{2}H_{\_daily} - \delta^{2}H_{\_seaso\_Iso\text{-}GSM}$ ($a_{\_synoptic}$). The relative contributions of spatial and synoptic variations correspond to $a_{\_seaso}$ and $a_{\_synoptic}$, respectively. This will be the upper bound for the contribution of synoptic-scale variations, since some of the systematic errors of Iso-GSM will be included in the synoptic component. This is equivalent to using the seasonal mean of Iso-GSM and the raw time series of observations.

2. If we assume that the error is purely seasonal mean, i.e., $\in = \in_{\_seaso}$ and $\in_{\_synoptic} = 0$, then

$$\delta^{2}H_{\_daily} = (\delta^{2}H_{\_seaso\_Iso\text{-}GSM} - \in) + \delta^{2}H_{\_synoptic\_Iso\text{-}GSM}. \quad (9)$$

   To evaluate the contribution of these two terms, we calculate the slopes of $\delta^{2}H_{\_daily\_Iso\text{-}GSM}$ as a function of $\delta^{2}H_{\_seaso\_Iso\text{-}GSM} - \in$ ($a_{\_seaso}$) and of $\delta^{2}H_{\_daily} - (\delta^{2}H_{\_seaso\_Iso\text{-}GSM} - \in)$ ($a_{\_synoptic}$). This will be the lower bound for the contribution of synoptic-scale variations, since we expect Iso-GSM to underestimate the synoptic variations.

The same analysis is also performed for δ^2H retrieved from IASI and the Iso-GSM simulation q (Table 2) and reanalysis q (Table 3).

3 Spatial and seasonal variations

3.1 Raw time series

Our survey of the vapor isotopes yields two snapshots of the isotopic distribution along the route (Figs. 4 and 5). Figure 4 shows the variations of observed 10 min averaged surface vapor δ^{18}O and d-excess along the survey route across China during the pre-monsoon and monsoon campaigns. The figure also shows the concurrent meteorological data from the weather station installed on the vehicle, and the water vapor content recorded by the Picarro water vapor isotope analyzer as a comparison. We extract daily precipitation amount (P daily) and average precipitation amount over the entire observation period of about 1 month for each observation location (P mean) (mm d^{-1}) from GPCP. The vapor δ^{18}O shows high magnitude variations in both seasons. A general decreasing–increasing trend overlapped with short-term fluctuations is observed during the pre-monsoon period, whereas no general trend but frequent fluctuations characterized the monsoon period. The δ^{18}O range is much larger during the pre-monsoon period (varying between -44 ‰ and -8 ‰) than during the monsoon period (from -11 ‰ to -23 ‰). Most measured vapor d-excess values range from 5 ‰ to 25 ‰ during the pre-monsoon period and from 10 ‰ to 22 ‰ during the monsoon period.

Comparison with the concurrently observed meteorological data shows a robust air temperature (T) dependence of the vapor δ^{18}O variations. In particular, the general trend of δ^{18}O is roughly consistent with T variation during the pre-monsoon period (Fig. 4a and g). During the pre-monsoon period, humidity (Fig. 4e and i), P mean (Fig. 4k), and vapor δ^{18}O (Fig. 4a) are much higher in southwestern China (at the beginning and end of the campaign) than in any other regions. Humidity, q, and P mean also vary consistently throughout the route during the monsoon period (Fig. 4f, j, and l). Synoptic effects on the observed vapor isotopes are discussed in detail in Sect. 4.3 and 4.6.

3.2 Spatial variations

The spatial distribution of the observed vapor δ^{18}O and d-excess during the two surveys in different seasons are presented in Figure 5. During the pre-monsoon period, we find a South–North gradient of vapor δ^{18}O (Fig. 5a). The vapor δ^{18}O ranges from -8 ‰ to -16 ‰ in southern China to as low as -24 ‰ to -44 ‰ in the North. A roughly similar spatial pattern is observed for the vapor d-excess during the pre-monsoon period (Fig. 5c). The d-excess value ranges from 10 ‰ to 30 ‰ in southern China and from -10 ‰ to $+20$ ‰ (most observations with values from 5 ‰ to $+20$ ‰) in northern China. In previous studies, a higher precipitation d-excess during the pre-monsoon period was also observed in the Asian monsoon region owing to the lower relative humidity (RH) at the surface in the moisture source region (Tian et al., 2007; Jouzel et al., 1997). The same reason probably explains the higher vapor d-excess in southern China observed here. Alternatively, the high d-excess in South China could also result from the moisture flow from the Indian/Pacific Ocean, or from the deeper convective mixed layer in South China compared to North China. The lower d-excess values (as low as -10 ‰ to 10 ‰) in northern China (between 38 and 51° N) have rarely been reported in earlier studies. The spatial distribution of the observed vapor d-excess could reflect the general latitudinal gradient of d-excess observed at the global scale, with a strong poleward decrease in midlatitudes (between around 20 to 60°), which was found in previous studies on the large-scale distribution of d-excess in vapor (Thurnherr et al., 2020; Benetti et al., 2017) and precipitation (Risi et al., 2013a; Terzer-Wassmuth et al., 2021; Pfahl and Sodemann, 2014; Bowen and Revenaugh, 2003), based on both observations and modeling. During the monsoon period, the lowest values of vapor δ^{18}O are found in southwestern and northeastern China, with a range of -23 ‰ to -19 ‰ (Fig. 5b). Higher vapor δ^{18}O values up to -11 ‰ are found in central China. The vapor d-excess values (Fig. 5d) in western and northwestern China (91–109° E, 24–43° N) are roughly between 16 ‰ and 22 ‰, higher than in eastern China (mostly between 0 ‰ and 16 ‰).

We do not know whether these apparent spatial variations represent the seasonal mean or whether it is mainly affected by synoptic perturbations. We therefore use Iso-GSM simulation results and IASI satellite measurements to quantify the relative contributions of seasonal mean and synoptic perturbations in Sect. 3.3.

3.3 Disentangling seasonal mean and synoptic variations

Figure 6 shows the comparison of the measured vapor δ^2H, simulated δ^2H from Iso-GSM, and the δ^2H retrieved from IASI. Iso-GSM captures the variations in observed vapor δ^2H well during the pre-monsoon period, with a correlation coefficient of $r = 0.84$ ($p<0.01$) (Table S3). The daily simulation results during the monsoon period are roughly in the range of observations, but detailed fluctuations are not well captured, with $r = 0.24$ ($p>0.05$) (Table S3). The largest differences occur in the SR_1 zone. IASI captures variations better than Iso-GSM during the monsoon period, with $r = 0.42$ ($p>0.05$). IASI observes over a broad range of altitudes above the ground level, so we expect lower δ^2H in IASI relative to ground-surface observations, but the variations of vapor isotopes are vertically coherent (Fig. 6). The systematic differences between IASI and ground-level observations do not impact the slope of the correlation, and thus does not impact the contribution estimation.

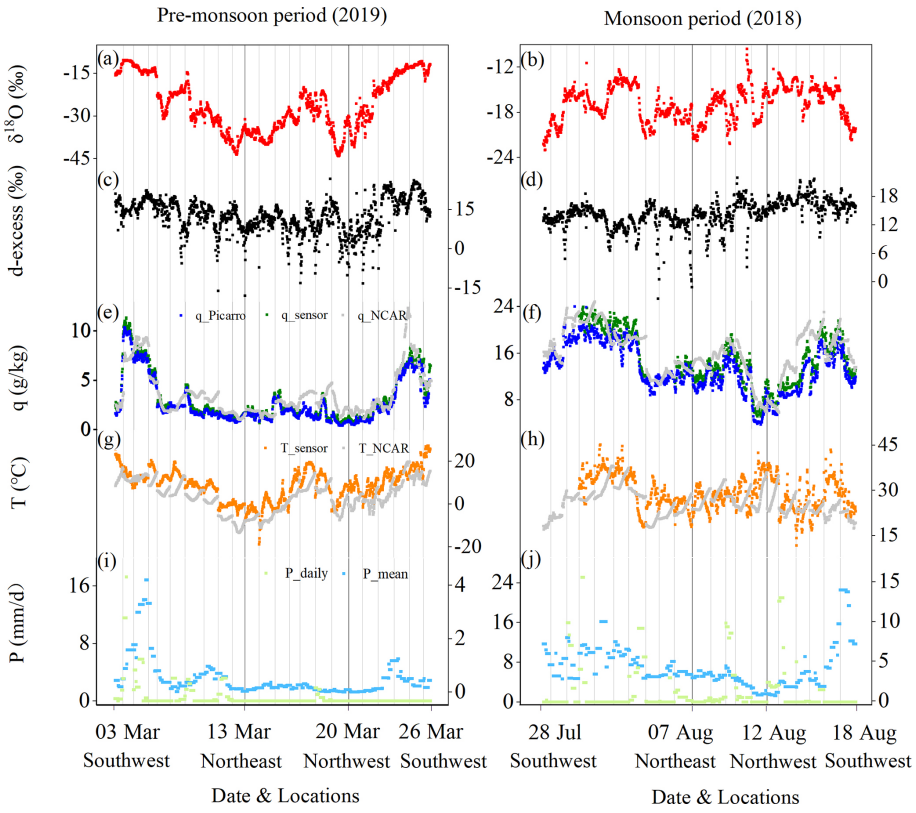

Figure 4. Measured vapor isotopic compositions and concurrent meteorological conditions along the survey routes during the pre-monsoon period (the left panel) and monsoon period (the right panel). **(a, b)** Vapor δ^{18}O (‰); **(c, d)** vapor d-excess (‰); **(e, f)** specific humidity q (g kg^{-1}) measured by sensor (in green), measured by Picarro (in blue), and linearly interpolated from NCAR reanalysis (in gray); **(g, h)** air temperature T (°C) measured by Picarro (in orange) and linearly interpolated from NCAR reanalysis (in gray); and **(i, j)** the daily precipitation amount P daily (in green, mm d^{-1}) and average precipitation amount over the entire observation period of about 1 month for each observation location P mean (in blue, mm d^{-1}) extracted from GPCP. Note that the vertical gray lines space the observations for 1 d.

The multiyear monthly means of δ^2H are smoother but similar to those for the daily outputs both from Iso-GSM and IASI (Fig. 6). Using the method in Sect. 2.6, taking into account the error, we calculate the relative contribution ranges of the seasonal mean and synoptic scale on our observed variations using q and δ^2H from Iso-GSM simulations, q from NCEP/NCAR reanalysis, and δ^2H from IASI.

During the pre-monsoon period, based on both the Iso-GSM simulation and NCEP/NCAR reanalysis, we can find that the seasonal mean contribution to the measured q is higher than the synoptic-scale contribution: a_{seaso} is 73 %–102 % from Iso-GSM and 77 %–92 % from reanalysis, whereas a_{synoptic} is 27 % to −2 % from Iso-GSM and 23 %–8 % from reanalysis (Tables 2 and 3). The relative contribution of seasonal mean spatial variations to the total measured variations in δ^2H (60 %–98 %) is also higher than that of synoptic-scale variations (40 %–2 %). This suggests that the observed variability in q and δ^2H is mainly due to spatial variability and marginally due to synoptic-scale variability. During the monsoon, seasonal mean spatial variations are also the main contributions to the observed variations of q (a_{seaso} is 71 %–82 % from Iso-GSM and 69 %–95 % from reanalysis, whereas a_{synoptic} is 29 %–18 % from Iso-GSM and 31 %–5 % from reanalysis). Since Iso-GSM does not capture daily variations of δ^2H very well during the monsoon period, the relative contribution has a large threshold range (a_{seaso} is 9 %–87 %, a_{synoptic} is 91 %–13 %) after accounting for the errors. Therefore, we can not conclude the dominant contribution on δ^2H from Iso-GSM outputs. IASI, which has a higher correlation with observations, provides an more credible range of a_{seaso}, about 53 %–84 %, and a_{synoptic} is 47 %–16 %. These suggest that during the monsoon period, the synoptic contribution can be significant but not dominant. Having understood the factors influencing the spatial and seasonal variation of vapor isotopes in Sect. 4, we will be able to better understand the reasons for the inconsistent performance of Iso-GSM during the pre-monsoon and monsoon periods (in Sect. 4.6).

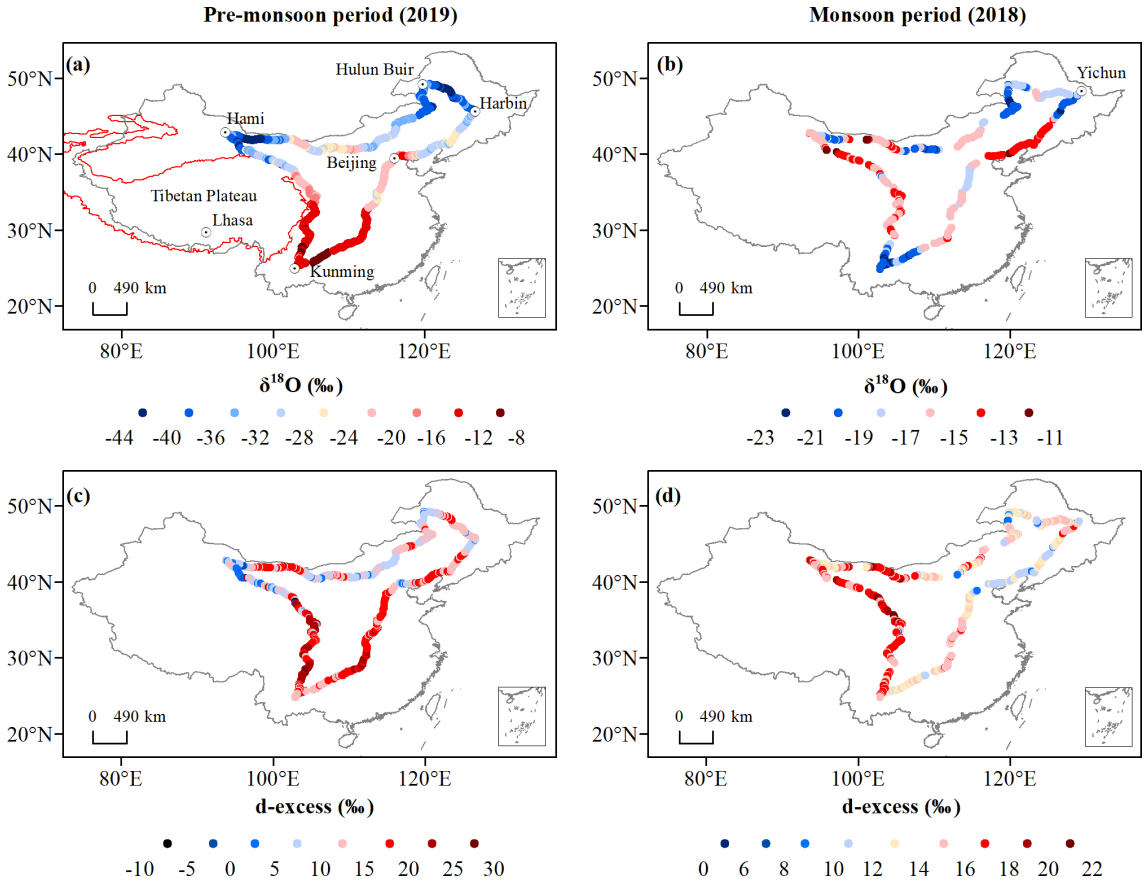

Figure 5. Spatial distribution of vapor δ^{18}O **(a, b)** and d-excess **(c, d)** during the pre-monsoon period **(a, c)** and the monsoon period **(b, d)**.

Table 2. The relative contribution (in fraction) of spatial variations for a given season (a_{seaso}) and of synoptic-scale variations (a_{synoptic}) to the daily variations of q and δ^2H simulated by Iso-GSM and retrievals from IASI. We checked that the sum of a_{seaso} and a_{synoptic} is always 1. The two values indicate the lower and upper bounds as calculated from Eqs. (8) and (9).

Period	Data	Variables	Contributions	
			a_{seaso}	a_{synoptic}
Pre-monsoon (2019)	Iso_GSM	q	0.73–1.02	0.27 to −0.02
		δ^2H	0.60–0.98	0.40–0.02
	IASI	δ^2H	1.06–0.94	−0.06–0.06
Monsoon (2018)	Iso_GSM	q	0.71–0.82	0.29–0.18
		δ^2H	0.09–0.87	0.91–0.13
	IASI	δ^2H	0.53–0.84	0.47–0.16

3.4 Seasonal variations

During the monsoon season, synoptic-scale and intra-seasonal variations contribute significantly to the apparent spatial patterns. However, since these variations are not dominant and have a smaller amplitude than seasonal differences, the comparison of the two snapshots do provide a representative picture of the climatological seasonal difference.

The climate in China features strong seasonality, and it is captured in the snapshots of vapor isotopes (Fig. 7). Since the observation routes of the two surveys are almost identical, we make a seasonal comparison of the observed vapor isotopes during the two surveys. The lines are drawn to distinguish between positive and negative values of seasonal isotopic differences. The seasonal differences $\delta^{18}\text{O}_{\text{monsoon}} - \delta^{18}\text{O}_{\text{pre-monsoon}}$ (Fig. 7a) show opposite signs in northern and

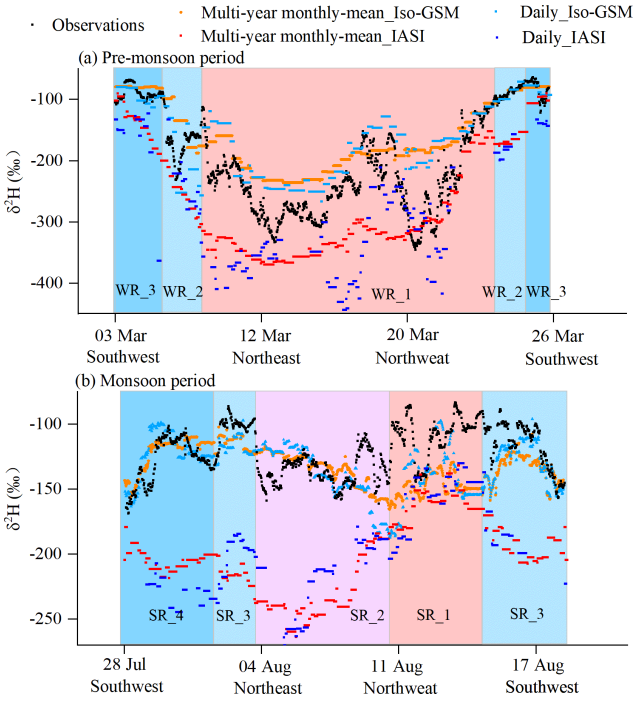

Figure 6. Comparison of observed vapor δ^2H (observations) with outputs of isotope-enabled general circulation model Iso-GSM and satellite IASI during the pre-monsoon period **(a)** and monsoon period **(b)**. The results in this graph are from the daily and multiyear monthly outputs for the sampling locations.

Table 3. The same as Table 2, but for reanalysis q.

Period	Variables	Contributions	
		a_seaso	a_synoptic
Pre-monsoon (2019)	q	0.77–0.92	0.23–0.08
Monsoon (2018)	q	0.69–0.95	0.31–0.05

southern China. In northern China, water vapor δ^{18}O values are higher during the monsoon period than during the pre-monsoon period, while the opposite is true in southern China. The boundary is located around 35° N. The largest seasonal contrasts occur in southwest, northwest, and northeast China, with seasonal δ^{18}O differences of −15 ‰, 30 ‰, and 30 ‰, respectively.

We also find a spatial pattern of vapor d-excess seasonality (Fig. 7b). The line separating the areas of positive and negative values of the d-excess$_{\text{monsoon}}$ − d-excess$_{\text{pre-monsoon}}$ differences coincides with the 120 mm mean precipitation line (Fig. S2f). In southeastern China, the water vapor d-excess is lower during the monsoon period than during the pre-monsoon period. The pattern of seasonal water vapor d-excess in northwestern China is the opposite. The two boundary lines separating the seasonal variations of δ^{18}O and d-excess do not overlap, suggesting different controls on water vapor δ^{18}O and d-excess.

4 Understanding the factors controlling the spatial and seasonal distributions

To interpret the spatial and seasonal variations observed both across China and in each region defined in Sect. 2.4, we investigate q–δ diagrams (Sect. 4.1), δ^{18}O–δ^2H relationships (Sect. 4.2), relationships with meteorological conditions at the local and regional scale (Sect. 4.3 and 4.4), the impact of air mass origin (Sect. 4.5), and synoptic events (Sect. 4.6).

4.1 q–δ diagrams

The progressive condensation of water vapor from an air parcel from the source region to the sampling site and the subsequent removal of condensate results in a gradual reduction of humidity and vapor isotope ratios. This relationship can be visualized in a q–δ diagram, which has been used in many studies of the vapor isotopic composition (Noone, 2012; Galewsky et al., 2016). Observations along the Rayleigh distillation line indicate progressive dehydration by condensation. Observations above the Rayleigh line indicate either mixing between air masses of contrasting humidity (Galewsky and Hurley, 2010) or evapotranspiration (Galewsky et al., 2011; Samuels-Crow et al., 2015; Noone, 2012; Worden et al., 2007). Observations below the Rayleigh line, even when considering the most depleted initial vapor conditions (light blue Rayleigh curve in Fig. 8b), indicate the influence of rain evaporation from depleted precipitation (Noone, 2012; Worden et al., 2007). Figure 8 shows the observed vapor q–δ^2H for different regions during the pre-monsoon (a) and monsoon (b) period. This figure will be interpreted in the light of meteorological variables along back trajectories (Fig. 2).

During the pre-monsoon period, most q–δ^2H measurements are located surrounding or overlapping the Rayleigh curve (the solid black curve in Fig. 8a). Therefore, the observed spatial pattern can mostly be explained by the gradual depletion of vapor isotopes by condensation. The data for the three moisture sources are distributed in different positions of the Rayleigh curve, and they relate to different moisture origins or different original vapor isotope values. This is confirmed by the back-trajectory analysis: the westerlies bring cold and dry air to northern China (WR_1, Figs. 3a, 2a and c), consistent with the vapor further along the Rayleigh distillation, and are thus very depleted (Fig. 5a). The observations in the WR_1 region (Fig. 3c) are closer to the q–δ^2H Rayleigh distillation curve calculated for the key moisture source regions of westerlies, providing further evidence of the influence of water vapor source on vapor isotopes. The relatively high T and q along the ocean-sourced air trajectory reaching southern China (WR_3, Figs. 3c, 2a and c) is consistent with an early Rayleigh distillation phase during moisture transport

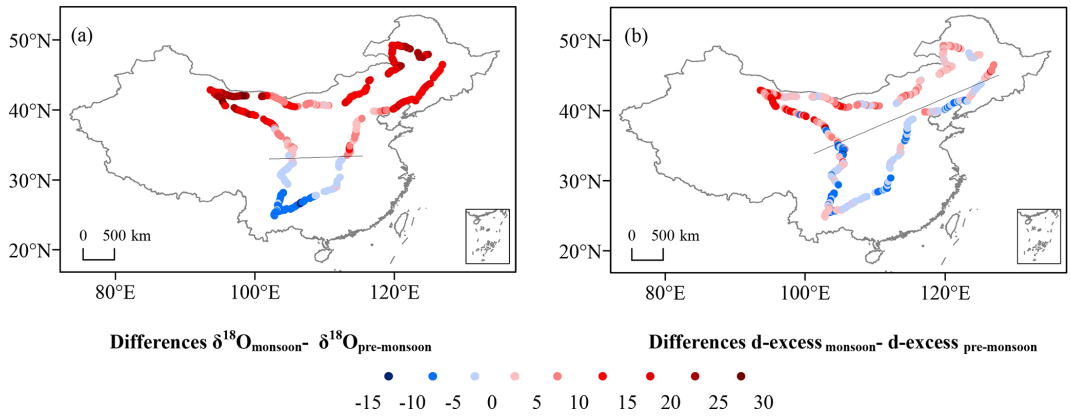

Figure 7. Spatial distribution of the isotope differences ($\delta^{18}O_{monsoon} - \delta^{18}O_{pre\text{-}monsoon}$ **(a)** and d-excess$_{monsoon}$ − d-excess$_{pre\text{-}monsoon}$ **(b)**) for the observation locations. The solid black lines separate the areas of positive and negative values of the differences.

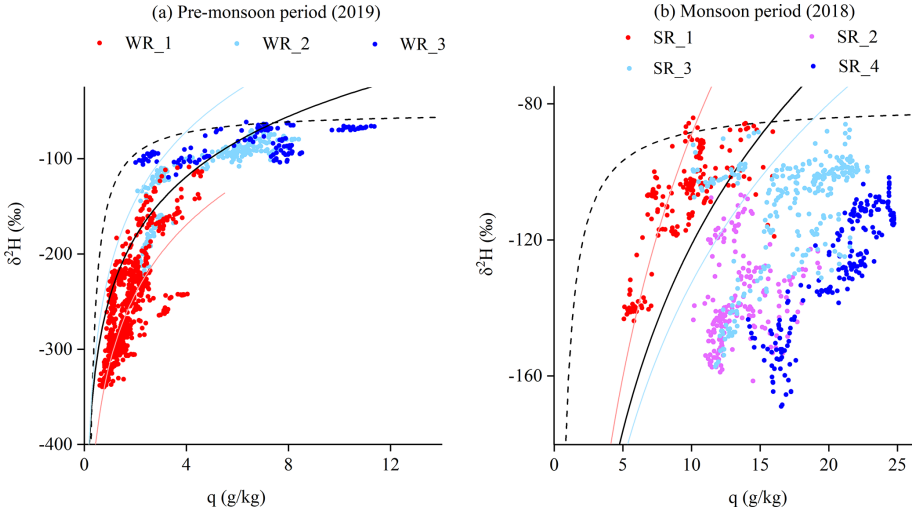

Figure 8. Scatterplot of observed vapor δ^2H (‰) versus specific humidity q ($g\,kg^{-1}$) during the pre-monsoon period **(a)** and monsoon **(b)** period. The solid black curves show the Rayleigh distillation line calculated for the initial conditions of $\delta^2H_0 = -50$ ‰ and $T = 15$ °C during the pre-monsoon period and $\delta^2H_0 = -80$ ‰ and $T = 25$ °C during the monsoon period. The mixing lines (dashed black curves) are calculated using a dry endmember with $q = 0.2\,g\,kg^{-1}$ and $\delta^2H = -500$ ‰ and air parcels for the corresponding Rayleigh curve as a wet endmember. The solid colored curves show the uncertainty range of the Rayleigh curve, calculated for different initial conditions of key moisture source regions: during March 2019, light red and light blue Rayleigh curves are calculated for key moisture source regions of westerlies ($\delta^2H_0 = -168.04$ ‰, $T = 5$ °C) and BoB ($\delta^2H_0 = -77.37$ ‰, $T = 26.46$ °C) separately in **(a)**; during July–August 2018, light red and light blue Rayleigh curves are calculated for key moisture source regions of westerlies ($\delta^2H_0 = -149.64$ ‰, $T = 6.16$ °C) and BoB ($\delta^2H_0 = -82.75$ ‰, $T = 27.69$ °C) separately in **(b)**. These initial δ^2H are derived from Iso-GSM, and the initial temperature and RH are derived from NCAR/NCEP 2.5° global reanalysis data.

and thus higher water vapor $\delta^{18}O$ in southern China (Fig. 5a). Some observations in the WR_3 region (Fig. 3c) are located below the q–δ^2H Rayleigh distillation curve, indicating the influence of rain evaporation (Noone, 2012; Worden et al., 2007). This is consistent with the fact that air originates from the BoB, where deep convection begins to be active, and thus rain evaporation become a source of water vapor.

During the monsoon period, we find a scattered relationship in the q–δ^2H diagram for different regions, implying different moisture sources and/or water recycling patterns during moisture transport. Data measured in the SR_1 region (Fig. 3i) fall above the Rayleigh distillation line (solid black curve in Fig. 8b), likely due to the presence of moisture originating from continental recycling. A larger number of q–δ^2H measurements (most of the measurements from the SR_2, SR_3, and SR_4 regions, Fig. 3i) are located below the Rayleigh curve, indicating moisture originating from the evaporation of raindrops within and below convective systems (Noone, 2012; Worden et al., 2007). In SR_3 and SR_4 regions, this is consistent with the high precipitation

rate along southerly and easterly back trajectories (Fig. 2f). The convection is active over the Bay of Bengal, Pacific Ocean, and southeastern Asia, as shown by the low OLR ($<240\,W\,m^{-2}$) in these regions (Fig. S3) (Wang and Xu, 1997). Therefore, a significant fraction of the water vapor originates from the evaporation of raindrops in convective systems. These results support recent studies showing that convective activity depleted the vapor during transport by the Indian and East Asian monsoon flow (Cai et al., 2018; He et al., 2015; Gao et al., 2013). In the SR_2 region, the relatively low water vapor $\delta^{18}O$, below the Rayleigh curve, is also probably associated with the evaporation of raindrops under deep convective systems. This is confirmed by the high precipitation rates along northerly back trajectories (Fig. 2f), reflecting summer continental convection.

In northern China, q–δ diagrams show stronger distillation during the pre-monsoon period (red dots in Fig. 8a). This suggests a "temperature-dominated" control. Very low regional T during the pre-monsoon period (Figs. S2a and 2a) are associated with low saturation vapor pressures and enhanced distillation, producing lower vapor $\delta^{18}O$. The T in summer is higher (Figs. S2b and 2b), allowing for higher vapor $\delta^{18}O$ (red dots in Fig. 8b). The $\delta^{18}O_{monsoon} - \delta^{18}O_{pre\text{-}monsoon}$ values in this region are therefore positive (Fig. 7a). In the South, q–δ diagrams suggest the stronger influence of rain evaporation during the monsoon period. Higher precipitation amounts significantly reduce $\delta^{18}O$ in the South (Fig. 2f), even though T was higher during the monsoon period than in pre-monsoon. This suggests a precipitation-dominated control in this region, explaining the negative values of $\delta^{18}O_{monsoon} - \delta^{18}O_{pre\text{-}monsoon}$. This seasonal pattern in $\delta^{18}O$ is consistent with the results in precipitation isotopes (Araguás-Araguás et al., 1998; Wang and Wang, 2001). The boundary line separating the seasonal variations of $\delta^{18}O$ is also consistent with a previous study on the seasonal difference in vapor $\delta^{2}H$ retrieved by the Technology Experiment Satellite (TES) and Greenhouse Gases Observing Satellite (GOSAT; Shi et al., 2020).

4.2 The $\delta^{18}O$–$\delta^{2}H$ relationship

The $\delta^{18}O$–$\delta^{2}H$ relationship is usually applied to diagnose the moisture source and water cycling processes related to evaporation. Figure 9 and Table 1 show the $\delta^{18}O$–$\delta^{2}H$ relationship for different regions in the two seasons. We also plot the East Asian meteoric water line (EAMWL) for a reference. Vapor $\delta^{18}O$–$\delta^{2}H$ is usually located above the meteoric water line owing to the liquid water and vapor fractionation.

During the pre-monsoon period (Fig. 9a), the data in northern China (WR_1, Fig. 3a) are located at the lower left area in the $\delta^{18}O$–$\delta^{2}H$ graph, with a similar slope and intercept as EAMWL ($\delta^{2}H = 8.04\ \delta^{18}O + 12.00$). This corresponds to air brought by the westerlies and following Rayleigh distillation. The linear relationship for the vapor in middle China (WR_2, Fig. 3b) has the steepest slope and highest intercept ($\delta^{2}H = 8.26\delta^{18}O + 23.15$). These properties are associated with a high d-excess, consistent with strong continental recycling by evapotranspiration (Aemisegger et al., 2014), as continental recycling is known to enrich the water vapor (Salati et al., 1979) and is associated with high d-excess (Gat and Matsui, 1991; Winnick et al., 2014). The high intercept is further consistent with a correlation between $\delta^{18}O$ and d-excess, which can typically result from continental recycling (Putman et al., 2019). The data for vapor originating from the BoB (WR_3, Fig. 3c) are located to the upper right of the EAMWL. Their regression correlation shows similar features ($\delta^{2}H = 7.98\ \delta^{18}O + 17.13$) to that of the monsoon season (with a slope of 8.21 and an intercept of 17.81). We find similar atmospheric conditions in the BoB (with the region marked as the rectangle in Fig. 3c and h) during the two observation periods, with $T = 26\,°C$ and $RH = 76\,\%$ during the pre-monsoon period and $T = 28\,°C$ and $RH = 78\,\%$ during the monsoon period, suggesting that the BoB source may have similar signals on vapor $\delta^{18}O$ and $\delta^{2}H$ in both seasons. These observed vapor $\delta^{18}O$–$\delta^{2}H$ patterns are consistent with the back-trajectory results indicating that the westerlies persist in northern China during the pre-monsoon period while moisture from the BoB has already reached southern China.

During the monsoon period (Fig. 9b), the data in northwestern China (SR_1, Fig. 3e) with continental moisture sources are located in the upper right of the graph but above the EAMWL, with the steepest slope and highest intercept for the linear $\delta^{18}O$–$\delta^{2}H$ relationship ($\delta^{2}H = 8.31\delta^{18}O + 20.92$). In contrast, the observations in southeastern China with BoB sources (SR_4, Fig. 3h) are located in the lower left of the graph, with a relatively lower intercept ($\delta^{2}H = 8.21\delta^{18}O + 17.81$). This is the opposite pattern compared to the pre-monsoon season. The observations from the SR_3 region (Fig. 3g) also have a low slope and low intercept ($\delta^{2}H = 7.49\ \delta^{18}O + 7.09$). This is consistent with the oceanic moisture from the Pacific Ocean. Also, these $\delta^{18}O$–$\delta^{2}H$ data are located in the upper right of the graph with a more scattered relation (with the lowest correlation coefficient), suggesting more diverse moisture sources. This is consistent with the mixing of water vapor from continental recycling and the Pacific Ocean (Fig. 3g). The observations in northeastern China (SR_2, Fig. 3f) are located at the lower left of the graph, suggesting the influence of condensation along trajectories in northern Asia (Fig. 2f). Compared to the SR_3 and SR_4 regions, the slope and intercept of the observations in SR_2 region are lower ($\delta^{2}H = 7.53\delta^{18}O + 5.13$), reflecting different origins of moisture.

4.3 Relationship with local meteorological variables

Here we analyze the relationship between vapor $\delta^{18}O$, d-excess, and local meteorological parameters for all observations and separately for the different regions (Fig. 10 and Table S1).

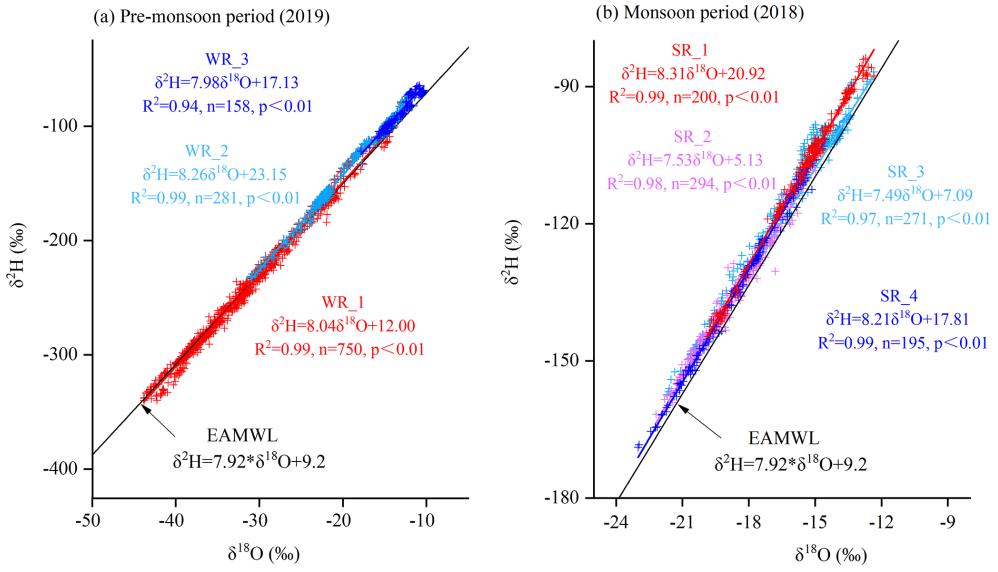

Figure 9. Regional patterns of vapor $\delta^{18}O$–$\delta^{2}H$ relation during pre-monsoon period **(a)** and monsoon **(b)** period, compared with the East Asia meteoric water line (EAMWL) (Araguás-Araguás et al., 1998).

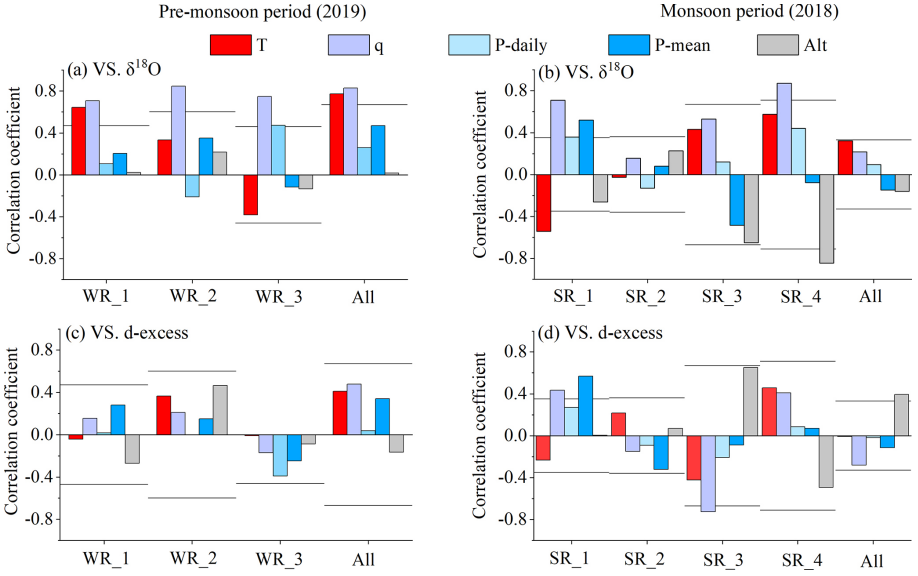

Figure 10. Regional patterns of the correlation between $\delta^{18}O$ **(a, b)**, d-excess, **(c, d)** and various local factors (temperature (T), specific humidity (q), daily precipitation amount (P daily), and average precipitation amount over the entire observation period for each observation location (P mean), and altitude (Alt)). **(a, c)** is for the pre-monsoon period and **(b, d)** is for the monsoon period. Horizontal lines indicate the correlation threshold for statistical significance ($p<0.05$), considered the degree of freedom.

We have taken particular care to estimate the statistical significance of the correlation coefficients. The statistical significance of a correlation depends on the correlation coefficient and on the degree of freedom D of the observed $\delta^{18}O$ and d-excess time series. Since these variables evolve smoothly in time and are sampled at a high frequency, the total number of samples overestimates the degree of freedom D of the time series. We thus estimated the degree of freedom D as τ/η, where τ is the length of the sampling period and η is the characteristic autocorrelation timescale of the time series (an example of this calculation is given in "III" of the Supplement). A similar method was used to calculate the degree of freedom of the signal in Roca et al. (2010). Table S2 summarizes the threshold for the correlation coefficient to be statistically significant at 95 % for the two seasons, the different regions, and the variable of interest.

During the pre-monsoon period, all observations taken together exhibit a "temperature effect" (the δ's decreasing

with temperature, Dansgaard, 1964) (Fig. 10a), with significant and positive correlation between $\delta^{18}O$ and T ($r = 0.77$, $p<0.05$, Table S1). This results from the high correlation between $\delta^{18}O$ and q ($r = 0.83$, $p<0.05$, Table S1), consistent with the Rayleigh distillation, and between T and q ($r = 0.54$, $p<0.05$), consistent with the Clausius Clapeyron relationship. The vapor $\delta^{18}O$ in the WR_1 (Fig. 3a) region shows similar correlations with T and q as for all observations. Rayleigh distillation thus contributes to the relationship between $\delta^{18}O$ and T observed in northern China. In contrast, no significant positive correlation between vapor $\delta^{18}O$ and T is observed in the WR_3 region with the BoB water source. This is consistent with the fact that the moisture from the BoB has already influenced southern China during the pre-monsoon period (Fig. 3c). The weak positive correlation in most regions between $\delta^{18}O$ and P daily and P mean might simply reflect the control of q q on observed vapor $\delta^{18}O$, due to the relatively high correlation between observed P mean and q, with $r = 0.58$ for all observations (Fig. 4).

During the monsoon period (Fig. 10b), no significant correlation emerges when considering all observations. Vapor $\delta^{18}O$ is still significantly correlated with q in the SR_1 (Fig. 3e, $r = 0.71$, $p<0.05$, Table S1) and SR_4 (Fig. 3h, $r = 0.87$, $p<0.05$, Table S1) regions. This is consistent with different degrees of rainout. This may reflect the synoptic-scale variations of convection. The absence of correlation with T suggests that the variations in q mainly reflect variations in relative humidity that are associated with different air mass origins or rain evaporation. The $\delta^{18}O$ is significantly anticorrelated with Alt in the SR_4 region ($r = -0.85$, $p<0.05$, Table S1), consistent with the "altitude effect" (the heavy isotope concentrations in fresh water decreasing with increasing altitude) in precipitation and water vapor (Dansgaard, 1964; Galewsky et al., 2016).

The vapor d-excess for all observations during the monsoon period (Fig. 10d) is positively correlated with Alt ($r = 0.39$, $p<0.05$, Table S1). One possible reason is that the vapor d-excess is lower in coastal areas at lower altitudes, while at higher altitudes in the West, more continental recycling of moisture leads to higher d-excess (Aemisegger et al., 2014). The positive correlation between d-excess and altitude is consistent with previous studies in region (Acharya et al., 2020). In the SR_1 region (Fig. 3e), in arid northwestern China, vapor d-excess is positively correlated with q ($r = 0.43$, $p<0.05$, Table S1) and P mean ($r = 0.57$, $p<0.05$, Table S1) during the monsoon period, suggesting that rain evaporation may also contribute to high d-excess (Kong and Pang, 2016). Other than these examples, the correlation coefficients between the d-excess and T, q, P, and Alt are not significant (Fig. 10c and d), indicating that the local meteorological variables are not strongly related to vapor d-excess, as was reported in previous studies for precipitation isotopes (Guo et al., 2017; Tian et al., 2003).

4.4 Relationship with meteorological variables along trajectories

Reconstructions of paleoclimates using ice core isotopes have relied on relationships with local temperatures, but many previous studies have suggested that water isotopes are driven by remote processes along air mass trajectories. In particular, they emphasized the importance of upstream convection in controlling the isotopic composition of water (Gao et al., 2013; He et al., 2015; Vimeux et al., 2005; Cai and Tian, 2016). We therefore perform a correlation analysis between vapor isotope observations and the temporal mean meteorological conditions along air mass trajectories. The meteorological conditions are averaged over the previous days (N from 1 to 10) prior to the observations.

The $\delta^{18}O$ values have the strongest correlations with T and q along air mass trajectories during the pre-monsoon period (Fig. 11a). The results show gradually increasing positive correlation coefficients as N changes from 10 to 3. This reflects the role of temperature and humidity along air mass trajectories and the large spatial and temporal coherence of T variations during the pre-monsoon period. During the monsoon period, the negative correlation coefficients between $\delta^{18}O$ and P (Fig. 11b) become more significant as N increases from 1 to 4 and less significant as N increases from 5 to 10. This result indicates a maximum impact of P during a few days prior to the observations, as observed also for precipitation isotopes (Gao et al., 2013; Risi et al., 2008a). It is further consistent with the influence of precipitation along back trajectories (Fig. 2f). Mixing depth (MixDep) is stably and positively correlated with d-excess. A hypothesis to explain this correlation is that when the MixDep is higher, stronger vertical mixing of convective system transports vapor with higher d-excess values from higher altitude to the surface (Galewsky et al., 2016; Salmon et al., 2019).

4.5 Relationship between water vapor isotopes and moisture sources

In Sect. 4.1 to 4.4, we have discussed that different moisture sources and corresponding processes on transport pathways are related to the observed spatial patterns both in vapor $\delta^{18}O$ and d-excess.

We also identify different isotopic values of vapor from different ocean sources during the monsoon period. The vapor $\delta^{18}O$ in the zone from Beijing to Harbin and western China with the Pacific Ocean and continental origins (SR_3 region, about $-17‰$ to $-13‰$) are higher than those in the southeast with BoB sources (SR_4 region, about $-23‰$ to $-15‰$) (Figs. 3i and 5b). In Sect. 4.1 and 4.2, we have shown that it is related to the extent of the Rayleigh distillation and rain evaporation associated with convection along trajectories. Earlier studies suggest that lower $\delta^{18}O$ values were observed from the Indian monsoon source than from Pacific Asian monsoon moisture due to the different origi-

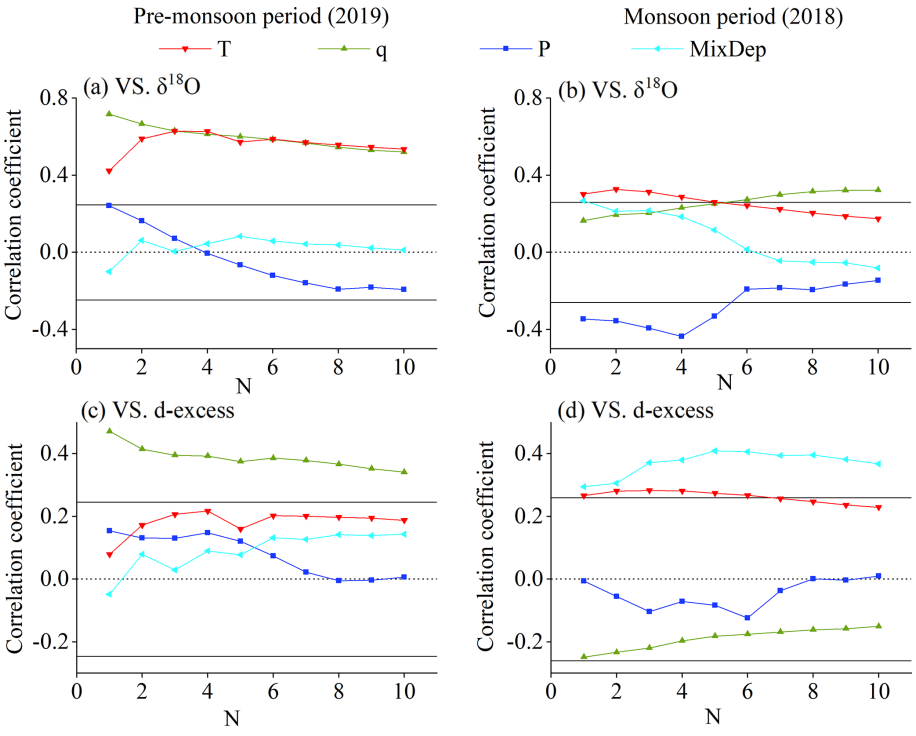

Figure 11. Correlation between $\delta^{18}O$ **(a, b)**, d-excess **(c, d)**, and various meteorological factors (air temperature (T), specific humidity (q), precipitation (P), and mixing depth (MixDep)) along the air mass trajectories during the pre-monsoon period **(a, c)** and monsoon period **(b, d)**. The x axis "N" represents the number of days prior to the observations (from 1 to 10 d). For example, when the number of days is 2, the correlations are calculated with the temporal mean of meteorological data along the air mass trajectories during the 2 d before the observations. Horizontal solid lines indicate the correlation threshold for statistical significance ($p<0.05$).

nal isotope values in the source regions (Araguás-Araguás et al., 1998). To better isolate the direct effect of moisture sources, we extract the initial vapor isotopes of the Indian and East Asian monsoon systems (the regions are marked as annotated rectangles in Fig. 3g and h) for the sampling dates of 2018 from the Iso-GSM model. The values are about $\delta^{18}O = -12‰$ and $\delta^{2}H = -83‰$ in the northern BoB and $\delta^{18}O = -14‰$ and $\delta^{2}H = -97‰$ in the eastern Pacific Ocean. The initial vapor isotope values of the two vapor sources are not significantly different. The initial vapor isotopes in the BoB are even slightly higher than those in the Pacific Ocean, contrary to moisture source hypothesis. The OLR was significantly lower in the BoB than in the Pacific Ocean (Fig. S3). This suggests that the deeper convection in the Indian Ocean leads to lower water vapor isotope ratios (Liebmann and Smith, 1996; Bony et al., 2008; Risi et al., 2008b, a) in southeastern China, rather than the initial composition of the moisture source.

Continental recycling probably also contribute to higher $\delta^{18}O$ in the SR_3 region (Figs. 3i and 5b) (Salati et al., 1979), especially in western China (Fig. 3i), which can be confirmed by the higher d-excess in this region (Fig. 5d) (Gat and Matsui, 1991; Winnick et al., 2014). Except the SR_3 region, continental recycling also has a strong influence on isotopes in the WR2 and SR1 regions, which is suggested by the high values of $\delta^{18}O$ and d-excess, back trajectories, the location on the q–δ diagram, and the higher slopes and intercepts of the $\delta^{18}O$–$\delta^{2}H$ relationship. In the opposite, in the zone from Beijing to Harbin (Fig. 3i), a greater proportion of water vapor from Pacific sources than continental recycling and in the early stage of Rayleigh distillation could result in high vapor $\delta^{18}O$ (Fig. 5b) but relatively low d-excess (Fig. 5d).

In previous studies, the d-excess has been interpreted as reflecting moisture source and evaporation conditions (Jouzel et al., 1997). During the pre-monsoon period, lower T and higher RH over evaporative regions for the vapor transported by the westerlies (Figs. 2a and g, S2a and g) reduces the non-equilibrium fractionation at the moisture source and produces lower vapor d-excess in the WR_1 region (Figs. 3a and 5c) (Jouzel et al., 1997; Merlivat and Jouzel, 1979). In contrast, higher T and lower RH over evaporative regions (Figs. 2a and g, S2a and g) for the vapor coming from the South leads to higher d-excess in southern China (WR_3, Figs. 3c and 5c). This is consistent with the global-scale poleward decrease in T and increase in surface RH over the oceans (despite the occurrence of very low RH at the sea ice edge during cold air outbreaks (Thurnherr et al., 2020; Aemisegger and Papritz, 2018)), resulting in global-scale poleward decrease in d-excess at mid-latitudes (Risi et al., 2013a; Bowen and Revenaugh, 2003). Alternatively, the

low d-excess during the night over the continent in Northern China during the pre-monsoon could also have contributions (Li et al., 2021). During the monsoon period, the lower vapor d-excess observed in eastern China (Fig. 5d) is likely a sign of the oceanic moisture, derived from source regions where RH at the surface is high (Figs. 2h and S2h), and thus reduces non-equilibrium fractionation and lower d-excess. The high d-excess values observed in western and northwestern China (Fig. 5d) reflect the influence of continental recycling (Fig. 3e and g).

The seasonal variation of moisture sources also results in a seasonal difference in d-excess (Fig. 8b). In southeastern China, RH over the ocean surface in summer is higher than in winter (Figs. S2g and h, and 2g and h), resulting in negative values of $\text{d-excess}_{\text{monsoon}} - \text{d-excess}_{\text{pre-monsoon}}$ (Fig. 8b). Northwestern China has an opposite pattern of seasonal vapor d-excess. This result is largely due to the extremely low vapor d-excess during the pre-monsoon period (Fig. 5c). Also, we speculate that a greater contribution of continental recycling leads to higher d-excess during the monsoon period than during the pre-monsoon period (Risi et al., 2013b) and the positive values of the $\text{d-excess}_{\text{monsoon}} - \text{d-excess}_{\text{pre-monsoon}}$ (Fig. 8b).

4.6 Possible reasons for the biases in Iso-GSM

In Sect. 3.3, we showed that Iso-GSM captured the isotopic variations during the pre-monsoon season better than during the monsoon season. We hypothesize that this mainly could be due to the larger contribution of synoptic-scale variations to the observed variations during the monsoon season. Iso-GSM performs well during the pre-monsoon season, when seasonal mean spatial variability dominates q and isotope. In contrast, it performs less well during the monsoon season, when isotopic variations are significantly influenced by the synoptic-scale variability. Among the synoptic influences, tropical cyclones, the BSISO and local processes probably played a role. For example, during our monsoon observations, the landfall of tropical cyclones Jongdari and Yagi corresponds to the low values of δ^{18}O we observed in eastern China (Fig. S7a). Bebinca corresponds to the low values of δ^{18}O we observed in southwestern China (Fig. S7a). Typhoons are known to be associated with depleted rain and vapor (Bhattacharya et al., 2022; Gedzelman, 2003). Three BSISO events occurred in China during about 28–31 July, 5–8 August, and 14–16 August (Fig. S8). The northward propagation of the NSISO is associated with strong convection (Kikuchi, 2021) (Fig. S8). Moreover, short-lived convective events frequently occurred during our observation period (Wang and Zhang, 2018). It is possible that these rapid high-frequency synoptic events are not fully captured by Iso-GSM. We expect that Iso-GSM captures the large-scale circulation. Yet, we notice that Iso-GSM underestimates the depletion associated with tropical cyclones (Fig. 12b). We hypothesize that given its coarse resolution, it underestimates the depletion associated with the mesoscale structure. This might contribute to the overestimation of vapor δ^{18}O in southeastern China (Fig. 12b). In northwestern China, Iso-GSM underestimates vapor δ^{18}O, but also underestimates precipitation, q, and T (Figs. 12b, d, f, and h and S4). It is possible that Iso-GSM underestimates the latitudinal extent of the monsoonal influence, which brings moist conditions, while overestimating the influence of continental air, bringing dry conditions associated with depleted vapor through Rayleigh distillation. It is also possible that Iso-GSM underestimates the enriching effect of continental recycling. During the pre-monsoon period, Iso-GSM overestimates the observed δ^{18}O along most of the survey route (Fig. 12a), with the largest difference in northwestern China, and underestimates the vapor δ^{18}O in the southern part of the study region. Our results are consistent with previous studies showing that many models underestimate the heavy isotope depletion in pre-monsoon seasons in subtropical and mid-latitudes, especially in very dry regions (Risi et al., 2012). This was interpreted as overestimated vertical mixing. The differences in δ^{18}O (Fig. 12a) and q (Fig. 12c) are spatially consistent. The overestimation of δ^{18}O therefore could be due to the overestimation of q and vice versa. These biases could be associated with shortcomings in the representation of convection or in continental recycling. Despite this, the good agreement during the pre-monsoon period is probably due to the dominant control by Rayleigh distillation on seasonal mean spatial variations of isotopes in this season, as concluded in the above. The q variation, in relation with T, drives vapor isotope variations and is well captured by Iso-GSM spatially, with significant correlations between observed and simulated q ($r = 0.84$, slope $= 0.70$ in Table S3) and T ($r = 0.87$, slope $= 0.70$ in Table S3), though q is overestimated in the North and underestimated in the South.

5 Conclusion

Our new vehicle-based observations document spatial and seasonal variability in surface water vapor isotopic composition across a large part of China. Both during the pre-monsoon and monsoon periods, it is clear that different moisture sources and corresponding processes on transport pathways explain the spatial patterns both in vapor δ^{18}O and d-excess (summarized in Fig. 13) as follows:

1. During the pre-monsoon period (Fig. 13a), the latitudinal gradient of vapor δ^{18}O and d-excess were observed. The gradient in δ^{18}O reflects the "temperature effect", and the Rayleigh distillation appears to be the dominant control, roughly consistent with earlier studies on precipitation. Vapor in northern China, derived from westerlies, and subject to stronger Rayleigh distillation (arrows fading from red to blue), is characterized by very low isotope ratios (blue shades). Less complete Rayleigh distillation (arrows fading from red to light

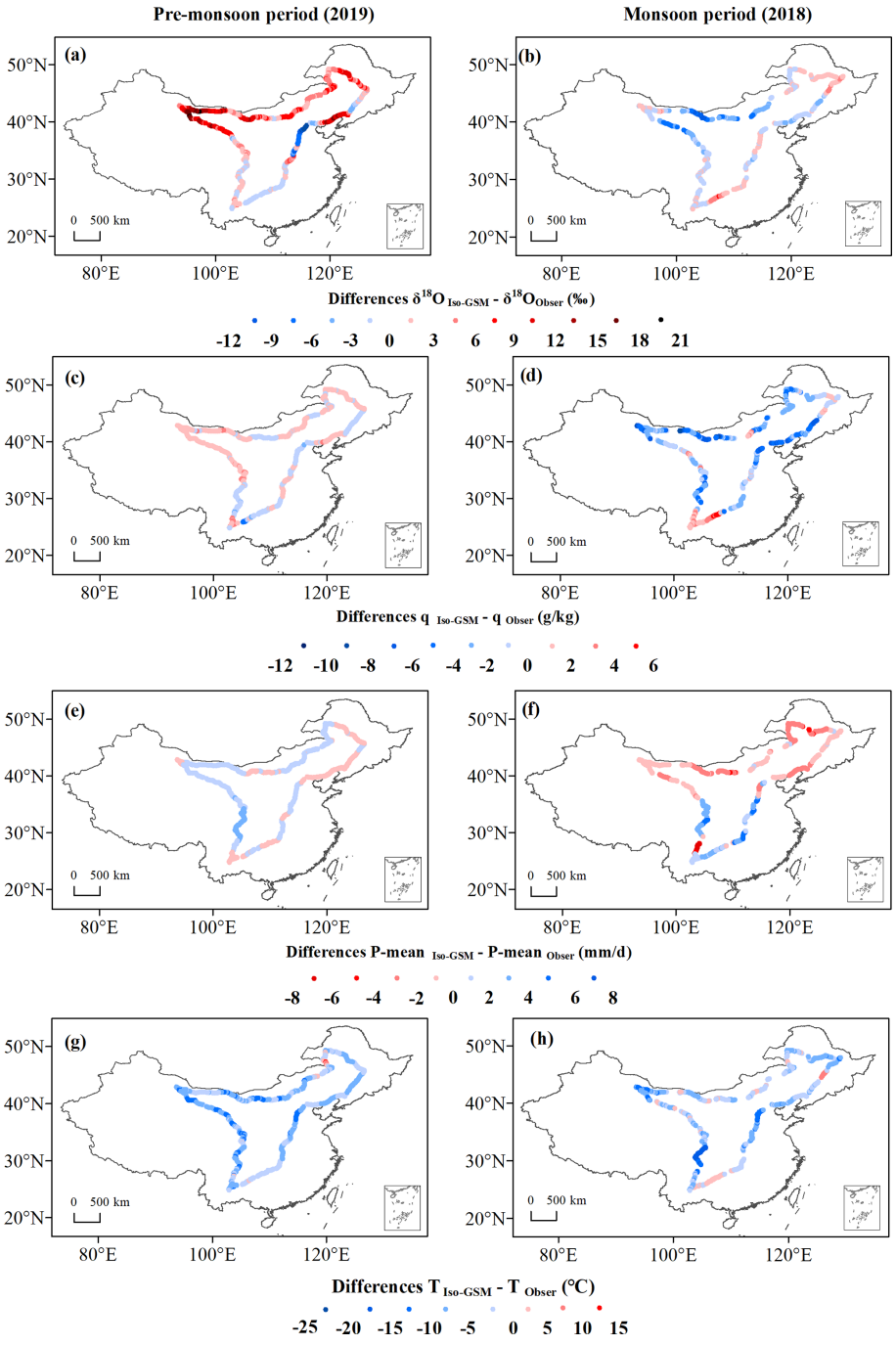

Figure 12. Spatial distribution of the differences between the outputs of Iso-GSM (subscripts are Iso-GSM) and observations (subscripts are Obser) during the pre-monsoon period (the left panel) and monsoon period (the right panel): $\delta^{18}O$ (**a** and **b**, ‰), specific humidity q (**c** and **d**, g kg^{-1}), average precipitation amount over the entire observation period for each observation location P mean **e** and **f**, mm d^{-1}), and temperature T (**g** and **h**, °C). Note that P mean Obser are interpolated from the GPCP dataset.

red) results in less depleted vapor in southern China (light red shades). The vapor d-excess in northern China is low (green triangles series), probably due to the high RH over high-latitude oceanic moisture sources for the vapor transported by the westerlies (green arrow), reducing the kinetic fractionation during ocean evaporation. In contrast, the lower RH over low-latitude moisture sources (yellow arrow) for the vapor transported to southern China leads to higher d-excess (yellow triangles series). Additional vapor sourced from continen-

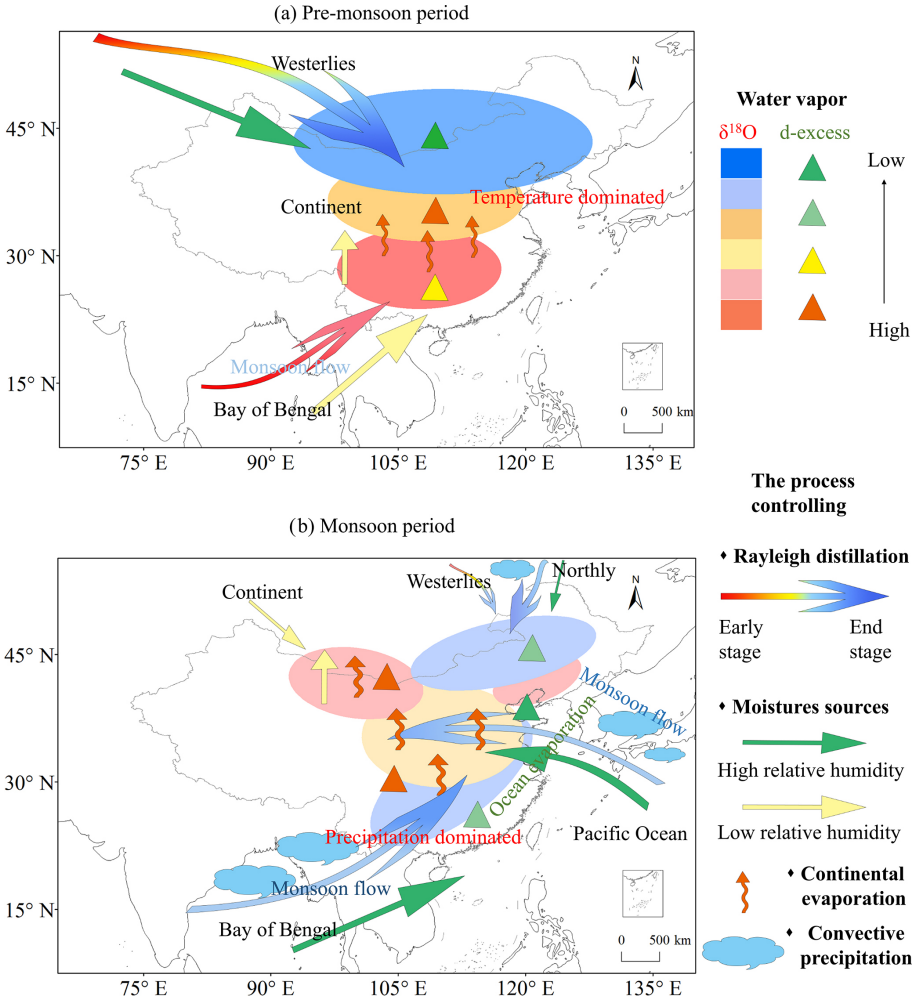

Figure 13. Schematic picture summarizing the different processes controlling the observed spatial patterns and seasonality of vapor isotopes. Color gradient arrows from red to blue represent the initial to subsequent extension of the Rayleigh distillation process along the water vapor trajectory, corresponding to high to low values of $\delta^{18}O$. The green arrows represent high relative humidity, the yellow arrows represent low relative humidity, the orange twisted arrows represent continental recycling, blue clouds represent strong and weak convective processes, green triangle series represents low values of d-excess; and the yellow triangle series represents high values of d-excess.

tal recycling (twisted orange arrows) further increases the d-excess values in middle China. This distribution is consistent with the back-trajectory results showing that during the pre-monsoon period, the vapor in southwestern China comes from the BoB, whereas westerly moisture sources still persist in northern China.

2. During the monsoon period (Fig. 13b), the lowest vapor $\delta^{18}O$ occurred in southwestern and northeastern China, and higher vapor $\delta^{18}O$ values were observed in between, while the d-excess features a West–East contrast. The relatively lower vapor $\delta^{18}O$ results from deep convection along the moisture transport pathway (blue clouds, arrows fading to blue). Meanwhile, the mixing with moisture from continental recycling (twisted orange arrows) increases the vapor $\delta^{18}O$ values in middle and northwestern China. We observed lower vapor $\delta^{18}O$ values when the moisture originates from the BoB than from the Pacific Ocean, consistent with stronger convection during transport. The dominance of oceanic wet moisture (green arrows) results in the lower vapor d-excess (green triangle series) in eastern China, whereas continental recycling produces higher vapor d-excess in western and northwestern China (yellow triangle series).

3. Variation in temperature drives the seasonal variations of vapor $\delta^{18}O$ in northern China, whereas convective activity along trajectories produces low vapor $\delta^{18}O$ during the monsoon season and drives the seasonal variation in South China. Seasonal d-excess variation reflects different conditions in the sources of vapor: in southeastern

China, it is mainly due to differences in the RH over the adjacent ocean surface, while in northwestern China, it is mainly due to the vapor transported by the westerlies during the pre-monsoon period and a great contribution of continental recycling during the monsoon period.

Iso-GSM simulations and IASI satellite measurements indicate that during the pre-monsoon period, the observed temporal variations along the route across China are mainly due to multiyear seasonal mean spatial variations and marginally due to synoptic-scale variations. During the monsoon season, synoptic-scale and intraseasonal variations might contribute significantly to the apparent spatial patterns. However, since these variations have a smaller amplitude than seasonal differences, the comparison of the two snapshots do provide a representative picture of the climatological seasonal difference.

Our study on the processes governing water vapor isotopic composition at the regional scale provides an overview of the spatial distribution and seasonal variability of water isotopes and their controlling factors, providing an improved framework for interpreting the paleoclimate proxy records of the hydrological cycle in low and mid-latitudes. In particular, our results suggest a strong interaction between local factors and circulation, emphasizing the need to interpret proxy records in the context of the regional system. This also suggests the potential for changes in circulation to confound interpretations of proxy data.

Data availability. The data acquired during the field campaigns can be accessed via the following: (1) https://doi.org/10.1594/PANGAEA.947606 (Wang and Tian, 2022a) and (2) https://doi.org/10.1594/PANGAEA.947627 (Wang and Tian, 2022b). Other data used can be downloaded from the corresponding websites which are listed in the text.

Supplement. The supplement related to this article is available online at: https://doi.org/10.5194/acp-23-3409-2023-supplement.

Author contributions. LT and DW designed the research. DW, and XW conducted the field observations. JC and GJB contributed to the data calibration. ZW and KY performed the Iso-GCM simulations. DW, CR, and LT performed the analysis. All authors contributed to the discussion of the results and the final article. DW drafted the paper with contributions from all co-authors. CR, LT, GJB, LZXL, ZW and JC checked and modified the paper.

Competing interests. The contact author has declared that none of the authors has any competing interests.

Disclaimer. Publisher's note: Copernicus Publications remains neutral with regard to jurisdictional claims in published maps and institutional affiliations.

Acknowledgements. The authors gratefully acknowledge NCAR/NCEP, GPCP and NOAA for provision of regional and large-scale meteorological data. We are grateful to the NOAA Air Resources Laboratory (ARL) that provided the HYSPLIT transport and dispersion model (http://ready.arl.noaa.gov/HYSPLIT.php, last access: March 2022) and the HYSPLIT-compatible meteorological dataset from GDAS. We thankfully acknowledge Yao Zhang, Xiaowen Zeng, and Min Gan for technical assistance. We thank Mingxing Tang and Ruoqun Zhang for partly participating in the field observations. We thank to Zhaowei Jing for the discussions on Rayleigh distillation lines, and we thankfully acknowledge Yao Li, Zhongyin Cai, and Rong Jiao for sharing some methods to use the Hysplit4 model. This work has been supported by the National Natural Science Foundation of China (grant nos. U2202208 and 42271143), the Applied Basic Research Foundation of Yunnan Province (grant no. 202201BF070001-021), and the Research Innovation Project for Graduate Students of Yunnan University (grant nos. 2018Z098 and 2021Y040).

Financial support. This research has been supported by the National Natural Science Foundation of China (grant nos. U2202208 and 42271143), the Applied Basic Research Foundation of Yunnan Province (grant no. 202201BF070001-021), and the Research Innovation Project for Graduate Students of Yunnan University (grant nos. 2018Z098 and 2021Y040).

Review statement. This paper was edited by Eliza Harris and reviewed by two anonymous referees.

References

Acharya, S., Yang, X., Yao, T., and Shrestha, D.: Stable isotopes of precipitation in Nepal Himalaya highlight the topographic influence on moisture transport, Quatern. Int., 565, 22–30, https://doi.org/10.1016/j.quaint.2020.09.052, 2020.

Aemisegger, F., Pfahl, S., Sodemann, H., Lehner, I., Seneviratne, S. I., and Wernli, H.: Deuterium excess as a proxy for continental moisture recycling and plant transpiration, Atmos. Chem. Phys., 14, 4029–4054, https://doi.org/10.5194/acp-14-4029-2014, 2014.

Aemisegger, F., Spiegel, J., Pfahl, S., Sodemann, H., Eugster, W., and Wernli, H.: Isotope meteorology of cold front passages: A case study combining observations and modeling, Geophys. Res. Lett., 42, 5652–5660, https://doi.org/10.1002/2015gl063988, 2015.

Aemisegger, F. and Papritz, L.: A climatology of strong large-scale ocean evaporation events. Part I: Identification, global distribution, and associated climate conditions, J. Climate, 31, 7287–7312, https://doi.org/10.1175/jcli-d-17-0591.1, 2018.

Aggarwal, P. K., Fröhlich, K., Kulkarni, K. M., and Gourcy, L. L.: Stable isotope evidence for moisture sources in the asian summer

monsoon under present and past climate regimes, Geophys. Res. Lett., 31, 239–261, https://doi.org/10.1029/2004gl019911, 2004.

Araguás-Araguás, L., Froehlich, K., and Rozanski, K.: Stable isotope composition of precipitation over southeast Asia, J. Geophys. Res.-Atmos., 103, 28721–28742, https://doi.org/10.1029/98jd02582, 1998.

Bailey, A., Toohey, D., and Noone, D.: Characterizing moisture exchange between the Hawaiian convective boundary layer and free troposphere using stable isotopes in water, J. Geophys. Res.-Atmos., 118, 8208–8221, https://doi.org/10.1002/jgrd.50639, 2013.

Benetti, M., Steen-Larsen, H. C., Reverdin, G., Sveinbjörnsdóttir, Á. E., Aloisi, G., Berkelhammer, M. B., Bourlès, B., Bourras, D., De Coetlogon, G., and Cosgrove, A.: Stable isotopes in the atmospheric marine boundary layer water vapour over the Atlantic Ocean, 2012–2015, Scientific Data, 4, 160128, https://doi.org/10.1038/sdata.2016.128, 2017.

Bershaw, J., Penny, S. M., and Garzione, C. N.: Stable isotopes of modern water across the Himalaya and eastern Tibetan Plateau: Implications for estimates of paleoelevation and paleoclimate, J. Geophys. Res.-Atmos., 117, D02110, https://doi.org/10.1029/2011jd016132, 2012.

Bhattacharya, S. K., Sarkar, A., and Liang, M. C.: Vapor isotope probing of typhoons invading the Taiwan region in 2016, J. Geophys. Res.-Atmos., 127, e2022JD036578, https://doi.org/10.1029/2022jd036578, 2022.

Bonne, J.-L., Behrens, M., Meyer, H., Kipfstuhl, S., Rabe, B., Schönicke, L., Steen-Larsen, H. C., and Werner, M.: Resolving the controls of water vapour isotopes in the Atlantic sector, Nat. Commun., 10, 1632, https://doi.org/10.1038/s41467-019-09242-6, 2019.

Bony, S., Risi, C., and Vimeux, F.: Influence of convective processes on the isotopic composition (δ^{18}O and δD) of precipitation and water vapor in the tropics: 1. Radiative-convective equilibrium and Tropical Ocean–Global Atmosphere–Coupled Ocean-Atmosphere Response Experiment (TOGA-COARE) simulations, J. Geophys. Res.-Atmos., 113, D19305, https://doi.org/10.1029/2008jd009942, 2008.

Bowen, G. J. and Revenaugh, J.: Interpolating the isotopic composition of modern meteoric precipitation, Water Resour. Res., 39, 1299, https://doi.org/10.1029/2003wr002086, 2003.

Bowen, G. J., Cai, Z., Fiorella, R. P., and Putman, A. L.: Isotopes in the Water Cycle: Regional-to Global-Scale Patterns and Applications, Annu. Rev. Earth Pl. Sc., 47, 457–479, https://doi.org/10.1146/annurev-earth-053018-060220, 2019.

Brown, J., Simmonds, I., and Noone, D.: Modeling δ^{18}O in tropical precipitation and the surface ocean for present-day climate, J. Geophys. Res.-Atmos., 111, D05105, https://doi.org/10.1029/2004jd005611, 2006.

Brubaker, K. L., Entekhabi, D., and Eagleson, P.: Estimation of continental precipitation recycling, J. Climate, 6, 1077–1089, https://doi.org/10.1175/1520-0442(1993)006<1077:eocpr>2.0.co;2, 1993.

Cai, Z. and Tian, L.: Processes governing water vapor isotope composition in the Indo-Pacific region: Convection and water vapor transport, J. Climate, 29, 8535–8546, https://doi.org/10.1175/JCLI-D-16-0297.1, 2016.

Cai, Z., Tian, L., and Bowen, G. J.: Spatial-seasonal patterns reveal large-scale atmospheric controls on Asian Monsoon precipitation water isotope ratios, Earth Planet. Sc. Lett., 503, 158–169, https://doi.org/10.1016/j.epsl.2018.09.028, 2018.

Dansgaard, W.: Stable isotopes in precipitation, Tellus, 16, 436–468, https://doi.org/10.1111/j.2153-3490.1964.tb00181.x, 1964.

Domrös, M. and Peng, G.: The climate of China, 1st edn., Springer Science & Business Media, 56–77, ISBN 9781315202068, https://doi.org/10.4324/9781315202068-4, 2012.

Draxler, R. R. and Hess, G.: An overview of the HYSPLIT_4 modelling system for trajectories, Aust. Meteorol. Mag., 47, 295–308, 1998.

Fiorella, R. P., Bares, R., Lin, J. C., Ehleringer, J. R., and Bowen, G. J.: Detection and variability of combustion-derived vapor in an urban basin, Atmos. Chem. Phys., 18, 8529–8547, https://doi.org/10.5194/acp-18-8529-2018, 2018.

Fiorella, R. P., Bares, R., Lin, J. C., and Bowen, G. J.: Wintertime decoupling of urban valley and rural ridge hydrological processes revealed through stable water isotopes, Atmos. Environ., 213, 337–348, https://doi.org/10.1016/j.atmosenv.2019.06.022, 2019.

Galewsky, J. and Hurley, J. V.: An advection-condensation model for subtropical water vapor isotopic ratios, J. Geophys. Res.-Atmos., 115, D16116, https://doi.org/10.1029/2009jd013651, 2010.

Galewsky, J., Rella, C., Sharp, Z., Samuels, K., and Ward, D.: Surface measurements of upper tropospheric water vapor isotopic composition on the Chajnantor Plateau, Chile, Geophys. Res. Lett., 38, 198–205, https://doi.org/10.1029/2011gl048557, 2011.

Galewsky, J., Steen-Larsen, H. C., Field, R. D., Worden, J., Risi, C., and Schneider, M.: Stable isotopes in atmospheric water vapor and applications to the hydrologic cycle, Rev. Geophys., 54, 809–865, https://doi.org/10.1002/2015rg000512, 2016.

Gao, J., MassonDelmotte, V., Risi, C., He, Y., and Yao, T.: What controls precipitation δ^{18}O in the southern Tibetan Plateau at seasonal and intra-seasonal scales? A case study at Lhasa and Nyalam, Tellus B, 65, 21043, https://doi.org/10.3402/tellusb.v65i0.21043, 2013.

Gat, J. R.: Oxygen and hydrogen isotopes in the hydrologic cycle, Annu. Rev. Earth Planet. Sc., 24, 225–262, https://doi.org/10.1146/annurev.earth.24.1.225, 1996.

Gat, J. R. and Matsui, E.: Atmospheric water balance in the Amazon Basin: an isotopic evapotranspiration model, J. Geophys. Res.-Atmos., 96, 13179–13188, https://doi.org/10.1029/91jd00054, 1991.

Gedzelman, S.: Probing hurricanes with stable isotopes of rain and water vapor, Mon. Weather Rev., 131, 1112–1127, https://doi.org/10.1175/1520-0493(2003)131<1112:phwsio>2.0.co;2, 2003.

Gorski, G., Strong, C., Good, S. P., Bares, R., Ehleringer, J. R., and Bowen, G. J.: Vapor hydrogen and oxygen isotopes reflect water of combustion in the urban atmosphere, P. Natl. Acad. Sci. USA, 112, 3247–3252, https://doi.org/10.1073/pnas.1424728112, 2015.

Gralher, B., Herbstritt, B., Weiler, M., Wassenaar, L. I., and Stumpp, C.: Correcting laser-based water stable isotope readings biased by carrier gas changes, Environ. Sci. Technol., 50, 7074–7081, https://doi.org/10.1021/acs.est.6b01124, 2016.

Guo, X., Tian, L., Wen, R., Yu, W., and Qu, D.: Controls of precipitation δ^{18}O on the northwestern Tibetan Plateau: A case study at Ngari station, Atmos. Res., 189, 141–151, https://doi.org/10.1016/j.atmosres.2017.02.004, 2017.

He, Y., Risi, C., Gao, J., Masson-Delmotte, V., Yao, T., Lai, C. T., Ding, Y., Worden, J., Frankenberg, C., and Chepfer, H.: Impact of atmospheric convection on south Tibet summer precipitation isotopologue composition using a combination of in situ measurements, satellite data, and atmospheric general circulation modeling, J. Geophys. Res.-Atmos., 120, 3852–3871, https://doi.org/10.1002/2014jd022180, 2015.

Hou, J., Huang, Y., Oswald, W. W., Foster, D. R., and Shuman, B.: Centennial-scale compound-specific hydrogen isotope record of Pleistocene–Holocene climate transition from southern New England, Geophys. Res. Lett., 34, L19706, https://doi.org/10.1029/2007gl030303, 2007.

Johnson, J. E. and Rella, C. W.: Effects of variation in background mixing ratios of N_2, O_2, and Ar on the measurement of $\delta^{18}O$–H_2O and $\delta^{2}H$–H_2O values by cavity ring-down spectroscopy, Atmos. Meas. Tech., 10, 3073–3091, https://doi.org/10.5194/amt-10-3073-2017, 2017.

Jouzel, J., Alley, R., Cuffey, K., Dansgaard, W., Grootes, P., Hoffmann, G., Johnsen, S., Koster, R., Peel, D., and Shuman, C.: Validity of the temperature reconstruction from water isotopes in ice cores, J. Geophys. Res.-Oceans, 102, 26471–26487, https://doi.org/10.1029/97jc01283, 1997.

Khaykin, S. M., Moyer, E., Krämer, M., Clouser, B., Bucci, S., Legras, B., Lykov, A., Afchine, A., Cairo, F., Formanyuk, I., Mitev, V., Matthey, R., Rolf, C., Singer, C. E., Spelten, N., Volkov, V., Yushkov, V., and Stroh, F.: Persistence of moist plumes from overshooting convection in the Asian monsoon anticyclone, Atmos. Chem. Phys., 22, 3169–3189, https://doi.org/10.5194/acp-22-3169-2022, 2022.

Kikuchi, K.: The boreal summer intraseasonal oscillation (BSISO): A review, J. Meteorol. Soc. Jpn. Ser. II, 99, 933–972, https://doi.org/10.2151/jmsj.2021-045, 2021.

Klein, E. S., Cherry, J., Young, J., Noone, D., Leffler, A., and Welker, J.: Arctic cyclone water vapor isotopes support past sea ice retreat recorded in Greenland ice, Scientific Reports, 5, 10295, https://doi.org/10.1038/srep10295, 2015.

Kong, Y. and Pang, Z.: A positive altitude gradient of isotopes in the precipitation over the Tianshan Mountains: Effects of moisture recycling and sub-cloud evaporation, J. Hydrol., 542, 222–230, https://doi.org/10.1016/j.jhydrol.2016.09.007, 2016.

Kurita, N.: Origin of Arctic water vapor during the ice-growth season, Geophys. Res. Lett., 38, L02709, https://doi.org/10.1029/2010gl046064, 2011.

Li, Y., An, W., Pang, H., Wu, S. Y., Tang, Y., Zhang, W., and Hou, S.: Variations of Stable Isotopic Composition in Atmospheric Water Vapor and their Controlling Factors – A 6-Year Continuous Sampling Study in Nanjing, Eastern China, J. Geophys. Res.-Atmos., 125, e2019JD031697, https://doi.org/10.1029/2019jd031697, 2020.

Li, Y., Aemisegger, F., Riedl, A., Buchmann, N., and Eugster, W.: The role of dew and radiation fog inputs in the local water cycling of a temperate grassland during dry spells in central Europe, Hydrol. Earth Syst. Sci., 25, 2617–2648, https://doi.org/10.5194/hess-25-2617-2021, 2021.

Liebmann, B. and Smith, C. A.: Description of a complete (interpolated) outgoing longwave radiation dataset, B. Am. Meteorol. Soc., 77, 1275–1277, 1996.

Liu, J., Xiao, C., Ding, M., and Ren, J.: Variations in stable hydrogen and oxygen isotopes in atmospheric water vapor in the marine boundary layer across a wide latitude range, J. Environ. Sci., 26, 2266–2276, https://doi.org/10.1016/j.jes.2014.09.007, 2014.

Liu, Y., Cobb, K. M., Song, H., Li, Q., Li, C.-Y., Nakatsuka, T., An, Z., Zhou, W., Cai, Q., and Li, J.: Recent enhancement of central Pacific El Niño variability relative to last eight centuries, Nat. Commun., 8, 15386, https://doi.org/10.1038/ncomms15386, 2017.

McKinney, C. R., McCrea, J. M., Epstein, S., Allen, H., and Urey, H. C.: Improvements in mass spectrometers for the measurement of small differences in isotope abundance ratios, Rev. Sci. Instrum., 21, 724–730, https://doi.org/10.1063/1.1745698, 1950.

Mei'e, R., Renzhang, Y., and Haosheng, B.: An outline of China's physical geography, The World in Outline, 497–520, https://doi.org/10.1017/cbo9781316530399.026, 1985.

Merlivat, L. and Jouzel, J.: Global climatic interpretation of the deuterium-oxygen 18 relationship for precipitation, J. Geophys. Res.-Oceans, 84, 5029–5033, https://doi.org/10.1029/jc084ic08p05029, 1979.

Noone, D.: The influence of midlatitude and tropical overturning circulation on the isotopic composition of atmospheric water vapor and Antarctic precipitation, J. Geophys. Res.-Atmos., 113, D04102, https://doi.org/10.1029/2007jd008892, 2008.

Noone, D.: Pairing Measurements of the Water Vapor Isotope Ratio with Humidity to Deduce Atmospheric Moistening and Dehydration in the Tropical Midtroposphere, J. Climate, 25, 4476–4494, https://doi.org/10.1175/jcli-d-11-00582.1, 2012.

Pausata, F. S. R., Battisti, D. S., Nisancioglu, K. H., and Bitz, C. M.: Chinese stalagmite $\delta^{18}O$ controlled by changes in the Indian monsoon during a simulated Heinrich event, Nat. Geosci., 4, 474–480, https://doi.org/10.1038/ngeo1169, 2011.

Pfahl, S. and Sodemann, H.: What controls deuterium excess in global precipitation?, Clim. Past, 10, 771–781, https://doi.org/10.5194/cp-10-771-2014, 2014.

Putman, A. L., Fiorella, R. P., Bowen, G. J., and Cai, Z.: A global perspective on local meteoric water lines: Meta-analytic insight into fundamental controls and practical constraints, Water Resour. Res., 55, 6896–6910, https://doi.org/10.1029/2019wr025181, 2019.

Risi, C., Bony, S., and Vimeux, F.: Influence of convective processes on the isotopic composition ($\delta^{18}O$ and δD) of precipitation and water vapor in the tropics: 2. Physical interpretation of the amount effect, J. Geophys. Res.-Atmos., 113, D19306, https://doi.org/10.1029/2008jd009943, 2008a.

Risi, C., Bony, S., Vimeux, F., Descroix, L., Ibrahim, B., Lebreton, E., Mamadou, I., and Sultan, B.: What controls the isotopic composition of the African monsoon precipitation? Insights from event-based precipitation collected during the 2006 AMMA field campaign, Geophys. Res. Lett., 35, 851–854, https://doi.org/10.1029/2008gl035920, 2008b.

Risi, C., Bony, S., Vimeux, F., and Jouzel, J.: Water-stable isotopes in the LMDZ4 general circulation model: Model evaluation for present-day and past climates and applications to climatic interpretations of tropical isotopic records, J. Geophys. Res.-Atmos., 115, D12118, https://doi.org/10.1029/2009jd013255, 2010.

Risi, C., Noone, D., Worden, J., Frankenberg, C., Stiller, G., Kiefer, M., Funke, B., Walker, K., Bernath, P., Schneider, M., Wunch, D., Sherlock, V., Deutscher, N., Griffith, D., Wennberg, P. O., Strong, K., Smale, D., Mahieu, E., Barthlott, S., Hase, F., Garcia, O., Notholt, J., Warneke, T., Toon, G., Sayres, D., Bony, S., Lee,

J., Brown, D., Uemura, R., and Sturm, C.: Process-evaluation of tropospheric humidity simulated by general circulation models using water vapor isotopologues: 1. Comparison between models and observations, J. Geophys. Res.-Atmos., 117, D05303, https://doi.org/10.1029/2011jd016621, 2012.

Risi, C., Landais, A., Winkler, R., and Vimeux, F.: Can we determine what controls the spatio-temporal distribution of d-excess and ^{17}O-excess in precipitation using the LMDZ general circulation model?, Clim. Past, 9, 2173–2193, https://doi.org/10.5194/cp-9-2173-2013, 2013a.

Risi, C., Noone, D., Frankenberg, C., and Worden, J.: Role of continental recycling in intraseasonal variations of continental moisture as deduced from model simulations and water vapor isotopic measurements, Water Resour. Res., 49, 4136–4156, https://doi.org/10.1002/wrcr.20312, 2013b.

Roca, R., Chambon, P., Jobard, I., Kirstetter, P.-E., Gosset, M., and Bergès, J. C.: Comparing satellite and surface rainfall products over West Africa at meteorologically relevant scales during the AMMA campaign using error estimates, J. Appl. Meteorol. Clim., 49, 715–731, https://doi.org/10.1175/2009jamc2318.1, 2010.

Salati, E., Dall'Olio, A., Matsui, E., and Gat, J. R.: Recycling of water in the Amazon basin: an isotopic study, Water Resour. Res., 15, 1250–1258, https://doi.org/10.1029/wr015i005p01250, 1979.

Salmon, O. E., Welp, L. R., Baldwin, M. E., Hajny, K. D., Stirm, B. H., and Shepson, P. B.: Vertical profile observations of water vapor deuterium excess in the lower troposphere, Atmos. Chem. Phys., 19, 11525–11543, https://doi.org/10.5194/acp-19-11525-2019, 2019.

Samuels-Crow, K. E., Galewsky, J., Sharp, Z. D., and Dennis, K. J.: Deuterium excess in subtropical free troposphere water vapor: Continuous measurements from the Chajnantor Plateau, northern Chile, Geophys. Res. Lett., 41, 8652–8659, https://doi.org/10.1002/2014gl062302, 2015.

Sánchez-Murillo, R., Durán-Quesada, A. M., Esquivel-Hernández, G., Rojas-Cantillano, D., Birkel, C., Welsh, K., Sánchez-Llull, M., Alonso-Hernández, C. M., Tetzlaff, D., and Soulsby, C.: Deciphering key processes controlling rainfall isotopic variability during extreme tropical cyclones, Nat. Commun., 10, 4321, https://doi.org/10.1038/s41467-019-12062-3, 2019.

Saranya, P., Krishan, G., Rao, M., Kumar, S., and Kumar, B.: Controls on water vapor isotopes over Roorkee, India: Impact of convective activities and depression systems, J. Hydrol., 557, 679–687, https://doi.org/10.1016/j.jhydrol.2017.12.061, 2018.

Schmidt, M., Maseyk, K., Lett, C., Biron, P., Richard, P., Bariac, T., and Seibt, U.: Concentration effects on laser-based δ^{18}O and δ^{2}H measurements and implications for the calibration of vapour measurements with liquid standards, Rapid Commun. Mass Sp., 24, 3553–3561, https://doi.org/10.1002/rcm.4813, 2010.

Schneider, D. P. and Noone, D. C.: Spatial covariance of water isotope records in a global network of ice cores spanning twentieth-century climate change, J. Geophys. Res.-Atmos., 112, D18105, https://doi.org/10.1029/2007jd008652, 2007.

Shi, X., Risi, C., Pu, T., Lacour, J. l., Kong, Y., Wang, K., He, Y., and Xia, D.: Variability of isotope composition of precipitation in the southeastern Tibetan Plateau from the synoptic to seasonal time scale, J. Geophys. Res.-Atmos., 125, e2019JD031751, https://doi.org/10.1029/2019jd031751, 2020.

Steen-Larsen, H. C., Johnsen, S. J., Masson-Delmotte, V., Stenni, B., Risi, C., Sodemann, H., Balslev-Clausen, D., Blunier, T., Dahl-Jensen, D., Ellehøj, M. D., Falourd, S., Grindsted, A., Gkinis, V., Jouzel, J., Popp, T., Sheldon, S., Simonsen, S. B., Sjolte, J., Steffensen, J. P., Sperlich, P., Sveinbjörnsdóttir, A. E., Vinther, B. M., and White, J. W. C.: Continuous monitoring of summer surface water vapor isotopic composition above the Greenland Ice Sheet, Atmos. Chem. Phys., 13, 4815–4828, https://doi.org/10.5194/acp-13-4815-2013, 2013.

Steen-Larsen, H. C., Risi, C., Werner, M., Yoshimura, K., and Masson-Delmotte, V.: Evaluating the skills of isotope-enabled General Circulation Models against in-situ atmospheric water vapor isotope observations, J. Geophys. Res., 122, 246–263, https://doi.org/10.1002/2016jd025443, 2017.

Tan, M.: Circulation effect: response of precipitation delta δ^{18}O to the ENSO cycle in monsoon regions of China, Clim. Dynam., 42, 1067–1077, https://doi.org/10.1007/s00382-013-1732-x, 2014.

Terzer-Wassmuth, S., Wassenaar, L. I., Welker, J. M., and Araguás-Araguás, L. J.: Improved high-resolution global and regionalized isoscapes of δ^{18}O, δ^{2}H and d-excess in precipitation, Hydrol. Process., 35, e14254, https://doi.org/10.1002/hyp.14254, 2021.

Thompson, L. G.: Ice core evidence for climate change in the Tropics: implications for our future, Quaternary Sci. Rev., 19, 19–35, https://doi.org/10.1016/s0277-3791(99)00052-9, 2000.

Thompson, L. G., Yao, T., Mosley-Thompson, E., Davis, M., Henderson, K., and Lin, P.-N.: A high-resolution millennial record of the South Asian monsoon from Himalayan ice cores, Science, 289, 1916–1919, https://doi.org/10.1126/science.289.5486.1916, 2000.

Thompson, L. O., Mosley-Thompson, E., Davis, M., Lin, P., Yao, T., Dyurgerov, M., and Dai, J.: "Recent warming": ice core evidence from tropical ice cores with emphasis on Central Asia, Global Planet. Change, 7, 145–156, https://doi.org/10.1016/0921-8181(93)90046-q, 1993.

Thompson, L. O., Yao, T., Davis, M., Henderson, K., Mosley-Thompson, E., Lin, P.-N., Beer, J., Synal, H.-A., Cole-Dai, J., and Bolzan, J.: Tropical climate instability: The last glacial cycle from a Qinghai-Tibetan ice core, Science, 276, 1821–1825, https://doi.org/10.1126/science.276.5320.1821, 1997.

Thurnherr, I., Kozachek, A., Graf, P., Weng, Y., Bolshiyanov, D., Landwehr, S., Pfahl, S., Schmale, J., Sodemann, H., Steen-Larsen, H. C., Toffoli, A., Wernli, H., and Aemisegger, F.: Meridional and vertical variations of the water vapour isotopic composition in the marine boundary layer over the Atlantic and Southern Ocean, Atmos. Chem. Phys., 20, 5811–5835, https://doi.org/10.5194/acp-20-5811-2020, 2020.

Tian, L., Yao, T., Schuster, P. F., White, J. W. C., Ichiyanagi, K., Pendall, E., Pu, J., and Yu, W.: Oxygen-18 concentrations in recent precipitation and ice cores on the Tibetan Plateau, J. Geophys. Res.-Atmos., 108, 4293, https://doi.org/10.1029/2002jd002173, 2003.

Tian, L., Yao, T., Li, Z., MacClune, K., Wu, G., Xu, B., Li, Y., Lu, A., and Shen, Y.: Recent rapid warming trend revealed from the isotopic record in Muztagata ice core, eastern Pamirs, J. Geophys. Res.-Atmos., 111, D13103, https://doi.org/10.1029/2005jd006249, 2006.

Tian, L., Yao, T., MacClune, K., White, J. W. C., Schilla, A., Vaughn, B., Vachon, R., and Ichiyanagi, K.: Stable isotopic variations in west China: A consideration of

moisture sources, J. Geophys. Res.-Atmos., 112, D10112, https://doi.org/10.1029/2006jd007718, 2007.

Tian, L., Yu, W., Schuster, P. F., Wen, R., Cai, Z., Wang, D., Shao, L., Cui, J., and Guo, X.: Control of seasonal water vapor isotope variations at Lhasa, southern Tibetan Plateau, J. Hydrol., 580, 124237, https://doi.org/10.1016/j.jhydrol.2019.124237, 2020.

Van Breukelen, M., Vonhof, H., Hellstrom, J., Wester, W., and Kroon, D.: Fossil dripwater in stalagmites reveals Holocene temperature and rainfall variation in Amazonia, Earth Planet. Sc. Lett., 275, 54–60, https://doi.org/10.1016/j.epsl.2008.07.060, 2008.

Vimeux, F., Gallaire, R., Bony, S., Hoffmann, G., and Chiang, J. C.: What are the climate controls on δD in precipitation in the Zongo Valley (Bolivia)? Implications for the Illimani ice core interpretation, Earth Planet. Sc. Lett., 240, 205–220, https://doi.org/10.1016/j.epsl.2005.09.031, 2005.

Wallace, J. M. and Hobbs, P. V.: Atmospheric science: an introductory survey, International Geophysics Series, ISSN 0074-6142, Elsevier Academic Press, 483 pp., ISBN 012732951X, 9780127329512 2006.

Wang, B.: Rainy season of the Asian–Pacific summer monsoon, J. Climate, 15, 386–398, https://doi.org/10.1175/1520-0442(2002)015<0386:rsotap>2.0.co;2, 2002.

Wang, B. and Xu, X.: Northern Hemisphere summer monsoon singularities and climatological intraseasonal oscillation, J. Climate, 10, 1071–1085, https://doi.org/10.1175/1520-0442(1997)010<1071:nhsmsa>2.0.co;2, 1997.

Wang, D. and Tian, L.: Vehicle-based in-situ observations of the water vapor isotopic composition across China during the monsoon season 2018, PANGAEA [data set], https://doi.org/10.1594/PANGAEA.947606, 2022a.

Wang, D. and Tian, L.: Vehicle-based in-situ observations of the water vapor isotopic composition across China during the pre-monsoon season 2019, PANGAEA [data set], https://doi.org/10.1594/PANGAEA.947627, 2022b.

Wang, D. and Wang, K.: Isotopes in precipitation in China (1986–1999), Sci. China Ser. E, 44, 48–51, https://doi.org/10.1007/bf02916789, 2001.

Wang, G., Lan, H., and Liu, Z.: Stable isotope record of super typhoon Lekima (2019), Atmos. Res., 264, 105822, https://doi.org/10.1016/j.atmosres.2021.105822, 2021.

Wang, Q. and Zhang, L.: Analysis of the August 2018 atmosphere circulation and weather, Meteorological Monthly, 44, 1501–1508, 2018.

West, J. B., Bowen, G. J., Dawson, T. E., and Tu, K. P.: Isoscapes: understanding movement, pattern, and process on Earth through isotope mapping, Springer Nature, 511 pp., ISBN 9789048133536, 2009.

Winnick, M. J., Chamberlain, C. P., Caves, J. K., and Welker, J. M.: Quantifying the isotopic "continental effect", Earth Planet. Sc. Lett., 406, 123–133, https://doi.org/10.1016/j.epsl.2014.09.005, 2014.

Worden, J., Noone, D., Bowman, K., and Tropospheric Emission, S.: Importance of rain evaporation and continental convection in the tropical water cycle, Nature, 445, 528–532, https://doi.org/10.1038/nature05508, 2007.

Wright, H. E.: Global climates since the last glacial maximum, University of Minnesota Press Minneapolis, 569 pp., ISBN 9780816621453 0816621454, 1993.

Yao, T., Ding, L., Pu, J., Liu, J., and Yang, Z.: Characteristic of δ^{18}O in snow and its relation with moisture sources in Tanggula Mountains, Tibetan Plateau, Chinese Sci. Bull., 36, 1570–1573, 1991.

Yoshimura, K. and Kanamitsu, M.: Specification of External Forcing for Regional Model Integrations, Mon. Weather Rev., 137, 1409–1421, https://doi.org/10.1175/2008mwr2654.1, 2009.